Probing the Dynamics of Red Fluorescent Protein Variants using NMR Spectroscopy: How Directed Development Affected Protein Dynamics

by

Laura A. Johnson

B.S., Montana State University, 2008

A thesis submitted to the

Faculty of the Graduate School of the

University of Colorado in partial fulfillment

of the requirements for the degree of

Doctor of Philosophy

College of Arts & Sciences Department of Chemistry & Biochemistry

2013

This thesis entitled:
Probing the Dynamics of Red Fluorescent Protein Variants using NMR Spectroscopy: How Directed Development Affected Protein Dynamics
written by Laura A. Johnson
has been approved for the College of Arts & Sciences Department of Chemistry & Biochemistry

Arthur Pardi

Deborah Wuttke

Amy Palmer

Date

The final copy of this thesis has been examined by the signatories, and we find that both the content and the form meet acceptable presentation standards of scholarly work in the above mentioned discipline.

Johnson, Laura A. (Ph.D., Biochemistry)

Probing the Dynamics of Red Fluorescent Protein Variants using NMR Spectroscopy: How Directed Development Affected Protein Dynamics

Thesis directed by Prof. Arthur Pardi

Fluorescent proteins are commonly used genetically encodable tools for probing intracellular events in real time. Red fluorescent proteins (RFPs) are particularly useful because scattering and absorption are reduced in cells excited at longer wavelengths. Development of RFPs with increased quantum yield and wavelength of emission, among other photophysical properties, is an active area of research; but the optimization of one property is often accompanied by other deleterious effects. This work explores how differences in the photophysical properties of various RFPs may arise from changes in protein dynamics as a product of protein directed development. NMR relaxation experiments were used to probe ps-ns dynamics for the backbone amides, as well as the chromophore tyrosine $C^{\beta}H$ of mCherry, mRaspberry and mRojoB, three closely related monomeric RFPs with different quantum yields. Results indicate restricted dynamics in the backbone amides and the chromophore tyrosine $C^{\beta}H$ of the three monomeric RFPs tested. The results of NMR relaxation dispersion experiments suggested differences in μs-ms timescale dynamics in the backbone amides and δ, δ, and γ methyls of isoleucine, leucine and valine residues, respectively, among the same three RFPs. Hydrogen-deuterium exchange experiments were used to show that tdTomato, a dimeric RFP with a high quantum yield, has a higher propensity for local unfolding compared with monomeric mCherry and mRojoB, which have substantially lower quantum yields suggesting small degrees of local unfolding does not abolish fluorescence quantum yield in FPs. Differences in the temperature dependence of fluorescence and secondary structure were observed using fluorescence and CD spectroscopy supporting the idea that directed development affected global stability. How the directed development of RFPs with optimized photophysical properties affects protein dynamics is discussed.

Dedication

To Daisy

Acknowledgements

My graduate experience under the guidance of my advisor, Dr. Arthur Pardi, at the University of Colorado was made possible by years of interactions with other extraordinary teachers. My mom introduced me to the scientific processes when I was in elementary school, helping me test whether peas from store-bought seeds grew better in our garden than those grown from replanting seeds from the previous years' harvest. My dad lived what he preached in his environmental engineering classes and passed on his love for the environment to his children, teaching us conservation and mindful consumption. My sister, Katie, set a good example of work-life balance between academics and extra-curricular activities, and now runs, bikes and skis with me here in Colorado.

I would like to acknowledge my high school teachers Mr. Wenstrom, Mrs. Page, and Ms. Beale, for passing on their love of math, chemistry and biology to me. My college advisor, Dr. Pinet, encouraged me not to stop working when I had accomplished what was required of me academically. I thank him for sharing his love for his academic field and profession. I thank my PhD advisor for the opportunity to work in his lab and for teaching me to challenge myself in every aspect of my scientific career. Thanks to a previous member of the Pardi lab, Lisa Warner, who introduced to me to red fluorescent proteins and NMR. Thanks to my committee members for their advice and support, especially Deborah Wuttke for providing critical feedback on my thesis.

I am so grateful for the love and support from my wonderful friends and family. Thanks especially to Dan Hickstein for listening to me when I was excited about science and also when I wasn't. Again, Mom, Dad and Katie, without your support, this journey would have been impossible. Thank you.

Contents

Chapter

Tables

Table

Figures

Figure

Chapter 1

Introduction

1.1 The History and Directed Development of Fluorescent Proteins

The use of bioluminescent molecules to probe intracellular events in real time changed the face of cell biology. After the initial discovery of the light producing reaction between luciferin and luciferase in 1885 [1], the quest for novel bioluminescent systems began. During purification of the bioluminescent protein, aequorin, from the jellyfish species *Aequorea victoria*, a companion protein, green fluorescent protein (GFP), was discovered by Shimomura in 1962 [2]. Unlike luciferase and aequorin which produce light through enzymatic reactions with substrates, only light and molecular oxygen were required for the use of GFP as a tool to monitor intercellular events [3]. This advantage lead to the development of GFP as a genetically encodable probe through the isolation and recombinant expression of the gene encoding GFP in bacteria and *C. elegans* [4, 5]. Fluorescent proteins have since been discovered in organisms across several phyla of life [6]. The phylum Anthozoa has more than a dozen examples of naturally occurring fluorescent proteins that are thought to mediate the interactions between corals and algae [7].

In 1994, Heim, Prasher and Tsien started performing mutagenesis on the wild-type GFP to create variants that absorbed and fluoresced at different wavelengths [8]. The solution of the crystal structure of GFP, an eleven-stranded β-barrel protein surrounding an internal α-helix, in 1996 aided in the development of novel FPs targeting residues near the chromophore for mutation [9]. Mutagenesis allowed for the creation of a color palette of fluorescent proteins that fluoresced from blue to yellow [10]. Since the initial discovery of GFP, fluorescent proteins spanning the visible spectrum have been developed [2, 11–14]. In 2008, the

Nobel Prize was awarded to Roger Tsien, Martin Chalfie and Osamu Shimomura for their contributions to the fluorescent protein field.

Red fluorescent proteins (RFPs) are particularly useful tools for studying whole animals due to reduced optical scattering and auto-fluorescence at wavelengths longer than 650-700 nm, in a range known as the optical window [15–19]. A naturally occurring red fluorescent protein, named DsRed, was isolated from an Anthozoa species of coral was isolated in 1999, thereby expanding the color palette of available fluorescent proteins [20]. Another naturally occurring red fluorescent protein, eqFP578, was isolated from a sea anemone *Entacmaea quadricolor* [21]. Both naturally occurring red fluorescent proteins were found to form oligomers. Wild-type red fluorescent protein, DsRed, was found to be an obligate tetramer, and eqFP578 an obligate dimer. The use of DsRed or eqFP578 as a protein tag for monitoring protein expression was hindered by their oligomeric states, which could cause artificial interactions between proteins when recombinantly expressed. Thus, a monomeric variant of DsRed, mRFP1.0, was developed in the Tsien lab [22]. From mRFP1, the mFruit series was developed which introduced an additional set of monomeric fluorescent protein variants that fluoresced at a range of wavelengths from green to red [23]. Similarly, monomeric variants of eqFP578, called TagRFP and mKate, were developed [21]. The pursuit of an even more red shifted fluorescent protein is ongoing. mRaspberry (λ_{em}=625 nm) [24] and mRojoB (λ_{em}=631 nm) [25] were developed in the Tsien and Mayo labs, respectively, with the goal of increasing the wavelength of fluorescence emission. Many techniques have been used to develop new RFPs including error prone PCR [12, 22], rational design of cite specific mutations [25], or somatic hypermutation [26] and subsequent colony screening or flow cytometry [27, 28]. Combined, the various techniques used to generate novel FPs will be referred to as 'directed development'.

The crystal structures solved for DsRed and one of the mFruits, mCherry, were found to be highly structurally homologous to GFP. As in GFP, 3 amino acids, located in the internal α-helix of the protein, form the chromophore through self-catalyzed cyclization, dehydration and oxidation reactions [11]. These reactions form the conjugated system that absorbs and emits light in the visible region of the spectrum. However, an additional oxidation step during the formation of the red chromophore extends the conjugated system, thus increasing the wavelength of absorption and emission relative to the GFP chromophore [29]. Figures 1.1, 1.2, and 1.3 show a side view of cartoon of the crystal structure of mCherry, along with a

top down view looking into the interior of the β-barrel, and the structure of the chromophore formed from the amino acids methionine, tyrosine, and glycine [30]. Although the precise mechanism of chromophore formation is still in dispute [6], the general scheme for red fluorescent protein chromophore formation is shown in Figure 1.4.

Fluorescent proteins are valuable tools used as genetically encodable probes with a range of applications from monitoring protein expression and localization [5], to protein-protein interactions [11], and intracellular metabolites [32,33]. The availability of FPs with a range of excitation and emission wavelengths allows simultaneous monitoring of multiple proteins of interest. Due to the wide range of applications of these genetically encodable tools in cell biology, the optimization of photophysical properties such as quantum yield, wavelength of emission, and photostability in fluorescent proteins has been widely pursued [22, 23, 34–37].

The fluorescence quantum yield is the ratio of the number of photons fluoresced to those absorbed and is directly related to brightness by the product of quantum yield and the extinction coefficient. The photostability of a fluorophore refers to the number of photons a fluorophore emits before undergoing irreversible photo-destruction of the chromophore, rendering it non-fluorescent. The number of photons fluorescent proteins can output before photo-degradation is between 10^4 to 10^5 [38]. The brightness of a fluorophore depends on both the quantum yield and the extinction coefficient, ϵ (Equation 1.1). The quantum yield, Φ, is defined as the ratio of the number of photons fluoresced to the number absorbed (Equation 1.2). The quantum yields of FPs currently range from less than 0.1 to greater than 0.9 and extinction coefficients from less than 10,000 M^{-1} to larger than 100,000 M^{-1}.

$$Brightness = \Phi \times \epsilon \tag{1.1}$$

$$\Phi = \frac{\#\text{ photons fluoresced}}{\#\text{ photons absorbed}} \tag{1.2}$$

Wild-type RFPs have been isolated from coral [20] and sea anemones [21] and are obligate dimers or tetramers, but the protein-protein interfaces were disrupted during the development of monomeric proteins for use as genetically encodable probes [21–23, 39]. Wild-type tetramer DsRed has a quantum yield of 0.79,

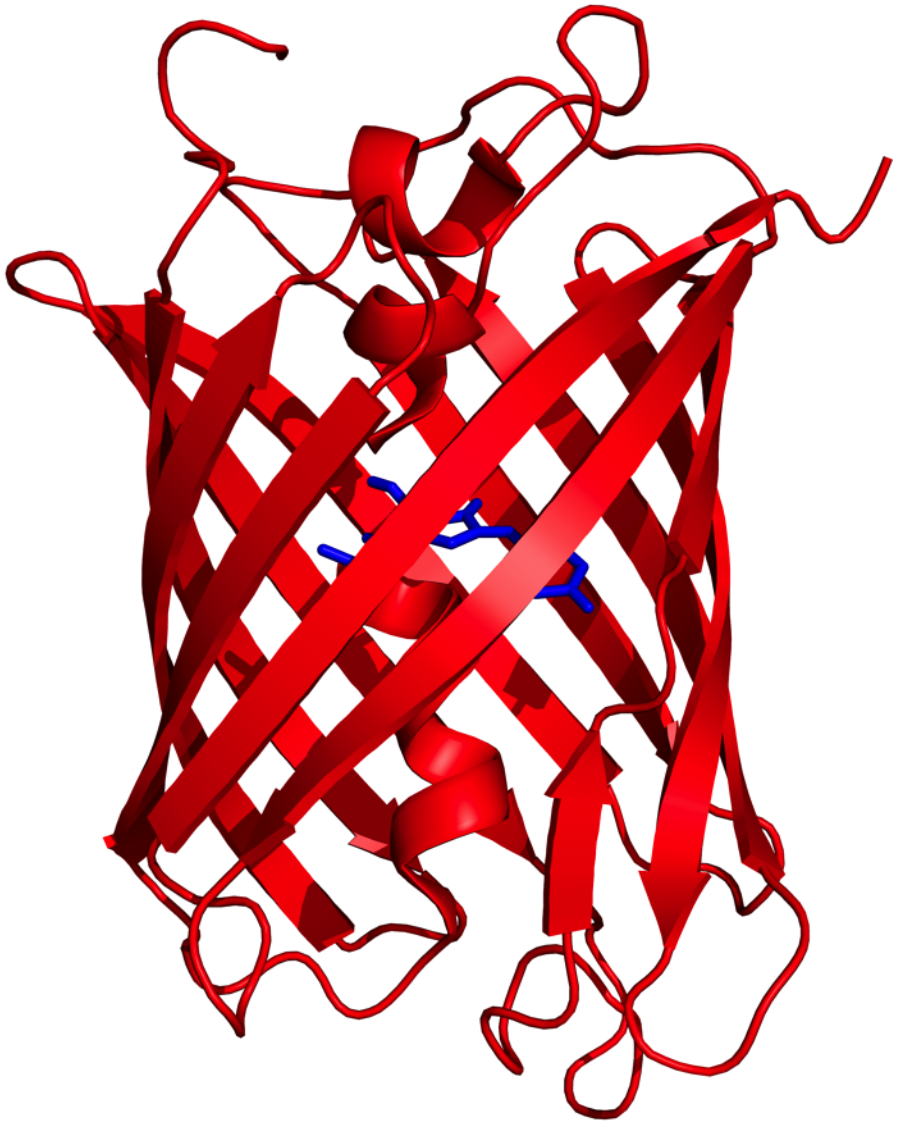

Figure 1.1: The crystal structure of mCherry with the chromophore in blue [31].

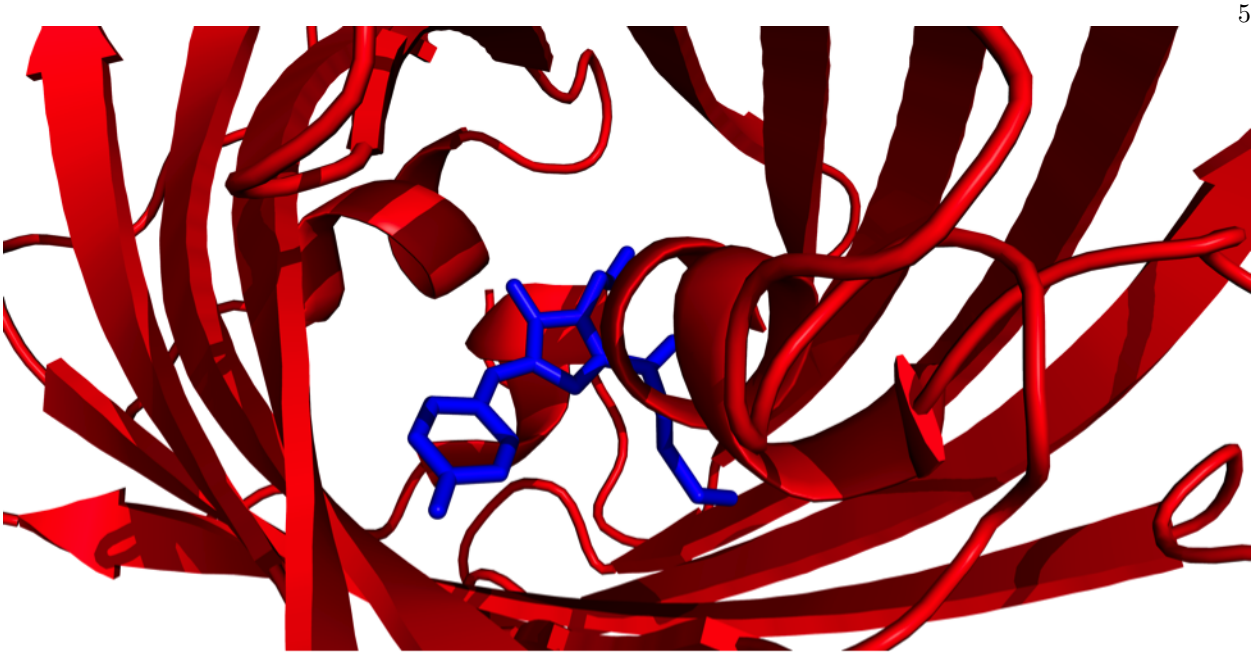

Figure 1.2: The crystal structure of mCherry (PDB code 2H5Q). The chromophore (blue) of mCherry is located inside the β-barrel, in the internal α-helix.

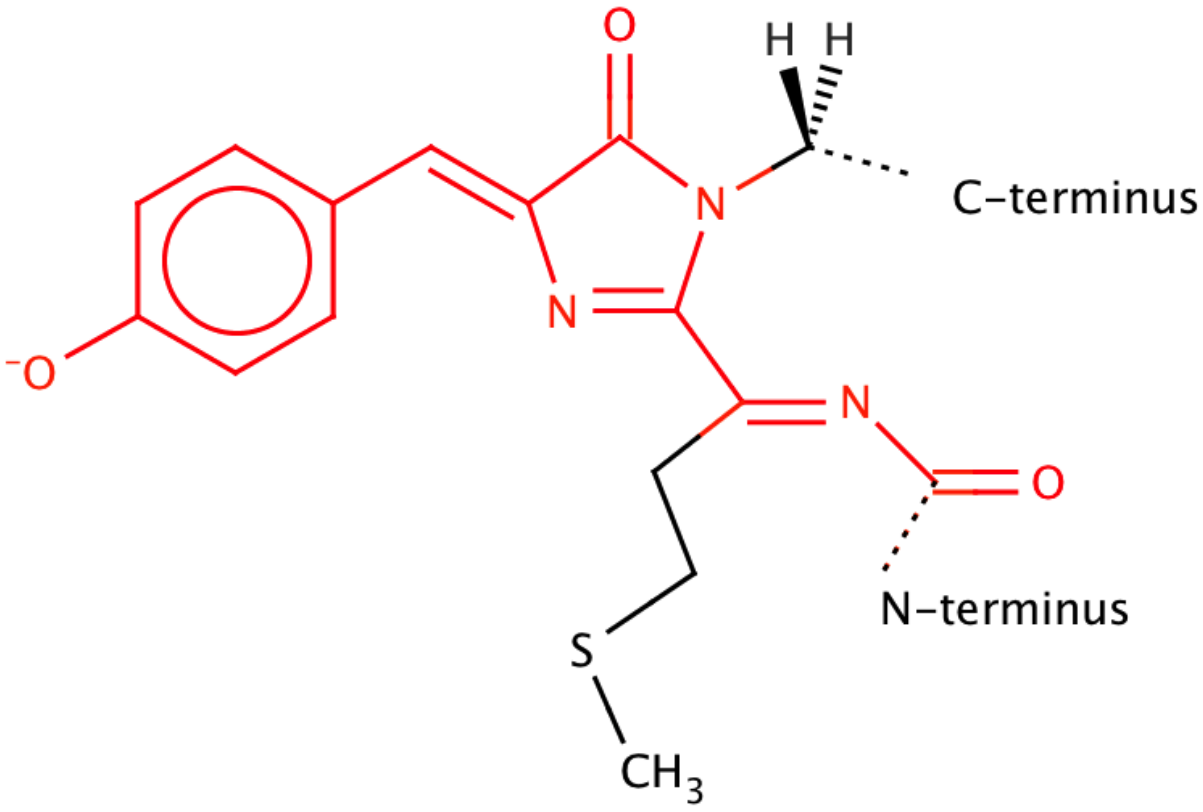

Figure 1.3: The chromophore of the RFPs studied in this work is formed from methionine, tyrosine and glycine amino acids through self-catalyzed cyclization via dehydration and oxidation reactions.

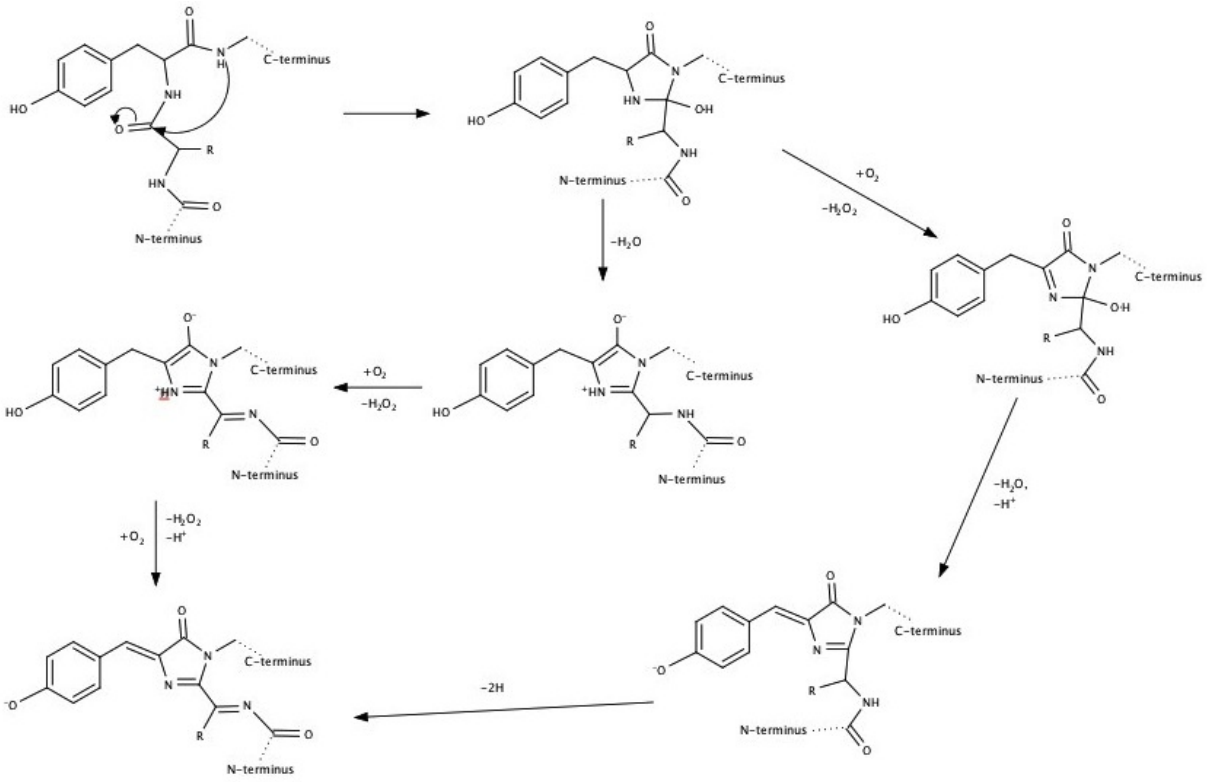

Figure 1.4: A self-catalyzed cyclization reaction occurs when the lone pair of electrons from the glycine amide nitrogen attacks the carbonyl carbon of the tyrosine. Several dehydration and oxidation steps produce the mature chromophore which has one double bond between the tyrosine C^{β} and the imidazolinone ring and another between the methionine amide nitrogen and C^{α}. Hydrogen peroxide is produced by several of the oxidation steps. The phenyl oxygen is deprotonated at neutral pH in the set of RFPs studied in this work, which have chromophore phenol pK_as less than 5.

much higher than the subsequently developed monomeric RFPs with quantum yields less than 0.25 [22]. The mechanisms by which disruption of the protein-protein interface(s) leads to reduced quantum yield are not understood. This is a general problem in development of FPs with improved cell biological properties. The optimization of one property, such as oligomeric state, brightness, or photostability, often comes at the expense of another useful property. It has been hypothesized that the tetramer and dimer interfaces of FPs provide stability [40], but the results of previous studies proved inconclusive [41].

The studies presented here probe the backbone and chromophore dynamics of a set of related RFPs with different emission wavelengths and quantum yields. The 4 proteins compared are monomeric mCherry, mRojoB, mRaspberry, and the obligate tandem-dimer tdTomato, all of which were developed from wild-type protein DsRed [22,23,25,26]. The majority of the experiments performed in this work were NMR spectroscopy based, and therefore dynamics of the large, $>$ 100 kDa wild-type DsRed were not measured for comparison due to experimental limitations. Rather, tdTomato, a dimer more closely related to the wild-type than the three monomers studied was probed in this work as a proxy for a wild-type RFP. Figure 1.5 depicts the RFP family tree for the proteins discussed in this work, and Figure 1.6 depicts the locations of the point mutations between variants mapped onto the crystal structures. The quantum yields, wavelengths of emission, and number of mutations from DsRed for these proteins are given in Table 1.1. Tetramer DsRed contains 2 sets of protein-protein interfaces, the AC and the AB (Figure 1.7). Dimeric tdTomato retains one of the 2 protein-protein interfaces in tetrameric DsRed (Figure 1.7) and shows only a small reduction in quantum yield (from 0.79 to 0.69). Only the AC interface remains in dimeric RFP, dimer2, from which tdTomato was created through the addition of an amino acid linker between the C terminus of the first subunit and the N terminus of the second. The first monomeric RFP, mRFP1 was created from dimer2 by disrupting the remaining AC interface. However, additional compensatory mutations were required to regain fluorescence as the original monomer, mRFP0.1 was only weakly fluorescent [22]. The role of the remaining interface in maintaining the fluorescence of tdTomato is not understood, though the side chains of several amino acids located at this interface form contacts with the chromophore and therefore are likely to affect its physical properties. NMR relaxation, hydrogen-deuterium exchange (HDX) experiments, fluorescence, absorption and circular dichroism spectroscopy were used to study the dynamics [42] and solvent accessibility [43] for

Table 1.1: Photophysical properties for a set of red fluorescent proteins derived from DsRed [23, 25].

protein	Mutations from DsRed	ε (M^{-1} cm^{-1})	$\lambda_{max\ absorption}$ (nm)	$\lambda_{max\ emission}$ (nm)	Φ
DsRed	0	75,000	558	583	0.79
tdTomato	26[a]	138,000	554	581	0.69
mRFP1	33	50,000	584	607	0.25
mCherry	53	101,000	587	611	0.22
mRaspberry	40	62,000	600	625	0.15
mRojoB	55	61,000	598	631	0.06

[a] The residues in the linker in tdTomato were not counted.

a set of RFPs. How the process of directed development affected the dynamics within a set of RFPs was explored.

1.2 Factors Influencing Fluorescence Quantum Yield

Fluorescence is a physical phenomenon in which the absorption of a photon, a process that occurs on the timescale of 10^{-15} s, results in the re-emission of a lower energy photon on a slower timescale of 10^{-9} s (Figure 1.8). Most molecules are not fluorescent and, upon absorption of a photon, simply relax back to the ground state through non-radiative pathways such as vibration, a process that occurs on the timescale of 10^{-12} s. Molecules with many vibrational degrees of freedom, for example molecules without double bonds, have a larger number of potential vibrational relaxation pathways than sterically constrained molecules. In contrast, fluorescent molecules tend to be highly conjugated and/or cyclic and thus have fewer vibrational modes that could provide non-radiative relaxation pathways.

The overlap of vibrational modes in both the ground and excited electronic states depends on the number of vibrational modes and the energy spacing between the ground and excited electronic states. Fermi's Golden Rule and the energy gap law state that the energy difference between excited and ground electronic states is inversely related to the rate of non-radiative relaxation from the excited to the ground state [44, 45]. The larger the energy gap, the less likely the vibrational modes of ground and excited state will overlap and provide a non-radiative relaxation pathway from the excited to the ground state. Therefore, fluorescent molecules tend to have larger differences in energy between their ground and excited electronic

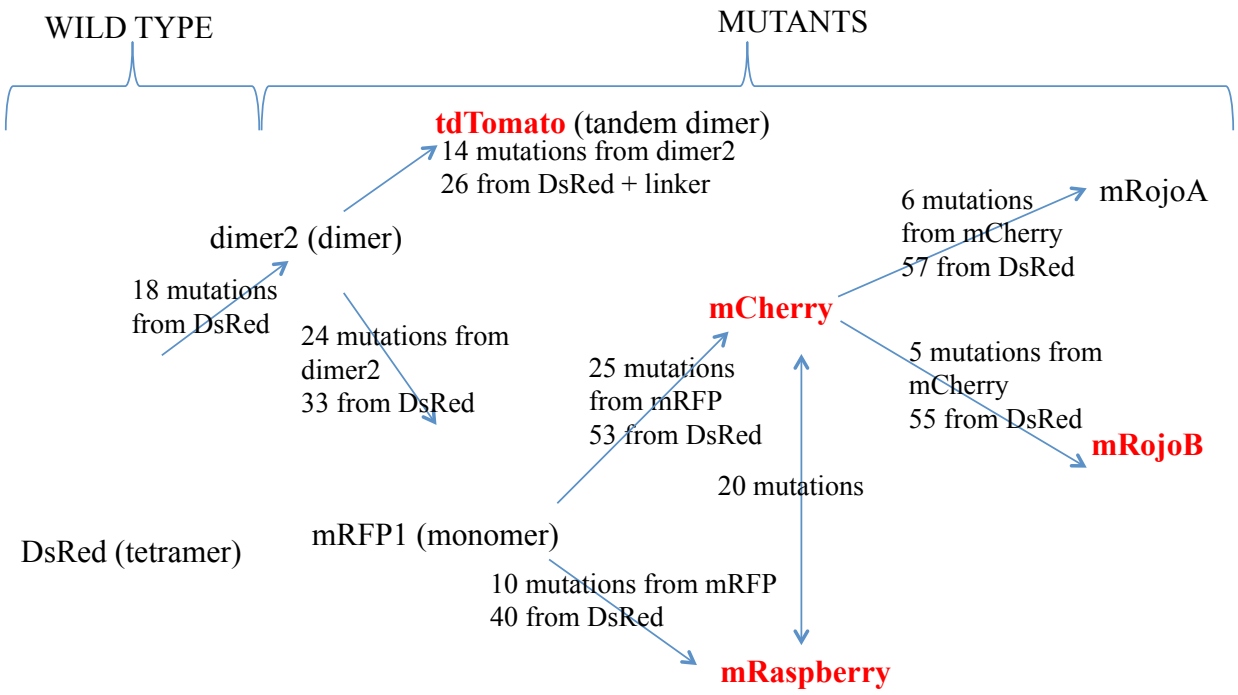

Figure 1.5: The directed development of monomeric RFPs from the wild-type, DsRed is depicted. The number of mutations from the wild-type protein, as well as the precursor for each RFP is given [23, 25, 26]. The RFPs whose names are highlighted in red were studied in this work.

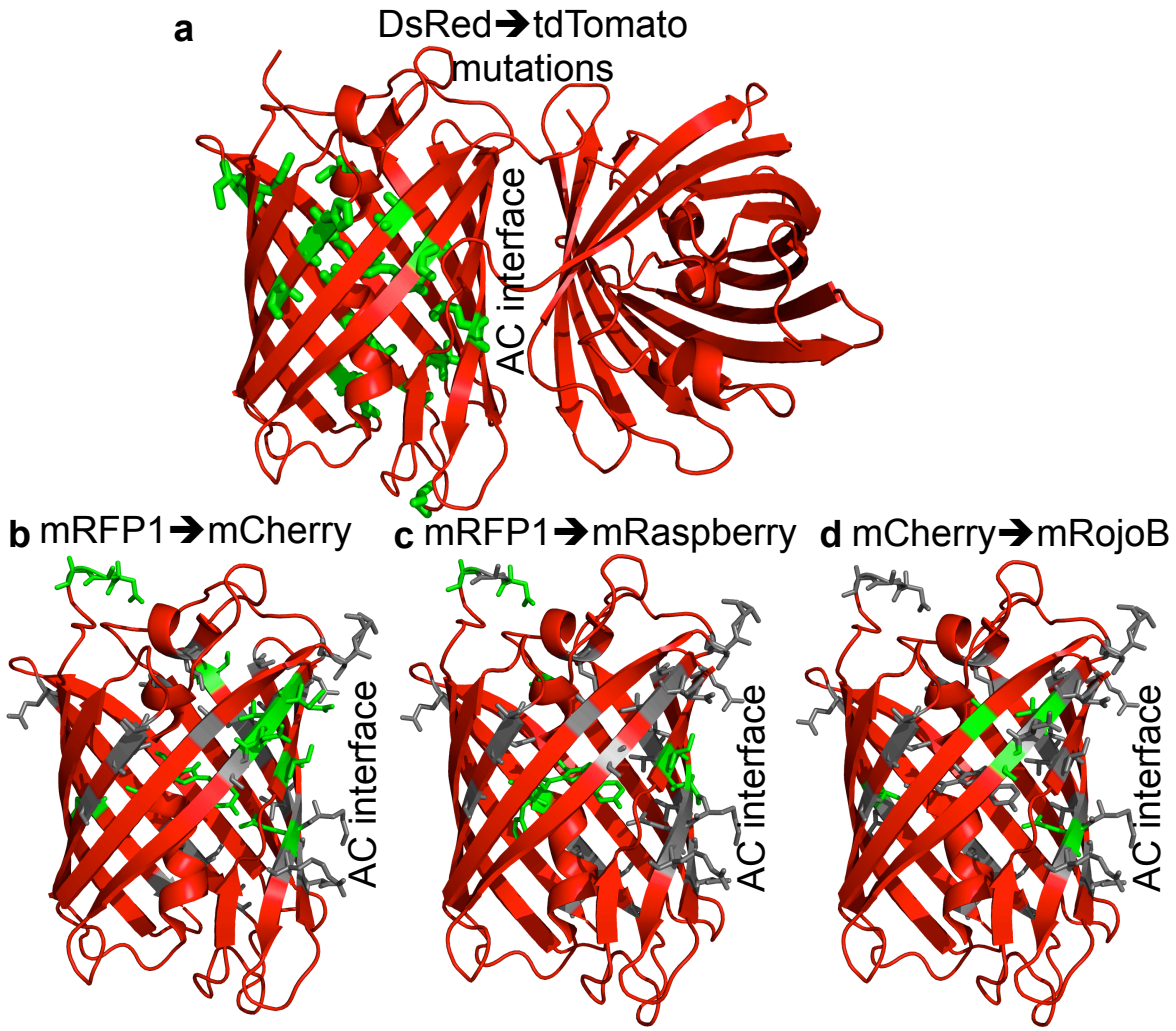

Figure 1.6: (a) The point mutations between dimeric RFP, tdTomato and the wild-type, DsRed are mapped in green on the crystal structure of DsRed (PDB code 1zgo) in which only the A and C subunits are shown. The mutations are only marked on the A subunit for simplicity. The linker is not shown. The point mutations between the wild-type protein and the first monomeric RFP, mRFP1, are shown in grey in b-d mapped onto the crystal structure of mCherry. The point mutations between mCherry (b), mRaspberry (c) and mRojoB (d) and their precursors (mRFP1, mRFP1, and mCherry, respectively) are marked in green.

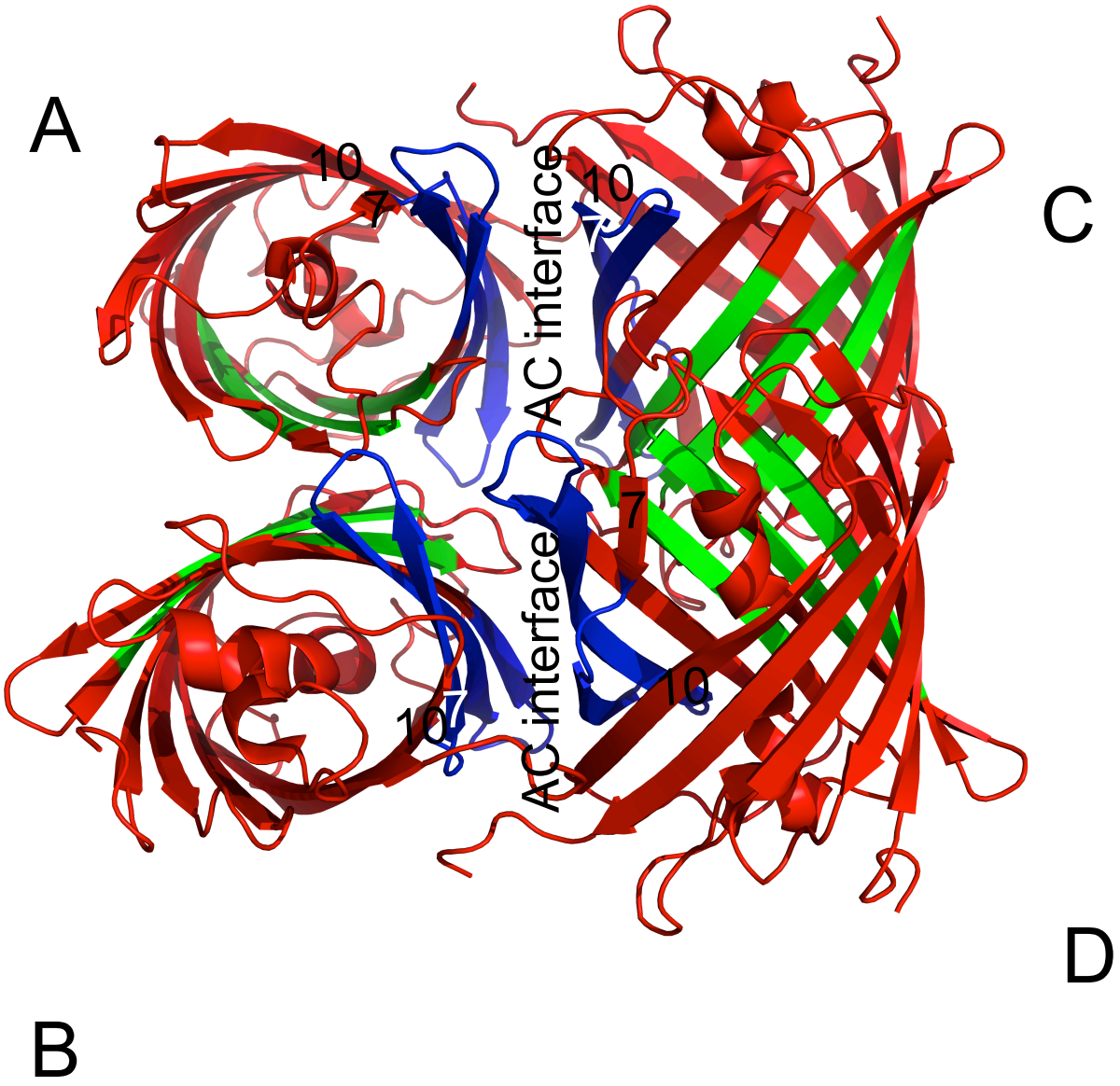

Figure 1.7: The crystal structure of wild-type tetrameric RFP, DsRed, with residues along the AB interface highlighted in green and AC interface highlighted in blue [13]. The AC interface is retained in the dimer tdTomato. The four subunits, A-D, the AC interfaces, and strands 7 and 10, which are discussed throughout the text, are labeled.

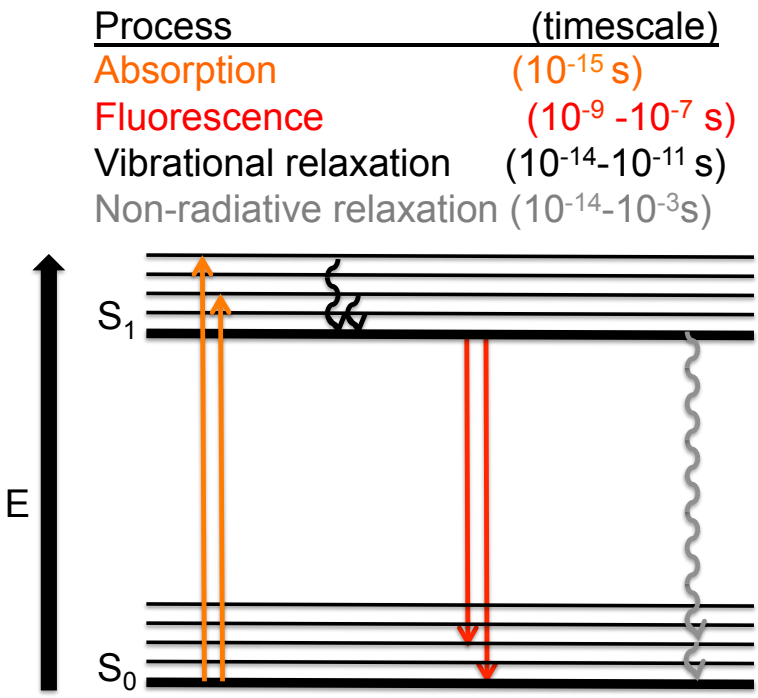

Figure 1.8: A Jablonski diagram indicating electronic transitions between different electronic (thick black lines, S_0 and S_1) and vibronic (thin black lines) energy states. The timescales for given transitions are indicated.

states, than non-fluorescent molecules.

The overarching principle that influences quantum yield is the relative rate of radiative versus non-radiative relaxation (Equation 1.3). The timescales of competing pathways dictate the mechanism by which an excited molecule returns to the ground state. Therefore, since the fastest relaxation pathway is the most probable, relaxation via available vibration pathways generally out-competes relaxation via fluorescence pathways.

$$\Phi = \frac{k_{\mathrm{rad}}}{k_{\mathrm{rad}} + k_{\mathrm{non-rad}}} \tag{1.3}$$

k_{rad} is the rate constant for radiative relaxation and $k_{non-rad}$ is the rate constant for non-radiative relaxation. When comparing several GFP variants with more than 10-fold decreased quantum yields relative to the wild-type GFP, the rate constants for the non-radiative relaxation pathways were increased in the mutants with lower quantum yields by more than 10-fold [46]. The more variable of the two terms in Equation 1.3 is the rate of non-radiative relaxation. Four important physical factors that influence this rate are chromophore planarity, dynamics, protonation state, and protection from fluorescence quenchers. Fluorophores are often highly conjugated and contain rings, which induce molecular planarity. Planarity allows for the π bonds to align and enables maximum electron delocalization. Several studies have shown that FPs with more planar chromophores have higher quantum yields [31, 47, 48]. Higher quantum yields in more planar chromophores can be explained by the larger difference in energy spacing between ground and excited electronic states in the planar conformation relative to the non-planar conformations [49, 50]. Decreased planarity in the chromophores of FPs can arise from increased twist and tilt between the two planar rings of the chromophore [31]. Upon excitation, the double bond character at the bridge between the two rings of the chromophore decreases [51] allowing for more rotation about the bridging bonds when other steric restraints are absent. This rotation decreases planarity as well as the energy spacing between ground and excited electronic states both of which contribute to an increase in the rate of non-radiative relaxation [51]. In FPs, the protein matrix surrounding the chromophore prevents torsion of the excited state chromophore through steric hinderance [49] when compared to a synthetic chromophore in solution, thus decreasing the rate of non-radiative relaxation and increasing the quantum yield. The protein matrix

also rigidifies the chromophores of FPs through hydrogen bonds and Van der Waals interactions [52]. FP mutants that allow chromophore torsion away from planarity tend to have lower quantum yields [53], further demonstrating the importance of chromophore planarity for high quantum yields.

Dynamics also affect the quantum yield of a fluorophore, and will be discussed in detail in the next section. Briefly, dynamics occurring in the chromophore itself or in nearby molecules may affect the quantum yield by providing non-radiative relaxation pathways. Therefore, decreasing the thermal energy by reducing the temperature increases quantum yield as demonstrated by the fact that a synthetic GFP chromophore is not fluorescent in solution at room temperature but regains fluorescence when the solution is cooled to 77 K [54]. In addition, reducing dynamic bond vibrations by increasing pressure corresponds with increased quantum yield in some RFP variants [55]. Dynamics occurring within the chromophore, for example a torsion of the chromophore away from planarity, may occur upon excitation and thus reduce quantum yield. Such torsion of the chromophore may be promoted by the decrease in double bond character at the bridge between the two rings of the chromophore or by motions from nearby side chains that might sterically clash with the chromophore.

The protonation state of the phenolic oxygen in the chromophore of FPs affects the quantum yield as well with the protonated state generally having a lower quantum yield [56]. The protonation state of the chromophore affects both absorption and emission. However, because fluorescence quantum yield is the ratio of photons fluoresced to absorbed, a decrease in both fluorescence and absorbance due to a change in protonation state would not equate with a decrease in quantum yield. Even accounting for decreased absorption, several studies have shown that the quantum yield of the protonated form of FP variants is lower than that of deprotonated. For example, the protonated form of YFP variant 10C has a lower quantum yield than the deprotonated form due to increased non-radiative relaxation [57]. In contrast to YFP 10C, wild-type GFP exists in an equilibrium between protonated and deprotonated states yet still maintains a high quantum yield of 0.8. However, prior to fluorescence of the protonated form of GFP, excited state proton transfer (ESPT) between the chromophore and a nearby side chain occurs at a rate faster than that of non-radiative relaxation [49, 58]. ESPT does not out-compete non-radiative relaxation in YFP variant 10C [57], therefore accounting for the decreased quantum yield in the protonated form. Other examples of

protonated FPs with decreased quantum yields relative to their deprotonated forms include photoactivatable and photoswitchable FPs, many of which rely on protonation and deprotonation to convert between dark and bright states, respectively [59–61]. The mechanism by which the deprotonated state of photoswitchable RFP Dronpa allows for an increase in quantum yield relative to the deprotonated state is a rigidifying hydrogen bonding interaction between the phenolate oxygen and a nearby side chain [62]. This interaction, among other structural differences between the bright and dark states is thought to increase the quantum yield relative to the dark, protonated state. Others have proposed that chromophore protonation in FPs is accompanied by a structural rearrangement near the chromophore, forcing the protonated form of chromophore into a non-planar state and thereby decreasing the quantum yield [63].

Collisional quenching is a non-radiative relaxation pathway that also affects quantum yield [64]. Molecular oxygen is a common fluorescence quencher. Although there are many other fluorescence quenchers, such as acrylamide, most are not commonly found in cells and are therefore less likely to affect *in-vivo* studies [64]. The quenching mechanism of molecular oxygen relies on an energy pairing between the excited singlet and triplet states of the chromophore and the ground and excited states of the quencher, respectively. The ground state electrons of paramagnetic molecular oxygen can be excited to a singlet state through a collision with an excited chromophore, resulting in energy transfer to molecular oxygen and quenching fluorescence via energy transfer [64]. The chromophores of properly folded fluorescent proteins are shielded by the β-barrel from fluorescence quenchers in the solvent. However, ns timescale or slower local unfolding events of the protein could provide pathways for fluorescence quenchers to reach the chromophore. In conclusion, while the quantum yield of fluorescent proteins is affected by many factors including chromophore planarity, dynamics, protonation state, and protection from fluorescence quenchers in the solvent, the relatively unexplored effect of RFP dynamics on quantum yield will be investigated in this work.

1.3 The Dynamic Nature of Proteins and How Dynamics Affect Fluorescence

Protein conformational exchange is often required in order for proteins to perform their many essential functions in living organisms. Therefore, although proteins are often depicted as static crystal structures, these representations only provide part of the important information about a protein. The term protein

dynamics is defined here as any temporal change of atomic coordinates [65]. Protein dynamics important for biological function span a range of temporal and spatial scales. For example, allostery often involves the rearrangement of protein subdomains and occurs on the μs-ms timescale, whereas faster timescale dynamics involve concerted motions of fewer atoms, for example methyl group rotations and side chain rotamerization (Figure 1.9). Structural comparisons of many FP variants have provided valuable information about the photophysical nature of fluorescent proteins. The crystal structures of GFP [9], the blue shifted variant BFP [10], the red wild-type protein DsRed [13], monomeric RFP variants [22], red shifted variants mRojoA and mRouge [25], variants with improved quantum yields [66], and variants with improved photostability [67] provide insight into how structure affects photophysical properties. For example, the crystal structures of several monomeric RFPs showed that the chromophore was less planar than that of the wild-type RFP, DsRed, suggesting that decreased chromophore planarity may be contributing to the decreased quantum yields of the monomers [31]. In addition, the crystal structures of GFP variants with improved quantum yields suggested that conformational exchange had been eliminated relative to the precursor, and this was thought to have contributed to the increased quantum yield. Studies probing fluorescent protein dynamics have also been reported, though fewer studies of RFP dynamics [68, 69] than of GFPs [62, 70–78] have been reported.

The photophysical properties of a fluorescent protein are strongly dependent on the local environment of the chromophore which is surrounded by a tightly packed core of amino acid side chains and is protected from quenching agents such as molecular oxygen [9–11, 16, 31, 41, 47, 51, 59–61, 63, 71, 74–76, 78–103]. Additionally, the surrounding protein structure is thought to keep the chromophore rigid; thus, preventing non-radiative decay and hindering *cis-trans* isomerization which can convert the chromophore to a non-fluorescent state [46, 47, 49, 52, 59–61, 67, 73, 79, 81, 99, 104–106]. Dynamics also affect the photophysical properties of the chromophore, in particular the quantum yield, either by providing alternative relaxation pathways for the excited state or by perturbing the equilibrium between bright and dark states [63, 69, 83, 84, 93, 98, 107–110]. For example, an isolated FP chromophore is not fluorescent at room temperature but recovers fluorescence when cooled to 77 K indicating that fluorescence increases with decreased thermal energy, perhaps due to increased rigidity or decreased collisional quenching by molecules in the solvent [54, 111]. Dynamics in the

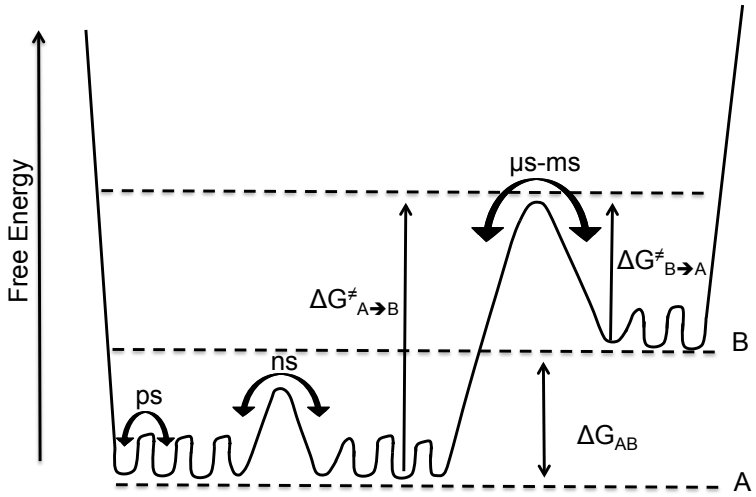

Figure 1.9: A schematic of an energy landscape for a molecule that interconverts between 2 populations, A and B, on the μs-ms timescale at equilibrium. Due to the available thermal energy, bond rotations and side chain rotamerization are also occurring on the sub-nanosecond timescale at equilibrium. This figure was adapted from a figure in reference [65].

backbone and side chains surrounding the chromophore may also decrease quantum yield by providing alternative relaxation pathways for an excited state chromophore [49, 78]. Previous studies on the dynamics of FP variants have been useful in discovering factors contributing to decreased quantum yields, although more data is currently available for GFP variants than for RFP variants. For example, molecular dynamics studies on the monomeric RFP mCherry predicted breathing between β strands 7 and 10, which could enhance access of molecular oxygen to the chromophore [69], although no comparison was made for the precursor RFPs which have higher quantum yields. However, detected differences in dynamics between several GFP mutants have been monumental in developing the understanding of how to develop FPs with improved quantum yields. The difference in quantum yields between 2 GFP variants, Cerulean (Φ=0.44) and ECFP (Φ=0.36) has been attributed to increased ns timescale dynamics in strand 7 of ECFP predicted by performing molecular dynamics simulations on the crystal structures of Cerulean and ECFP [72]. In addition, data from a ^{19}F NMR experiment suggested the chromophore of ECFP underwent conformational exchange [71] that might promote collisional quenching of the chromophore. The data from the 2 aforementioned studies were used to rationalize the difference in quantum yields between ECFP and Cerulean. Another study found 2 regions of electron density in strand 7 of the crystal structures ECFP, but only one such region in yet another CFP variants, SCFP3A (Φ=0.56), and supported the idea that increased flexibility in ECFP may be lowering its quantum yield [112]. The development of the brightest CFP variants came through the use of identified regions of dynamics and attempts to eliminate these regions of dynamics. The work presented here complements previous studies by demonstrating differences in protein dynamics within a set of closely related RFPs, and discusses how the process of protein development may have affected these dynamics.

One goal of this research collaboration with Drs. Amy Palmer and Ralph Jimenez, was to develop an RFP bright and photostable enough to use in single molecule studies. To achieve this, the quantum yield of currently available red fluorescent proteins would need to be improved. Monomeric GFPs with improved quantum yields mCerulean3 (Φ=0.87) and mTurquoise2 (Φ=0.93) were designed through the process of rational design, providing evidence that this goal is achievable. Both proteins were developed through the introduction of a series of mutations into wild-type GFP. Wild type GFP has a quantum yield of 0.8, but GFP mutants designed with the goal of decreasing the wavelength of emission have decreased quantum yields:

Cyan Fluorescent Protein (CFP) W7, Φ=0.67 [8,113], and enhanced CFP designed by Clonetech to improve maturation efficiency at 37°, Φ=0.36. Still more mutations were introduced to improve quantum yield, and SCFP3A (Φ=0.56) [114], Cerulean (Φ=0.49) [115], mCerulean3 (Φ=0.87) [116], mTurquoise (Φ=0.84) [112] and mTurquoise2 (Φ=0.93) [66] were developed. See Table 1.2 for the list of FPs and their quantum yields.

Table 1.2: A set of related fluorescent proteins developed with the goal of improving the quantum yields in cyan fluorescent proteins.

Protein[a]	**Parent (mutations)**	**Quantum Yield**
GFP	Wild Type	0.79
CFP	GFP (Y66W)	Low (N.A.)[b]
ECFP	CFP (S65T F64L N146I M153T V163A)	0.36
Cerulean	ECFP (S72A/Y145A/H148D)	0.49
mCerulean3	Cerulean (H148G/T65S)	0.87
SCFP3A	ECFP (H148D)	0.56
mTurquoise	SCFP3A (T65S)	0.84
mTurquoise2	mTurquoise (I146F)	0.93

[a] For citations please refur to the discription found in the text of the development of these fluorescent proteins.

The approach to developing cyan fluorescent proteins with improved quantum yields, led by the Gadella Jr. lab, was multifaceted. In some cases NMR, X-ray crystallography, and computational approaches allowed for the identification of potentially dynamic regions of the protein which were subsequently targeted for mutation with the aim of rigidifying the environment of the chromophore. In other cases, the same techniques were used to confirm rigidifying affects of the mutations. ^{15}N NMR relaxation experiments and the program Model Free [117] were used to show that the β barrel of GFPuv (Φ= 0.8) was rigid on ps-ns timescale, with dynamics on the μs-ms timescale found only the β turns [74]. Several of the mutated residues in ECFP relative to CFP, including N146I, were shown to form Van der Waals interactions with chromophore based on molecular dynamics simulations and were thought to be important in rescuing fluorescence in ECFP relative to CFP [72]. NMR spectroscopy [71] and X-ray crystallography [118] were used to ascertain that His148, located in strand 7 of the β barrel, could flip between 2 positions, one of which allowed the side chain to collisionally quench the chromophore of ECFP [71]. The mutation H148D was made in ECFP, and the quantum yield of the resulting SCFP3A improved more than 50%. The fluorescent protein, Cerulean,

was developed from SCFP3A by several mutations including Y145A which had also been found in multiple conformations in the crystal structure of ECFP [115]. The T65S mutation was incorporated into SCFP3A to yield mTurquoise [112] (quantum yield 0.83) and mCerulean3 (quantum yield 0.87). Energy calculations showed that a hydrogen bond with the chromophore was stabilized and a Van der Waals contact prevented collisional quenching of the chromophore in mTurquoise relative to SCFP3A due to this T65S mutation [66]. Comparison of the crystal structures of ECFP, Cerulean, SCFP3A and mTurquoise revealed differences in the position of residue Ile164, located near the chromophore and prompted the I146F mutation [66]. This mutation was found to further stabilize the energy of the excited state and increase conformational homogeneity in the crystal structure of mTurquoise2 at strand 7 relative to SCFP3A and mTurquoise and thus increase the quantum yield [66]. The success in the development of CFPs with improved quantum yields is encouraging and demonstrates the ability to use information on the differences in dynamics to design novel FPs with improved quantum yields.

Several important considerations when comparing the quantum yields of tdTomato, mCherry, mRaspberry and mRojoB are that each RFP was developed with a different goal and using different techniques. While tdTomato was developed to interrupt the AB interface of tetrameric DsRed [22], mCherry was developed to improve the brightness, maturation efficiency and tolerance for protein fusions of the monomeric RFP mRFP1 [23], and mRaspberry [26] and mRojoB [25] were developed to increase the wavelengths of emission. Notably, none of these variants were designed to improve the quantum yield of the precursor RFP. Therefore, one might expect that the quantum yields of each RFP would be decreased relative to the precursor as the mutants were not being selected for improved quantum yield. In addition, the degree to which the quantum yield decreased during each development of each mutant may shed light on important structural (or dynamic) features promoting the relatively higher quantum yields of the precursor. For instance, the drastic decrease in quantum yield after monomerization suggests the AC interface residual in tdTomato is important for fluorescence. In addition, the chromophore packing in mCherry may be important in promoting a higher quantum yield than the two red-shifted mutants mRaspberry and mRojoB. In addition to the different goals for development different techniques were used. While tdTomato was developed using random mutagenesis through error-prone PCR, mCherry using a combination of saturation mutagenesis at targeted locations as

well as random mutatgenesis with error-prone PCR of the whole gene, mRaspberry using somatic hypermutation random mutagenesis, and mRojoB using a combination of structure based rational design, and computational pre-screening. Specifically, in the case of mRojoB, several specific amino acids were targeted for mutation to particular residues with the aim of increasing electron density in particular regions of the excited chromophore in order to increase the wavelength of emission [25]. This method of rational design is in contrast with the random mutagenesis technique used to generate tdTomato, mCherry and mRaspberry. In developing each of these three proteins, several orders of magnitude more mutants were screened before obtaining the end results compared with the development of mRojoB [25]. This difference in approach may have had consequences on the quantum yields of the resulting mutants. Perhaps the decreased number of mutants screened during development of mRojoB decreased the probability of identifying a red-shifted mutant with more than a third of the fluorescence quantum yield of the precursor.

Several factors could be causing the decreased quantum yields in monomeric RFPs relative to one another as well as to their dimeric and tetrameric precursors. In this work differences in dynamics are explored in order to complement previous studies comparing protein structures. Dynamics on 2 timescales could be affecting the quantum yields: sub-ns timescale and ns-longer timescales. First, increased sub-ns dynamics near the chromophore could provide non-radiative relaxation pathways, for example via torsion away from planarity [53, 119, 120] or via collisional quenching of the excited state chromophore by nearby side chains [72]. The ps-ns dynamics of the backbone amides, in particular those that are within 5 Å of the chromophore, and of the chromophore tyrosine C^{β} of 3 monomeric RFPs were therefore measured. Second, the relative populations of molecules in bright, fluorescent states versus the dark, non-fluorescent states, interconverting on a timescale slower than that of fluorescence, will affect the quantum yield of the equilibrium population. The relative populations of locally unfolded, possibly non-fluorescent, states were therefore measured using hydrogen deuterium exchange and NMR spectroscopy. Differences in ps-ns dynamics or local unfolding among RFP variants may provide insight into the cause of decreased quantum yields of monomeric RFPs.

1.4 Rationale For Comparing the Dynamics of Red Fluorescent Protein Variants

In all biological applications but especially when studying a cellular process involving a low copy number protein, optimization of photophysical properties such as photostability and quantum yield is important for fluorophore utility. Highly photostable FPs allow intracellular events to be monitored over longer time periods relative to less photostable FPs. In addition to photostability, it is imperative that the fluorescent protein be bright enough to facilitate detection. Currently available monomeric red fluorescent proteins ($\lambda_{em}>$ 600 nm) have much lower quantum yields ($\leq$0.25 [22]) than fluorescent proteins with shorter wavelengths of emission, such as mTurquoise, ($\lambda_{em,max}$=474 nm, Φ>0.9) [66]. While shorter wavelength emitting FPs are useful tools, RFPs are particularly valuable due to decreased scattering and background auto-fluorescence at longer wavelengths. Thus, research is ongoing to improve the quantum yields of RFPs.

The lower quantum yields of monomeric RFPs may be due to increased chromophore flexibility relative to the chromophore of wild-type RFP, DsRed. Current approaches to improve the fluorescence quantum yield of fluorescent proteins include both random and directed mutagenesis of residues near the chromophore. In addition, some groups targeted other regions in which dynamics had been predicted based on B-factors from crystal structures of FPs [66]. However, few studies of residue-specific dynamics in the monomeric RFPs have been reported. The goal of the experiments presented in this work was to assess whether the differences quantum yields between RFP variants could be attributed to structural dynamics. This information would be highly useful in the development of brighter RFPs.

Additionally, the RFPs studied in this work lack at least one of the 2 protein interfaces found in the wild-type tetramer, DsRed. As protein interfaces are generally thought to stabilize protein tertiary structure [41, 121], the disruption of the protein-protein interfaces present in wild-type tetramer DsRed was expected to be structurally destabilizing, especially in the monomeric RFPs. Global protein unfolding was monitored using spectroscopic methods including fluorescence and circular dichroism. In addition, local unfolding and solvent accessibility of RFP variants were characterized using hydrogen deuterium exchange and fluorescence quenching assays. The set of RFPs compared in this work included tdTomato, mCherry, mRasp-

berry and mRojoB. The dimer, tdTomato, was compared with monomeric RFPs, mCherry, mRaspberry, and mRojoB, to test the idea that the residual protein-protein interface in tdTomato stabilizes tertiary structure and inhibits local unfolding. The stability and solvent accessibility of wild-type protein, DsRed, has been compared to dimer2 and monomer RFP1 previously [41]. While a previous study showed that DsRed and mRFP1 were more kinetically stable than the dimer, the monomer was found to be most thermodynamically stable [41]. These results may contradict the idea that protein-protein interfaces are conformationally stabilizing, and indicate that more studies are necessary to better understand the effects of directed development on RFP conformational stability.

1.5 Using Nuclear Magnetic Resonance Spectroscopy to Study Protein Dynamics

Nuclear magnetic resonance (NMR) spectroscopy is a powerful tool for studying protein structure and dynamics. NMR spectroscopy relies on the nuclear magnetic moments (hereafter referred to as spin) aligning with an external magnetic field. The external magnetic fields used for biological NMR experiments are generally between 11.7 and 21 Tesla, close to 6 orders of magnitude stronger than the magnetic field strength of the Earth. These high magnetic fields shift the Boltzmann distribution of the nuclear spins to favor alignment with the external field. The Boltzmann distribution of the nuclear spins is described by the following equation:

$$\frac{N\downarrow}{N\uparrow} = e^{-\Delta E/k_B T} \tag{1.4}$$

where E is the difference in energy between a nuclear spin aligned with (N↑) and against (N↓) the external magnetic field, k_B is the Boltzmann constant and T is temperature. ΔE can be calculated using the following equation:

$$\Delta E = \gamma \hbar B_0 \tag{1.5}$$

where γ is the gyromagnetic ration of the nuclei, $\hbar$ is Planck's constant divided by 2π, and B_0 is

the strength of the external magnetic field. Radiowave radiation can be used to perturb the equilibrium distribution of nuclear spins, and force the them to orient perpendicular to the external magnetic field. While aligned perpendicular to the external magnetic field the nuclear spins precess about the z axis. This precession, occurring at the Larmor frequency, induces an electrical current in a detector and provides a readout of the Larmor frequency of the nuclei to the observer. Slight differences in this Larmor frequency, called chemical shift, provide structural information about a molecule, while differences in the relaxation rates provide information about the dynamics of the molecule.

The use of NMR to study large molecules like proteins is often quite challenging due to spectral overlap and poor signal-to-noise resulting from unfavorable relaxation properties. The development of 2-dimensional NMR techniques represented a breakthrough in the field of protein NMR by abating the spectral crowding issue [122]. One of the most commonly used NMR spectra for studying proteins is called the ^{1}H-^{15}N heteronuclear single quantum correlation spectrum (HSQC) which correlates ^{1}H and bound ^{15}N atoms and thus produces a peak for most backbone amides in a protein. Bax developed methodologies for the backbone assignment of larger proteins using triple resonance labeling and 3-dimensional NMR techniques [123].

The use of NMR to study protein dynamics is a highly technical, yet incredibly information rich field of biophysics. NMR experiments can be used to study dynamics on a wide range (ps-s) of timescales (Figure 1.10). NMR relaxation experiments have been developed to study ps-ns dynamics of large biomolecules. In the late 1980s, the Wagner and Bax labs published NMR experiments for measuring the ^{13}C and ^{15}N relaxation parameters T_1, T_2 and hetNOE (described in detail in the following section) in large molecules such as proteins [124–126]. Peter Wright, Josh Wand and coworkers showed that proteins displayed regions of increased flexibility on the ps-ns timescale near the N and C termini as well as in loops or proteins [127,128] by measuring ^{15}N relaxation parameters. These approaches have since become standard experiments for probing the dynamic nature of proteins in solution.

1.5.1 NMR Relaxation Studies of ps-ns Dynamics

Proteins undergo ps-ns dynamics which can be detected using NMR relaxation experiments (Figures 1.9 and 1.10). When probing protein ps-ns dynamics, the relaxation parameters R_1, in-phase R_2, and

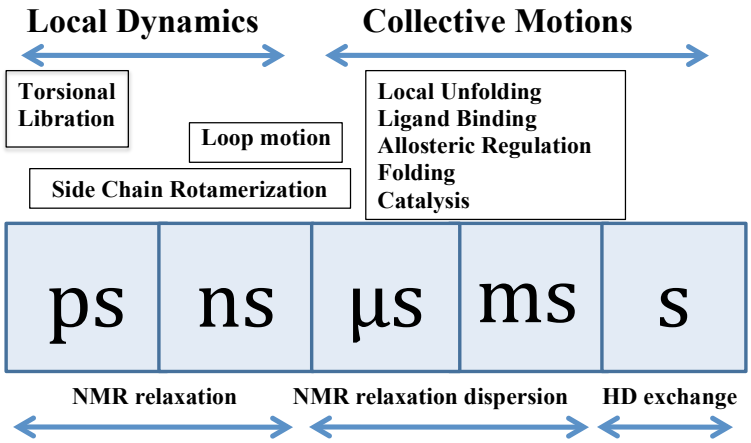

Figure 1.10: Timescales for protein dynamics and the NMR techniques used to probe dynamics on these timescales.

hetNOE are generally measured for protein backbone amide nitrogens in an ^{15}N-labeled protein. R_1 and R_2 will be discussed first. When performing an NMR experiment, nuclear spins are excited to a higher energy state and subsequently relax back to the equilibrium population with characteristic relaxation rate constants called R_1 (spin-lattice, or longitudinal relaxation rate constant) and R_2 (spin-spin, or transverse relaxation rate constant). R_1 and R_2 are the inverses of relaxation time constants T_1 and T_2, respectively, introduced in the previous section. R_1 describes the rate at which excited nuclear spins recover the z component of nuclear magnetization (the population difference between the aligned and anti-aligned spins), and R_2 describes the rate at which the nuclear spins lose coherence in the xy plane [42]. NMR relaxation is caused by fluctuating magnetic fields occurring at the frequency corresponding the energy difference from the ground and excited states of the nuclear spins [129]. Fluctuating magnetic fields are created by dynamic nuclear spins and by the movement of the nuclear spin relative to the external magnetic field [129]. Thus, these rate constants are affected by the tumbling speed of the overall protein in solution and the local environment of the nucleus, which is affected for example by internal ps-ns dynamics occurring nearby. Therefore, relaxation rate constants contain information about internal ps-ns dynamics. The global tumbling of a protein in solution is described by its correlation function and characteristic time constant, τ_c. However, the tumbling of individual bond vectors within the protein, described by the effective correlation time constant τ_e, is affected by both the global tumbling and internal dynamics [129]. The main mechanisms through which oscillating magnetic fields cause relaxation for ^{13}C and ^{15}N (the 2 most commonly probed nuclei when studying protein ps-ns dynamics) are dipole-dipole and chemical shift anisotropy for R_1 and R_2, as well as chemical exchange for R_2 [129]. Complete descriptions of the mechanisms affecting relaxation have been reported elsewhere [130–132].

R_1 and R_2 are measured by 2 different experiments. R_1 is measured using an inversion-recovery experiment. In the inversion-recovery experiment, the nuclear spins are first inverted, thus aligning them along the negative z axis. The relaxation delay time (τ) before the nuclear spins are flipped to the xy plane for signal detection is arrayed. Using the vector model, the location of the magnetization (represented by the thick black arrows) at each stage of the inversion-recovery experiment is presented in Figure 1.11. As the magnetization of the sample relaxes back to equilibrium with the characteristic rate constant, R_1, the

detectable signal changes according to:

$$M_z = M_0 \left(1 - 2e^{-R_1 \tau}\right) \tag{1.6}$$

where M_z is the magnetization, M_0 is the equilibrium magnetization and τ is the relaxation delay time before the nuclear spins were flipped into the *xy* plane for detection. A set of experiments is collected by arraying the value of τ. The peak intensities are fit to a decaying exponential as a function of this relaxation delay time, from which the rate constant R_1 is obtained. A variation of the inversion-recovery experiment depicted in Figure 1.11 is used for measuring ^{15}N R_1 in a 2-dimensional experiment, but the principle of R_1 relaxation is similar. However, the peak intensities as a function of the relaxation delay time are fit to a simple decaying exponential function (Equation 1.7) when measuring ^{15}N R_1 using a 2-dimensional experiment.

A spin-echo experiment is used to measure R_2. The vector model is used to describe the location of the magnetization at each stage of the spin-echo experiment in Figure 1.12. The nuclear spins are first excited by aligning them along the x axis. Following excitation, the nuclear spins begin to dephase as they precess about the *z* axis. This dephasing is due to both chemical shift (the unique Larmor frequency of each nucleus) and spin-spin relaxation. The characteristic rate constant for this type of relaxation is called R_2. During a spin-echo experiment, while the nuclear spins precess about the *z* axis, a refocusing pulse is applied. After the subsequent delay time equivalent to that which occurred prior to the refocussing pulse, the dephasing effect caused by chemical shift is refocussed. The refocussing pulse and subsequent delay time will not recover signal lost due to R_2 relaxation, and so similar to the inversion-recovery experiment, longer relaxation delay times return the smaller signal intensities. Again, a more complicated NMR pulse sequence is used to measure ^{15}N R_2 using a 2-dimensional experiment, but the principle remains the same.

$$M_z = M_0 e^{-R_1 \tau} \tag{1.7}$$

The nuclear Overhauser effect (NOE) is a dipole-dipole mediated cross-relaxation mechanism through which the equilibrium magnetization of a nuclear spin is perturbed by a nearby relaxing nuclear spin [133].

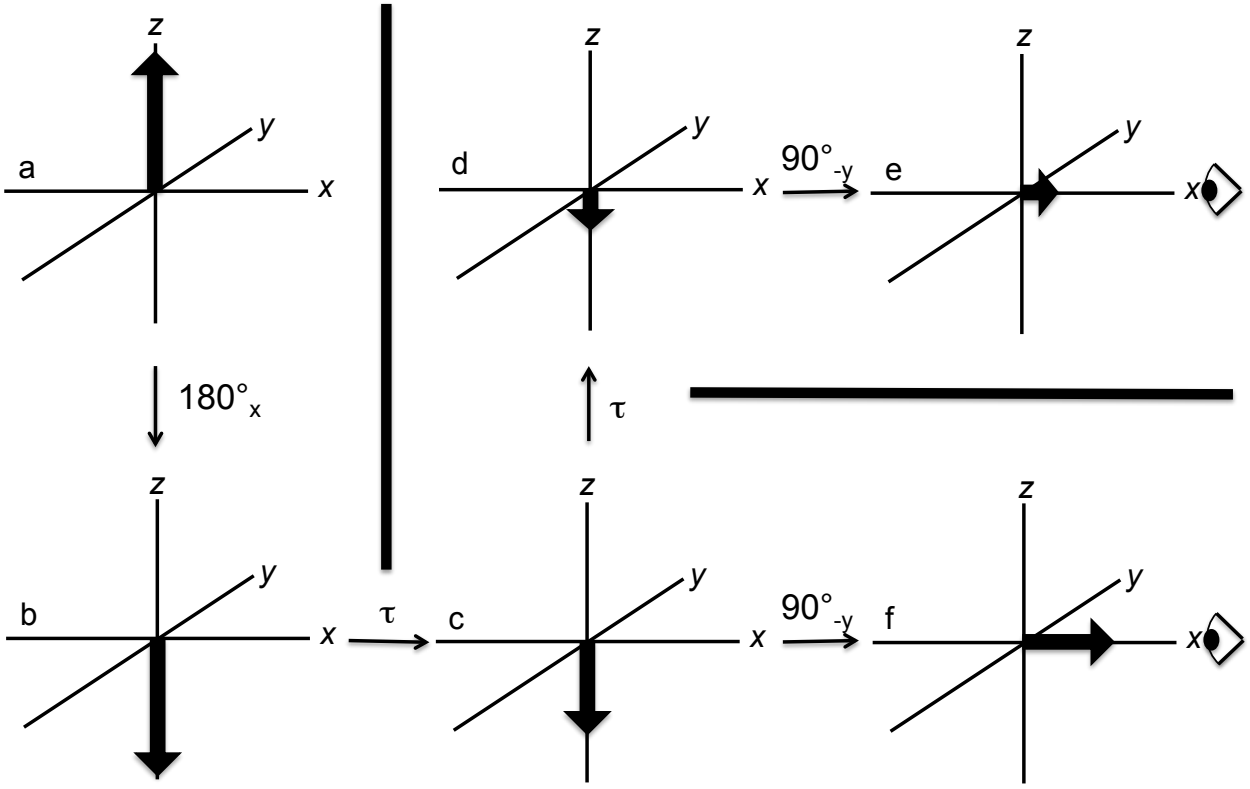

Figure 1.11: The schematic of the NMR inversion-recovery experiment is depicted here using the vector model. Here, the vector model is being used to describe where the magnetization is during the pulse sequence used to measure T_1 relaxation. In (a) the magnetization is at equilibrium along the z axis, aligned with the external magnetic field. In (b) after a 180° pulse has been applied along x, the magnetization is along the negative z axis. In (c) and (d) the magnetization is relaxing back towards equilibrium for varying amounts of time. Finally, in (e) and (f) after a 90° pulse has been applied along negative y, the magnetization is along the x axis, where the detector (represented as a side view of an eye) is positioned. Because the sample was allowed to relax for different amounts of time (τ) before the final 90° pulse, the signals detected in (e) and (f) will be of different magnitudes.

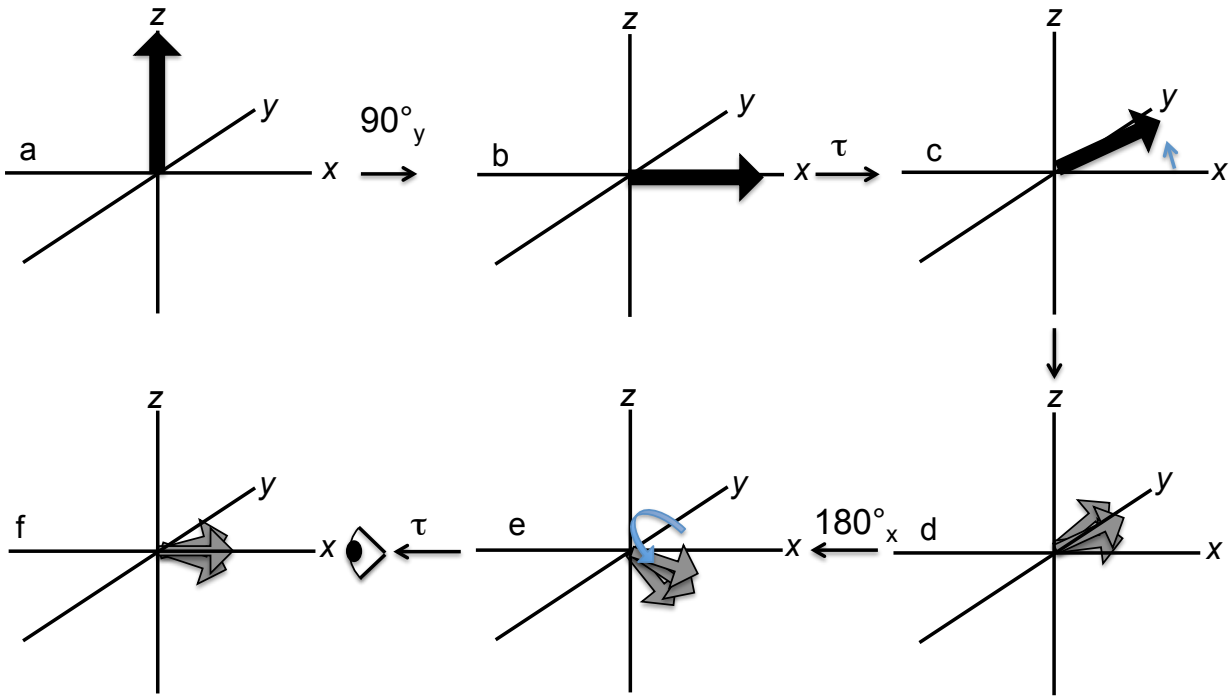

Figure 1.12: The schematic of the NMR spin-echo experiment is depicted here using the vector model. Here, the vector model is being used to describe where the magnetization is during the pulse sequence used to measure T_2 relaxation. In (a) the magnetization is at equilibrium along the z axis, aligned with the external magnetic field. In (b) after a 90° pulse has been applied along y, the magnetization is along the x axis. In (c) the magnetization begins to precess about the z axis, and in (d) the dephasing effect of T_2 relaxation is represented by the 3 grey arrows, each which has a smaller magnitude than the initial equilibrium magnetization. A 180° pulse is applied along x, and the magnetization is flipped about the x axis (e). Precession occurs for the same amount of time as before (d), the returning the magnetization to the x axis where the detector is positioned. The sample should be allowed to relax for different amounts of time (τ) before and after the 180° refocussing pulse. This will cause the magnitude of the signal in (f) to change as a function of τ.

More practically speaking, the NOE is a through-space phenomenon in which the magnetization of nuclear spins at position B is enhanced by relaxation of nuclear spins at position A (Figure 1.13). The rate of magnetization enhancement at position B depends on the distance between the 2 nuclei (inversely proportional to the distance raised to the power of 6) [133]. Therefore, NOEs are helpful in determining molecular structures from NMR data since they are generally only detected between nuclear spins that are within 5 Å of one another [133].

The NOE can occur between 2 of the same type of nuclear spins or between 2 different types of nuclear spins, which is called a heteronuclear NOE or hetNOE. $\{^1H\}$-^{15}N and $\{^1H\}$-^{13}C hetNOE experiments are often used in conjunction with ^{15}N or ^{13}C R_1 and R_2 experiments to probe protein dynamics on the ps-ns timescale. Like the relaxation rate constants R_1 and R_2, both global tumbling (described by the time constant τ_c) and internal dynamics affect the hetNOE [129, 133] (Figure 1.14). Less efficient NOE (NOEs closer to 0) occurs with larger rotational correlation times such as the global rotational correlation times for most proteins [133, 134] (Figure 1.14). Thus, protein $\{^1H\}$-^{15}N or $\{^1H\}$-^{13}C hetNOEs are often close to zero except in loops or tails where the effective correlation time constant, τ_e, is often smaller. More rigorous descriptions of factors influencing the NOE have been described previously [42, 131].

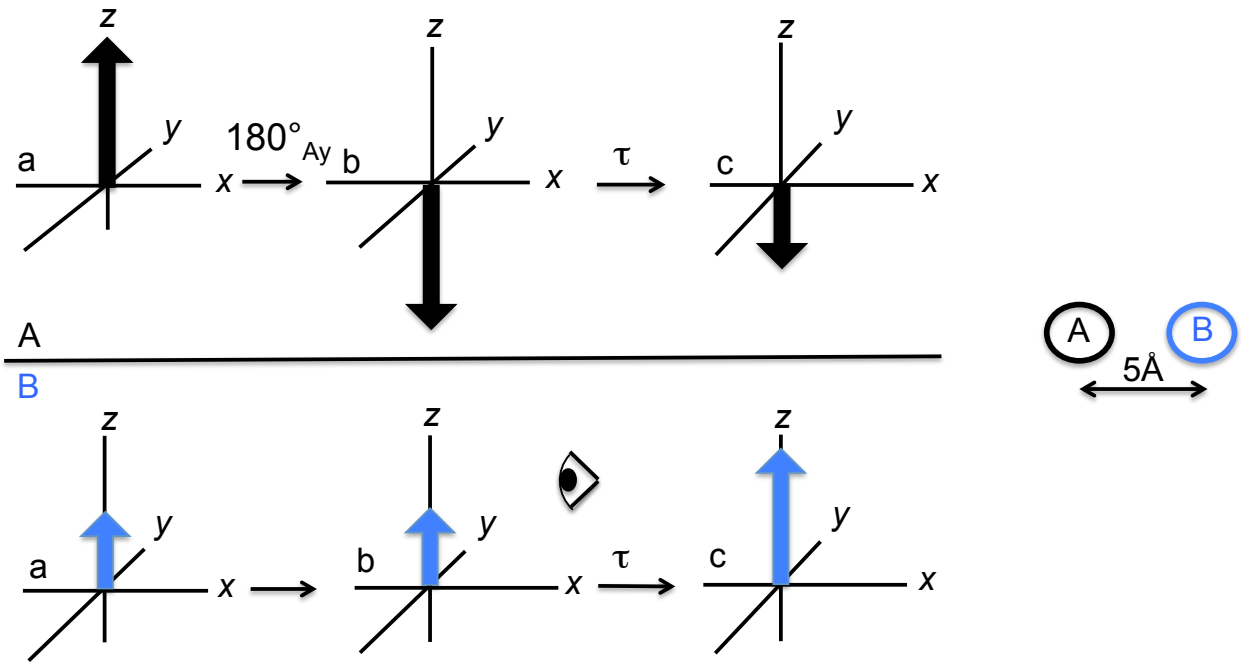

Figure 1.13: The schematic of the NMR NOE enhancement between nuclei A and B is depicted here using the vector model. In (a) the magnetization is at equilibrium along the z axis for nuclei A and B. In (b) after a 180° pulse has been applied along y to nuclear spin A, the magnetization of A is along the negative z axis. In (c) the magnetization is relaxes back towards equilibrium for nuclear spin A. For nuclear spin B, the magnetization is enhanced due to the NOE between A and B.

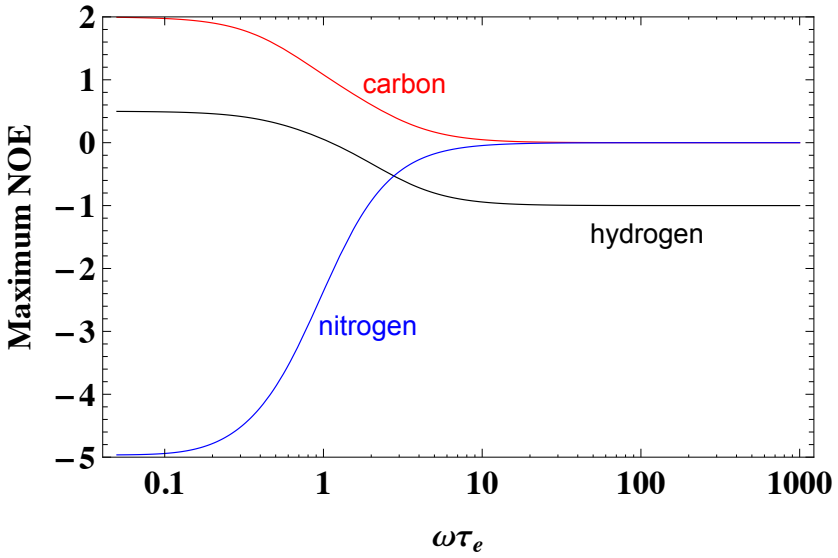

Figure 1.14: The graph provides a qualitative description of the dependence of the maximum NOE for hydrogen (black), carbon (red), and nitrogen (blue) on the effective rotational correlation time constant (τ_e) and Larmor frequency (ω). The effective rotational correlation time constant depends on both the global tumbling of the overall molecule and on internal motion.

$\{^1H\}$-^{15}N hetNOE (as well as $\{^1H\}$-^{13}C hetNOE and ^1H-^1H NOE) values are reported as the ratio of 2 peak intensities: one from the spectrum collected in the presence of a pre-saturation pulse (which induces the NOE) and one from a reference spectrum collected without the pre-saturation pulse. The $\{^1H\}$-^{15}N hetNOE is always negative, the $\{^1H\}$-^{13}C hetNOE is always positive, and the homonuclear ^1H-^1H NOE may be positive or negative depending on the rotational correlation time constant (Figure 1.14). Since the $\{^1H\}$-^{15}N hetNOE ranges from 0 to ≈-5 (Figure 1.14), the intensities in the presaturated spectrum (I_{sat}) can range from I_{ref} (in the absence of NOE), to I_{ref}-5I_{ref} (when the NOE is ≈-5). The reported ratio of peak intensities (I_{sat}/I_{ref}) therefore ranges from 1 to ≈-4, with smaller values indicative of faster tumbling.

These NMR relaxation parameters, R_1, R_2, and $\{^1H\}$-^{15}N hetNOE were used to compare backbone amide and chromophore tyrosine C^β ps-ns dynamics within and between three monomeric RFP variants in order to gain insight into the differences in quantum yields.

1.5.2 Internal ps-ns Dynamics as Described by the Order Parameter

An order parameters for a backbone amide bond describes the magnitude of the ps-ns timescale internal dynamics for that bond [135]. Measured NMR relaxation parameters R_1, R_1, and NOE are affected by both internal dynamics and global tumbling, and therefore, a special treatment of the data is necessary in order to understand the magnitude of internal motion. Using the Model Free formalism [135], the contributions from internal motions and global tumbling can be deconvoluted. A currently available user friendly program that employs the Model Free formalism is Tensor2 [136] and requires ^{15}N relaxation parameters and structural coordinates as input, returning backbone amide order parameters as output.

The measured relaxation parameters are fit to equations 1.8-1.10 relating spectral density to R_1, R_2 and NOE which assume that relaxation is dominated by dipolar coupling and chemical shift anisotropy [126, 137]:

$$R_1 = d^2\{J(\omega_A - \omega_X) + 3J(\omega_X) + 6J(\omega_A + \omega_X)\} + c^2 J(\omega_x) \tag{1.8}$$

$$R_2 = 0.5d^2\{4J(0) + J(\omega_A - \omega_X) + 3J(\omega_X) + 6J(\omega_A) + 6J(\omega_A + \omega_X)\} + \frac{1}{6}c^2\{J(\omega_X) + 4J(0)\} \tag{1.9}$$

$$\text{NOE} = 1 + \left[\left(\frac{\gamma_A}{\gamma_X}\right) d^2\{6J(\omega_A + \omega_X) - J(\omega_A + \omega_X)\}\frac{1}{R_1}\right] \tag{1.10}$$

where

$$d^2 = \frac{0.1\gamma_A^2\gamma_x^2h^2}{4\pi^2}\left(\frac{1}{r_{AX}^3}\right)^2 \tag{1.11}$$

and

$$c^2 = \left(\frac{2}{15}\right)\gamma_X^2 B_0^2(\sigma_\parallel - \sigma_\perp)^2 \tag{1.12}$$

In equations 1.8-1.12, A is ^{1}H, X is ^{15}N, J(ω) is the spectral density, γ_i is the gyromagnetic ratio for spin i, h is Plank's constant, r_{AX} is the internuclear distance between ^{1}H and ^{15}N, B_0 is the external magnetic field

strength, and $\sigma_{\|}$ and $\sigma_{\perp}$ are the parallel and perpendicular components of the axially symmetric chemical shift tensor for ^{15}N. Hiyama et al. showed that the assumption that the chemical shift tensor for a peptide amide ^{15}N is axially symmetric is valid and that the difference $\sigma_{\|}$-$\sigma_{\perp}$=-160 ppm [138].

Tensor2 selects one of five models to which to fit the relaxation data, and reports an S^2 value and associated error, as well as additional parameters depending on the model [136]. Models 1-5 relate the spectral density, order parameter, correlation time for internal motion, and, in some cases, chemical exchange. Using the spectral density function determined using the measured relaxation parameters and diffusion tensor, Tensor2 uses one of the following models to fit the data:

NOTE: Equations 1.13-1.15 assume fully isotropic diffusion. Extensions of these equations that account for the diffusion tensor of molecules tumbling either axially or fully anisotropically are described in references [139] and [140], respectively.

Model 1) Internal dynamics are not contributing to the relaxation (τ_i <20ps, where τ_i is the rotational correlation time for internal motion and is related to the global (τ_c) and effective (τ_e) rotational correlation times by τ_e^{-1}=τ_c^{-1} +τ_i^{-1}) (Figure 1.15)

$$J(\omega) = \frac{2}{5}\left[\frac{S^2\tau_c}{1+\omega^2\tau_c^2}\right] \tag{1.13}$$

Model 2) Internal dynamics contribute to relaxation (ps-ns)

$$J(\omega) = \frac{2}{5}\left[\frac{S^2\tau_c}{1+\omega^2\tau_c^2} + (1-S^2)\frac{\tau_e}{1+\omega^2\tau_e^2}\right] \tag{1.14}$$

Model 3) Model 1 with an additional chemical exchange contribution

Model 4) Model 2 with an additional chemical exchange contribution

Model 5) Has both a very fast and a slower internal motion (rotational correlation time constant for the fast motion, $\tau_f \ll \tau_s \ll \tau_c$ of overall tumbling). Here S_f^2 and S_s^2 $\neq$1 and τ_e=τ_c^{-1} +τ_s^{-1} as $\tau_f \rightarrow 0$.

$$J(\omega) = \frac{2}{5} S_s^2 \left[\frac{S_f^2 \tau_c}{1 + \omega^2 \tau_c^2} + (1 - S_f^2) \frac{\tau_e}{1 + \omega^2 \tau_e^2} \right] \tag{1.15}$$

A χ^2 for each model is calculated using a least squares method (1.16) to optimize the target function.

$$X^2 = \sum_i \left[\frac{R_{i,n}^{\text{meas}} - R_{i,n}^{\text{calc}}}{\sigma_{i,n}^{\text{meas}}} \right]^2 \tag{1.16}$$

Here, $\mathrm{R}_{i,n}^{meas}$ and $\mathrm{R}_{i,n}^{calc}$ are the experimental and calculated relaxation rate constants or hetNOE values respectively, and $\sigma_{i,n}^{meas}$ is the estimated uncertainty in the measured values. The model is selected using Monte Carlo simulations to determine whether the introduction of an additional parameter into the model is statistically significant. The F statistic is used to determine which model is used (1.17):

$$F = \frac{(N - n)(\chi_m^2 - \chi_n^2)}{(n - m)\chi_n^2} \tag{1.17}$$

where N is the number of variables being fit by m and n parameters.

For whichever model is selected, the following parameters are fit:

Model 1) S^2

Model 2) S^2, τ_i

Model 3) S^2, R_{ex}

Model 4) S^2, τ_i, R_{ex}

Model 5) S_f^2, S_s^2, and τ_i for the slower motion

1.5.3 NMR Relaxation Dispersion Studies of μs-ms Dynamics

Protein conformational exchange can occur on the μs-ms timescale (Figure 1.9) and has been shown to be important for protein function [141, 142]. For example, the opening of the"lid" of the nucleotide binding domain of adenylate kinase occurs on the μs-ms timescale and has been shown to be the rate limiting step for catalysis [143]. Conformational exchange occurring on the μs-ms timescale can sometimes be detected using NMR relaxation dispersion experiments (Figure 1.10). However, lack of detection of dynamics does not preclude their existence. NMR experiments have been developed for measuring chemical exchange of

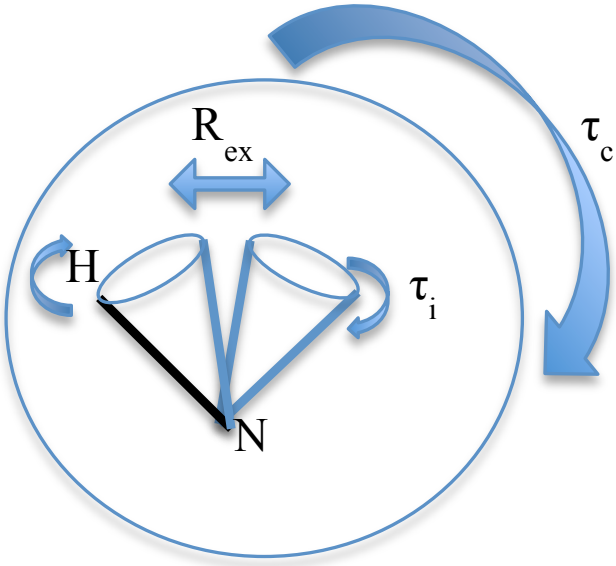

Figure 1.15: The time constant for the global tumbling of a molecule in solution is described by τ_c and for the internal motion of bond by τ_i. R_{ex} is the exchange rate constant for conformational exchange between 2 states.

^{15}N nuclei in proteins using Carr-Purcell-Meiboom-Gill (CPMG) [144, 145] based methods [146–148]. The Torchia lab developed an NMR technique for detecting μs-ms dynamics in side chain methyl groups in proteins [149], which the Kay lab improved to enable quantification of these dynamics using relaxation dispersion experiments in large proteins [150, 151]. NMR relaxation dispersion experiments have provided insight into the dynamic nature of protein side chain methyl groups [152]. NMR relaxation dispersion experiments have also been used to answer questions about the mechanisms of proteins. For example, the Kern and Kay labs showed that the catalytic mechanism of a prolyl isomerase depends on a global conformational rearrangement that was detected using relaxation dispersion experiments [153]. In addition, relaxation dispersion experiments have been used to infer the structure of a lowly (<3%) populated protein folding intermediate that is essentially invisible to other biochemical techniques [154].

Relaxation dispersion experiments can be used to measure dynamics occurring on the μs-ms timescale, provided that 1) the states between which the molecule is converting have different chemical shifts and 2) that each state is significantly populated [155]. For example, states A and B in Figure 1.9 should have distinct chemical shifts, and state B would should be at least 0.5% of the total population if μs-ms dynamics were to be detected using NMR relaxation dispersion experiments. Exchange rate constants for the interconversion between states, the relative populations of the states, as well as the chemical shift difference between the states can be obtained from fitting data to equations relating NMR peak intensity to these parameters (see Equation 1.18), however, to extract all of these parameters from the data, the experiments need be performed at more than one magnetic field strength.

The NMR pulse sequence used to detect μs-ms dynamics is similar to that used to measure R_2 relaxation. Relaxation dispersion experiments use refocusing pulses similar to those described in the spin-echo experiment used to measure R_2 (Figure 1.16). However, the relaxation delay time is kept constant in NMR relaxation dispersion experiments, and more than one refocussing pulse is applied during the constant R_2 relaxation delay time. The frequency of the refocussing pulses during the relaxation delay time is arrayed instead of the relaxation delay time. This allows R_2 relaxation to be factored out of the equation during data analysis, and the conformational exchange rate constant can be measured instead. If the molecule undergoes conformational exchange during the relaxation delay time, in the limit of refocussing pulse frequency = 0

Hz, the chemical shift will not be refocused as its Larmor frequency will have changed. Faster refocussing pulses will prevent loss of signal during the relaxation delay time relative to slower refocussing pulses, again provided criteria (1) and (2) are met and that μs-ms dynamics are occurring. By increasing the frequency of refocusing pulses during the relaxation delay the molecule will have less time and therefore be less likely to exchange between conformations. Relative to low frequency refocussing pulses, high frequency refocussing pulses will increase signal intensity if μs-ms timescale dynamics are occurring. Therefore exchange rate constants for μs-ms dynamics can by obtained by observing the change in peak intensity as a function ofthe frequency of refocussing pulses.

Exchange rate constants, chemical shifts, and populations can be determined from data obtained using relaxation rate constants, making this a powerful technique for understanding protein dynamics in solution. Under certain conditions, the exchange rate constant between 2 states can be extracted by plotting the peak volumes against the frequency of refocusing pulses and subsequently fitting the curves. Equation 1.18 is used to fit the data when the exchange is occurring in the fast limit, *i.e.* when $\Delta\omega \ll \mathrm{k}_{ex}$ where k_{ex} is the sum of the forward and reverse rate constants for the conformational exchange being interrogated [42].

$$R_{2,\mathrm{eff}}\left(\nu_{\mathrm{CPMG}}\right) = R_2^0 + \frac{p_A p_B \Delta\omega^2}{k_{\mathrm{ex}}}\left(1 - \frac{4\nu_{\mathrm{CPMG}}\tanh(\frac{k_{\mathrm{ex}}}{4\nu_{\mathrm{CPMG}}})}{k_{\mathrm{ex}}}\right) \tag{1.18}$$

R_2^0 is the relaxation rate constant without contribution from chemical exchange and $\mathrm{R}_{2,eff}$ takes into account the effect of chemical exchange. p_A and p_B are the relative populations of the molecule in 2 chemically distinct states assuming 2 state exchange, $\Delta\omega$ is the chemical shift difference of the heteronuclei being monitored with the CMPG experiment, k_{ex} is the exchange rate constant for exchange, and ν_{CPMG} is the frequency of refocusing pulses.

The data from the relaxation dispersion experiments will be used to determine whether differences in μs-ms dynamics are present between mCherry, mRaspberry and mRojoB. This information may provide clues as to whether differences in dynamics are contributing to differences in quantum yields.

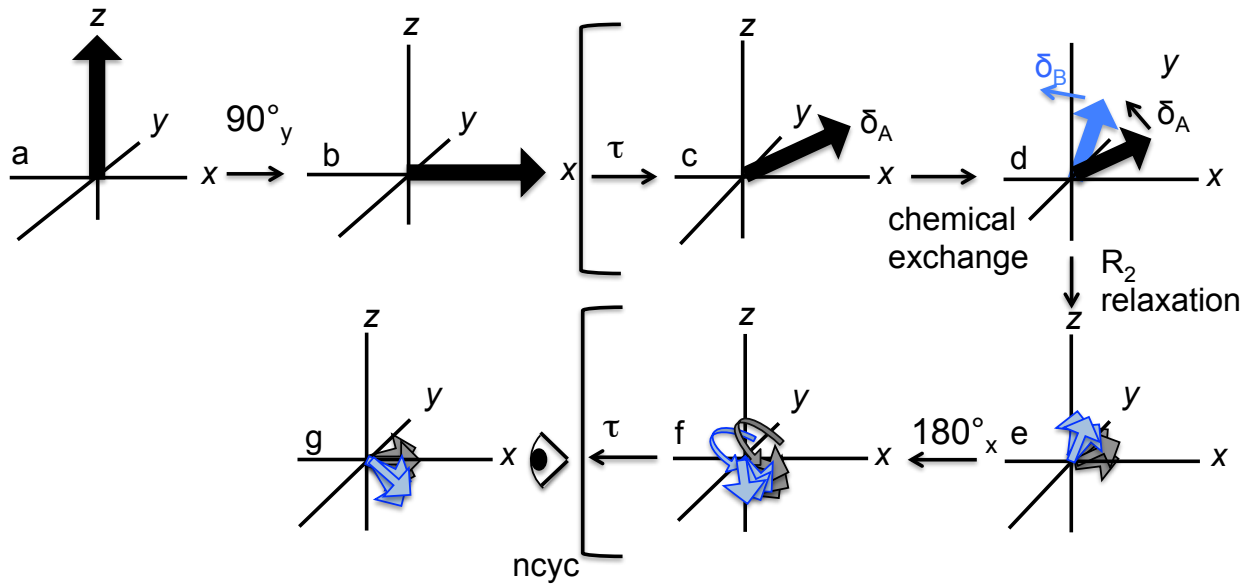

Figure 1.16: The schematic of the NMR relaxation dispersion experiment is depicted here using the vector model. Here, the vector model is being used to describe where the magnetization is during the pulse sequence used to measure μs-ms dynamics. In (a) the magnetization is at equilibrium along the z axis, aligned with the external magnetic field. In (b) after a 90° pulse has been applied along y, the magnetization is along the x axis. In (c) the magnetization begins to precess about the z axis and in (d) chemical exchange occurs, and part of the population shits to a new chemical environment which has a distinct chemical shift. The blue and black arrows precess with different Larmor frequencies. In (e) the dephasing effect of R_2 relaxation is represented by the 3 grey or blue arrows, each which has a smaller magnitude than the initial equilibrium magnetization. After a 180° pulse is applied along x, and the magnetization is flipped about the x axis in (f). Precession occurs for the same amount of time as before (d), the returning the grey magnetization to the x axis where the detector is positioned. The τ-180°-τ motif indicated between the brackets is repeated ncyc times during the constant relaxation delay period. ncyc is varied during the course of the experiment. If chemical exchange is occurring, the magnitude of the signal observed in (g) changes as a function of ncyc, (i.e. of the frequency of the refocussing pulses).

1.5.4 Protein Local Unfolding and Solvent Accessibility

Proteins in solution exist in a distribution of states from completely folded, to partially or fully unfolded [156]. Therefore depicting a protein as a static structure is not only inaccurate, but it may also lead to incorrect assumptions protein function. An understanding of protein dynamics may provide insight into protein function [157]. In particular, the function of fluorescent proteins is highly dependent on the proper folding of the tertiary structure and maturation of the chromophore. Due to the importance of tertiary structure on the photophysical properties of FPs, changes in fluorescence [80, 87, 158–161] and absorption [94, 97, 162] spectra are often monitored to detect changes in the local environment of the chromophore. The loss of fluorescence in FPs has been attributed to protein denaturation, increased flexibility of the chromophore, and exposure to fluorescence quenchers [80, 87, 158–161]. In fact, the isolated chromophore is not fluorescent outside of the β-barrel above 77 K [163]. Therefore, protection from the solvent and provision of a rigid framework for the chromophore are two important roles of the surrounding protein matrix.

Hydrogen Deuterium Exchange NMR Spectroscopy

Hydrogen-deuterium exchange (HDX) is a powerful technique to probe the solvent accessibility of hydrogens within a protein. It has been used to study a variety of biochemical phenomena including local and global unfolding [43,164–168], as well as solvent occlusion due to oligomeric interfaces or binding interactions [169–173]. HDX experiments can help elucidate an unfolding pathway [174, 175], or detect the presence of functionally relevant conformational exchange. HDX has been used to gain insight into substrate selectivity [176], locate protein-ligand interaction sites [177], and help determine the structure of higher order protein complexes [178].

Two models have been proposed to explain the exchange of hydrogens bound to the protein with those in the solvent: the structural unfolding model and the solvent penetration model [43]. A detailed explanation of the two models has been described previously [43]. Briefly, the former of the two models assumes that in order for exchange to occur, the protein must undergo a conformational rearrangement that exposes the hydrogen to the solvent, also called a local unfolding event. In this model, hydrogens on the protein surface may be still be slow to exchange if involved in a hydrogen bond that inhibits exchange. The hydrogen bonds

must break during a local unfolding event to allow for exchange. The latter of the two models assumes that solvent accessibility based on the static protein structure primarily dictates the rates of exchange, and thus that structurally buried hydrogens exchange when solvent molecules penetrate into the interior of the protein. Although there is still debate on which of these two models more accurately describes hydrogen deuterium exchange data, several notable problems with the solvent penetration model are 1) its inability to explain the vastly different rates of exchange for surface hydrogens and 2) the difficulty of charged species, like OH^- anions that are required for catalyzing exchange, entering the hydrophobic interior of a well folded protein. Although the structural unfolding model was once discredited due to biochemical data supporting a two state unfolding model for proteins, more recent data supports the idea that many proteins have locally unfolded states that could help explain hydrogen exchange data using the structural unfolding model [43].

Protein conformational exchange can occur between fully folded and partially unfolded states, with the fully folded state having the lowest free energy and the partially-unfolded states having higher free energies [65]. Figure 1.9 depicts an energy landscape for a molecule that converts between 2 populations, A and B, on the μs-ms timescale at equilibrium. Available thermal energy allows for conformational exchange on the μs-ms timescale. If an exchange event repositions a formerly buried hydrogen, or breaks a protecting hydrogen bond, the hydrogen will be more likely to exchange [43]. Figure 1.17 depicts a simplified reaction for a local unfolding event leading to hydrogen exchange. The observed rate constant for exchange is governed by the equilibrium constant for the local unfolding event depicted. One underlying assumption used to analyze HDX data is that the protein is folded, ie that $k_{cl} \gg k_{op}$. Under the structural unfolding model, two working limits have been established in the field of HDXl: the EX1 (open-limited) condition, and EX2 (pre-equilibrium) condition. Under the EX1 limit, $k_{int} \gg k_{cl}$, and the observed exchange rate constant is equal to k_{op} [179] or the rate constant for a local unfolding event. Under the EX2 limit, $k_{cl} \gg k_{int}$, and the observed exchange rate constant is equal to $K_{op} \times k_{int}$, where K_{op} is the equilibrium constant for the unfolding event [179]. Therefore, in the EX2 limit, the observed exchange rate constant will be reflective of the thermodynamics of this unfolding event as well as the intrinsic rate of exchange for the unfolded peptide (k_{int}). EX2 is almost always observed for folded proteins in the pH range of 4-7 [174].

Using NMR to monitor HDX provides atomic resolution of the exchange process. Typically, to detect

Figure 1.17: A simplified reaction for an unfolding event leading to the deprotection of a hydrogen, thus exposing it to exchange with the solvent. k_{op} and k_{cl} are the forward and reverse rate constants for the unfolding event,respectively, and k_{int} is the intrinsic rate constant for exchange of the protein in the unfolded state. The equilibrium constant for the unfolding even can be calculated as $K_{op}=k_{op}/k_{cl}$.

exchange in proteins using NMR, the peak volumes in an $^{1}H^{15}N$ HSQC correlation spectrum for amide groups are monitored as a function of time. The peaks in the spectrum will decrease in intensity as the amide protons exchange for deuterons over time. Thus, with assignments, residue specific exchange rate constants can be measured, from which information about solvent accessibility and protein dynamics can be inferred. For a given amino acid sequence, temperature and pH, protection factors can be calculated as the ratio of the observed exchange rate constant and the exchange rate constant for the proton in an unfolded polypeptide chain. Protection factors account for variables independent of solvent accessibility and allow for comparison of exchange characteristics between different proteins and experiments. Protection factors ranging from <1 to $> 10^8$ have been measured [180,181] signifying the presence of a wide variety of protein structure and flexibility in the known proteome. Protection factors within regions of β-sheet secondary structure have also been found to span 8 orders of magnitude [179,182].

Fluorescence Quenching

Fluorophores are subject to fluorescence quenching from molecules in the solvent. Fluorescence quenchers may operate through collisional quenching where the energy of an absorbed photon is transferred from an excited state fluorophore to the quencher, thus resulting in non-radiative relaxation [64]. In FPs, fluorescence quenching by molecules in the solvent is inhibited by the protein matrix surrounding the chromophore. However, channels or fluctuations in the protein structure may allow fluorescence quenchers in the solvent to penetrate the β-barrel and reach the chromophore. Of particular relevance to FPs is molecular oxygen, which is a fluorescence quencher and is usually present in fluorescent proteins samples as it is in fact necessary for chromophore maturation [11, 29]. However, while molecular oxygen is necessary for the formation of the chromophore, it can also lead to its destruction. Molecular oxygen is able to penetrate the β

barrel of a well-folded protein [83] and not only quench fluorescence, but is also important in photobleaching mechanisms [69].

The quantum yield of fluorescent proteins depends on the ability to protect the chromophore from fluorescence quenchers. One hypothesis for the high quantum yield of the wild-type tetramer, DsRed, relative to monomeric RFPs is that protein interfaces provide a stronger shield against quenchers [22]. This hypothesis was previously tested for a set of red fluorescent proteins using acrylamide as a quencher. The tryptophans of the monomer mRFP1 were more prone to quenching than those in dimer2 or DsRed [41]. However, this study also found that the chromophore of dimer2 was the most susceptible quenching of the 3 RFPs, despite having a residual interface that is proposed to shield the β-barrel from quenchers [41]. Therefore the hypothesized role of oligomeric interfaces in FPs is still in question. The relative degree of chromophore and tryptophan quenching by acrylamide for tdTomato, mCherry, mRaspberry and mRojoB was measured to further assess the role of oligomeric interfaces in RFPs.

1.6 Overview

The spectroscopic studies presented in this work were used to explore critical biophysical parameters of red fluorescent proteins variants. Using a curated set of RFPs developed from DsRed, dynamics within RFPs were probed using NMR spectroscopy. Insights gained from these experiments were to evaluate how the process of RFP directed development affected protein dynamics and local unfolding. In addition, the contribution of dynamics to the differences in quantum yields of these proteins is discussed. These results will be useful in the development of novel RFPs.

Chapter 2

Fast (ps-ns) Timescale Dynamics of Red Fluorescent Protein Variants

2.1 Introduction

Commonly used RFP variants were developed from naturally occurring, oligomeric RFPs, to generate monomeric, red-shifted probes for studying live cells. However, during the directed development process, the quantum yields of the resulting monomeric RFPs decreased. A complete understanding of the decreased quantum yields in the monomeric variants relative to the wild-type oligomers is lacking. In addition, monomeric RFP variants were designed to increase the wavelength of fluorescence emission which was achieved at the expense of quantum yield in the case of mRaspberry (Φ=0.15) and mRojoB (Φ=0.06). Within the set of monomeric red fluorescent proteins studied here, the quantum yields range from 0.22 (mCherry) to 0.06 (mRojoB). As dynamics faster than the timescale of fluorescence are known to provide non-radiative relaxation pathways for an excited state chromophore, differences in sub-ns dynamics may be contributing to differences in quantum yield. Therefore, in order to explore this possibility, the ps-ns dynamics of the backbone amides and chromophore tyrosine $C^{\beta}H$ of mCherry, mRaspberry and mRojoB were measured using NMR relaxation experiments. NMR relaxation experiments were not performed on tdTomato in order to probe backbone amide ps-ns dynamics due to the unfavorable relaxation properties of large proteins; the molecular weight of tdTomato is 54 kDa.

2.1.1 NMR Assignment

NMR spectroscopy is a powerful technique for studying proteins in solution partly because residue specific information can be obtained. In order to obtain residue specific information, the protein must

first be assigned. Each peak in an NMR spectrum can be assigned to a specific atom or in the case of multidimensional NMR, 2 or more atoms. For example, a commonly collected protein NMR spectrum is called a ^{1}H-^{15}N heteronuclear single quantum correlation, or HSQC, spectrum. This spectrum correlates nitrogens covalently bound to hydrogens. Therefore, in a ^{1}H-^{15}N HSQC spectrum, one peak arises for the backbone amide nitrogen and bound hydrogen for each residue, with a few exceptions. Amino acid amide groups have characteristic chemical shifts, or regions of the ^{1}H-^{15}N HSQC spectrum in which they appear. This helps in the assignment process, but many proteins contain hundreds of amino acids and so require specific strategies for assignment that will be described in the methods section. Assignment is an important step when solving an NMR structure, but is also useful when probing residue specific dynamics. Once assigned, the results of additional NMR experiments probing dynamics of individual amide groups, can be mapped onto known structures of the protein of interest.

2.1.2 Using NMR Relaxation Experiments to Probe ps-ns Dynamics

A fluorophore must be rigid to fluoresce lest an excited state fluorophore relax via thermal fluctuations. Structural perturbations to the chromophore, such as torsion away from planarity, occurring on the timescale of fluorescence could promote non-radiative relaxation pathways and thereby decrease the quantum yield [49,108]. Similarly, nearby residues could promote non-radiative relaxation of the excited state chromophore by perturbing the environment of the chromophore. As dynamics might decrease the quantum yield of an FP, differences in dynamics may be partly responsible for observed differences in quantum yields. ps-ns dynamics occurring in the chromophore tyrosine C$^{\beta}$Hs and backbone amides of mCherry, mRaspberry, and mRojoB were measured using ^{13}C and ^{15}N NMR relaxation experiments.

R_1, R_2, and hetNOE values measured with NMR relaxation experiments contain information about the global tumbling of and the internal dynamics within a molecule. These NMR relaxation parameters can be used to determine an order parameter that quantifies internal mobility using the model free formalism [135] which was developed to deconvolute information about the global tumbling of a molecule in solution from internal dynamics [129]. The order parameter, S, describes the amplitude of the internal motion and can range from 0 to 1 with values closer to 0 indicating increased internal flexibility [135]. Order parameters

for assigned nuclei in the protein can be compared with other residues within one protein, or between different proteins, to probe for regions of increased internal dynamics. For example, the order parameters were compared between RFP variants to probe for differences in internal dynamics that might affect the photophysical properties of the fluorophores. In addition, R_1, R_2, and hetNOE values were measured for a carbon located in the chromophore of 3 red fluorescent proteins to assess whether differences in dynamics were occurring within, or nearby, the chromophore itself.

2.2 Methods

2.2.1 NMR Assignment Methods

Protein Expression, Purification, and NMR Sample Preparation

The pET11a plasmids containing the genes for N-terminal 6-His tagged mCherry, mRaspberry, and mRojoB were obtained from Dr. Steve Mayo's lab at the California Institute of Technology. The gene encoding tdTomato was obtained in a pET28a plasmid from Dr. Ralph Jimenez's lab at the University of Colorado at Boulder and contains a Tobacco Etch Virus (TEV) site for cleaving the N-terminal 6-His tag.

The plasmids were transformed using heat shock into BL21 (DE3) pLysS cells and plated on LB agar plates containing the appropriate antibiotic to select for cells containing the plasmid. (Chloramphenicol was not used, however, and therefore pLysS cells were not necessary for protein expression.) Ampicillin was used for mCherry, mRojoB, and mRaspberry in pET11a and kanamycin for tdTomato in pET28a. A single colony was picked from the plate and grown in 10 mL of LB supplemented with either 100 μg/mL ampicillin (mCherry, mRojoB, and mRaspberry) or 50 μg/mL of kanamycin (tdTomato) for 5-8 hours at 37°C with shaking at 220 rpm. The cells were then pelleted and resuspended in 50 mL of M9 minimal media supplemented with 2 g/L $^{14}NH_4Cl$ and 4 g/L $^{1}H^{12}C$ glucose and grown for ≈16 h (overnight). The cells were then pelleted and resuspended to an optical density at 600 nm (OD_{600}) of approximately 0.1 in 1 L of M9 minimal media (Table 2.1) supplemented with the desired isotopic label(s). Proteins used for non-NMR experiments were grown as described, replacing the minimal media with LB.

1 g/L 98% $^{15}NH_4Cl$ (Sigma-Aldrich) and 3 g/L 99% ^{13}C-labeled glucose (Sigma-Aldrich) were added

Table 2.1: Minimal Media Recipe

Combine To Make 1 L Minimal Media[a]	Final concentration
100 mL 10X M9 salts[b]	1X
1 mL 1 M $MgSO_4$	1 mM
1 mL 0.1 M $CaCl_2$	100 μM
0.5 mL trace metals[c]	
10 mL vitamins (100X MEM from Gibco)	1X
1 mL 10 mg/mL Thiamine	10 μg/mL
10 mL 30% glucose (30 g/100 mL)	3 g/L
1 g ammonium chloride	1 g/L
5 mL 200X kanamycin stock (or) 1 mL 1000X ampicillin stock	50 mg/L (or) 100 μg/L

[a] All stock solutions are autoclaved or sterile filtered with a 0.2 μM filter.
[b] 10X M9 Salts contains 128 g $Na_2HPO_4 \bullet 7H_2O$, 30 g KH_2PO_4, and 5 g NaCl in 1 L of H_2O.
[c] The trace metals solution contains 27 g $FeCl_3 \bullet 6H_2O$, 1.3 g $ZnCl_2$, 2.0 g $Na_2MoO_4 \bullet 2H_2O$, 2.5 g $CaCl_2 \bullet 2H_2O$, 2.0 g $CoCl_2 \bullet 6H_2O$, 1.3 g $CuCl_2 \bullet 2H_2O$, 3.3 g $MnCl_2 \bullet 4H_2O$, 0.5 g H_3BO_3 and 100 mL HCl in 1 L of H_2O. Aliquots of this sterile filtered solution are stored at -20°C.

to the media when expressing protein to be used in 3D NMR experiments for backbone assignment. $^{15}NH_4Cl$ (1 g/L) was added to the media when expressing protein used for NMR relaxation, relaxation dispersion, or hydrogen deuterium exchange experiments. $^{15}NH_4Cl$ (1 g/L), 97% ^{2}H, ^{12}C glucose (3 g/L) (Sigma-Aldrich), ^{1}H, ^{12}C alanine (20 mg/L, natural abundance), and ^{2}H, ^{15}N ISOGROW (1 g/L) (Sigma-Aldrich) were added to the M9 media, which was prepared in 99.8 % D_2O when expressing tdTomato to be used for HDX experiments. The D_2O and ^{2}H, ^{12}C glucose were used to improve NMR data quality by enhancing the relaxation properties of the large protein. By expressing tdTomato with ^{1}H, ^{12}C alanine, protein concentration could be monitored by the NMR peak volumes of non-exchangeable protons. ^{2}H, ^{15}N ISOGROW was added to the media to improve protein yield. $^{13}C^{\beta}$ tyrosine (25 mg/L) (Sigma-Aldrich) was added to deuterated M9 media when expressing protein to be used for NMR relaxation experiments probing the chromophore tyrosine $C^{\beta}H$. Section 3.2.1 describes the labeling protocol in detail for expression of proteins specifically ^{1}H, ^{13}C labeled at the δ methyl groups of isoleucine and valine residues and the γ methyl groups of valine residues.

Proteins specifically ^{13}C labeled at the chromophore tyrosine C^{β} were expressed in a variant of BL21 (DE3) pLysS cells called CT19 cells, which lack aminotransferases responsible for adding and removing the amino groups of aromatic, branched chained hydrophobic, and alanine amino acids [183]. This cell line was used to prevent scrambling of the ^{13}C label, for example by the transamination and subsequent degradation of the C^{β} labeled tyrosine which could lead to incorporation of the ^{13}C label in another amino acid. The minimal media used for this auxotrophic cell line was supplemented with the twenty amino acids and additional nutrients as described previously [184]. Table 2.2 describes the supplemented amino acids added to the 50 mL overnight culture, and Table 2.3 describes the supplemental amino acids and additional nutrients added to the media used for protein expression. The recipe from Table 2.1 was followed during protein expression, with the omission of the nitrogen source and M9.

For all protein expression protocols, the 1 liter cell cultures were divided into five 1 L baffled flasks and grown at 37°C with shaking at 220 rpm until reaching an OD_{600} of 1 at which time the temperature was reduced to 24°C and IPTG (Gold Bio Technology, Inc.) was added to a concentration of 1 mM to induce RFP expression. The proteins were expressed for 12 to 24 hours before harvesting.

The cells were harvested by centrifugation at 5000 rpm using a Beckman centrifuge equipped with a

Table 2.2: Supplemental Amino Acids for Overnight Culture of CT19 Cells [184].

Amino Acid[a]	Amount per Liter (mg)
Alanine	600
Asparagine monohydrochloride	100
Aspartate sodium salt monohydrate	200
Glutamate sodium salt hydrate	550
Isoleucine	50
Leucine	60
Phenylalanine	75
Serine	500
Tryptophan	35
Tyrosine	35
Valine	100

[a] L-amino acids.

Table 2.3: Supplemental Nutrients for Protein Expression in CT19 Cells [184].

Amino Acids[a]	Amount per Liter (g)
Alanine	0.5
Arginine monohydrochloride	0.4
Asparagine	0.4
Aspartate sodium salt monohydrate	0.4
Cysteine	0.05
Glutamate sodium salt hydrate	0.4
Glutamine	0.65
Glycine	0.55
Histidine	0.1
Isoleucine	0.23
Leucine	0.23
Lysine	0.42
Methionine	0.25
Phenylalanine	0.13
Proline	0.1
Serine	2.1
Threonine	0.23
$^{13}C^{\beta}$ Tyrosine[b]	0.025
Valine	0.23
Nucleobases	
Adenine	0.5
Guanosine	0.65
Thymine	0.2
Uracil	0.5
Cytosine	0.2
Salts	
Sodium Acetate trihydrate	1.5
Succinic Acid	1.5
Ammonium Chloride	0.5
Sodium Hydroxide	0.85
Potassium Phosphate (Dibasic)	10.5

[a] L-amino acids
[b] This differs from the protocol in Muchmore et al. 1989, which calls for 0.085 g/L specifically labeled tyrosine.

JA-10 rotor, the supernatant discarded, and the cell pellet frozen at -20°C until proceeding to the protein purification process. Bacterial protein extraction reagent (Thermo Scientific) was added to the thawing cell pellet to aid in cell lyses. The cells were subsequently resuspended in 50 mM Tris pH 8, 300 mM NaCl, 10 mM imidazole, and Complete EDTA-Free Protease Inhibitor (Roche) and sonicated on ice. The samples were then centrifuged at 16,000 rpm for 30 minutes using a Beckman centrifuge equipped with a JA-20 rotor. The supernatant was decanted off and saved. The pelleted cellular debris was discarded, while the supernatant was passed over a NiNTA column (Qiagen) pre-equilibrated in 50 mM Tris pH 7, 300 mM NaCl, and 10 mM imidazole. Proteins were eluted with 50 mM Tris pH 7, 300 mM NaCl, and 0.6 M imidazole. tdTomato was further treated with TEV protease by combining the column fractions containing the visibly pink protein with a 500 μL aliquot of TEV protease prepared by the Pardi lab and dialyzing in 50 mM Tris pH 8, 2 mM DTT, and 0.5 mM EDTA overnight. All proteins were concentrated to less than 6 mL and further purified using FPLC over a HiLoad G75 Superdex 16/60 size exclusion column (GE Life Sciences) pre-equilibrated in 20 mM Tris pH 7, 50 mM NaCl, and 5 mM DTT. SDS-PAGE was performed on the sizing column fractions to assess protein purity (for all proteins) and TEV cleavage efficiency (for tdTomato, only).

The purified proteins were concentrated using GE Healthcare Vivaspin 20 columns with a 10 kDa molecular weight cutoff to concentrations ranging from 0.2 to 1 mM as determined using absorption spectroscopy at the wavelength of the mature chromophore (Table 1.1). A final sample of 300 μL concentrated protein, 10% D_2O, and 0.15 mM TSP was pipetted into a Shigemi NMR tube. The $^{13}C^{\beta}$ tyrosine labeled protein samples were buffer swapped into 20 mM d-11 Tris pH 7, 50 mM NaCl, 5 mM DTT, 0.15 mM TSP and >99% D_2O prior to NMR data collection.

NMR Backbone Assignment of mCherry

All NMR experiments were performed on a Varian Inova-600 or a VNMRS 800 MHz spectrometer, each equipped with a triple resonance, z-axis gradient cryogenic probe. Temperature and pH were varied from 25-30°C and pH 7 to 8, respectively, to optimize the quality of ^{1}H-^{15}N HSQC spectrum of a 0.6 mM sample of ^{1}H, ^{15}N-labeled mCherry. All spectra used for assignment were thereafter collected at 30°C and pH 7. The following 3-dimensional NMR experiments were performed using ^{13}C, ^{15}N-labeled mCherry to assign the

backbone amides using standard methods [42,185]: CACB(CO)NH TROSY, HNCACB TROSY, and HNCO TROSY. Varian's BioPack pulse sequences were used. Both NMRPipe [186] and CCPNMR Analysis [187] were used for NMR data analysis. Briefly, NMR data were processed by applying a time domain solvent filter followed by a cosine squared apodization function, zero filling, and Fourier transforming and phase correcting the direct dimension. The data from 2-dimensional spectra were then transposed followed by linear prediction, application of a cosine apodization function, zero filling, and Fourier transforming and phase correcting the indirect dimension. The filenames and parameters for the NMR spectra collected for assignment are provided in Table A.5. The amino acid sequence and the peak lists for the ^{1}H-^{15}N HSQC, CACB(CO)NH TROSY, HNCACB TROSY, and HNCO TROSY spectra were submitted to the MANI PINE server [185] for automated assignment. The assignments were also performed manually using strip plots generated in CCPNMR Analysis. Figure 2.1 shows which atoms are correlated in a CBCA(CO)NH and a HNCACB spectrum and how to use the NMR spectra to connect peaks stemming from sequential residues in a protein. In addition, the chemical shifts of the α and β carbons are indicative of the amino acid type and so aid in the assignment process.

Chromophore Tyrosine $C^{\beta}H$ Assignment of mCherry, mRaspberry and mRojoB

The tyrosine C^{β} within the chromophore of $^{13}C^{\beta}$ tyrosine labeled sample of mCherry was assigned. Comparison of ^{1}H-^{13}C HSQC spectra of mCherry enriched with $^{13}C^{\beta}$ versus natural abundance was used to locate a peak that was much more intense in the spectrum of the $^{13}C^{\beta}$ labeled sample. The BioPack sensitivity enhanced gChsqc.c pulse sequence was used with carbon decoupling during acquisition. The carbon carrier frequency was set to 125 ppm and 0.00145 s and 0.0013 s were used for the carbon and proton INEPT periods, respectively, which correspond to a J_{CH} of 172 and 192 Hz, respectively. The chromophore tyrosine C^{β} of mRaspberry and mRojoB were also assigned via spectral overlay with that of mCherry. The ^{1}H-^{13}C HSQC spectra of tyrosine $^{13}C^{\beta}$ labeled mRaspberry and mRojoB were collected at 37°C, and with the carbon carrier frequency set to the chemical shift of the chromophore tyrosine C^{β} (140 ppm). In addition, INEPT times were changed to 0.0017 s and 0.0016 s in the spectrum collected of the $^{13}C^{\beta}$ tyrosine labeled sample of mRaspberry. The J_{CH} coupling constant was measured for the chromophore tyrosine C^{β} (150 Hz) by modifying the pulse sequence to remove proton decoupling during t_1 and then measuring the coupling in

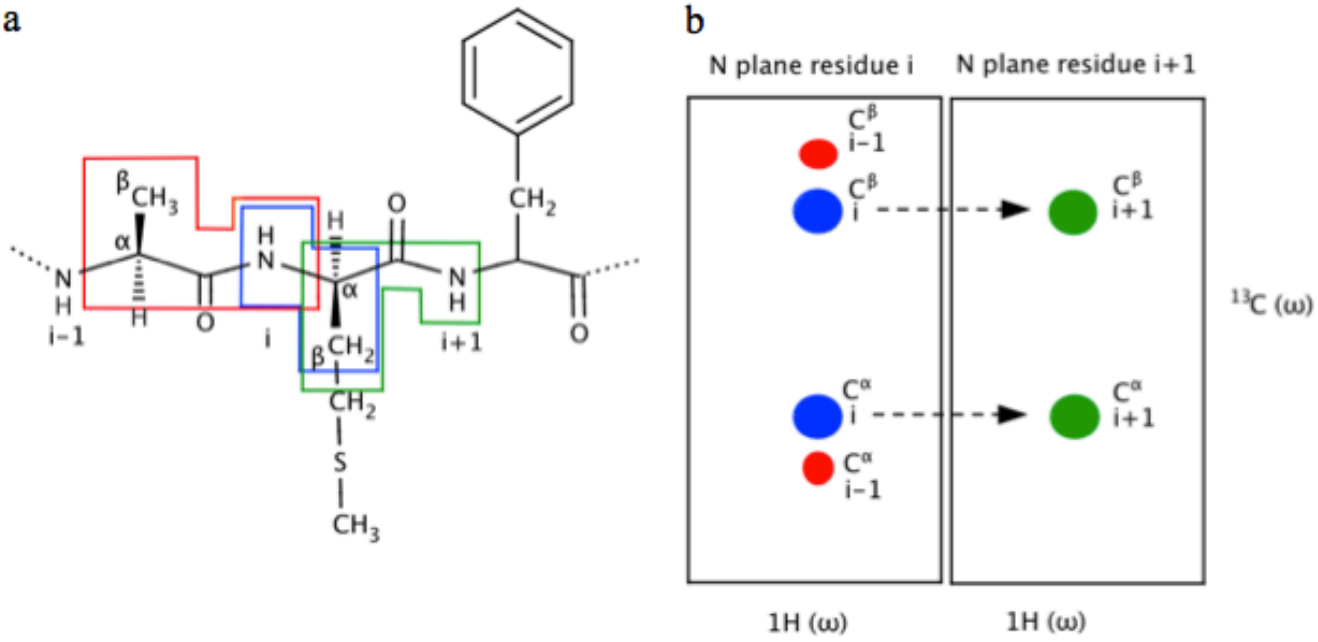

Figure 2.1: (a) Three amino acids in a polypeptide chain: i-1 is alanine, i is methionine, and i+1 is phenylalanine. The boxes surround the atoms which are correlated in a CBCA(CO)NH (black) and an HNCACB (red and blue) NMR 3-dimensional correlation spectrum. (b) Two slices of 3-dimensional NMR spectrum correlating the C^{α}, C^{β}, and backbone amide nitrogen and proton within one amino acid (left HNCACB, blue), or the C^{α}, C^{β}, and backbone amide nitrogen of the neighboring amino acid (left red and right CBCA(CO)NH, green).

the carbon dimension of the resulting spectrum. By labeling the chromophore tyrosine with a single ^{13}C, issues such as carbon-carbon coupling that would have complicated data analysis were avoided.

NMR Backbone Amide Assignment Transfer by Spectral Overlay

The goal of NMR backbone amide assignment transfer by spectral overlay was to assign the backbone amides of tdTomato, mRaspberry and mRojoB while sidestepping the time consuming and costly processes of ^{13}C, ^{15}N labeling protein samples and collecting 3-dimensional NMR spectra. To transfer the assignments from the 30°C spectrum of mCherry to those of mRaspberry and mRojoB, the 30°C ^{1}H-^{15}N HSQC TROSY spectra were overlaid using the program CCPNMR Analysis. The peaks were overlaid so that the largest percentage of peaks in the 2 spectra were overlapping.

Assignments were transferred to peaks in the ^{1}H-^{15}N HSQC TROSY spectra of mRaspberry and mRojoB that overlapped with only one peak from the mCherry spectrum. If multiple peaks overlapped with a single peak in the other spectrum, an assignment was not transferred. If a peak in the spectrum of mRaspberry or mRojoB was the closest peak to a single peak in the spectrum of mCherry, the assignment was transferred in certain cases depending on whether the surrounding peaks in the spectra of mRaspberry or mRojoB were assigned (see Figure 2.10 for examples).

To transfer the assignments to the spectra of mCherry, mRaspberry, mRojoB and tdTomato collected at 37°C, a similar procedure was followed as that described to transfer assignments between spectra collected at 30°C. To transfer assignments to the spectrum of mRojoB collected at 37°C, the spectra of mRojoB collected at 30°C, of mCherry at 30°C and of mCherry at 37°C were overlaid with that of mRojoB at 37°C. This aided in assignment transfer by observing trends in peak shifts between the pair of spectra of mCherry and the pair of spectra of mRojoB (see Figure 2.11 for an example). The same strategy was used when transferring assignments to the spectra of mRaspberry collected at 37°C. Since no spectrum of tdTomato was collected at 30°C, the overlay of the spectra of tdTomato at 37°C, mCherry and 30°C and mCherry at 37°C were used to transfer backbone amide assignments from mCherry to tdTomato.

2.2.2 NMR Relaxation Experiments Methods

Backbone Amides

NMR ^{15}N R_1 and $R_{1\rho}$ relaxation experiments, as well as heteronuclear nuclear Overhauserver effect ($\{^1$H$\}$-^{15}N hetNOE) experiments were performed at 37°C on ^{15}C-labeled samples of mCherry, mRaspberry, and mRojoB using a 600 MHz Varian spectrometer. As stated previously, NMR relaxation experiments were not performed on the tandem dimer, tdTomato, due to the unfavorable relaxation properties of large proteins; the molecular weight of tdTomato is 54 kDa. $R_{1\rho}$ experiments were collected instead of R_2 experiments to eliminate the contribution of chemical exchange to R_2, and $R_{1\rho}$ values were later converted to R_2 values. BioPack gNhsqc.c pulse sequences were used employing the TROSY method when measuring R_1 and decoupling when measuring $R_{1\rho}$. When measuring R_1 and $R_{1\rho}$, the relaxation delay times were arrayed randomly from 0 to 1,600, and from 0 to 300 milliseconds, respectively (Table A.1). Duplicates of at least one relaxation time delay were collected to assess systematic errors between measurements. To determine whether the sample remained stable at 37°C, spectra were overlaid and analyzed for shifting peaks during the course of the experiment.

The sets of 2-dimensional spectra were analyzed with the program CCPNMR Analysis. An NMR series was created to link all experiments within the set of 2-dimensional spectra used to measure R_1 or $R_{1\rho}$. Using the CCPNMR Analysis built-in function, the ^{15}N R_1 and $R_{1\rho}$ values and errors for the backbone amides were calculated by fitting peak intensities as a function of the delay time to a decaying exponential [187]. The errors for the singlet set of R_1 or $R_{1\rho}$ data were calculated by CCPNMR's built-in covariance method from the exponential fit of the data for each resonance [129, 187]. Error calculations by fitting one set of R_1 or $R_{1\rho}$ data to a single exponential are standard for the field [188].

The $R_{1\rho}$ values were converted to R_2 values using

$$R_2 = \frac{R_{1\rho} - R_1 \cos^2\theta}{\sin^2\theta} \tag{2.1}$$

$$\theta = \arctan\left(\frac{\gamma B_1}{\Delta\omega}\right) \tag{2.2}$$

where γB_1 is the ^{15}N spin-lock frequency, and $\Delta\omega$ is the difference in chemical shift (in Hz) between the peak and the carrier frequency [189]. The ^{15}N R_1 and R_2 values were then used to calculate effective

rotational correlation time constants, τ_e, for the individual backbone amides of mCherry, mRojoB, and mRaspberry using equation 2.3 as described previously [42]. The τ_e errors were calculated using the errors for R_1 and R_2 error propagation [190] according to Equation 2.4. Equation 2.3 can be used for data collected at high magnetic fields (500 MHz or greater), assuming a rigid, spherical protein, in the limit of slow molecular motion ($\tau_c \gg 0.5$ ns) for proteins of up to about 25 kDa assuming that relaxation is dominated by dipolar and CSA relaxation mechanisms [126].

$$\tau_e = \frac{1}{4\pi\nu_{\text{nuc}}}\sqrt{6\left(\frac{R_2}{R_1}\right) - 7} \tag{2.3}$$

where ν_{nuc} is the Larmor frequency for the nucleus of interest.

$$\text{Error}_{\tau_e} = \left(\left(\frac{3R_2}{4\pi\nu_{\text{nuc}}}\right)\left(6\frac{R_2}{R_1} - 7\right)^{.5}\left(\frac{R_{1\text{err}}}{R_1^2}\right)^2\right)^{.5} + \left(\left(\frac{-3R_2^2}{R_1 4\pi\nu_{\text{nuc}}}\right)\left(6\frac{R_2}{R_1} - 7\right)^{-.5}\left(\frac{R_{2\text{err}}}{R_2^2}\right)^2\right) \tag{2.4}$$

The $\{^1\text{H}\}$-^{15}N hetNOE value was calculated by taking the ratio of the peak volume of the presaturated spectrum to that of the reference spectrum, I_{sat}/I_{ref}, (Figure 2.2). The errors for the $\{^1\text{H}\}$-^{15}N hetNOE values were calculated from the single set of spectra using error propagation [190] (Equation 2.5) and the signal-to-noise ratios for each individual peak in the presaturated and the reference $\{^1\text{H}\}$-^{15}N hetNOE spectra. This approach for error calculation may be used when replicate data are not collected [129]. NMRPipe's built-in function was used to estimate the error in both the reference and presaturated spectra [186]. The average ^{1}H-^{15}N τ_e was calculated from a trimmed data set to determine the rotational correlation time constant for the global tumbling, τ_c, of the protein in solution. The trimmed data set excluded: a) values from residues whose matching $\{^1\text{H}\}$-^{15}N hetNOE values were negative and b) values that were more than one standard deviation from the average of the full data set. Values more than one standard deviation from the average were excluded as small R_1/R_2 ratios are indicative of increased μs-ms timescale dynamics and large R_1/R_2 ratios are indicative of increased ps-ns timescale dynamics [129]. The average $\{^1\text{H}\}$-^{15}N hetNOE value was calculated using the same criteria as used to calculate the average τ_e.

$$\text{Error}_{\text{hetNOE}} = \sqrt{\left(\frac{1}{\text{PeakVol}_{\text{ref}}}\right)^2 \text{Noise}_{\text{Sat}}{}^2 + \left((-\text{PeakVol}_{\text{presat}})(\text{PeakVol}_{\text{ref}}{}^{-2})\right)^2)(\text{Noise}_{\text{Ref}})^2} \tag{2.5}$$

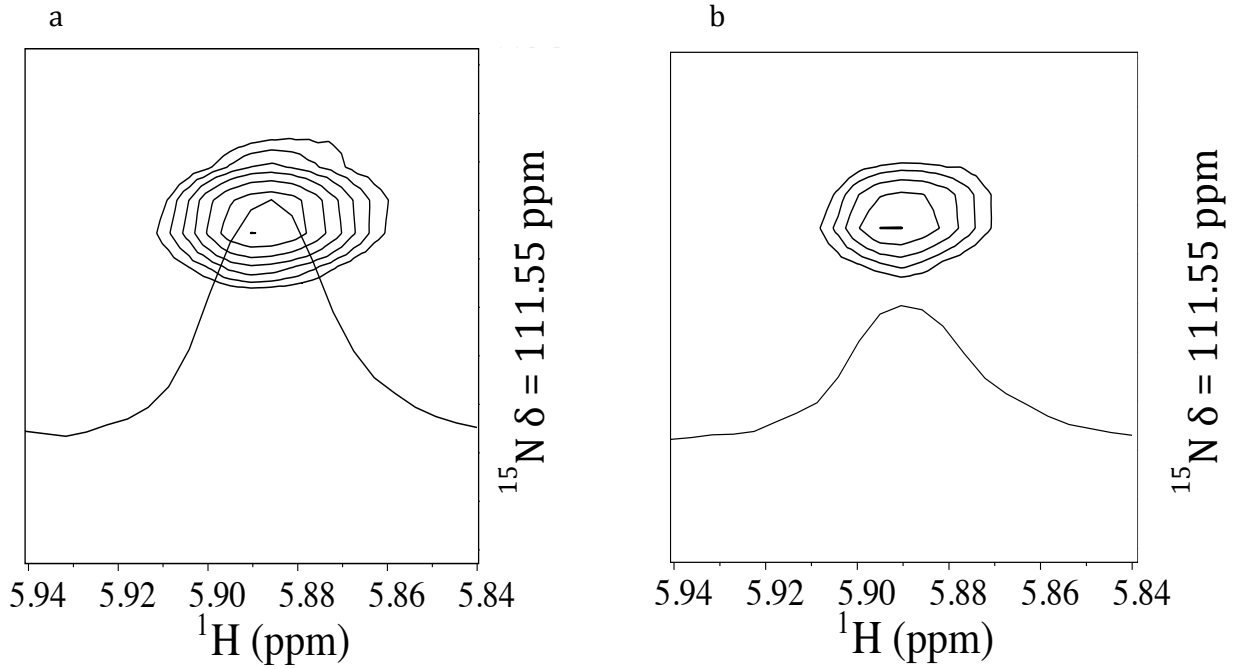

Figure 2.2: The reference {^{1}H}-^{15}N hetNOE (a) and pre-saturated {^{1}H}-^{15}N hetNOE spectrum (b) for the backbone amide of phenylalanine 69 of mRaspberry. The presaturated peak volume is smaller than that of the reference spectrum due to the negative NOE. The data were collected at 37°C.

Using Tensor2 to calculate backbone amide order parameters

The order parameters for the assigned backbone amides were calculated using the Model Free formalism [135] and the program Tensor2 assuming fully anisotropic tumbling [136]. Tensor2 determines the associated errors for the order parameters and additional fitted parameters (see Introduction [136]). ^{15}N relaxation parameters and errors were used as input for the program Tensor2. The crystal structure of mCherry, with H-atoms added using the web service MolProbity [191], was input into Tensor2 for the calculation of the diffusion tensor. A trimmed set of data, which excluded the mobile residues based on the criteria mentioned previously, was used to calculate the diffusion tensor. The average S^2 was calculated excluding mobile residues as decribed for the average {^{1}H}-^{15}N hetNOE and τ_e.

Chromophore Tyrosine $C^{\beta}H$

NMR ^{1}H-^{13}C R_1, $R_{1\rho}$ and R_2 relaxation experiments, as well as {^{1}H}-^{13}C hetNOE experiments were performed at 37°C on samples of mCherry, mRaspberry, and mRojoB containing a ^{13}C label at the

chromophore tyrosine C^{β} [42, 129]. Due to the large TROSY effect detected for the chromophore tyrosine C^{β}, TROSY based pulse sequences were used to measure R_1, $R_{1\rho}$ and R_2. The gNT1T2_trosy.c pulse sequence written by Youlin Xia was modified to measure ^{13}C R_1 and R_2. The new pulse sequence, called gCT1T2_trosy.c, was further modified to allow the relaxation delay times to be odd multiples of 2 ms rather than 10 ms and titled gCTT1T2_trosy_working.c. The relaxation delay times were varied within a set of 2-dimensional experiments and can be found in Table A.2. Using similar methods to those described in section 2.2.2, the ^{13}C R_1, $R_{1\rho}$, and R_2 values for the chromophore tyrosine C^{β} were measured by fitting peak intensities as a function of the delay time to a decaying exponential. The $R_{1\rho}$ value calculated for the chromophore tyrosine C^{β} of mCherry was converted to R_2 as described in the ^{15}N relaxation methods section 2.2.2 substituting ^{13}C for ^{15}N [189]. The $\{^1H\}$-^{13}C hetNOE values for the chromophore tyrosine C^{β}s of mCherry, mRojoB, and mRaspberry were calculated as I_{sat}/I_{ref} [192–194]. The saturation delay used in the $\{^1H\}$-^{13}C hetNOE experiment was 2 seconds.

2.3 Results

2.3.1 NMR Assignment Results

Pure protein samples were obtained for use in NMR and additional spectroscopic experiments, based on SDS-PAGE. Figure 2.3 shows SDS-PAGE gels for purifications of ^{15}N, ^{13}C-labeled mCherry, ^{15}N-labeled mRaspberry, ^{15}N-labeled mRojoB, ^{1}H, ^{15}N-labeled tdTomato, and $^{13}C^{\beta}$-tyrosine-labeled mCherry and mRojoB. It has been shown that RFP tends to cleave at the acylimine bond under denaturing conditions [29], thus explaining the two smaller molecular weight fragments in the gels of the monomers (a 9 and 19 kDa peptides is present below the full length 28 kDa peptide). Since tdTomato has more than one chromophore, during denaturation, it may cleave into as many as four fragments. Protein yields were generally $\geq$ 5 mg/L growth for monomeric RFPs: i.e. more than enough protein for a 300 μL 0.6 mM protein NMR sample in 1 L growth of monomeric RFPs or in a 2 L growth of the 54 kDa tdTomato when grown in deuterated medium.

NMR assignment was performed so that the results of additional NMR experiments could be mapped

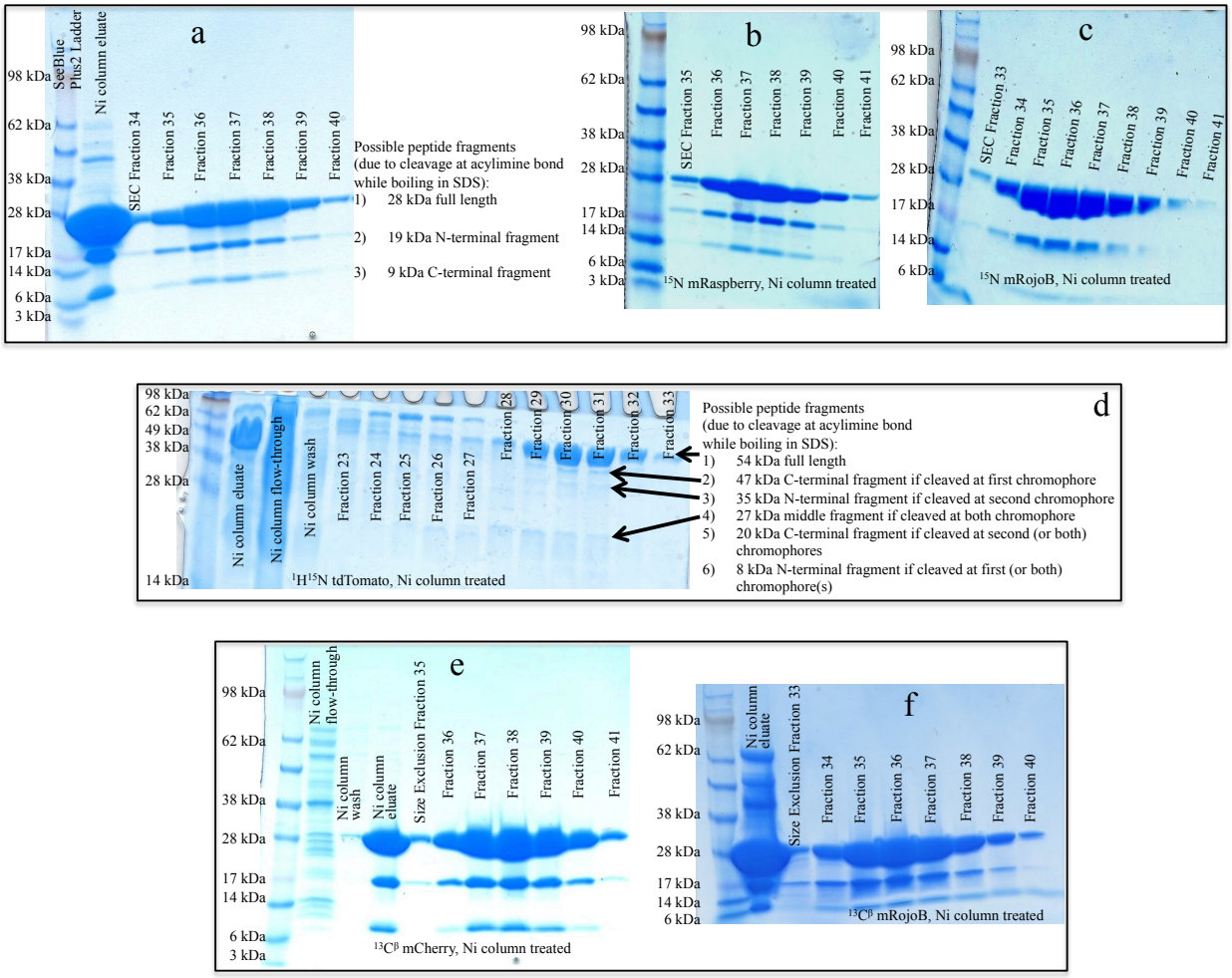

Figure 2.3: SDS-PAGE gels for purifications of a) ^{15}N, ^{13}C-labeled mCherry, b) ^{15}N-labeled mRaspberry, c) ^{15}N-labeled mRojoB, d) ^{1}H, ^{15}N-labeled tdTomato, and e) ^{13}C$^{\beta}$-tyrosine-labeled mCherry and f) mRojoB. During boiling in SDS buffer, the acylimine bond is prone to cleavage, thus fragmenting the protein into 19 and 9 kDa peptides.

onto the crystal structures of the RFPs. Assignments were made for 183 (75%) of the backbone amide nitrogens and protons of mCherry at 30°C. More than 95% of the mCherry assignments transferred to the spectra collected at 37°C leading to 72% of the backbone amides being assigned for mCherry at 37°C. Assignments were transferred to 24, 32, and 7% of the backbone amides of mRaspberry, mRojoB and tdTomato, respectively, 37°C. The backbone amide assignments are shown on the ^{1}H-^{15}N HSQC TROSY spectrum of mCherry in Figure 2.4, along with the crystal structure [31] illustrating that there is good coverage of the β-barrel secondary structure. The assignments of the backbone amides for mCherry at 30°C and 37°C, as well as for mRaspberry, mRojoB and tdTomato at 37°C are listed in Table C.1. Although tentative assignments were determined using the automated PINE server, only assignments that were confirmed manually via backbone connectivities from the HNCACB and CBCA(CO)NH spectra were deemed confident (Figure B.34). The NMR strip plots demonstrating the backbone connectivities using HNCACB and CBCA(CO)NH spectra are displayed in Figure B.34. Of the 160 assignments predicted by PINE with $\geq$ 90% confidence, 22 were misassigned as determined by manual verification. Of the residues containing a backbone amide hydrogen, 67 were predicted with $<$ 90 % confidence, and of these 6 were confirmed manually.

Assignments were further confirmed through the use of NOEs which indicate that two protons are close (within 5 Å) in space. Figures 2.5 and 2.6 depict how the ^{1}H-^{1}H NOESY ^{1}H-^{15}N HSQC spectrum was used to verify the assignments for histidine 30, methionine 31, and glutamate 32. NOEs were predicted between neighboring residues in the primary sequence as well as between strands when the amide protons on opposing strands were within 5 Å of one another. The detected amide-amide NOEs are indicated in Figure 2.6 as red arrows between residues.

When assigning the backbone amides, the expected number of peaks was compared to the observed number of peaks in a ^{1}H-^{15}N HSQC TROSY spectrum to assess whether complete assignment was possible. The number of expected peaks in the mCherry, mRojoB, and mRaspberry ^{1}H-^{15}N HSQC TROSY spectra are 243, 243, and 232, respectively, excluding peaks from asparagine, glutamine, lysine and arginine side chains. After cleaving the N-terminus at the TEV cleavage site, tdTomato has 478 residues. Due to the symmetry of the homodimer, most of the residues in one subunit of tdTomato should be chemically indistinguishable from the same amino acid in the second subunit, thus reducing the number of expected peaks by nearly 2

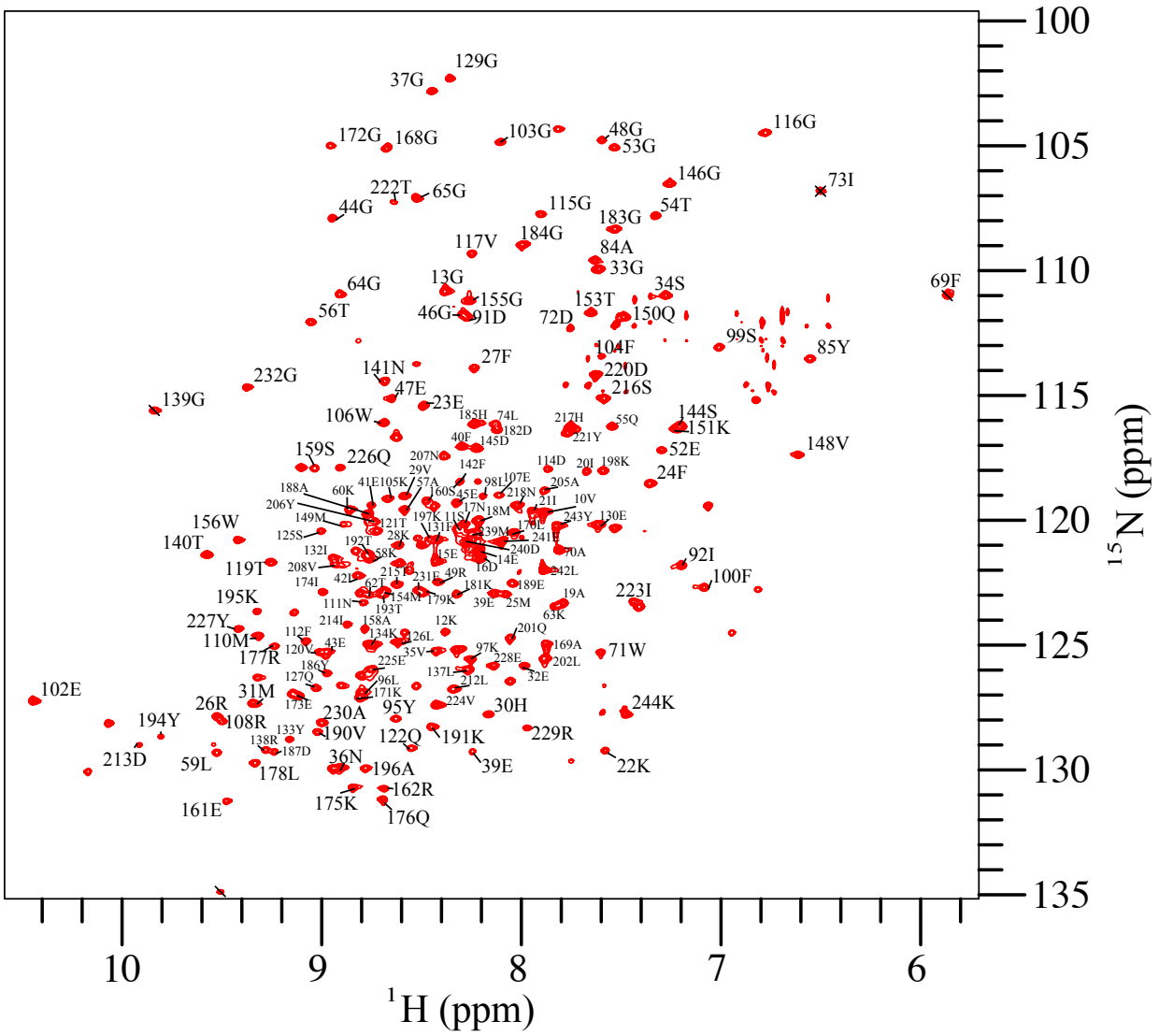

Figure 2.4: A 2D ^{1}H-^{15}N HSQC TROSY spectrum of mCherry in which more than 75% of backbone amides have been assigned. The spectrum was collected in one hour at 30°C at 600 MHz. The residues are numbered according to the construct used which has 13 additional residues at the N-terminus relative to the construct used for the determination of the crystal structure [31]. Assignments have been mapped onto a cartoon representation of the crystal structure of mCherry on the inset, where assigned and unassigned residues are in red and grey, respectively.

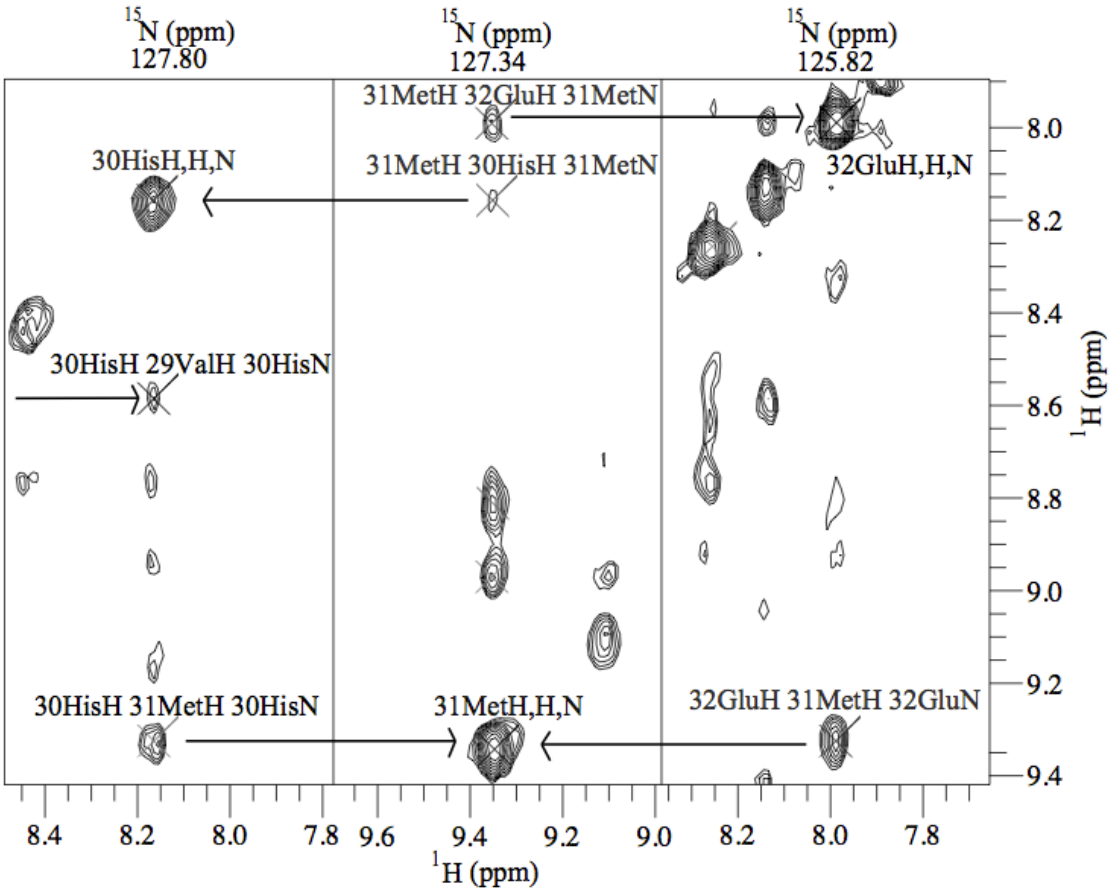

Figure 2.5: Three strips of a 3D ^{1}H-^{1}H NOESY ^{1}H-^{15}N HSQC spectrum of ^{1}H^{15}N mCherry. Cross peaks arise from backbone amide protons near (within 5 Å) in space and provide a method for assignment verification.

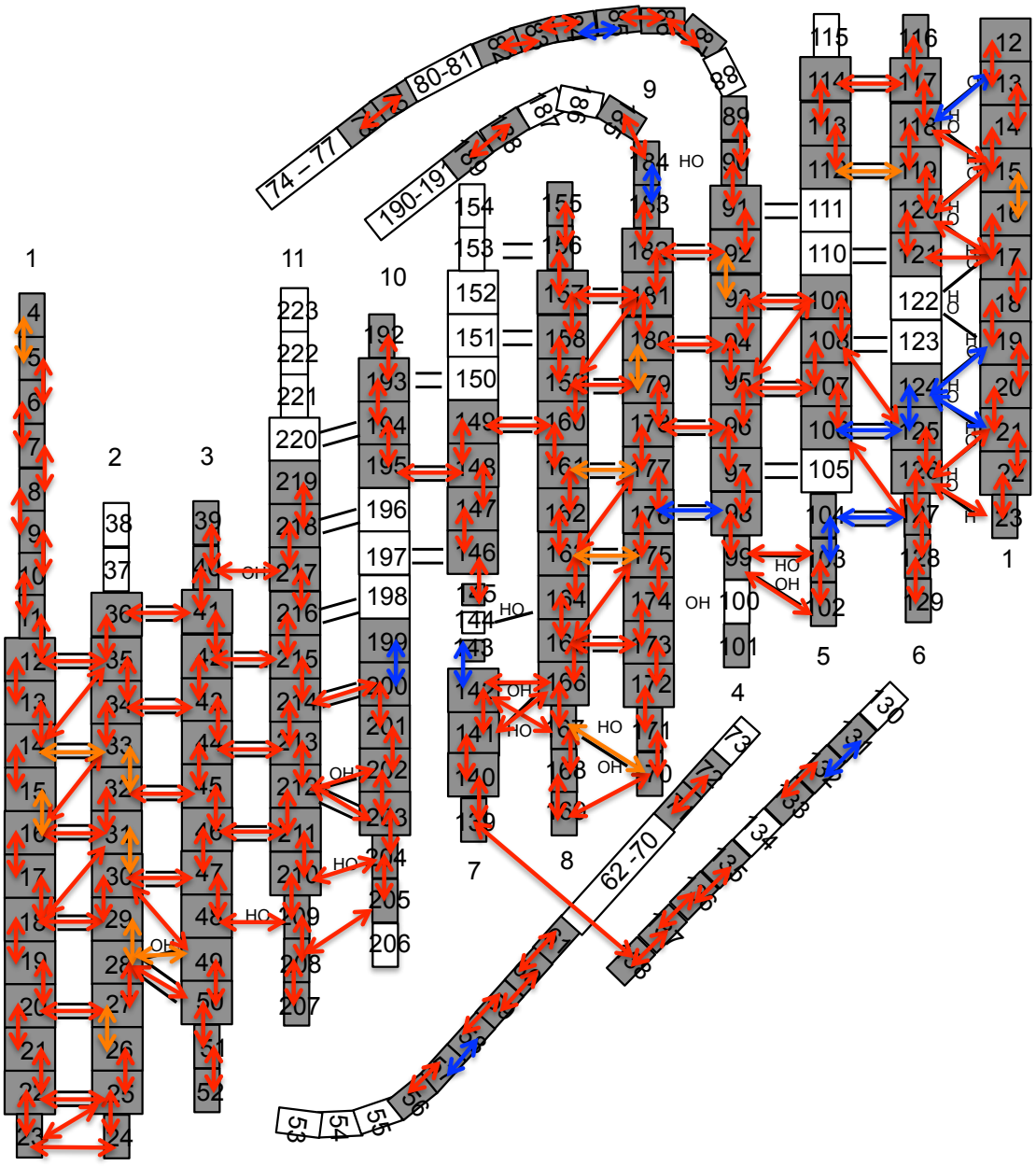

Figure 2.6: The NOEs mapped onto a topology diagram for mCherry. Squares represent individual residues in the β-barrel, while rectangles represent residues in loops, α-helices, or random coils. Residues 143-145 are an exception as they are shown as small squares but are located in the bulge in strand 7. Grey residues are assigned while white are unassigned. Red arrows indicated NOEs that were detected and blue arrows indicate NOEs that were expected but were not detected. Orange arrows indicate an NOE may have been present but that the two resonances were overlapped, and so a cross peak was not obviously present or absent. The strand number is given either directly below or above each β-strand. Two black lines between residues indicate two hydrogen bonds between residues. One black line indicates one H-bond between residues and is accompanied by the letters H and O to denote which residue is contributing the amide proton or carbonyl oxygen, respectively, to the H-bond.

fold [195–197]. Of the 478 residues in the protein, 255 have a unique chemical environment and result in a peak in the ^{1}H-^{15}N HSQC spectrum. However, the linker between the 2 subunits affects the symmetry of the molecule. Therefore it is likely that residues near the linker will be chemically distinct between the 2 subunits, and increase the number of expected peaks. 239, 229, 232, and 225 peaks were observed in the ^{1}H-^{15}N HSQC spectra of tdTomato, mCherry, mRaspberry and mRojoB, respectively, collected at 37°C. The standard deviation in peak volumes is larger in the spectra of mRojoB (0.7) and tdTomato (0.9) when compared to mCherry (0.5) or mRaspberry (0.5). The average peak volumes were calculated for the largest 239, 229, 232, and 225 peaks in the spectra of tdTomato, mCherry, mRaspberry, and mRojoB respectively.

Red fluorescent proteins are structurally homologous 11-stranded β-barrels surrounding an internal α-helix containing the chromophore. The known crystal structures of red fluorescent proteins are very similar. The crystal structures of mCherry and mRojoA (2 residues different from mRojoB) overlay with an RMSD of less than 0.3 Å (Figure 2.8) and those of mCherry and wild-type RFP, DsRed, overlay with an RMSD of 0.3 Å (Figure 2.9). However, the ^{1}H-^{15}N HSQC TROSY spectra of the 4 RFPs studied here, tdTomato, mCherry, mRaspberry and mRojoB, show substantial differences, therefore complicating assignment transfer between spectra (Figure 2.7). Comparison of ^{1}H-^{15}N HSQC TROSY spectra for mRojoB, mRaspberry and tdTomato, with that of mCherry yielded assignments for ≈30%, ≈20% and <10% of the backbone amides in mRojoB, mRaspberry, and tdTomato, respectively, for ^{1}H-^{15}N HSQC spectra collected at 37°C.

The strategies for assigning peaks that did not overlay perfectly with an assigned peak in the ^{1}H-^{15}N HSQC TROSY spectra of mCherry collected at 30°C were described briefly in the methods section. Several specific examples of assignment transfer are described here. The peaks for glycine 172 and aspartate 72 in the spectrum of mCherry collected at 30°C do not overlay with any peaks in the spectrum of mRojoB, however, the assignment was still transferred due to the lack of other unassigned nearby peaks in the spectrum of mRojoB (Figure 2.10). Furthermore, peaks shifted between the ^{1}H-^{15}N HSQC TROSy spectra collected at 30°C and at 37°C. While the spectra used for the assignment of mCherry were collected at 30°C, NMR experiments probing protein dynamics, including relaxation, relaxation dispersion, and hydrogen deuterium exchange, were carried out at 37°C. The rationale behind performing the dynamics experiments at 37°C rather than 30°C was to measure dynamics at the same temperature at which most biological studies using

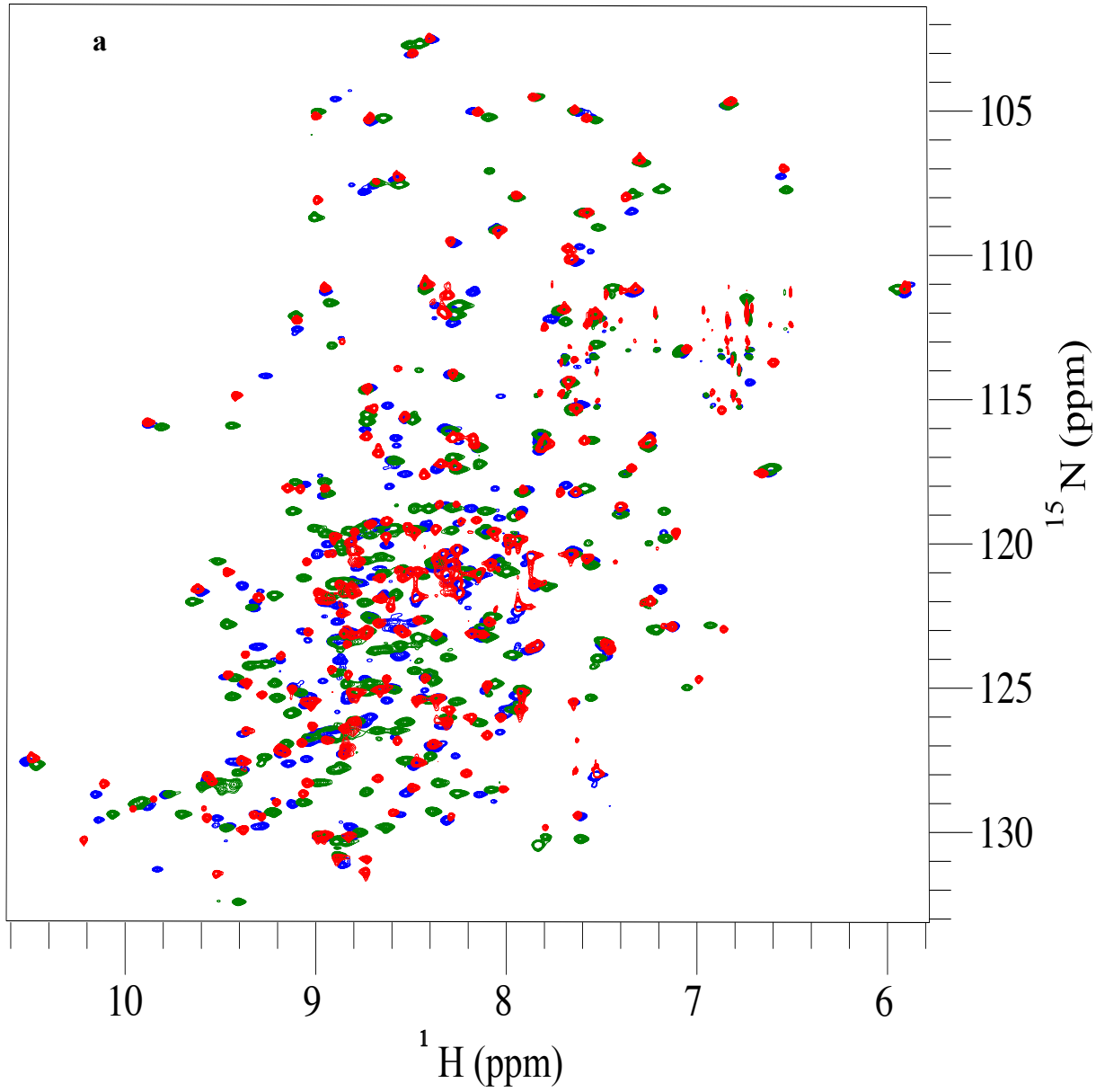

Figure 2.7: Continued on following page

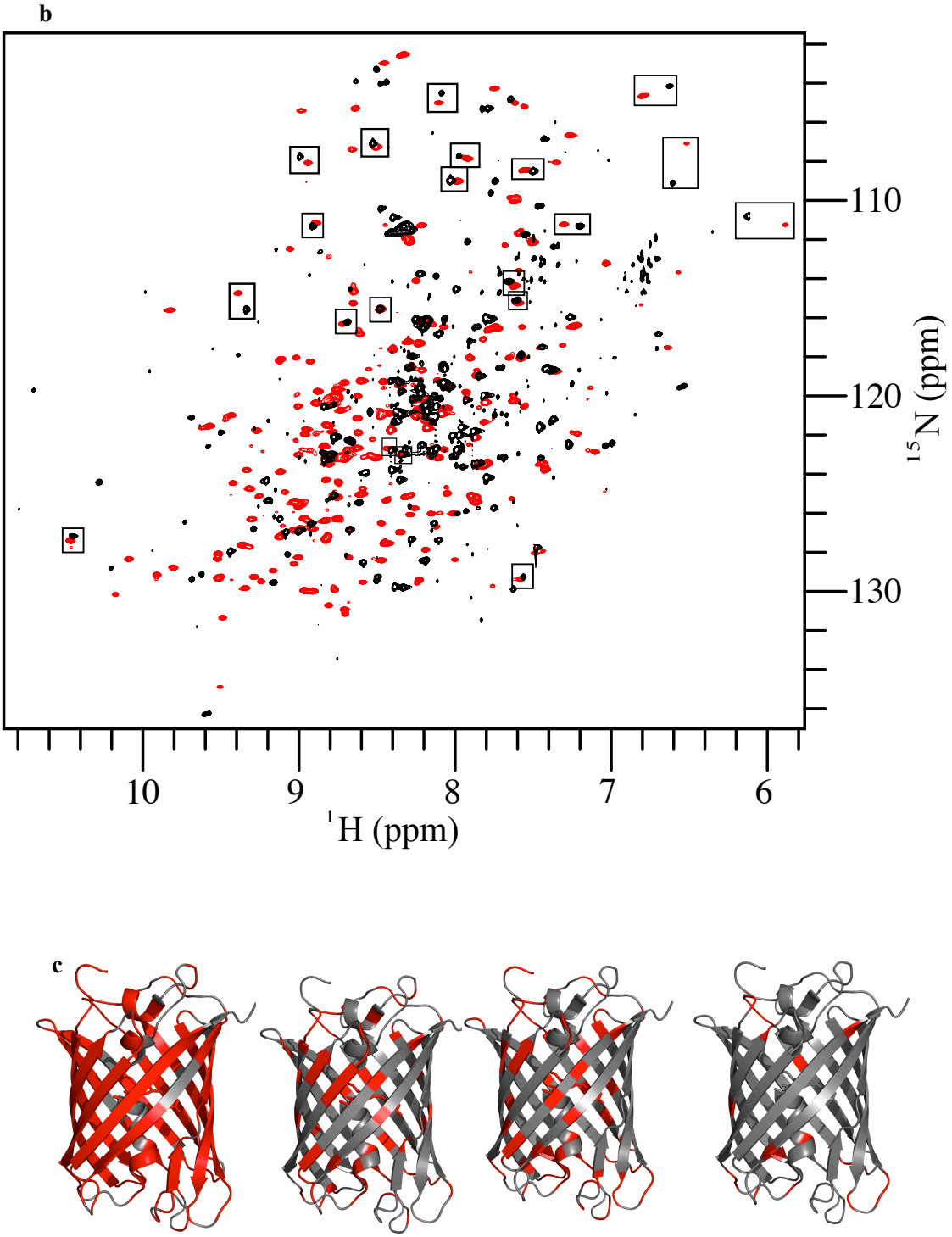

Figure 2.7: (a) Overlay of ^{1}H-^{15}N HSQC TROSY spectra of mCherry (red), mRojoB (blue), mRaspberry (green). (b) Overlay of ^{1}H-^{15}N HSQC TROSY spectra of mCherry (red), and tdTomato (black). The assignments that were transferred between mCherry and tdTomato are boxed. (c) From left to right, the assignments for mCherry, mRaspberry, mRojoB and tdTomato mapped onto the crystal structure of mCherry in red.

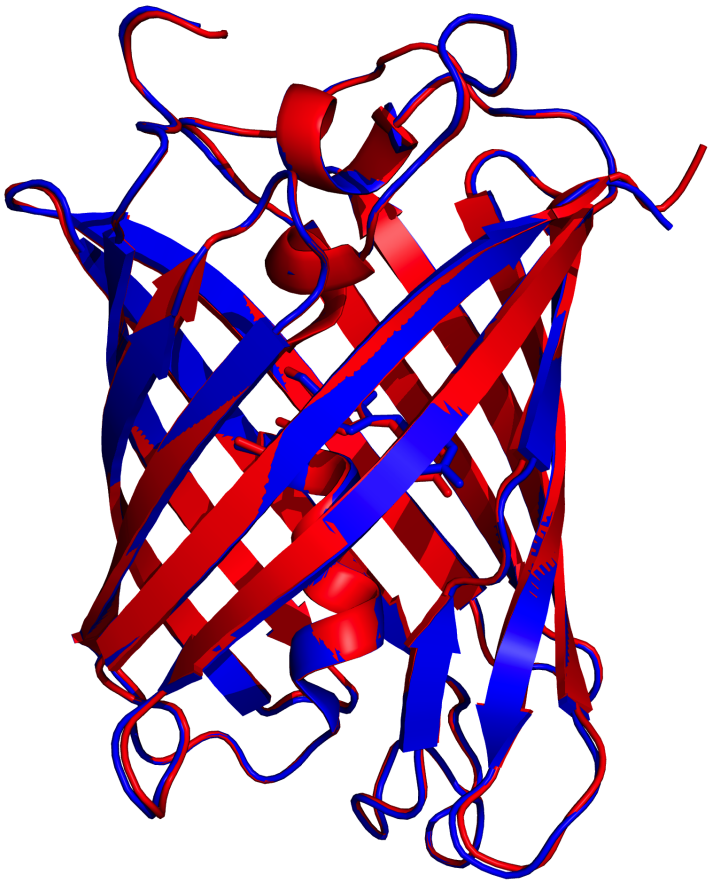

Figure 2.8: The crystal structure of mCherry (red) overlays with an RMSD of less than 0.3 Å with that of mRojoA (blue) when aligning all atoms in residues 4-223.

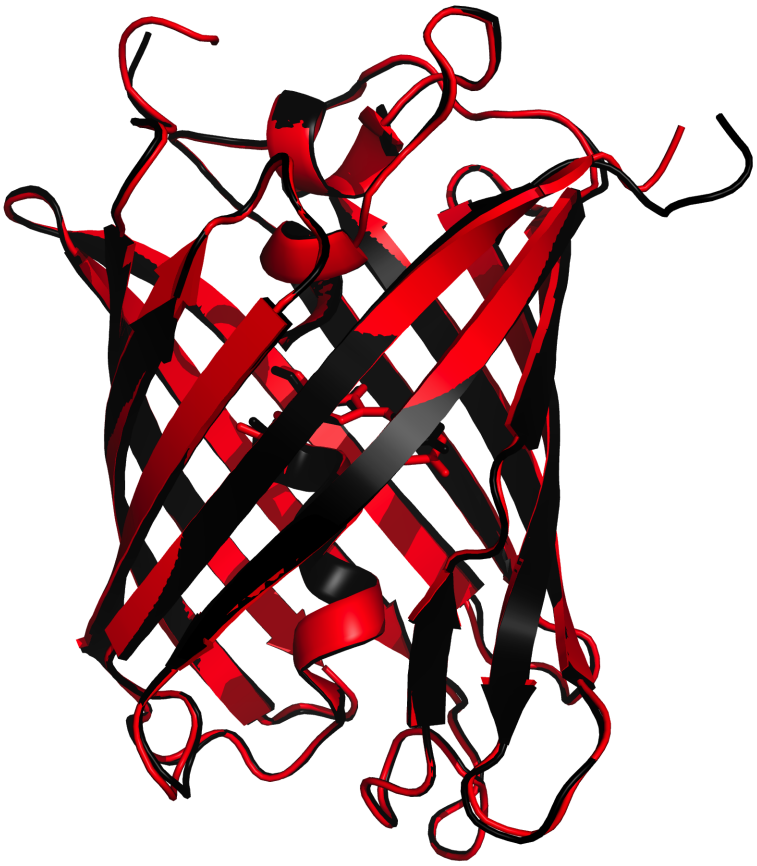

Figure 2.9: The crystal structure of mCherry (red) overlays with an RMSD of 0.3 Å with that of DsRed (black) when aligning all atoms in residues 4-223 of mCherry with Chain A residues 6-225 in DsRed.

fluorescent proteins are carried out. Probing dynamics under physiological conditions was important since dynamic processes are temperature dependent. An example of how assignments were transferred from spectra collected at 30°C to spectra collected at 37°C is described here. The peak assigned as alanine 57 in the 37°C spectrum of mRojoB does not overlay with a peak in the spectrum of mRojoB collected at 30°C or either spectra of mCherry (Figure 2.11). The peak in the spectrum of mRojoB was assigned to alanine 57 since the same downfield shift in the nitrogen dimension was observed for the pair of mCherry spectra collected at 30°C and 37°C as as in the pair of mRojoB spectra collected at 30°C and 37°C.

For each protein, a list of tentative and confident assignments at 37°C was made (Table C.2). For the spectra to which assignments were transferred from the spectrum of mCherry collected at 30°C, the confident assignments were those peaks that overlaid with a confidently assigned peak in the mCherry spectrum. The tentative assignments were those peaks that did not overlay with a peak in the mCherry spectrum but were closest to one confidently assigned peak in the 30°C mCherry spectrum or that overlaid with a tentatively assigned peak.

The assignments presented in Tables C.1 and C.2 list the amino acid sequence along with the chemical shifts. The sequences of the monomeric RFPs in these studies contained an N-terminal 6-His tag as well 7 additional residues relative to the sequence of the construct used for the crystal structure of mCherry. Thus, the residue numbering is different from that found in the pdb file for mCherry [31]. Both numbering schemes are listed in Tables C.1 and C.2. The residue numbering for mRaspberry and tdTomato are further complicated as they not contain a 4-residue insert before the first residue in the β-barrel as do mCherry and mRojoB. The numbering of the residues after the insert was kept consistent between mCherry, mRojoB, mRaspberry and tdTomato, although assignments were not transferred to mRaspberry or tdTomato for these 4 residues. The residue numbers for the tdTomato construct used in these studies (with N-terminal 6-His tag cleaved) and for the construct used for the crystal structure of DsRed [13] are listed for the assignments of tdTomato.

Chromophore Tyrosine C^{β}

The chromophore tyrosine C^{β} was assigned in mCherry, mRaspberry and mRojoB. Figure 2.12 shows the overlay of 2 ^{1}H-^{13}C HSQC spectra of mCherry: one that is tyrosine $^{13}C^{\beta}$ labeled and one that contains

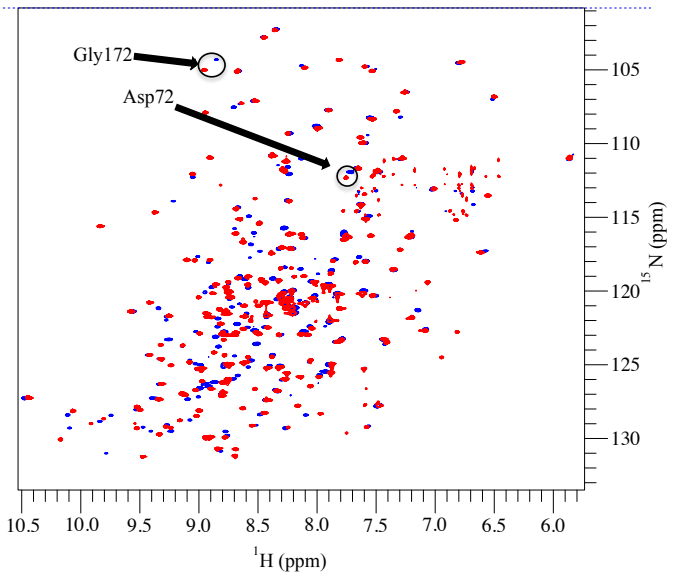

Figure 2.10: The ^{1}H-^{15}N HSQC of mCherry (red) and mRojoB (blue) collected at 30°C. The assignments for glycine 172 and aspartate 72 were transferred from mCherry to mRojoB despite having different chemical shifts in each protein.

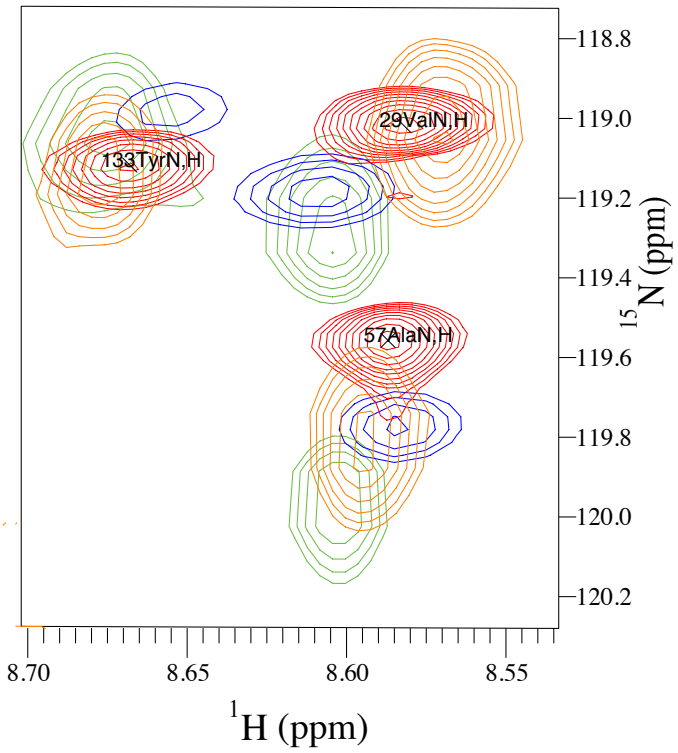

Figure 2.11: The ^{1}H-^{15}N HSQC of mCherry and mRojoB collected at 30°C (red and blue, respectively) and at 37°C (orange and green, respectively). The assignment for alanine 57 was transferred from mCherry at 30°C to mRojoB at 37°C despite the difference in chemical shifts. The downfield nitrogen chemical shift between 30°C and 37°C was observed for alanine 57 in both mCherry and mRojoB.

only natural abundance ^{13}C. The structure of the chromophore is also shown, and the peak assigned as the $^{13}C^{\beta}H$ is indicated. The chromophore tyrosine C^{β} has a distinct chemical shift due to a double bond between the α and β carbons. Overlay of the ^{1}H-^{13}C HSQC spectra of the $^{13}C^{\beta}$ tyrosine labeled samples of mRaspberry and mRojoB with that of mCherry confirmed the assignment of the chromophore tyrosine C^{β}s as the peaks appear in a region of the spectrum distinct from other tyrosine C^{β}s in the proteins (Figure 2.13). Both the proton and carbon chemical shifts are shifted downfield relative to other tyrosine C^{β}s.

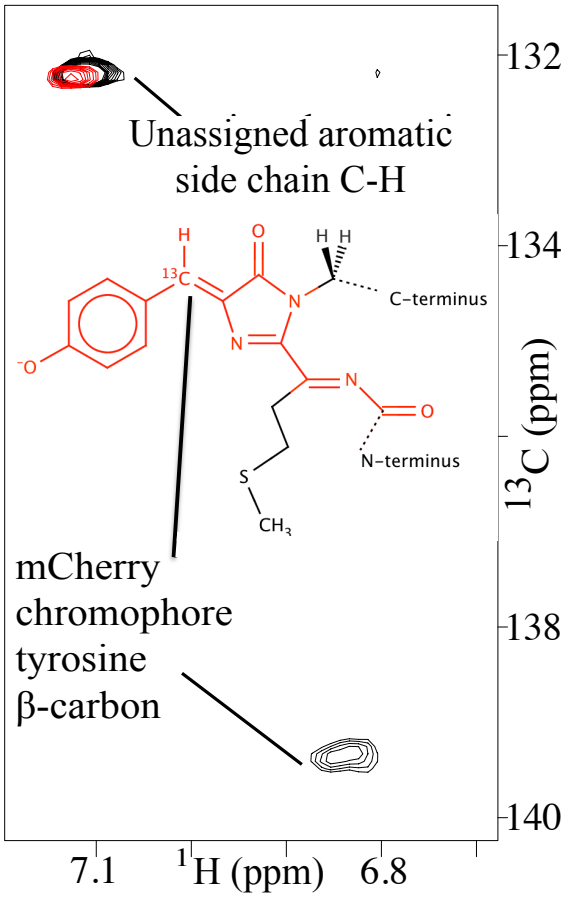

Figure 2.12: An overlay of 2 ^{1}H-^{13}C HSQC spectra of mCherry. The black spectrum is of tyrosine $^{13}C^{\beta}$ carbon labeled mCherry, where the red spectrum is on a natural abundance ^{13}C sample of mCherry. The other peaks are likely due to natural abundance ^{13}C in aromatic side chain carbons. Inset is the structure of the chromophore, with the tyrosine ^{13}C-labeled at the C^{β}.

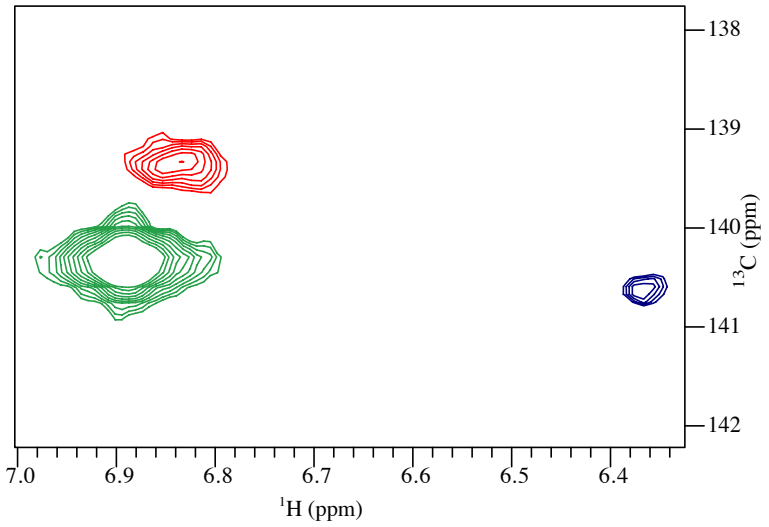

Figure 2.13: ^{1}H-^{13}C HSQC spectra the chromophore tyrosine C$^{\beta}$H of mCherry (red) collected at 30°C, mRaspberry (green) and mRojoB (blue) both collected at 37°C.

2.3.2 NMR Relaxation Results

Backbone Amide

The ^{15}N R_1 and R_2 values for each resonance, both assigned and unassigned, in the spectra of mCherry, mRaspberry and mRojoB were determined. Representative data and exponential fits are presented in Figures 2.14 and 2.15.

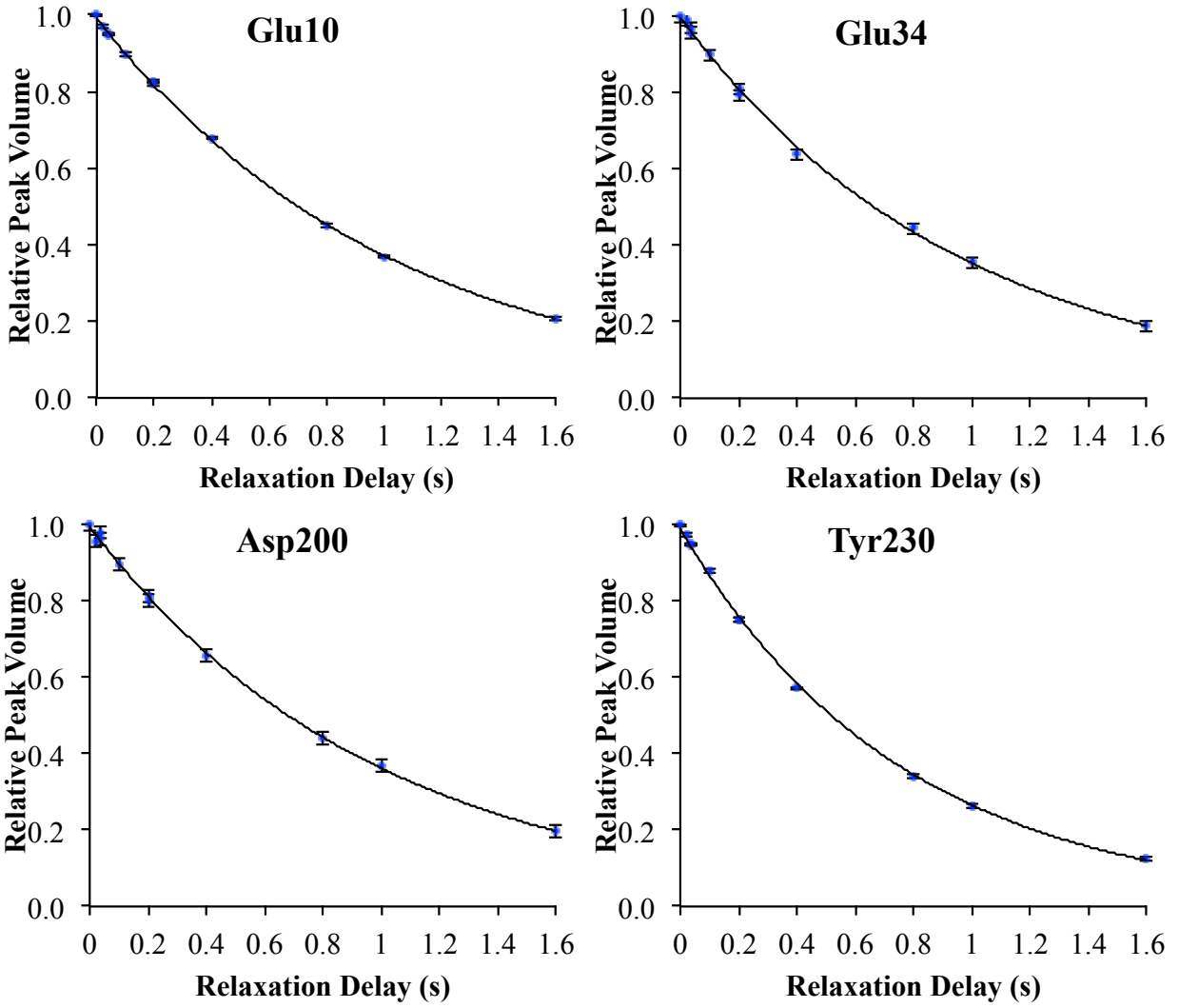

Figure 2.14: The ^{15}N R_1 relaxation rate constants were extracted from the decaying exponential function fit of the peak volumes versus the R_1 relaxation delay time. The blue circles are the peak volumes normalized to the volume at relaxation delay time 0. Error bars are shown and were calculated as the average difference in volume between duplicate data points collected for one relaxation delay time. The black curve is exponential function fit of the data. The data were collected at 37°C.

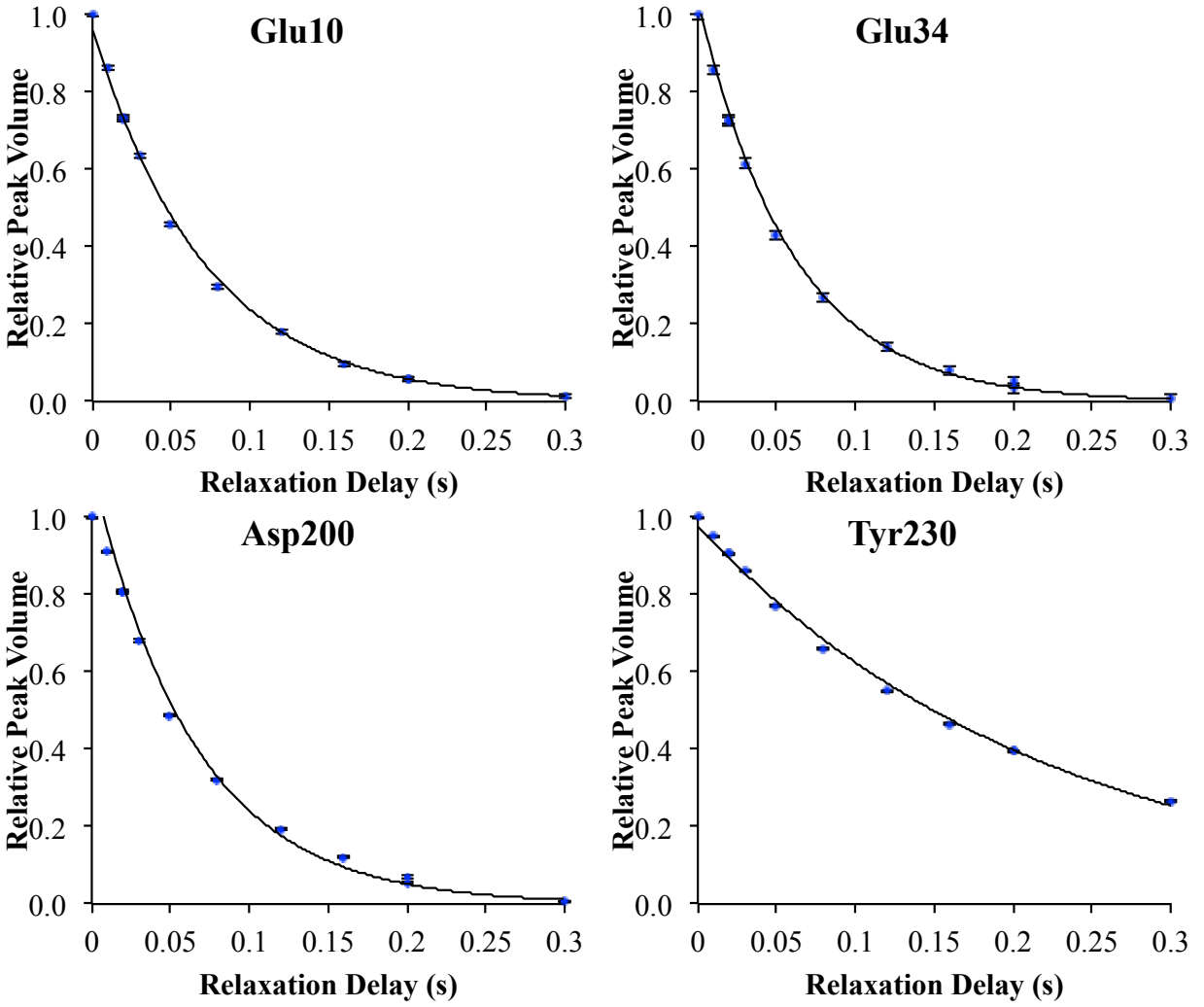

Figure 2.15: The ^{15}N $R_{1\rho}$ relaxation rate constants were extracted from the decaying exponential function fit of the peak volumes versus the $R_{1\rho}$ relaxation delay time. The blue circles are the peak volumes normalized to the volume at relaxation delay time 0. Error bars are shown and were calculated as the average difference in volume between duplicate data points collected for one relaxation delay time. The black curve is exponential function fit of the data. The data were collected at 37°C.

The backbone amide ^{15}N τ_e and $\{^1$H$\}$-^{15}N hetNOE values for mCherry, mRaspberry and mRojoB were determined for both assigned and unassigned residues. Histograms of ^{15}N τ_e, $\{^1$H$\}$-^{15}N hetNOE and order parameters for mCherry, mRaspberry and mRojoB are presented in Figures 2.16, 2.17, and 2.18 respectively. ^{15}N R_1, R_2, $\{^1$H$\}$-^{15}N hetNOE and S^2 values for assigned backbone amides in mCherry are

Table 2.4: Average ^{1}H-^{15}N τ_c, ^{1}H-^{15}N hetNOE, and order parameters for the backbone amides of 3 RFPs at 37°C.[a]

	mCherry	mRojoB	mRaspberry
^{1}H-^{15}N τ_c (ave.) (ns)	13.0 ± 0.2	11.9 ± 0.2	9.6 ± 0.2
Tensor2 ^{1}H-^{15}N τ_c (ns)	12.9	11.8 ± 0.04	9.6
{^{1}H}-^{15}N hetNOE (ave.)	0.80 ± 0.01	0.76 ± 0.04	0.86 ± 0.01
^{1}H-^{15}N S^2 (average)	0.96 ± 0.02	0.87 ± 0.02	0.97 ± 0.02

[a]The results for all three proteins were obtained from data collected on a 600 MHz spectrometer. The average τ_c and {^{1}H}-^{15}N hetNOE values were calculated excluding residues with negative hetNOEs, with τ_c s more or less than one standard deviation from the average before values were excluded, and with τ_c errors of larger than 10%. The Tensor2 calculated τ_c is reported for comparison.

presented in Figure 2.20. The ^{15}N R_1, R_2, {^{1}H}-^{15}N hetNOE and the S^2 values for the residues assigned in all 3 proteins are presented in Figure 2.19. Small R_1, {^{1}H}-^{15}N hetNOE and S^2 values and large R_2 values indicate increased internal mobility. {^{1}H}-^{15}N hetNOE values can range from 1 to -4 [134], with smaller values indicating increased dynamics on the ps-ns timescale [198]. Values above 0.7 generally are indicative of limited internal motion [199, 200]. ^{15}N R_1, R_2, {^{1}H}-^{15}N hetNOE and S^2 values for additional assigned residues in mCherry are presented in Figure 2.20. The S^2 values for all assigned residues in mCherry, mRaspberry, and mRojoB are presented in Table C.3. In addition to the S^2 values, the model used to fit the relaxation data, χ^2 value for model selection, exchange rate constants and associated errors, and second S_2^2 values predicted by Tensor2 are given. The S^2 values for all confidently assigned residues in mCherry are mapped onto the crystal structure in Figure 2.21. The S^2 values for all confidently assigned residues in mRaspberry and mRojoB are mapped onto the crystal structure of mCherry in Figure 2.22.

The ^{15}N R_1 and R_2 values were also used to calculate residue-specific rotational correlation time constants, τ_es, assuming isotropic tumbling [126]. The average τ_e was used to estimate the τ_c for global tumbling for each protein. The average {^{1}H}-^{15}N hetNOE and S^2 values were calculated for each monomeric RFP (Table 2.4), where these averages only included residues that showed no evidence of internal dynamics (see Methods Section 2.2.2).

Chromophore

The ^{13}C NMR relaxation parameters for the 3 proteins were compared to check for differences in

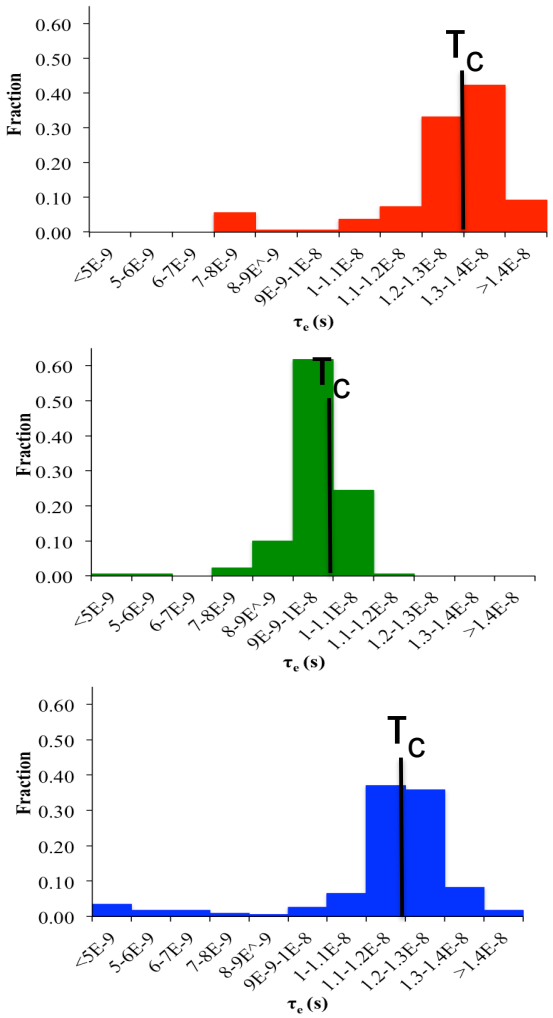

Figure 2.16: The backbone amide effective rotational correlation time constants (τ_es) for mCherry (red), mRaspberry (green), and mRojoB (blue). Most backbone amides are tumbling at the speed of the overall molecule, but some backbone amides in mRaspberry and mRojoB have smaller τ_es, indicative of faster tumbling. The global τ_c for each protein is shown. τ_es are presented for 67, 77, and 95% of the backbone amides of mCherry, mRaspberry, and mRojoB, respectively.

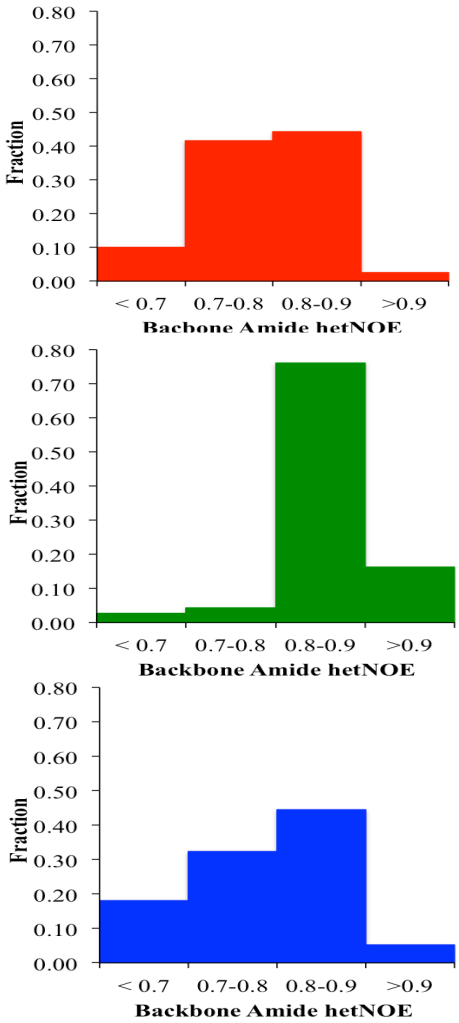

Figure 2.17: The backbone amide $\{^1H\}$-^{15}N hetNOE values for mCherry (red), mRaspberry (green), and mRojoB (blue). The $\{^1H\}$-^{15}N hetNOE values for most backbone amides are generally consistent with restricted internal dynamics. mRojoB exhibits the largest fraction of backbone amides with internal dynamics. $\{^1H\}$-^{15}N hetNOE values are presented for 92, 89, and 95% of the backbone amides of mCherry, mRaspberry, and mRojoB, respectively.

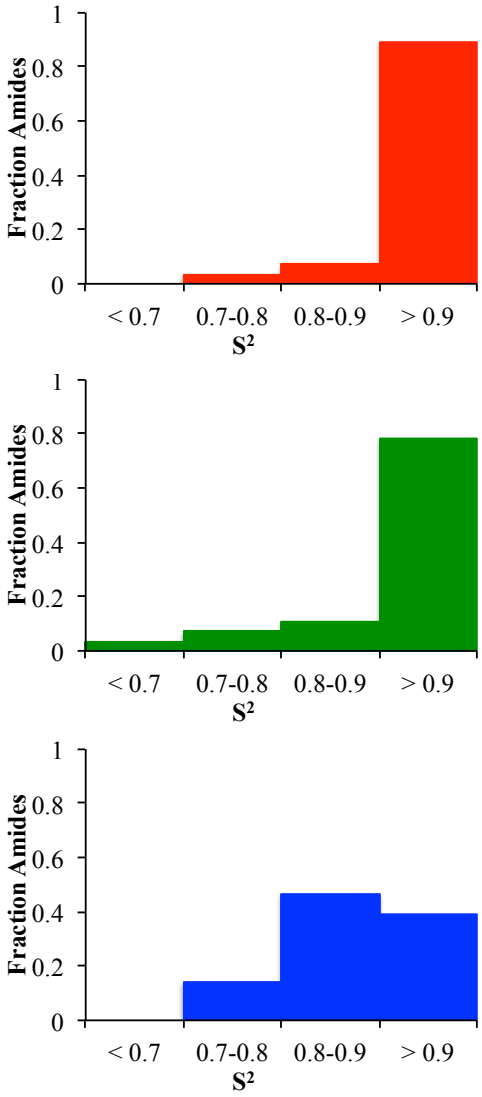

Figure 2.18: The backbone amide order parameters (S^2) for 28 residues in mCherry (red), mRaspberry (green), and mRojoB (blue). The order parameters for most backbone amides are consistent with restricted internal dynamics, but the fraction of backbone amides with order parameters less than 0.9 is largest in mRojoB.

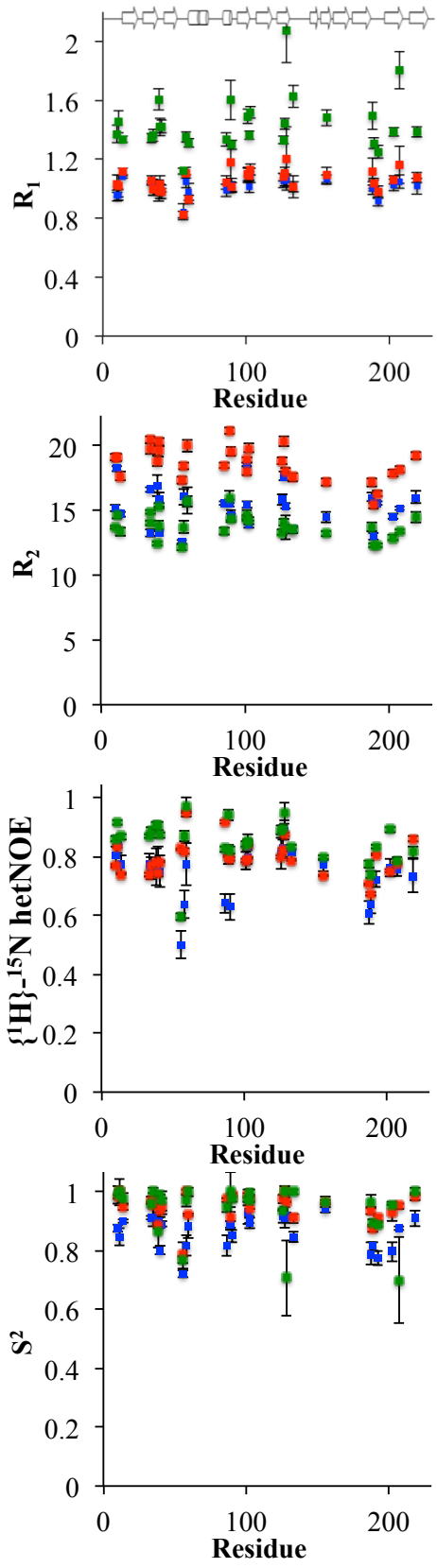

Figure 2.19: Backbone amide ps-ns timescale dynamics for mCherry (red), mRojoB (blue) and mRaspberry (green). The ^{1}H-^{15}N R_1 (a), R_2 (b), $\{^{1}H\}$-^{15}N hetNOE (c), and ^{1}H-^{15}N order parameters (S^2) (d) are shown for residues assigned in all 3 proteins. ^{15}N R_1, R_2, and $\{^{1}H\}$-^{15}N hetNOE values were calculated from data collected at 37°C on a 600 MHz spectrometer. The order parameters were calculated using the model free [135] program, Tensor2 [136].

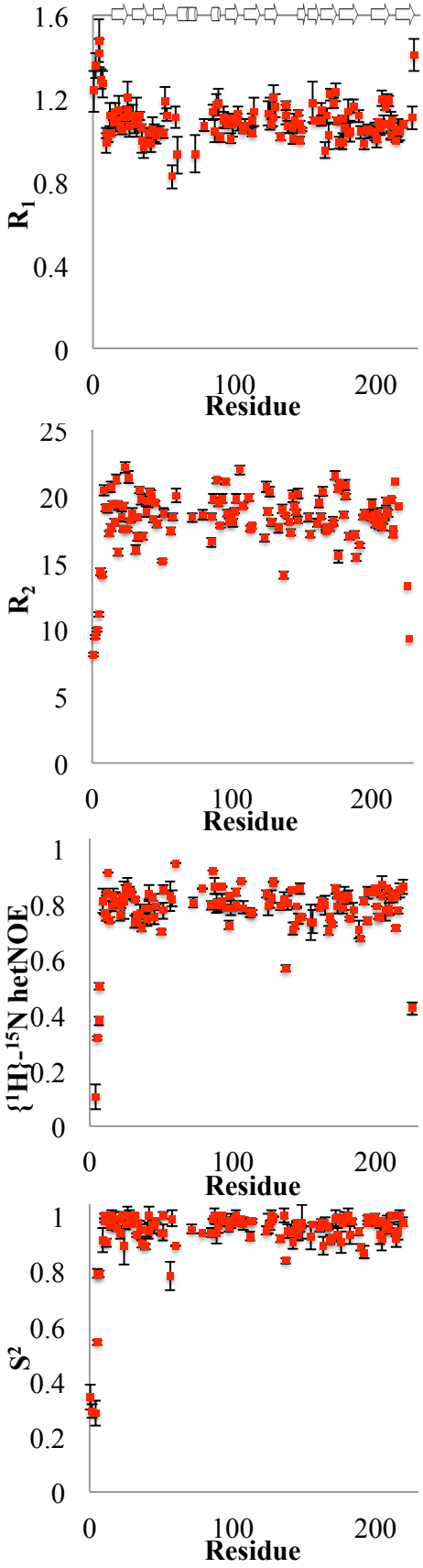

Figure 2.20: Backbone amide ps-ns timescale dynamics for all assigned residues in mCherry for which the associated errors for ^{1}H-^{15}N R_1 (a), R_2 (b), {^{1}H}-^{15}N hetNOE (c), and ^{1}H-^{15}N order parameters (S^2) (d) were less than 10%.

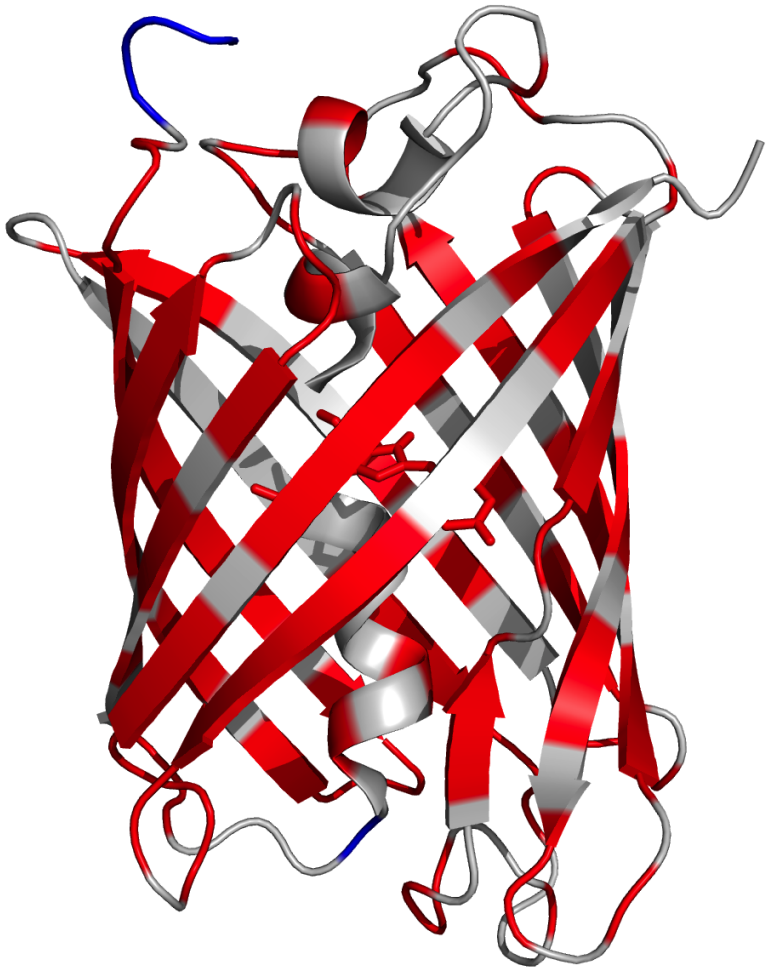

Figure 2.21: The backbone amide S^2 values mapped onto the crystal structure of mCherry. The red residues are those whose amide nitrogen S^2 values were between 1 than 0.8. The blue residues had backbone amide order parameters less than 0.8. The grey residues are either unassigned or did not have a calculated S^2 value.

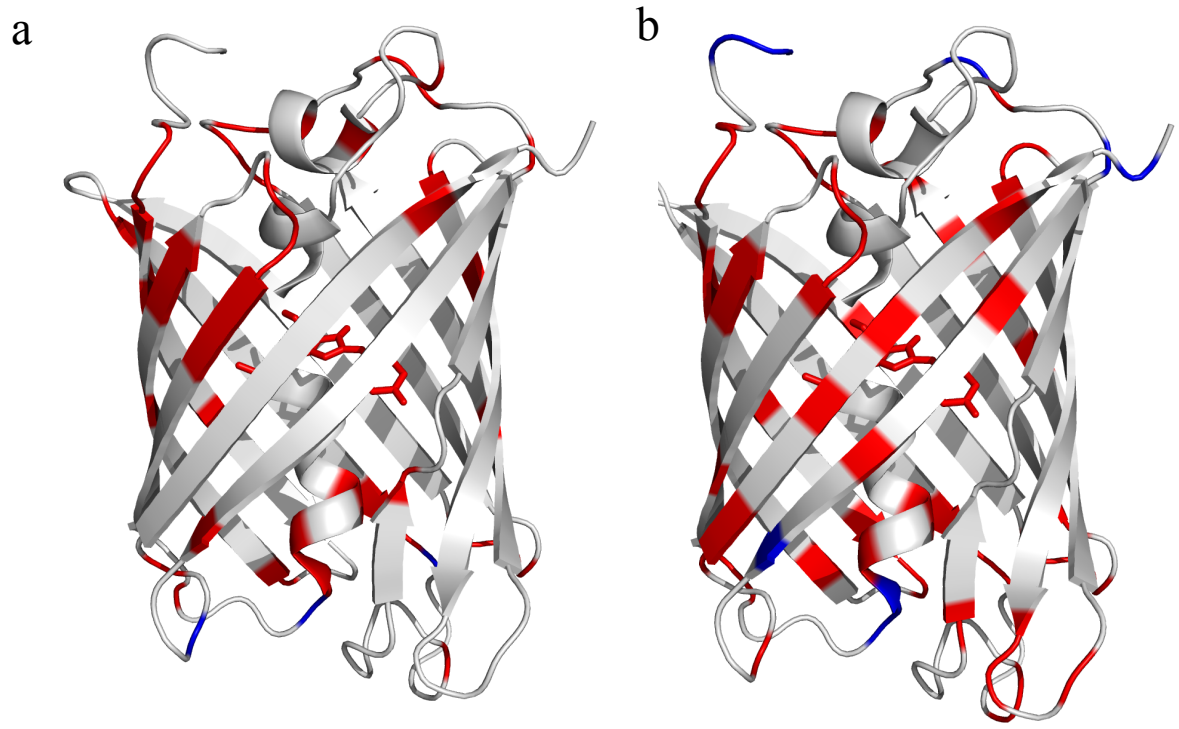

Figure 2.22: The S^2 values for the confidently assigned residues in mRaspberry (a) and mRojoB (b) are mapped onto the crystal structure of mCherry. The red residues are those whose amide nitrogen S^2 values were between 1 than 0.8. The blue residues had backbone amide order parameters less than 0.8. The grey residues are either unassigned or did not have a calculated S^2 value.

Table 2.5: Comparison of the ^{13}C R_1, R_2 and the $\{^1$H$\}$-^{13}C hetNOE values for the chromophore tyrosine C$^\beta$ and bound proton of 3 RFPs at 37°C.[a,b]

	mCherry	mRojoB	mRaspberry
$^{13}C^\beta$ R_1 (s^{-1})	0.8 ± 0.1	1.1 ± 0.2	0.6 ± 0.03
$^{13}C^\beta$ R_2 (s^{-1})	105 ± 2.2[c]	132 ± 19	143 ± 6
$\{^1$H$\}$-$^{13}C^\beta$ hetNOE	1.0 ± 0.3	1.1[d]	1.0 ± 0.01

[a] The data for mCherry and mRojoB were collected on a 600 MHz spectrometer, while the data for mRaspberry were collected on an 800 MHz spectrometer.
[b] The R_1 and R_2 errors were calculated by the program CCPNMR Analysis used to fit the relaxation data.
[c] $R_{1\rho}$ was measured for the chromophore tyrosine C$^\beta$ of mCherry, while R_2 was measured for mRojoB and mRaspberry.
[d] One, two and three sets of $\{^1$H$\}$-$^{13}C^\beta$ hetNOE data were collected for mRojoB, mRaspberry and mCherry, respectively. The $\{^1$H$\}$-$^{13}C^\beta$ hetNOE values reported for mCherry and mRaspberry are the averages, with the errors reflecting the range of values.

dynamics, specifically at the chromophore tyrosine C$^\beta$. The ^{13}C R_1, R_2 and $\{^1$H$\}$-^{13}C hetNOE values for the chromophore tyrosine C$^\beta$H in mCherry, mRaspberry and mRojoB are given in Table 2.5.

2.4 Discussion

Red fluorescent proteins are important tools in the biological sciences, however, currently available monomeric RFPs have sub-optimal quantum yields, which limits their use in many applications. In this work, NMR spectroscopy was used to try to understand the physical mechanisms underlying these low quantum yields. In general, fluorescent molecules with high quantum yields are rigid, a property that leads to molecules favoring radiative over dynamic non-radiative relaxation pathways from the excited state to the ground state. It was hypothesized that RFPs with lower quantum yields may contain regions of increased flexibility. ps-ns dynamics of the backbone amides and the chromophore tyrosine C$^\beta$ of 3 monomeric RFPs were measured.

Several factors could be causing the low quantum yields of monomeric RFPs. Increased sub-ns dynamics near the chromophore could provide non-radiative relaxation pathways, for example via torsion away from planarity [53, 119, 120] or via collisional quenching of the excited state chromophore by nearby atoms [72]. In addition, the relative populations of molecules in the bright, fluorescent state versus dark, non-fluorescent states will affect the quantum yield of the equilibrium population. ms-s timescale dynamics, indicative of

multiple populations in solution, can be detected in NMR spectra. The number of peaks in the spectra of tdTomato, mCherry, mRaspberry and mRojoB were used to qualitatively assess the possibility of multiple conformations in solution.

2.4.1 Manual Assignment Contradicted More than 10% of the NMR Assignments Predicted by PINE

More than 10% of the assignments predicted with $\geq$ 90% confidence by PINE were contradicted by manual assignment verification. Of those predicted with 100% confidence, 10 % were invalidated using manual assignment strategies. This result was surprising and demonstrates that PINE results should be used as a starting point for assignments and that manual verification is crucial. The discrepancy between PINE and manual assignment may be due to low signal-to-noise ratios in the 3D spectra used to connect the backbone amides of neighboring residues or by high tolerance settings used to match peaks between spectra. The poor signal-to-noise in the 3D spectra may have caused incomplete peak lists to be submitted to PINE as input for the automated assignment by PINE. The 3D spectra of large proteins have low signal-to-noise due to unfavorable relaxation properties and temporal limitations. For example, the HNCACB and CBCA(CO)NH spectra collected for mCherry required more than 8 days of spectrometer time in order to obtain adequate resolution in all 3 dimensions. During manual assignment, additional difficult-to-detect peaks with low signal-to-noise were identified while combing through the 2D ^{1}H-^{15}N planes of a 3D spectrum at a particular carbon frequency in attempt to link neighboring peaks, however several residues were still missing peaks in the 3D spectra due to low sign-to-noise. The second potential cause of the discrepancy between manual and PINE assignments, high tolerance settings in PINE, refers to the threshold beyond which two chemical shifts are considered different. When linking resonances, PINE accepts peaks within 0.25 ppm in the ^{15}N and ^{13}C dimensions and 0.02 ppm in the ^{1}H dimension [185]. In more than one instance during manual assignment, two resonances that were linked by PINE were deemed unlinked during manual verification due to differing carbon chemical shifts. Decreasing the tolerance for differences in chemical shift in the carbon dimension may increase the accuracy of PINE-predicted assignments. PINE users have the option of overriding the standard settings [185]. In order to obtain more accurate results from PINE,

iterative rounds of automated and manual assignment steps should be taken to refine the peak lists, and manual adjustment of the tolerances for peak matching should be considered by PINE users.

2.4.2 Transferred NMR Backbone Amide Assignments are Less Confident

Traditional NMR assignment strategies were used to confidently assign 75% of the backbone amides of mCherry at 30°C. However, the spectral overlay of mCherry with the tdTomato, mRaspberry and mRojoB was imperfect, therefore the assignment transfer between spectra resulted in less-confident assignments of the backbone amides of mRaspberry, mRojoB and tdTomato at 37°C. For mCherry, only minor peak shifting occurred between 30°C and 37°C allowing transfer of 95% of the assignments from mCherry at 30°C to mCherry at 37°C (Figure 2.23). However, the spectral overlay between mCherry and the structurally homologous mRaspberry, mRojoB and tdTomato yielded less than 40% assignment transfer in each case due to poor spectra overlay (Figures 2.7 and 2.7). Because the assignment transfer was incomplete, the confidence in each transferred assignment is lower than if all of the assignments were transferrable. Thus, the residue-specific comparison of dynamics between proteins should be interpreted carefully, and the described studies would benefit from traditional assignment of tdTomato, mRojoB and mRaspberry.

2.4.3 Spectral Differences May Indicate Differences in ms-s Timescale Dynamics or in Solution Structures

Difference in Backbone Amide Chemical Shifts Among NMR Spectra of RFP Variants May be Indicative of Differences in Solution Structures

The ^{1}H-^{15}N HSQC TROSY spectra of the 4 RFPs studied varied considerably, displaying differences in range of peak volumes and chemical shifts (Figure 2.7). The differences in chemical shifts were unexpected given the high degree of structural similarity of the crystal structures of DsRed, mCherry, and mRojoA (Figures 2.8 and 2.9). The ^{1}H-^{13}C HSQC spectra of the tyrosine C$^{\beta}$H labeled samples of mCherry, mRaspberry and mRojoB also showed differences (Figure 2.13). The differences in chemical shift between variants indicate an altered chemical environment between proteins. The crystal structures mCherry and mRojoA clearly show that the conformation of the mRojoA chromophore is more twisted than in mCherry (Figure 2.24).

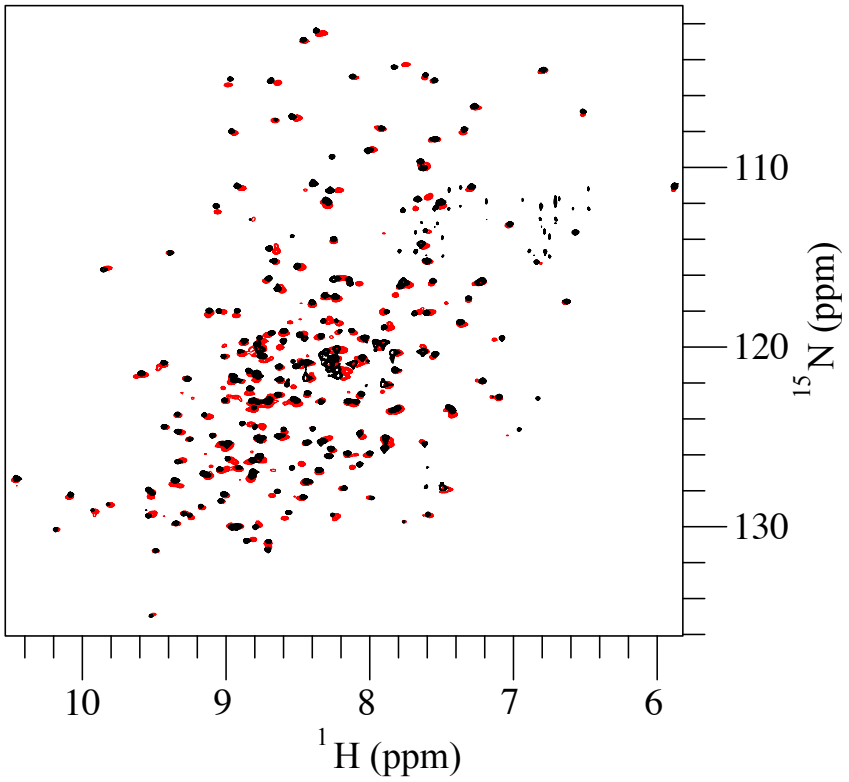

Figure 2.23: The overlay of the ^{1}H-^{15}N HSQC spectra of mCherry at 30 (black) and 37°C (red).

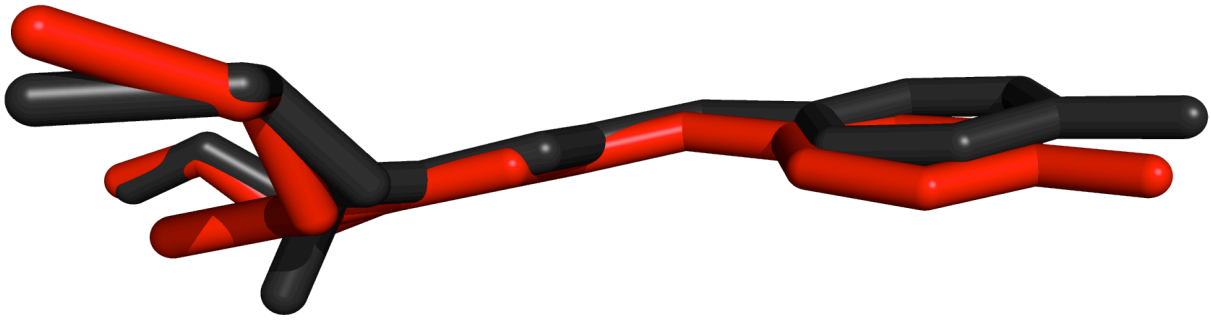

Figure 2.24: The overlay of the crystal structures of the chromophores of mCherry (red) and mRojoA (black) shows differences in planarity, particularly in the twist.

While it is possible that mRojoA and mRojoB have different structures, an increased twist in the mRojoB chromophore relative to mCherry may be contributing to the altered chemical environment of the mRojoB chromophore tyrosine C^{β}Hs relative to the mCherry chromophore and thus the chemical shift.

NMR is exquisitely sensitive to changes in the chemical environment, and even small structural differences may drastically change the chemical environment. Therefore, perhaps the small structural differences between RFPs explain the deviations among NMR spectra. Alternatively, the differences in spectra may suggest that the solution structures are much more distinct than the rigid crystal models. A previous study comparing more than 100 protein structures that have been determined using both solution NMR and X-ray crystallography found the structures determined by the two different techniques overlaid with RMSDs between about 1.5 and 2.5 Å and that only very seldomly do buried side chains differ in conformation [201]. These findings suggest that it is unlikely that large differences in solution structures are accounting for the differences in NMR spectra between RFP variants with similar crystal structures. Additionally, the assumption that similar structures produce similar NMR data has been used to identify structural homologues in the PDB through the input of unassigned NMR data and chemical shift assignment prediction strategies [202, 203]. The success of the programs described in these articles again highlights the validity of the assumption that solution and crystal structures are often quite similar. Based on these results, the differences in the solution structures of mCherry, mRaspberry and mRojoB would be predicted to be quite similar due to their similar crystal structures (Figure 2.8) and thus not account for the large differences in

NMR spectra.

While solution and crystal structures are often quite similar [201] there are documented cases of deviations between crystal and solution structures. One study found differences in structures when comparing the solution and crystal structures of serum albumin homologues from human and bovine [204]. While the crystal and solution structures of BSA overlaid quite well, differences were detected between the crystal and solution structure of HSA [204]. Another study compared the NMR spectra for the serine protease, thrombin, bound to 6 different ligands and found that while the crystal structures of thrombin bound to different ligands overlaid with RMSDs of < 1 Å [205], the NMR spectra were quite different [206]. This indicated differences in solution structures that were not apparent in the cystal structures, perhaps due to stabilization due to crystal contacts [206]. Therefore, the similarity in FP crystal structures may not hold in solution, supporting the idea that the differences in solution structures may account for differences in NMR spectra. The differences between solution structures of HSA and BSA were attributed to differences in primary sequence in particular in solvent exposed regions where the hydrophobicity differed between proteins. NMR assignments for mRojoB would likely transfer more readily for residues in regions of homologous solution structure. When analyzing the residues for which assignments were transferrable between mCherry and mRojoB, however, a mixture of both hydrophobic and hydrophilic residues are represented (Figure 2.25). However, of the 4 residues that differ in hydrophobicity between mCherry and mRojoB (16, 163, 197, and 215), 163, 197, and 215 are all clustered near a region in which few assignments were transferred to mRojoB (Figure 2.25). This supports the idea that the solution structures deviate in this region and therefore account for the difference in NMR spectra and difficulty in assignment transfer.

In addition, cases of large NMR spectral deviations between proteins with similar structures have been documented. For example, solution structures of the oxidized and reduced forms of the C-terminal domain of NleG2-3 overlay with an RMSD of less than 2 Å, yet their ^{1}H-^{15}N HSQC spectra are quite different [207]. Another example of two solution structures that overlay with an RMSD of less than 4 Å and whose NMR spectra are substantially different are two protein homologues of Bacteriophage γ Ea8.5 protein [208]. It may be, therefore, that solution structures with RMSDs as low as 2 Ås (and perhaps even lower) may have significantly different NMR spectra, confirming the idea that NMR is exquisitely sensitive to changes in

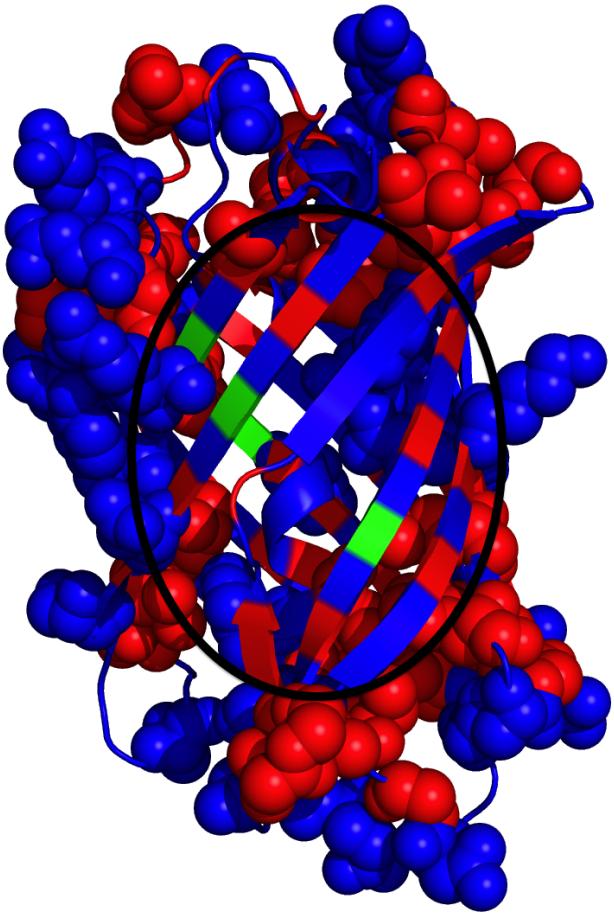

Figure 2.25: The crystal structure of mCherry is shown with hydrophobic residues displayed in red and hydrophilic residues displayed in blue. The assignments that transferred to mRojoB are displayed as spheres, and the residues that differed in hydrophobicity between mCherry and mRojoB are displayed in green. A lack of assignments localize to a region in which 3 of the 4 residues that differ in hydrophobicity are located. Since solution structures of homologues have been shown to deviate in regions of differing hydrophobicity [204], this finding suggests a difference in solution structure may account for the difficulty in assignment transfer between mCherry and mRojoB.

the chemical environment. In the case of the C-terminal domain of NleG2-3, the NMR spectra indicated that $> 50\%$ of the residues in the protein were undergoing conformational exchange between oxidized and reduced conformations thus resulting in 2 peaks per backbone amide in a ^{1}H-^{15}N HSQC spectrum [207]. Thus, it is also possible that the differences in NMR spectra between RFP variants is at least in part due to conformational exchange; i.e. that the difference in NMR spectra can be accounted for by a difference in solution structure between the oxidized and reduced conformations [207]. Similarly, the largest deviations in chemical shift between the two homologues of Ea8.5 correspond with the largest deviations in solution structures. Figure 2.26 shows the overlay of the two solution structures and the difference in backbone amide nitrogen chemical shifts. The difference in chemical shift and overlay of the structures of the oxidized and reduced forms of NleG2-3 are found in reference [207]. These two examples support the idea that differences in chemical shift correspond with differences in the solution structures. The difference in chemical shift and overlay of the spectra for the oxidized and reduced forms of NleG2-3 are found in reference [207]. Based on these examples of differences in solution structures and thus NMR spectra for proteins with similar crystal and even solution spectra, one can conclude that the differences in NMR spectra between the RFPs studied here are likely attributable to differences, which may be minor, in solution structures.

Difference in Peak Volumes May be Indicative of Intermediate Exchange

Another significant difference between NMR spectra was the wider range of backbone amide peak volumes in the ^{1}H-^{15}N HSQC TROSY spectrum of mRojoB (0.7) compared to mCherry (0.5). The range in peak volumes was defined as σ/i_{ave} where σ is the standard deviation in peak volumes and i_{ave} is the average peak volume. The difference in peak volumes could simply be due to differences in relaxation properties and thus signal intensities. However, dynamics on a timescale slower than that of NMR ($\mathrm{k}_{ex} \ll \Delta\omega$ where $\mathrm{k}_{ex}=\mathrm{k}_{fwd}+\mathrm{k}_{rev}$, k_{fwd} and k_{rev} are the rate constants for a protein undergoing conformational exchange, and $\Delta\omega$ is the difference in chemical shifts between the two conformations) could also explain the wider range of peak volumes in the spectrum of mRojoB. Slow timescale dynamics in which one backbone amide fluctuates between 2 conformations could produce 2 distinct peaks. Distinct populations of each conformation between which the protein converts would result in distinct peak volumes for each of the peaks resulting from a single backbone amide. Multiple peaks per backbone amide with varying intensities may be contributing to the

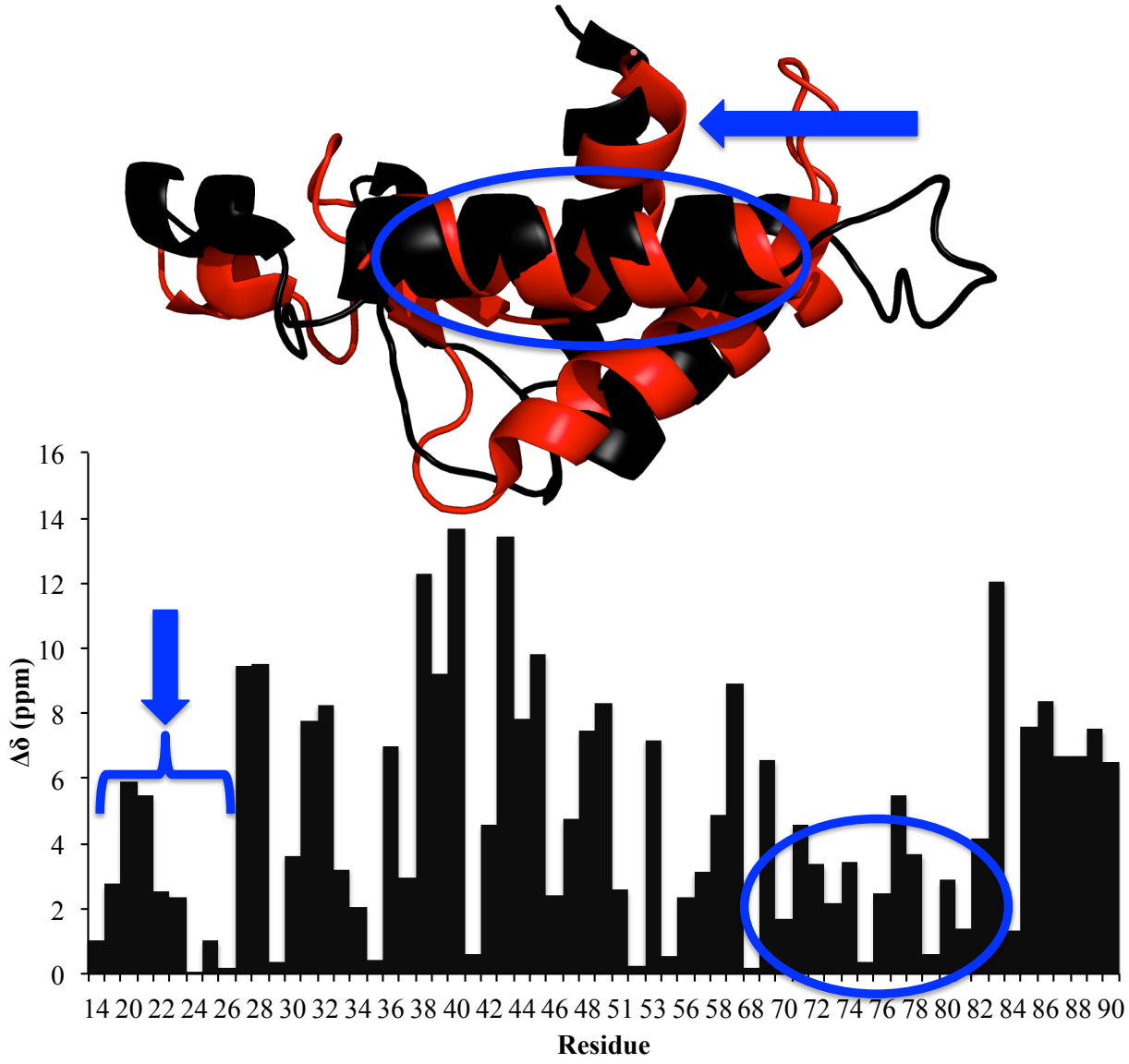

Figure 2.26: The overlay of the NMR solution structures of the Ea8.5 protein from *E. coli* (PDB 2M7A, black) and *P. putida* (2M7B, red). The difference in chemical shift for the backbone amide nitrogen is plotted per residue, with the regions with the least difference in chemical shift indicated. α helix1 is marked by blue arrows, and α helix3 by a blue oval. The chemical shifts were obtained from the BMRB as entries 19178 and 19179 for the *E. coli* and *P. putida* homologues, respectively.

wide range in peak volumes detected in mRojoB relative to mCherry. Some peaks in the mRojoB spectrum also appeared to be broadened, which is indicative of intermediate timescale dynamics ($k_{ex} \approx \Delta\omega$). Similarly, the spectra of tdTomato have a larger range in peak volumes than did those of mCherry or mRojoB. The standard deviation divided by the average peak volume for the largest 239 peaks in the ^{1}H-^{15}N HSQC TROSY spectrum of ^{2}H-^{15}N-labeled (also labeled uniformly with ^{1}H amide hydrogens and ^{1}H-^{14}N alanine amide groups) tdTomato was 0.9, larger than the same parameter calculated for both mRojoB (0.7), mCherry (0.5) and mRaspberry (0.5). The average peak volume for tdTomato was calculated for the largest 239 peaks in the spectrum, although additional smaller peaks were present. The number 239 was obtained by setting the contour level of the spectrum such that fewer than the expected number of peaks were observed. If the contour level were lowered to include additional, smaller peaks, the number of peaks was larger than 255 (the expected number of peaks). In fact, over 350 peaks were observed in total with a range of peak volumes divided by the average peak volume (for all $\approx$ 350 peaks) of (1.24). This number *is* larger than the expected number of peaks and is therefore indicative of multiple interconverting populations in solution which would result in more than one peak per unique backbone amide.

Further supporting the possibility of intermediate exchange are the locations of unassigned residues in mCherry. In the NMR spectra of mCherry at 37°C, missing assignments are clustered in the internal α helix, in β strands 5 and 6, and in strands 7, 10 and 11 near one end of the β barrel. Missing assignments could be due to low signal-to-noise in the NMR spectra resulting in difficulty connecting resonances using the 3D HNCACB and CBCA(CO)NH spectra. One such cause of low signal-to-noise is intermediate exchange ($k_{ex} \approx \Delta\omega$). Therefore, the missing assignments may be due to flexibility in the β barrel in these regions. This hypothesis of intermediate exchange for strands 7 and 10 is substantiated by results of the hydrogen-deuterium exchange experiment presented in Chapter 3 and by results of previous studies that suggested flexibility in this region of other FPs [66, 163].

2.4.4 Backbone Amides and Chromophore Tyrosine C$^{\beta}$s are Mostly Rigid on ps-ns Timescale

Backbone Amides of mRojoB Display the most Internal Dynamics

^{15}N backbone amide S^2 values provide information on internal ps-ns dynamics [135,136]. If dynamics on this timescale perturb the environment of the chromophore they could promote non-radiative relaxation and reduce the fluorescence quantum yield. Although caution was taken when transferring assignments (see Methods), the ability to confidently compare results for particular residues in mRaspberry, mRojoB and tdTomato is limited as discussed in section 2.4.2. Even so, the data still provide valuable insight into differences in protein dynamics among the RFP variants. Histograms, averages, and mapping of assigned residues are used here to display data and compare results among RFP variants. The τ_es and $\{^1$H$\}$-^{15}N hetNOEs for most backbone amides (both assigned and unassigned) in mCherry, mRaspberry and mRojoB are consistent with restricted internal dynamics (Figures 2.16 and 2.17, respectively). Most backbone amide τ_e values are centered about the value τ_c, or the time constant for global tumbling of the molecule, indicating they are rigid within the context of the overall protein (Figure 2.16). In addition, most backbone amide $\{^1$H$\}$-^{15}N hetNOE values are larger than 0.7, a commonly accepted threshold for the identification of restricted internal dynamics on the ps-ns timescale (Figure 2.17). However, mRojoB has a larger population of backbone amides with low τ_e and $\{^1$H$\}$-^{15}N hetNOE values relative to mCherry and mRaspberry, indicative of increased internal dynamics. These residues displaying internal dynamics may be enabling non-radiative relaxation pathways for the excited state chromophore, thereby reducing the quantum yield of mRojoB. However, the lack of assignments prevents the identification of the locations of many of these residues displaying internal dynamics. The internally dynamic backbone amides may be distal to the chromophore and therefore unable to directly promote non-radiative relaxation. Thus a concrete explanation for the contribution of internal dynamics to the low quantum yield of mRojoB requires more complete assignments.

For most of assigned the backbone amides in mCherry, mRaspberry and mRojoB, the order parameter was calculated and compared between RFPs (Figure 2.18). The average backbone amide S^2 for each protein was larger than 0.8 (Table 2.4), indicating restricted backbone ps-ns dynamics [209–211]. Some amides in the loops and termini of mCherry, which has the largest number of resonance assignments, have S^2 values less than 0.8, but these residues are distant (more than 10 Å) from the chromophore (Figure 2.21). For the confidently assigned amides in mRaspberry and mRojoB backbone amides with order parameters lower than 0.8 are also distant from the chromophore (Figure 2.22). Of the 28 backbone amides for which

order parameters were calculated in each of the three monomers, most showed restricted internal dynamics. However, the largest fraction of amides with order parameters less than 0.9 were found in mRojoB (Figure 2.18). Although values larger than 0.8 are generally accepted as indicators of restricted internal dynamics, the internal motion of a bond with an order parameter > 0.8 may induce fluorescence quenching through collisional quenching. Therefore, the lower order parameters in mRojoB are consistent with a lower quantum yield caused by collisional quenching.

Monomer-Dimer Equilibrium in Solution may Affect Calculated Order Parameters

A monomer-dimer equilibrium in solution may affect the relaxation properties and thus, the predicted backbone amide order parameters. The chemical environment of the residues at the monomer-dimer interface and potentially others would be altered upon dimerization. Therefore, if two populations were present in solution due to a monomer-dimer equilibrium, more than one peak per backbone amide would be present in a ^{1}H-^{15}N HSQC spectrum. In addition to changing the chemical environment, exchange on the ms timescale, a timescale on which monomerization-dimerization may occur, could increase R_2 relaxation rate constants and therefore peak widths (Figure 2.27).

Although changing the concentration should not affect dynamics it would affect the equilibrium populations (Figure 2.27). If in slow exchange ($k_{ex} \ll \Delta\omega$ where $k_{ex}=k_{dimerization}+k_{monomerization}$), an increase in protein concentration would increase the concentration of the dimer and would be noted as a shift in the relative peak heights of the two resonances stemming from the same residue in the protein. If in fast exchange ($k_{ex} \gg \Delta\omega$), a shift in ω would be noted. Residues in intermediate-fast or intermediate-slow exchange ($k_{ex}>\Delta\omega$ and $k_{ex}<\Delta\omega$ rather than $k_{ex} \gg \Delta\omega$ or $k_{ex} \ll \Delta\omega$, respectively, and therefore, broadened peaks since k_{ex} is more similar to $\Delta\omega$) would be affected by an increase in concentration similarly to how fast and slowly exchanging peaks would be affected. Therefore, a concentration dependence series of NMR spectra could be used to help assign peaks that are in slow (or intermediate-slow) exchange as two peaks stemming from the same residue, or to determine whether peaks that are in fast (or intermediate-fast) exchange as being affected or unaffected by a change in chemical environment upon dimerization. A change in concentration would not necessarily affect the rates of exchange, and therefore, a concentration dependence series of NMR spectra could not be used to determine whether peak broadening were due to

monomerization-dimerization dynamics.

Although monomerization-dimerization dynamics in solution could affect R_2 relaxation, $R_{1\rho}$ relaxation experiments were performed in order to eliminate the exchange contributions to the measured R_2 relaxation rate constants. None-the-less, to determine whether the proteins were behaving as monomers under the given conditions, the rotational correlation times for global tumbling were converted to molecular weights using an approximation that assumes the proteins are spherical [212]. A study by Rossi et al. found that the τ_c (in ns) of a rigid spherical protein at 25°C is approximately 0.6 × Molecular Weight (M.W.) for proteins up to about 25 kDa [212]. However, the ^{15}N relaxation experiments were performed at 37°C; thus, according to Stokes-Einstein-Debye Relation [213] (Equation 2.6), the τ_c should be scaled by a factor of 37/25 to correct for the temperature at which the ^{15}N relaxation data were collected.

$$\tau_c = \frac{4\pi\eta r^3}{3k_B T} \tag{2.6}$$

The viscosity of water, η is 0.7×10^{-3} kg/(m·s) at 37°C, the Boltzmann constant, k_B, is equal to 1.38×10^{-23} (kg·m^2)/(K·s^2), r is the hydrodynamic radius of the spherical molecule and T is the temperature in Kelvin. The M.W.s of mCherry, mRaspberry and mRojoB estimated using Rossi et al.'s approximation were 31, 23 and 29 kDa, respectively. The estimated M.W.s for mCherry and mRojoB were higher than expected, as the actual M.W.s were 27.8 kDa, and were consistent with mCherry and mRojoB existing in a monomer-dimer equilibrium. This finding is consistent with some of the differences in peak volumes in mCherry and mRojoB relative to mRaspberry stemming from monomer-dimer equilibrium in solution.

Misassignments may Affect Calculated Order Parameters

Due to incomplete assignments as well as large errors in several calculated input values, order parameters were not calculated for every backbone amide, and therefore a complete analysis and comparison of internal dynamics of the backbone monomeric RFPs was not possible. Based on the available data, internal ps-ns dynamics are most prevalent in mRojoB. However, other factors may be causing this apparent increase in internal dynamics. For example, misassigned residues could be affecting the calculated order parameters. As discussed in section 2.4.2, the assignments for mRojoB and mRaspberry were transferred from mCherry via overlay of ^{1}H-^{15}N HSQC TROSY spectra and are therefore less confident due to imperfect overlay of the

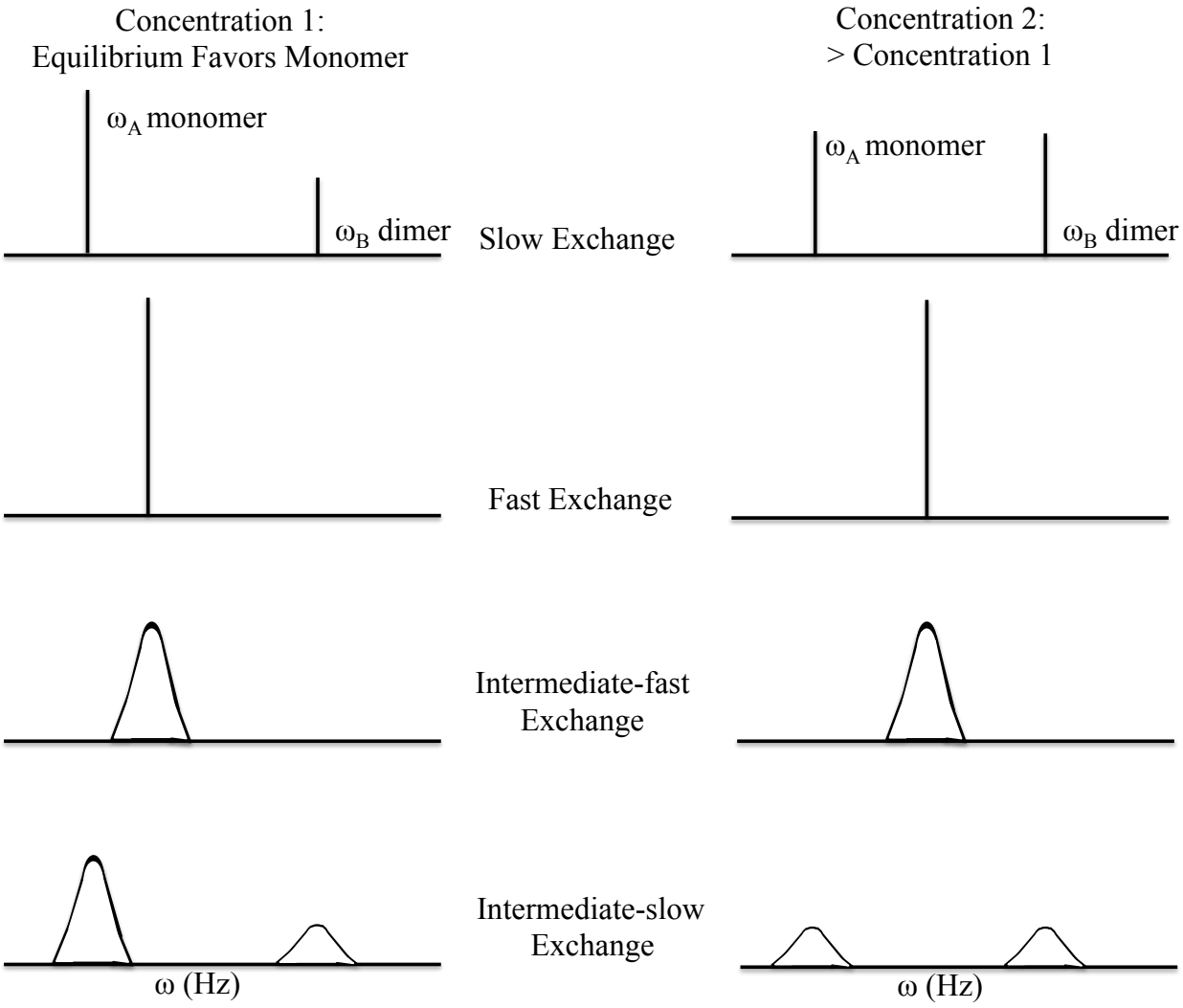

Figure 2.27: Hypothetical 1D NMR spectra for a protein amide proton in either fast, slow, intermediate-fast or intermediate-slow exchange, and how concentration would affect the spectra. A change in concentration will affect the relative populations of a protein undergoing exchange between two states, if higher concentrations favor one state over the other (for example the dimeric state with ω_A).

spectra. Misassignments would affect the calculation for the diffusion tensor, and thus the individual backbone amide order parameters calculated by Tensor2. Therefore, while suggestive, the observed differences in average backbone amide order parameter cannot be confidently attributed to differences in internal ps-ns dynamics.

Monomeric RFPs Remained Stable in Solution During Data Collection

In order to accurately measure relaxation parameters, it is important not only that the protein be a pure monomer, but also that the structure remain stable during the course of the experiment when measuring relaxation rate constants. Figure 2.28 shows an overlay of spectra collected for mCherry, mRaspberry and mRojoB during the course of the backbone amide relaxation experiments at 37°C. While the spectra overlay fairly well, the differences in the spectrum collected after several days at 37°C indicate the presence of more unfolded protein [168, 214] (Figure 2.28). However, the relaxation delay times were arrayed randomly to avoid systematic errors such as structural changes in the protein over time.

ps-ns Dynamics Near the Chromophore or Strands 7-10 are Restricted

Mechanisms that have been proposed to reduce the quantum yield of FPs include structural perturbations that decrease the planarity of the chromophore [31, 77] or promote collisional quenching of the chromophore by nearby side chains [72]. Thus, increased dynamics of residues around the chromophore could lead to a reduction in quantum yield. Of the 27 residues in mCherry that contain atoms within 5 Å of the chromophore, order parameters were calculated for 13 backbone amides in mCherry (residues 14, 42, 44, 93, 95, 143, 146, 148, 161, 181, 199, 214 and 215), and the S^2 values for each of these residues was greater than 0.9 (Table C.3). The backbone amides themselves of residues 44, 146, 214 and 215 are within 5 Å of the chromophore. Thus, there was no evidence of increased backbone dynamics for the amides of residues containing atoms near the chromophore in mCherry. Order parameters were calculated for 4 residues within 5 Å of the chromophore in mRaspberry (14, 42, 43, 143 with only the backbone amide of residue 43 being within 5 Å of the chromophore) and in mRojoB (14, 109, 181 and 214, with only the backbone amide of residue 214 being within 5 Å of the chromophore), and again these backbone amides showed no evidence of internal dynamics (Tables C.3 and C.3). However, the dynamics of the amides do not necessarily correlate with those of the side chains [152], and additional experiments probing the side chain dynamics near the

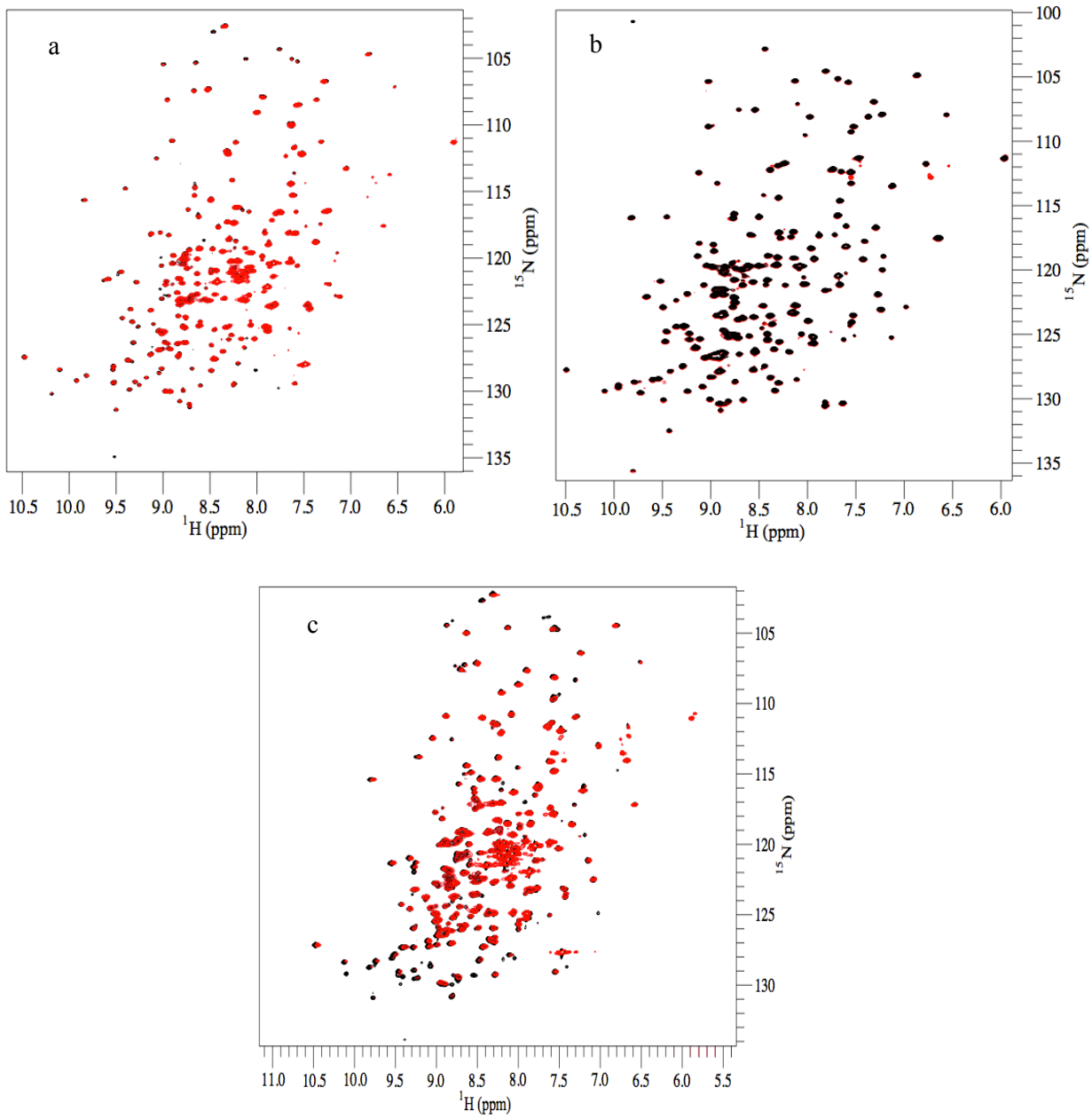

Figure 2.28: Overlaid ^{15}N HSQC R_1 and $R_{1\rho}$ spectra for mCherry (a), mRaspberry (b), and mRojoB (c) during course of experiment at 37°C, with the relaxation time delay set to 0 s. The black NR_1 spectrum of mCherry was collected 3 days before the red $NR_{1\rho}$ spectrum, and the sample was held at 37°C between spectra. The spectra overlay well, though the central peaks in the $NR_{1\rho}$ spectrum are less well disperse. The black $NR_{1\rho}$ spectrum of mRaspberry was collected 3 days before the red NR_1 spectrum, and the sample was kept at 37°C between spectra. The spectra overlay well. The peaks in the center of the $NR_{1\rho}$ spectrum remain very well dispersed, although several peaks have shifted. The black NR_1 spectrum of mRojoB was collected only one day before the red $NR_{1\rho}$ spectrum, and the sample was kept at 37°C between acquisition of the 2 spectra. The peaks in the $NR_{1\rho}$ spectrum have shifted slightly, and the central peaks in the $NR_{1\rho}$ spectrum are more intense and less well disperse, suggesting the sample may have not have remained stable during data collection period [168, 214].

chromophores should be performed. Other backbone amides nearby the chromophore may have increased ps-ns dynamics in mRaspberry and mRojoB but were not detected here due to lack of assignments. In addition, the studies performed in this work were performed on RFPs in the ground state, and additional dynamics may be present in the excited states. Therefore, probing the dynamics of RFPs in the excited states may reveal differences in dynamics that contribute to differences in quantum yields. Restricted backbone dynamics have been previously reported for a GFP variant, GFPuv, [74] further supporting the model that FPs are highly rigid and that rigidity is important for fluorescence.

Dynamics in strand 7 of fluorescent proteins are thought to affect fluorescence [69, 72]. For example, conformational exchange occurring in strand 7 of ECFP was eliminated in SCFP3A, which has increased quantum yield [72]. In addition, a previous molecular dynamics study suggested that strand 7 of mCherry displayed larger amplitude structural fluctuations relative to a YFP variant, Citrine [69]. The dynamics of this region were compared to better understand where molecular oxygen might be entering the β-barrels of mCherry and YFP. Also, NMR studies showed more extensive line broadening of backbone resonances in the dark state then the bright state of the photoswitchable RFP, Dronpa [62]. Such line broadening may be due to ms dynamics [130] indicative of interconverting populations. These dynamics were observed at the former protein-protein interface in the wild-type tetramer, which was disrupted in the monomeric RFP variant, Dronpa [62]. Based on insight previous studies have gained into the apparent relationships between dynamics of these particular regions and fluorescence quantum yield, dynamics in residues near the chromophore and in strands 7-10 were examined more carefully in mCherry, mRaspberry and mRojoB. In mCherry, backbone amide order parameters for residues 141-147 in β-strand 7 and 197-204 in β-strand 10 ranged from 0.9 to 1.0, which is similar to the range of order parameters for the other β-sheets (Table C.3). Thus, the NMR relaxation data for mCherry showed no evidence for increased structural fluctuations of β-strands 7 or 10 compared to the rest of the β-barrel. The limited number of assignments for mRojoB and mRaspberry precluded detailed analysis of dynamics in this region. Amide 203 of strand 10 had S^2 values of 0.96 and 0.80 in mRaspberry and mRojoB, respectively. Amide 143 from β-strand 7 had an S^2 value of 0.99 in mRaspberry (Tables C.3 and C.3). These data are consistent with a restricted internal dynamics and again provide no additional clues as to the differences in quantum yields between monomeric RFPs.

Chromophore Tyrosine $C^{\beta}H$ in mCherry, mRasperry and mRojoB is Rigid on ps-ns Timescale

The chromophore tyrosine C^{β}Hs of mCherry, mRaspberry, and mRojoB were probed for ps-ns dynamics using ^{13}C NMR relaxation experiments. Structural perturbations to the chromophore, such as torsion away from planarity could decrease the fluorescence quantum yield by promoting non-radiative relaxation pathways for an excited state chromophore [49,108]. The chromophore tyrosine C^{β}H is located at the bridge between the imidazolinone and phenyl rings of the chromophore (Figure 2.12). Twist and tilt of the bridge have been detected in FPs and have been proposed to be a source for nonadiabatic crossing [49] thus affecting the quantum yield [31]. Such structural perturbations, if occurring on the ps-ns timescale, may be detected using NMR relaxation experiments. Increased dynamics would be indicated by increased {^{1}H}-^{13}C hetNOE and R_1 values, and decreased R_2 values. {^{1}H}-^{13}C hetNOEs can range from 1 to 3, with smaller values indicating increased rigidity on the ps-ns timescale [192–194, 215]. Previous studies measuring {^{1}H}-^{13}C hetNOEs for aromatic carbons in the nucleotide bases of RNAs have shown increased {^{1}H}-^{13}C hetNOE values in loops compared to stems which were thought to be more rigid, [216]. In proteins {^{1}H}-^{13}C hetNOE values generally increase farther from the protein backbone, indicative of increased flexibility [193]. The relaxation parameters for the chromophore tyrosine C^{β}Hs of mCherry, mRaspberry, and mRojoB are indicative of highly rigid environments (Table 2.5) with hetNOE values close to 1, and R_1 and R_2 in the expected range for molecules tumbling with correlation time constants of ≈10 ns, as would molecules with molecular weights of ≈ 20-30 kDa. Thus the {^{1}H}-^{13}C hetNOE, ^{13}C R_1 and ^{13}C R_2 values are consistent with the chromophore being held rigid within the ≈ 25 kDa protein.

Previous work supports the idea that the chromophore of mCherry and other FPs are quite rigid. Increasing pressure, thus reducing flexibility, increases the quantum yields for many FPs, but not for mCherry [55]. This suggests it is already rigid at ambient pressure. Another study using ^{19}F NMR relaxation to probe ps-ns dynamics of the chromophore of a GFP variant concluded that the chromophore was rigid on the ps-ns timescale [71]. Despite the generally accepted concept that the chromophores of FPs are in a rigid environment, chromophore dynamics have been reported. Differences in dynamics between the bright and dark state chromophore were suggested in the photoswitchable RFP, Dronpa. Unlike the bright state, the dark state of Dronpa is doesn't form a hydrogen bond with a nearby serine side chain, and is thus thought

to be more flexible [62].

The ^{13}C relaxation data for the chromophore tyrosine C$^{\beta}$H of the 3 monomeric RFPs do not support the idea that differences in dynamics at or near the chromophore are contributing to differences in quantum yields. However, other regions of the chromophore, for example the phenolic or imidazolinone rings, could be probed for dynamics to further test the hypothesis that differences in dynamics contribute to differences in quantum yield. Again, the species studied were in the ground state, but quantum yield may be more sensitive to dynamics of the excited states. Useful information about dynamic differences may be gained by performing additional relaxation experiments, for example, on the excited state of the FPs by continual illumination of the NMR sample as has been done previously by introducing a fiberoptic cable into the probe of the NMR spectrometer [70].

2.5 Summary: Subtle or as yet Undiscovered Differences in ps-ns Dynamics of Monomeric RFPs Cause Differences in Quantum Yield

NMR ^{15}N and ^{13}C relaxation experiments were used to measure the ps-ns dynamics of the backbone amides and chromophore tyrosine C$^{\beta}$H of mCherry, mRaspberry and mRojoB. Dynamics on this timescale could affect quantum yield, for example by perturbing the environment of the excited state chromophore and thus providing non-radiative relaxation pathways. However, based on the convention that backbone amides with order parameters of larger than 0.8 are considered rigid, the NMR relaxation data suggest all 3 proteins are rigid on the ps-ns timescale. This finding is consistent with the idea that fluorescent molecules must be rigid for radiative relaxation to outcompete non-radiative forms of relaxation. However, while the average backbone amide order parameters suggest the RFPs are rigid, residue specific dynamics might affect quantum yield. An individual dynamic backbone amide could perturb the chromophore environment, and lack of assignments in mRaspberry and mRojoB prevented analysis for many residues near the chromophore. Therefore, additional assignments of backbone amides, as well as experiments probing dynamics of side chains in combination with side chain assignment, may provide valuable insight into differences in dynamics that might be causing differences in the quantum yields. NMR relaxation experiments probing side chain carbons for ps-ns dynamics have been performed on large proteins [217] and may prove useful to compared the

dynamics in RFP variants since several methyl groups are within 5 Å of the chromophore.

Despite the average backbone amide order parameters suggesting rigid protein backbones, the RFP with the lowest quantum yield, mRojoB, also has the lowest average backbone amide order parameter and more backbone amides with order parameters less than 0.9 than either mCherry or mRaspberry. This data is consistent with increased collisional quenching due to internal dynamics reducing the quantum yield of mRojoB relative to mCherry and mRaspberry. The data in conjunction with the trend in quantum yield among the three RFPs studied suggest that a cutoff of 0.8 for a backbone amide may not be "rigid" enough to preclude collisional quenching of fluorescence and that different guidelines should be used when probing dynamics of fluorescent molecules.

Chapter 3

Conformational Exchange, Local Unfolding, and Solvent Accessibility of Red Fluorescent Protein Variants

3.1 Introduction

The directed development of FPs with optimized photophysical properties has been an active area of research for nearly 2 decades [8]. Decreased scattering from longer wavelength emitting FPs has made the pursuit of brighter monomeric RFPs of particular importance, especially when studying multicellular organisms [16].

During protein directed development, the optimization of one physical property is often accompanied by unfavorable changes in another useful property [33]. In the set of red fluorescent proteins studied in this work, monomerization coincided with a decreased quantum yield as did increasing the wavelength of emission (tdTomato: Φ=0.69, λ_{em} = 581 nm, mCherry: Φ=0.22, λ_{em} = 610 nm, mRaspberry: λ_{em} = 625 nm and Φ=0.15, and mRojoB: λ_{em} = 631 nm and Φ=0.06). The results of the experiments described in this work provide a basis for understanding whether other physical properties, such as protein dynamics and solvent accessibility, were affected during directed development. The experiments described in this chapter were performed to assess whether conformational exchange on timescales slower than that of fluorescence was affected during RFP directed development and whether differences in dynamics correlate with the differences in quantum yield. The conformational exchange (such as local unfolding events) as well as the solvent accessibility of tdTomato, mCherry, mRaspberry and mRojoB were compared using NMR relaxation dispersion, hydrogen-deuterium exchange and fluorescence quenching experiments.

3.1.1 NMR Relaxation Dispersion Experiments

NMR relaxation dispersion experiments are often used to monitor conformational exchange occurring on the μs-ms timescale. Protein dynamics on this timescale typically correspond rearrangements of groups of atoms, for example the rotamerization of amino acid side chains. Relaxation dispersion experiments were performed on the backbone amides of mCherry, mRaspberry and mRojoB and the side chain methyls of isoleucine, leucine and valine residues of mCherry and mRojoB. Dynamics on the μs-ms timescale are not likely to provide non-radiative relaxation pathways to an excited state chromophore due to fluorescence lifetimes being on the order of a nanosecond. However, dynamics on the μs-ms timescale may still affect the fluorescence quantum yield since μs-ms dynamics are indicative of interconverting populations, and the population weighted average quantum yield is observed (Figure 3.1). The population weighted average quantum yield would be lowered by a non-fluorescent population. For example, a previous NMR study on a GFP variant found evidence of ms dynamics which converted the protein between 2 conformations, one of which was thought to be non-fluorescent [71]. Isoleucine 146, located on strand 7, was hypothesized to have a mechanism for collisional quenching of the chromophore in the non-fluorescent conformation [71]. In addition, the fluorescence quantum yield of a locally unfolded state of GFP has been shown to have 10% than that of the fully folded form [165]. The Kuwajima group also showed that an acid-induced unfolding intermediate of GFP is non-fluorescent [158]. The Jackson group, too, noticed greater that 2-state unfolding using fluorescence as a probe to monitor chemically-induced denaturation, indicating that the unfolding intermediate of GFP had a different fluorescence quantum yield from the fully folded and fully unfolded states [165]. Therefore, probing conformational exchange may provide valuable insight into differences in quantum yields. In addition, any differences detected may improve the understanding of the effect protein directed development had on protein dynamics.

3.1.2 Hydrogen Deuterium Exchange Experiments

Hydrogen deuterium exchange (HDX) experiments can be used to measure solvent accessibility and conformational exchange, for example local unfolding events that allow buried or hydrogen bonded protons to exchange with deuterons in the solvent [218]. HDX experiments were performed on tdTomato, mCherry

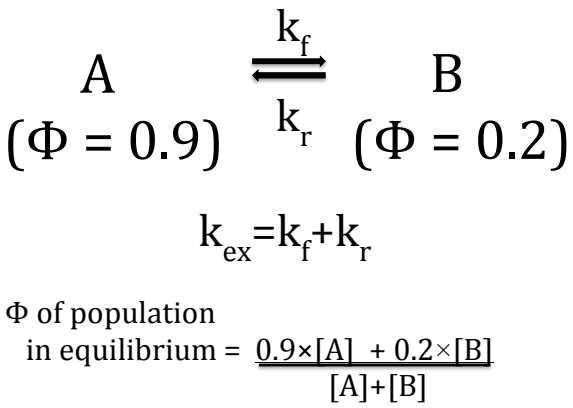

Figure 3.1: Two interconverting populations, A and B, represent 2 conformations of a fluorescent protein that have different quantum yields. In solution, the observed quantum yield is the population weighted average of the 2 quantum yields. The exchange between populations can be detected using NMR relaxation dispersion experiments, provided that 1) the exchange occurs on the μs-ms timescale, 2) that the different populations have distinct chemical shifts, and 3) that significant populations are present in each state [155]. The exchange rate constant, k_{ex} is defined as the sum of the forward and reverse exchange rate constants and can be extracted from the data.

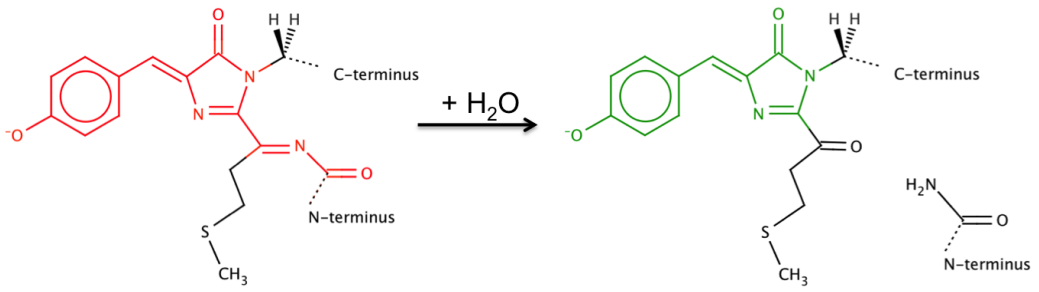

Figure 3.2: Upon denaturation, the red fluorescent protein chromophore is prone to hydrolysis and cleavage of the acylimine bond thus fragmenting the protein into two polypeptides [29]. This converts the RFP chromophore into a species that absorbs light of a similar wavelength to that of GFP.

and mRojoB to gain insight into the relative propensities for local unfolding and to better understand the effect directed development had on local unfolding. In addition, the results may provide insight into the differences in quantum yield among these 3 RFPs. As discussed previously, locally unfolded states may have different quantum yields from the fully folded state. Therefore, the detection of significantly populated locally unfolded states may provide clues as to whether local unfolding is contributing to the observed differences in quantum yield.

3.1.3 Absorption Spectra Changes Post Incubation at 37°C in D_2O

One challenge when studying or using RFPs is the occurrence of covalent modification to the chromophore. The acylimine bond in the mature RFP chromophore cleaves under denaturing conditions (Figure 3.2) [29, 101]. The absorption profile of the cleaved chromophore is shifted to shorter wavelengths and thus more closely resembles the absorption of the off-target GFP-like form of the chromophore.

Absorption spectra for the chromophores of RFPs change upon denaturation, suggesting covalent modification to the chromophore upon solvent exposure [94, 97, 162]. The acylimine bond of RFPs may cleave under denaturing conditions, thus fragmenting the protein into 2 polypeptide chains and reverting the chromophore into a GFP like form [29] (Figure 3.2). The wavelength at which the chromophore absorbs and fluoresces is highly dependent on the number of conjugated double bonds, the chromophore environment, and the protonation and oxidation states. Thus, modification of the chromophore or its environment is often detectable with absorption spectroscopy. Absorption spectra were collected before and after each protein was

incubated at 37°C to determine whether changes to the environment of the chromophore occurred during HDX experiment.

3.1.4 Fluorescence Quenching by Acrylamide

Fluorescence quenching by collisional quenchers provides another non-radiative relaxation pathway and thus lowers the quantum yield [64]. Fluorescent protein chromophores are more sheltered from fluorescence quenchers in the interior of a well-folded protein than in an unfolded protein. Yet solvent penetration or local unfolding events may allow fluorescence quenchers to penetrate the exterior of the protein and contact the chromophore or the structurally buried tryptophans [219] (Figure 3.3). Therefore, monitoring the fluorescence of the buried chromophore and tryptophans can provide information about the accessibility of the protein interior to solvent. Susceptibility to fluorescence quenching by acrylamide was measured for the chromophores and tryptophans of tdTomato, mCherry, mRaspberry and mRojoB to gain insight into differences in quantum yields. Although all 4 RFPs studied have similar tertiary structures, tdTomato contains a dimer interface which was thought to play a role in preventing solvent from entering the interior of the protein.

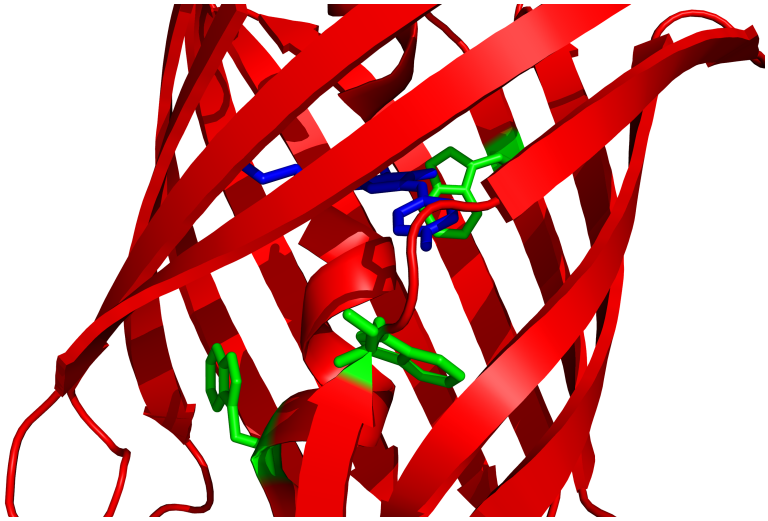

Figure 3.3: The RFPs studied here, tdTomato, mCherry, mRaspberry and mRojoB all contain the same 3 tryptophan residues and chromophore. The crystal structure of mCherry is shown with the chromophore in blue and the tryptophan residues in green.

The current understanding of the differences in quantum yields among the RFP variants tdTomato, mCherry, mRaspberry and mRojoB is incomplete at best. The results of the experiments presented in this work will provide insight into changes in dynamics that occurred during RFP directed development that may contribute to differences in quantum yields. The results from the NMR relaxation dispersion and HDX experiments provided valuable information about the conformational exchange occurring in tdTomato, mCherry, mRaspberry and mRojoB. The fluorescence quenching results provided a better understanding of the role of the dimer interface in tdTomato.

3.2 Methods

3.2.1 NMR Relaxation Dispersion Experiments Methods

Labeling: ^{13}C *ILV Methyl*

The protocol for protein expression of the ^{15}N-labeled mCherry, mRaspberry and mRojoB samples used for the ^{15}N relaxation dispersion experiments is described in section 2.2.1. The isoleucine, leucine and valine (ILV) ^{1}H-^{13}C methyl group and otherwise fully deuterated protein labeling strategy has been described

previously [220]. Briefly, 2 metabolic precursors for ILV residues were prepared prior to protein expression. The 2 precursors, 2-keto-3-(methyl-d3)-butyric acid-4-^{13}C sodium salt, and 2-ketobutyric acid-4-^{13}C sodium salt hydrate (Figure 3.4) were purchased from Sigma-Aldrich/Isotec. α-ketoisovalerate (2-keto-3-(methyl)-butyric acid) is a metabolic precursor for leucine and valine, and α-ketobutyrate (2-ketobutyric acid) is a metabolic precursor for isoleucine. A 25 mM stock solution of 2-keto-3-(methyl-d3)-butyric acid-4-^{13}C sodium salt was prepared in D_2O at pH 12.5 and incubated at 45°C for 2-3 h. A 2.7 mM stock solution of 2-ketobutyric acid-4-^{13}C sodium salt hydrate was prepared in D_2O at pH 10.5 and incubated at 45°C for 20 h. The incubation allowed for exchange of the proton(s) on carbon-3 to exchange for deuterons. The exchange of the protons for deuterons in the precursors was monitored using 1D proton NMR to confirm full exchange had occurred. Precursors that are deuterated at carbon-3 can also be purchased from Sigma-Aldrich/Isotec. The 2-keto-3-(methyl-d3)-butyric acid-4-^{13}C sodium salt is obtained from Sigma-Aldrich/Isotec as a racemic mixture containing the ^{13}C label at either one of the methyl groups (Figure 3.4a). Thus, the leucine and valine methyl groups are 50% ^{1}H, ^{13}C-labeled relative to 100% efficient labeling.

The protocol for protein expression is similar to that which was described in section 2.2.1. Deuterated M9 and $^{15}NH_4Cl$ were used for the expression of ILV ^{1}H-^{13}C methyl-labeled samples. In addition, 1 hour before induction with IPTG, 28 mL of stock solution of 2-keto-3-(methyl)-butyric acid (final concentration of 700 μM), and 153 mL of stock solution of 2-ketobutyric acid (final concentration of 400 μM) were added to the 1 L cell growth for protein expression.

NMR Relaxation Dispersion of Backbone Amides

NMR TROSY based Carr-Purcell-Meiboom-Gill (CPMG) [144,145] relaxation dispersion experiments were used to measure μs-ms dynamics of protein backbone amide nitrogens [148]. The data were collected at 37°C on ^{1}H, ^{15}N-labeled samples of mCherry, mRaspberry and mRojoB, using the pulse sequence N15_CPMG_Rex_NH_trosy_lek_600.c developed in the Kay lab. The constant R_2 relaxation delay time, time_T2, during which the train of CPMG refocusing pulses was applied was set to 20 ms. A set of 2-dimensional experiments was collected by arraying the frequency of refocusing pulses, ν_{CPMG}, from 150 to 1000 Hz (Table A.3). The data were collected as a pseudo-3-dimensional spectrum and were deconvoluted post acquisition to extract the set of 2-dimensional spectra with arrayed refocusing pulse frequency.

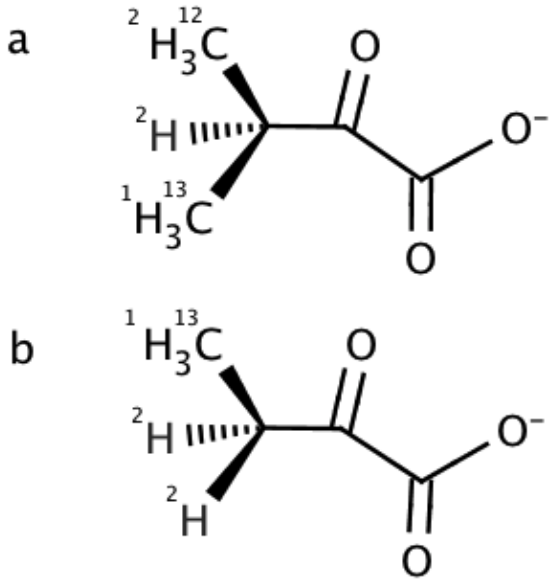

Figure 3.4: a) The chemical structure of the metabolic precursor for leucine and valine, the R enantiomer of 2-keto-3-(methyl-d3)-butyric acid-4-^{13}C,3-d1. b) The chemical structure of the precursor for isoleucine, 2-ketobutyric acid-4-^{13}C,3,3-d2.

The spectra were processed and imported into CCPNMR Analysis for data analysis. For each unique resonance the $R_{2,eff}$ (Equation 3.1) from the was compared between spectra collected with ν_{CPMG}=150 and 1000 Hz.

$$R_{2,\text{eff}} = -\frac{1}{T}\ln\left[\frac{I(\nu_{\text{CPMG}})}{I(0)}\right] \tag{3.1}$$

T is the constant R_2 relaxation delay time, ν_{CPMG} is the frequency of the refocusing pulse, and I is the peak intensity at a particular value of ν_{CPMG}. In order to comb the data for the presence of dynamic residues, a threshold of 4 s^-1 for the decrease of $R_{2,eff}$ measured at 150 relative to 1000 Hz was chosen, a slightly more stringent cut off than what has been done previously [221]. If the $R_{2,eff}$ decreased by $\geq$ 4 s^-1, the peak was considered dynamic and a more detailed analysis of the dynamics was taken. For qualifying resonances, the $R_{2,eff}$ was plotted against the pulsing frequency. Exchange rate constants and associated errors were determined by fitting the data to Equation 1.18 [142] using Mathematica's built-in function "NonlinearModelFit". In Equation 1.18 k_{ex} is the sum of the forward and reverse rate constants for conformational exchange, and $\Delta\omega$ is the difference in chemical shift between the 2 conformational states, A and B, whose populations are p_A and p_B, respectively [142]. Errors were calculated for each value of $R_{2,eff}$ using error propagation and Equation 3.2 where the noise in the spectrum collected with ν_{CPMG}=0 and with ν_{CPMG}> 0 were the errors in peak volumes in the spectra collected with ν_{CPMG}=0 or ν_{CPMG}> 0, respectively.

$$\text{Error}_{\text{R2,eff}} = \sqrt{\left(\frac{1}{\tau_{\text{cpmg}}\text{PeakVol}_{\nu=0}}\right)^2 \text{Noise}_{\nu=0}{}^2 + \left(\frac{1}{\tau_{\text{cpmg}}\text{PeakVol}_{\nu>0}}\right)^2 \text{Noise}_{\nu>0}{}^2} \tag{3.2}$$

NMR Relaxation Dispersion of ILV Methyl Groups

CPMG based ^{1}H-^{13}C HMQC relaxation dispersion experiments were used to probe μs-ms dynamics of the δ, δ, and γ methyls of isoleucine, leucine and valine residues, respectively (Figure 3.5) [151]. The data were collected at 37°C using the NMR pulse sequence hmqc_CH3_exchange_bigprotein_800_lek_v4.c developed by the Kay lab. Data were collected in 2 interleaved sets of experiments. In the first set used to probe isoleucine methyl dynamics, the carbon carrier frequency was set to 13.3 ppm, and to 23.3 ppm in the

second set used to probe leucine and valines. The carbon offset was set near to the center of the range of carbon frequencies for either the isoleucines or the leucines and valines, respectively, as errors are introduced into the data when the carrier frequency at which the refocusing pulses are applied is far from the chemical shift of the resonance being probed [151]. The constant R_2 relaxation delay time was set to 40 ms with the frequency of refocusing pulses (ν_{CPMG}) arrayed from 25 to 1000 Hz (Table A.4). The data were processed and analyzed as described for the ^{15}N relaxation dispersion experiments. The difference in $R_{2,eff}$ values was calculated for ν_{CPMG} values of 25 and 1000 Hz to determine which methyl groups were dynamic.

3.2.2 Hydrogen Deuterium Exchange Methods

Hydrogen deuterium exchange (HDX) was performed on ^{15}N-labeled samples of tdTomato, mCherry, and mRojoB expressed and purified as described in section 2.2.1. A ^{1}H-^{15}N HSQC TROSY spectrum for each protein was collected and used as a reference for the HDX experiment [222]. The proteins were exchanged into buffer containing >99% D_2O using Protein Desalting Spin Columns (Pierce). For mCherry, and mRojoB, sets of 2, 5, 10, 20, and 40 minute Best [223] ^{1}H-^{15}N HSQC spectra, modified for TROSY by Dr. Geoff Amrstrong, were collected in rapid succession after buffer exchange, thus allowing the rapidly exchanging backbone amide peak volumes to be monitored as a function of time. Sets of 3 to 4 spectra of 2 to 40-minute spectra were collected. After the first few hours of exchange, consecutive 1 hour ^{1}H-^{15}N HSQC spectra were collected for approximately 24 hours followed by a 1 hour spectrum every 3 to 4 hours for the next 72 hours. For tdTomato, due to signal-to-noise constraints, no 2-40 minute spectra were collected. Therefore 1 hour ^{1}H-^{15}N HSQC TROSY spectra were collected starting immediately following buffer exchange. The samples were incubated at 37°C for the remainder of the 10 weeks, during which time 1 hour ^{1}H-^{15}N HSQC spectra were collected periodically (Table A.6). All experiments were performed at 37°C.

The backbone amide peak volumes were monitored for 10 weeks. The time between H/D buffer exchange and the midway point of each spectrum was used when plotting the decaying peak volumes as a function of time (Figure 3.6b). The peak volumes were fit to decaying exponential functions as function of time to determine exchange rate constants, k_{ex}, and associated errors for the backbone amide hydrogens (Figure 3.6) using CCPNMR's built-in data fitting function [187]. Spectra collected during the first 2 days

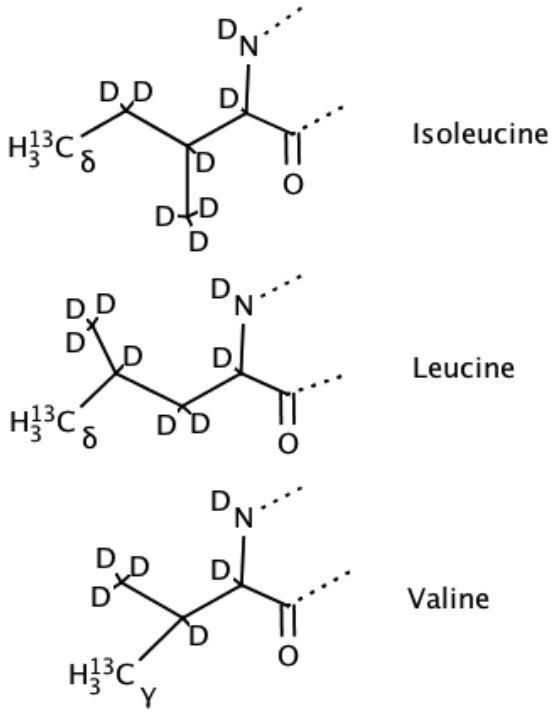

Figure 3.5: The chemical structures of isoleucine, leucine and valine with ^{1}H and ^{13}C at the γ, γ, and δ methyl groups, respectively. With the protein, 50% of each leucine and valine methyl group are ^{1}H-^{13}C-labeled, relative to 100% labeling efficiency. The exchangeable amide protons

were used when calculating exchange rate constants. Protection factors for each backbone amide proton were calculated from the k_{ex} to correct for primary structure effects [224–226]. Spectra collected at the end of the 10-week experiment were used to determine the % slower exchangers.

Amide protons were deemed fast exchangers if their peak volume decreased by >90% in the first 1.5 hours after exchange. The fast exchangers were assigned a k_{ex} of greater than 4×10^{-4} s^{-1}. The before-exchange spectra of mCherry and mRojoB were collected with 4 and 16 transients (nt) respectively, while the after-exchange spectra used to determine whether and amide proton was a fast exchanger was collected with nt=96. To correct for different levels of signal due to different values of nt, the peak volumes of the before-exchange spectrum were multiplied by the ratio of nt values used in the 2 experiments. For example, volumes in the before-exchange spectrum of mCherry were multiplied by 24 (96/4) to compensate for the difference in signal. The same procedure was used when determining whether a peak was a slow exchanger, defined as a peak with $\geq$ 50% of its original volume remaining after 10 weeks at 37°C. The slowly exchanging peaks were assigned a k_{ex} of less than 2 $\times10^{-7}$ s^{-1}. Any changes in protein concentration immediately following buffer exchange were corrected for by normalizing to the volumes of slowly exchanging amides for mCherry and mRojoB. For tdTomato, 1D proton spectra were collected before and immediately following exchange. The ratio of the peak volumes for the non-exchangable methyls to that of the internal reference, TSP, was compared before and after exchange to assess the change in protein concentration following buffer exchange. The % fast exchangers was calculated as the ratio of fast exchanging peaks to the total number of expected peaks in the protein.

3.2.3 Absorption Spectra Changes Post Incubation at 37°C in D_2O

Ten-Week Incubation

Absorption spectra for the NMR hydrogen deuterium exchange samples of mCherry, mRojoB and tdTomato were collected before and after the 10-13 week incubation at 37°C. The spectra were collected on the samples diluted in water to a concentration of ≈1 μM protein in 20 μM d-11 Tris pH 7, 50 μM NaCl, and 5 μM DTT. The absorption spectra were collected from 250 to 650 nm with 10 nm step size at room temperature immediately following the dilution in water. A Bio-Tek Instruments PowerWave X microplate

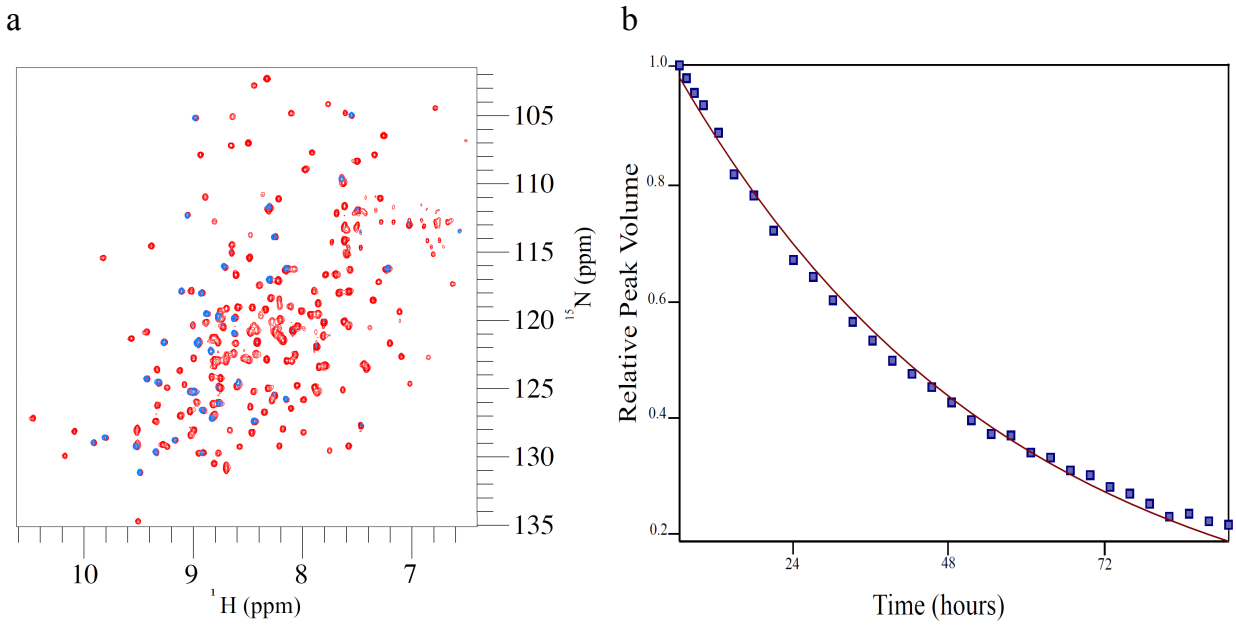

Figure 3.6: a) A 5-minute 2D ^{1}H-^{15}N HSQC of mCherry before exchange into deuterated buffer (red) and a 1 hour spectrum after 10 weeks of incubation in D_2O at 37°C (blue). b) The relative peak volumes of leucine 124 in mCherry over time. The data points were fit to a single exponential decay to extract a rate constant for exchange.

reader was used for the measurements. The absorption spectra were normalized to a value of 1 at 280 nm.

Two-Day Incubation

Absorption spectra for samples of ^{15}N-labeled mCherry, ^{13}C methyl ILV labeled mRojoB, and ^{2}H^{15}N tdTomato were collected immediately following buffer exchange of ≈0.2 mM protein samples into 100% deuterated buffer containing 20 mM d-11 Tris pH 7, 50 mM NaCl, and 5 mM DTT, and again after 2 days of incubation at 37°C in D_2O. The proteins were diluted with buffer to a concentration of 1 μM when acquiring the absorption spectra. The absorption spectra were collected from 250 to 650 nm with 5 nm step size using the Bio-Tek Instruments PowerWave X microplate reader.

3.2.4 Fluorescence Quenching by Acrylamide Methods

The tryptophan and chromophore fluorescence of tdTomato, mCherry, mRaspberry and mRojoB was monitored as a function of acrylamide concentration ranging from 0 to 0.5 M for the tryptophan quenching experiment, or 0 to 2.5 M for the chromophore quenching experiment. The protein samples used for these experiments were expressed with ^{15}N labeling, purified and concentrated as described in section 2.2.1, and stored in 20 mM Tris pH 7, 50 mM NaCl, and 5 mM DTT at 4°C prior to use. Visible range absorption spectra of the samples were collected prior to sample use. In a quartz cuvette, 2 mL of 1 μM protein samples were prepared in 20 μM Tris pH 7, 50 μM NaCl, and 5 μM DTT. Samples of approximately 1 μM solutions of tdTomato, mCherry, mRojoB and mRaspberry were used to ensure an optical density of less than 0.1 at the excitation wavelength. Acrylamide was titrated into the cuvette from a 5 M stock solution and mixed by pipetting. After each addition of acrylamide, a fluorescence spectrum was acquired. Using a Photon Technology International Quantamaster 40 steady-state fluorometer with the temperature regulated at 25°C, the tryptophan residues were excited at 295 nm, and fluorescence was monitored from 305 to 425 nm. The chromophores were excited at 540 nm, and fluorescence monitored from 550 to 650 nm. Slit widths for the excitation and emission monochromators were set to 0.5 mm (2 nm). Stern-Volmer constants were calculated for the tryptophans and chromophores by fitting the ratio of fluorescence intensities in the absence and presence of acrylamide to the Stern-Volmer equation.

$$\frac{I}{I_0} = 1 + K_{SV}[Q] \tag{3.3}$$

I and I_0 are the fluorescence intensities at 325 nm (tryptophan data) or the wavelength of the maximum fluorescence for the respective chromophores (chromophore data) in the presence and absence of acrylamide, respectively. K_{sv} is the Stern Volmer constant and [Q] is the concentration of the quencher, acrylamide. To account for the change in fluorescence due to decreased sample concentration upon addition of acrylamide, the fluorescence was multiplied by the ratio of the sample volume post and prior to dilution. The tryptophan quenching experiments were performed in triplicate, and the chromophore quenching experiments in duplicate.

3.3 Results

3.3.1 NMR Relaxation Dispersion Experiments Results

Backbone Amides of mCherry, mRaspberry and mRojoB

NMR relaxation dispersion experiments can be used to detect μs-ms timescale dynamics provided the interconverting populations have distinct chemical shifts and that each conformation is significantly populated [155]. NMR relaxation dispersion experiments probing the backbone amides of mCherry, mRaspberry and mRojoB, 3 related monomeric RFPs with different quantum yields, were performed. The results from these experiments were used to explore whether 1) global or local changes in dynamics occurred during RFP directed development and 2) whether dynamics correlate with differences in quantum yields. Dynamics on the μs-ms timescale were detected in 5, 4 and 3 % of the observed peaks in the ^{1}H-^{15}N HSQC spectra for mCherry, mRaspberry, and mRojoB, respectively. However, lack of detection in additional backbone amides does not preclude the existence of dynamics. Resonances for which the difference in $R_{2,eff}$ (Equation 3.1) from the ν_{CPMG} (the frequency of the refocussing pulses during the constant R_2 relaxation delay period)=150 and 1000 Hz spectra was $\geq$ 4 s^{-1}, plots of $R_{2,eff}$ versus ν_{CPMG}, or dispersion profiles, are presented in Figures 3.7, 3.8 and 3.9 for mCherry, mRaspberry and mRojoB, respectively. This difference of 4 s^{-1} was used as a filter to select resonances for which relaxation dispersion was present. Several resonances

were deemed not dynamic despite a difference in $R_{2,eff}$ of ≥ 4 s^{-1} (Figure 3.10) upon visual inspection. For the dynamic resonances, the exchange rate constants and $\Delta\omega p_1 p_2$ values extracted from fitting the data to Equation 1.18 are given in Table 3.1. $\Delta\omega p_1 p_2$ values are the product of the difference in chemical shift between and relative populations of the 2 states, assuming 2 state exchange. The terms cannot be separated when data is collected at only one magnetic field strength.

ILV Methyl Groups of mCherry and mRojoB

NMR relaxation dispersion experiments were used to measure μs-ms timescale dynamics in the side chain δ, δ, and γ methyl groups of isoleucine, leucine, and valine residues, respectively, in mCherry and mRojoB. Whether side chain methyl dynamics on the μs-ms timescale contribute to the difference in quantum yield was explored using these experiments. Dynamics on the μs-ms timescale were detected in 22 and 26% of the peaks observed in the ^{1}H-^{13}C HMQC spectra of ILV labeled mCherry and mRojoB, respectively. (Again, the lack of detection of dynamics in additional methyls does not preclude their existence.) The relaxation dispersion profiles for mCherry and mRojoB are presented in Figures 3.11 and 3.12 respectively, and the corresponding exchange rate constants and $\Delta\omega p_1 p_2$ values are presented in Table 3.2.

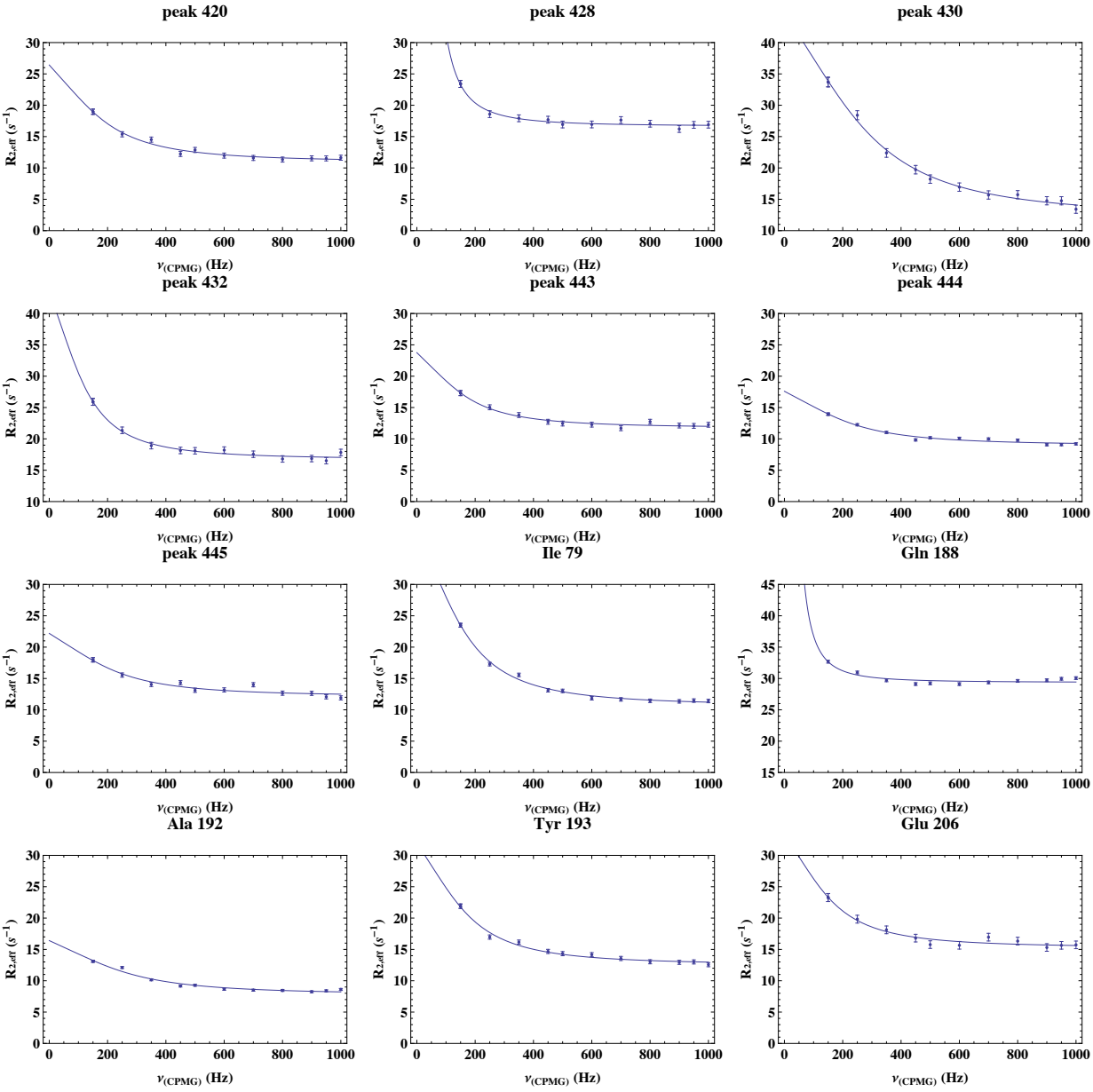

Figure 3.7: The relaxation dispersion profiles for mCherry backbone amides displaying μs-ms timescale dynamics are presented. $R_{2,eff}$ versus ν_{CPMG} plots were generated for peaks in which the $R_{2,eff}$ calculated in the spectrum collected with the lowest frequency of pulsing was at least 4 s^{-1} larger than the $R_{2,eff}$ calculated in the spectrum with the highest frequency of pulsing. The data were fit to Equation 1.18 (blue curve). The data were collected at 37°C.

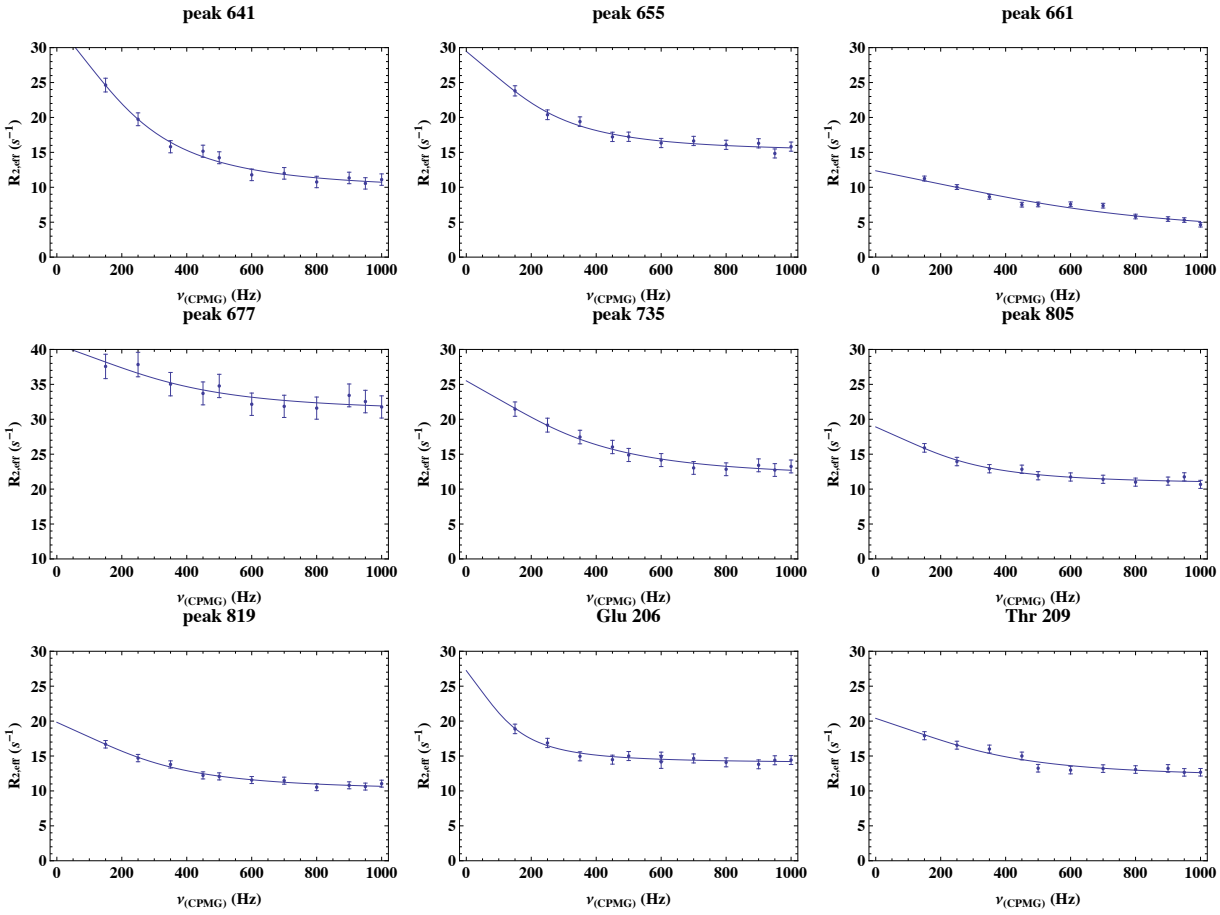

Figure 3.8: Relaxation dispersion profiles for backbone amides in mRaspberry in which μs-ms timescale dynamics were detected. $R_{2,eff}$ versus ν_{CPMG} plots were generated for peaks in which the $R_{2,eff}$ calculated in the spectrum collected with the lowest frequency of pulsing was at least 4 s^{-1} larger than the $R_{2,eff}$ calculated in the spectrum with the highest frequency of pulsing. The data were fit to Equation 1.18 (blue curve). The data were collected at 37°C.

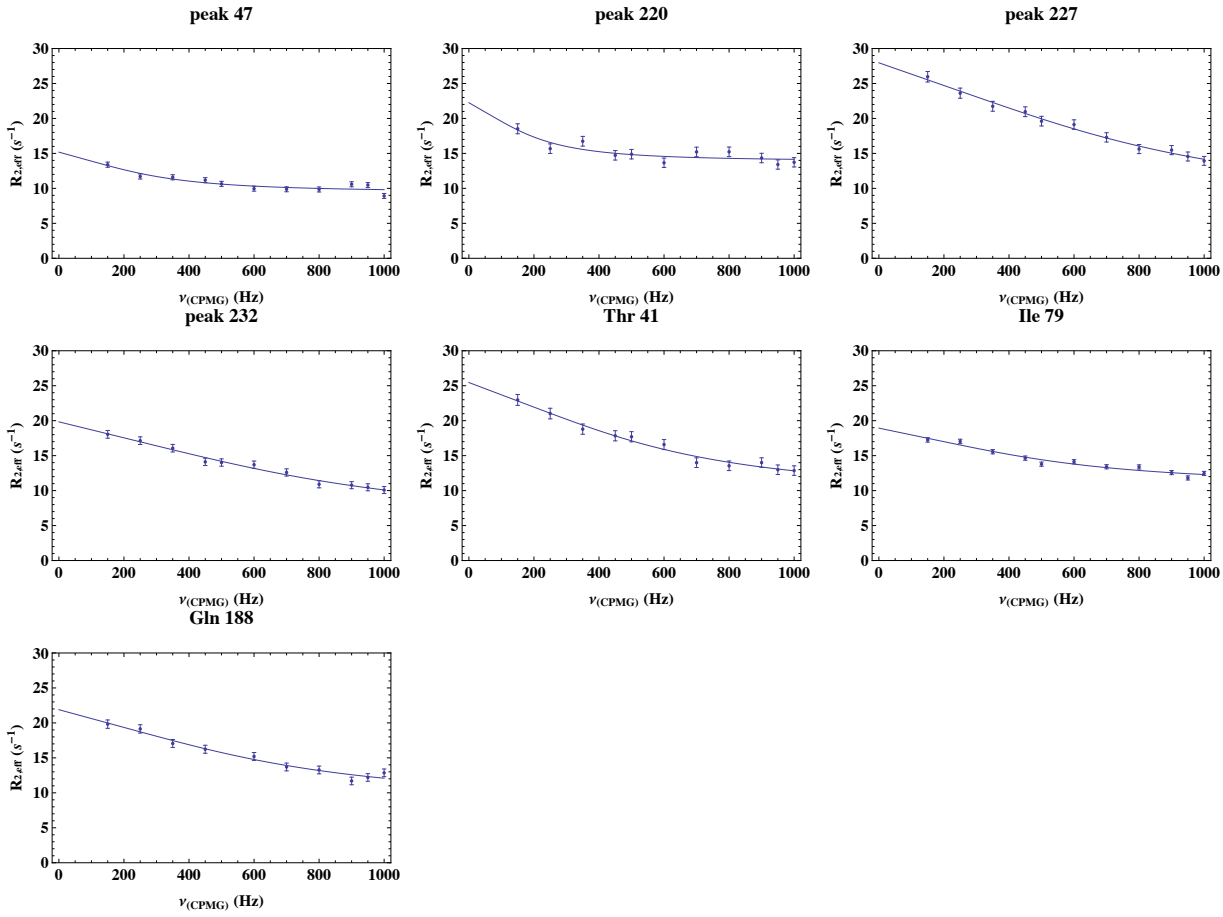

Figure 3.9: Relaxation dispersion profiles for backbone amides in mRojoB in which μs-ms timescale dynamics were detected. $R_{2,eff}$ versus ν_{CPMG} plots were generated for peaks in which the $R_{2,eff}$ calculated in the spectrum collected with the lowest frequency of pulsing was at least 4 s^{-1} larger than the $R_{2,eff}$ calculated in the spectrum with the highest frequency of pulsing. The data were fit to Equation 1.18 (blue curve). The data were collected at 37°C.

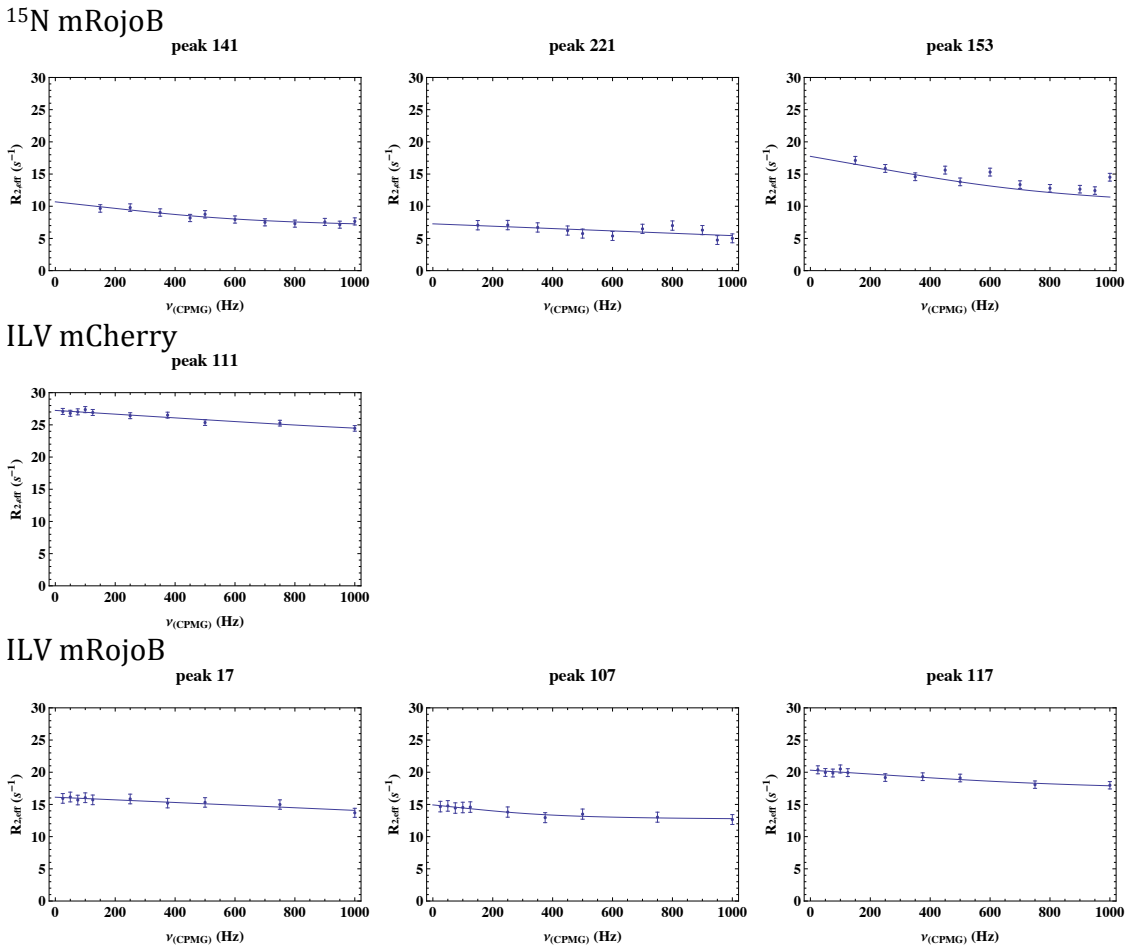

Figure 3.10: These relaxation dispersion profiles for backbone amides were generated for resonances if the $R_{2,eff}$ values for spectra collected with ν_{CPMG}=150 and 1000 Hz differed by $\geq$ 4 s^{-1}. However, these resonances were removed from the list of peaks in which dynamics were detected after inspection of the relaxation dispersion profile.

Table 3.1: Exchange rate constants and populations for backbone amides detected using CPMG relaxation dispersion experiments.[a]

mCherry Backbone Amides		
Residue	**k_{ex} (s^{-1})**	**$\Delta\omega p_1 p_2$**
peak 420	2000 ± 400	40000 ± 2000
peak 428	---	---
peak 430	4000 ± 200	100000 ± 6000
peak 432	2000 ± 400	40000 ± 3000
peak 443	2000 ± 400	30000 ± 2000
peak 444	3000 ± 500	20000 ± 2000
peak 445	3000 ± 800	30000 ± 4000
Ile 79	2000 ± 200	60000 ± 2000
Gln 188	---	---
Ala 192	3000 ± 500	30000 ± 3000
Tyr 193	2000 ± 300	40000 ± 2000
Glu 206	2000 ± 500	40000 ± 2000

mRojoB Backbone Amides		
Residue	**k_{ex} (s^{-1})**	**$\Delta\omega p_1 p_2$**
peak 47	4000 ± 1000	20000 ± 6000
peak 220	4000 ± 2000	20000 ± 5000
peak 227	10000 ± 2000	200000 ± 50000
peak 232	10000 ± 2000	150000 ± 40000
Thr 41	8000 ± 1000	100000 ± 20000
Ile 79	8000 ± 2000	50000 ± 20000
Gln 188	8000 ± 2000	100000 ± 30000

mRaspberry Backbone Amides		
Residue	**k_{ex} (s^{-1})**	**$\Delta\omega p_1 p_2$**
peak 641	4000 ± 400	80000 ± 5000
peak 655	2000 ± 600	40000 ± 4000
peak 661	8000 ± 2000	80000 ± 40000
peak 677	6000 ± 2000	50000 ± 20000
peak 735	8000 ± 1000	60000 ± 6000
peak 819	4000 ± 400	40000 ± 3000
Glu 206	4000 ± 2000	20000 ± 2000
Thr 209	8000 ± 2000	40000 ± 10000

[a] For unassigned residues, arbitrary peak numbers were assigned to peaks for referencing purposes. Assignments are given for those resides that were confidently assigned. Experiments were performed performed at 37°C. A "---" Indicates the value was not determined.

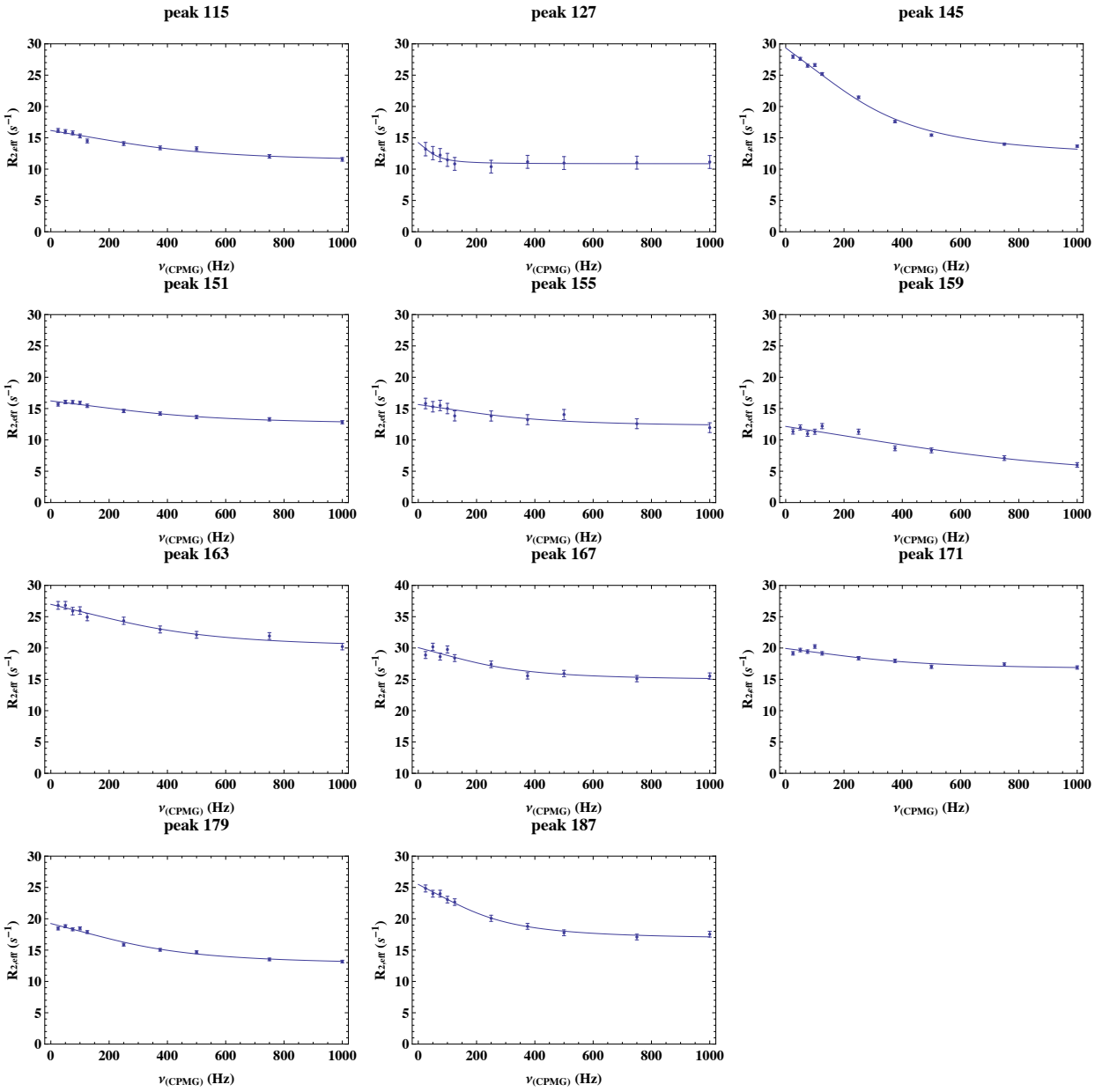

Figure 3.11: Continued on following page

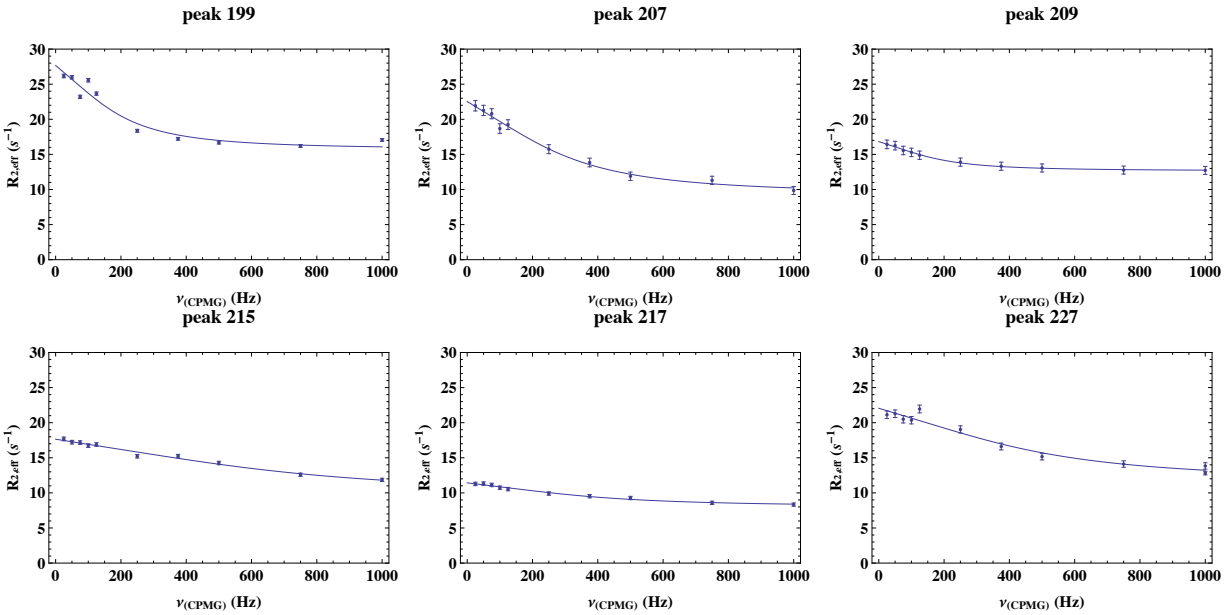

Figure 3.11: Relaxation dispersion profiles for the δ, δ, and γ isoleucine, leucine and valine methyl groups respectively, in mCherry. $R_{2,eff}$ versus ν_{CPMG} plots were generated for peaks in which the $R_{2,eff}$ calculated in the spectrum collected with the lowest frequency of pulsing was at least 4 s^{-1} larger than the $R_{2,eff}$ calculated in the spectrum with the highest frequency of pulsing. The data were fit to Equation 1.18 (blue curve). The data were collected at 37°C. All resonances are from leucine or valine methyls.

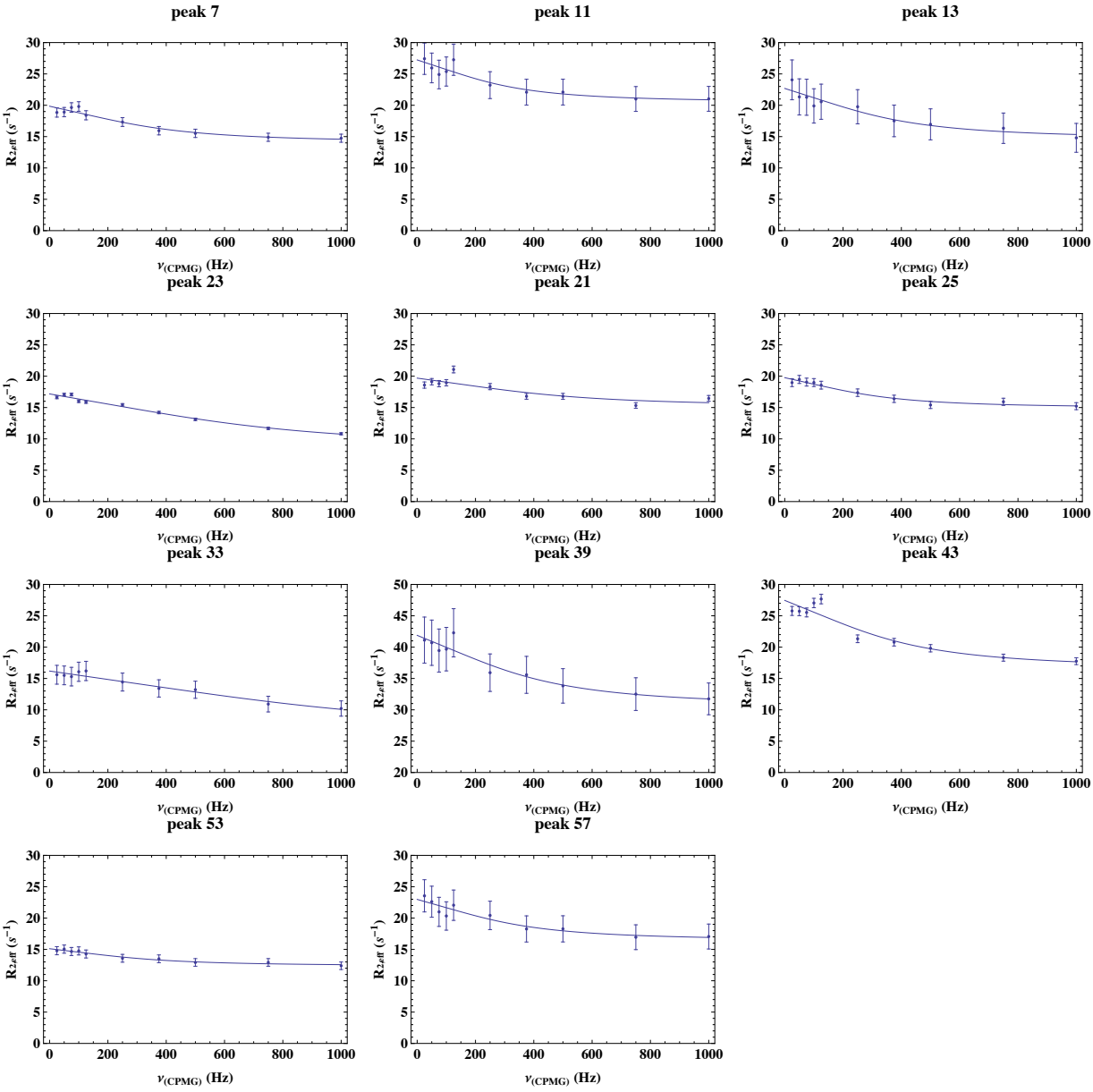

Figure 3.12: Continued on following page

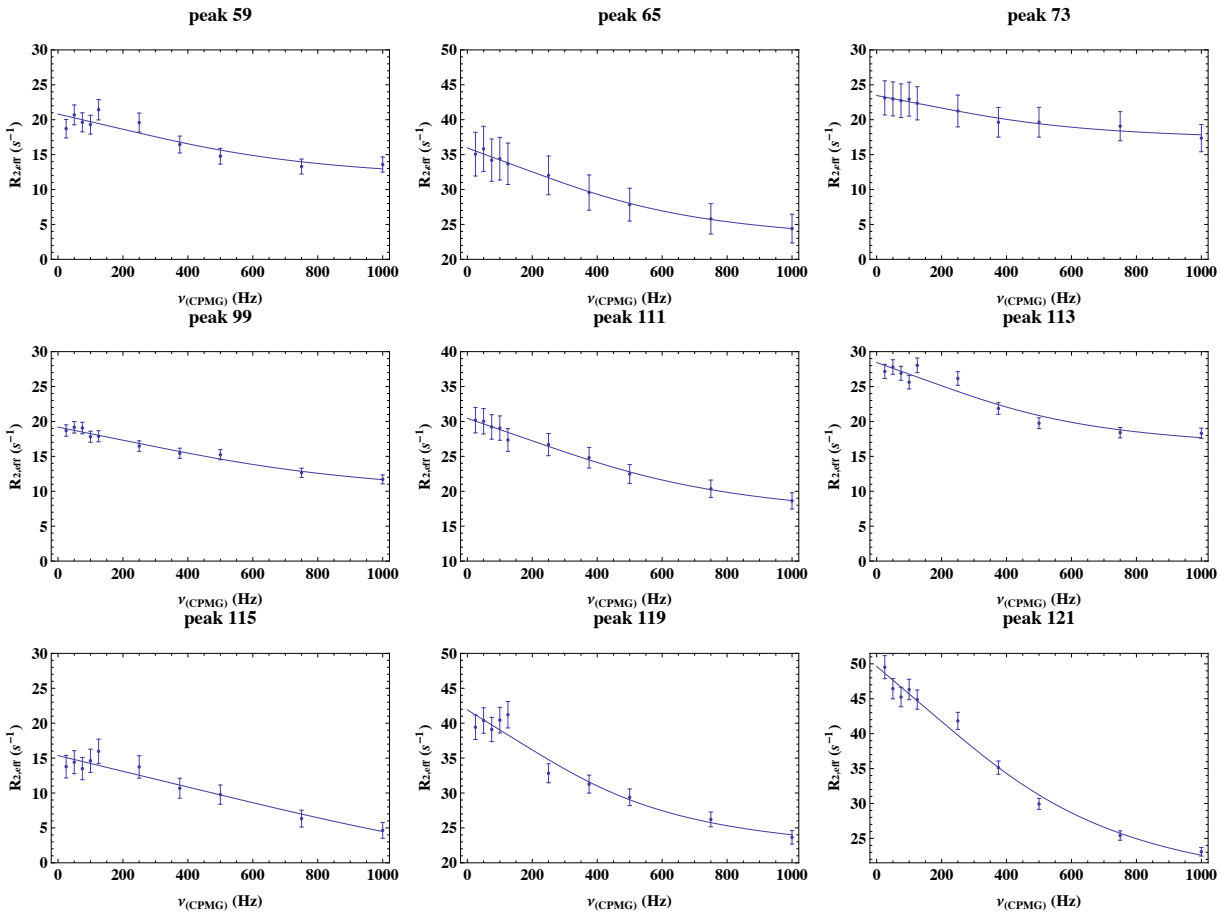

Note: Only peaks [7] , [11] , [13] and [23] are from isoleucines. The other peaks are leucines or valines.

Figure 3.12: Relaxation dispersion profiles for ILV methyl groups in mRojoB in which μs-ms timescale dynamics were detected. $R_{2,eff}$ versus ν_{CPMG} plots were generated for peaks in which the $R_{2,eff}$ calculated in the spectrum collected with the lowest frequency of pulsing was at least 4 s^{-1} larger than the $R_{2,eff}$ calculated in the spectrum with the highest frequency of pulsing. The data were fit to Equation 1.18 (blue curve). The data were collected at 37°C. Peaks 13, and 23 are isoleucine methyls and all others are leucine or valine methyls.

Table 3.2: Exchange rate constants and populations for methyl group dynamics detected using CPMG relaxation dispersion experiments.[a]

mCherry Isoleucines, Leucines and Valines		
Residue	**k_{ex} (s^{-1})**	**$\Delta\omega p_1 p_2$**
LV [115]	5000 ± 1000	30000 ± 8000
LV [127]	700 ± 200	2000 ± 500
LV [145]	4000 ± 400	70000 ± 8000
LV [151]	3000 ± 500	50000 ± 7000
LV [155]	4000 ± 2000	---
LV [159]	---	---
LV [163]	5000 ± 1000	40000 ± 9000
LV [167]	3000 ± 1000	20000 ± 8000
LV [171]	4000 ± 2000	---
LV [179]	4000 ± 600	30000 ± 5000
LV [187]	3000 ± 300	30000 ± 3000
LV [199]	2000 ± 600	30000 ± 8000
LV [207]	4000 ± 400	50000 ± 7000
LV [209]	2000 ± 200	9000 ± 600
LV [215]	9000 ± 2000	70000 ± 20000
LV [217]	5000 ± 700	20000 ± 3000
LV [227]	6000 ± 1000	60000 ± 20000

[a] Although the methyl groups were unassigned, arbitrary peak numbers were assigned for referencing purposes. Data were collected at 37°C.

[b] Some values were not determined as indicated by ≥50% errors, and are represented by "---" in this table.

mRojoB Isoleucines, Leucines and Valines		
Residue	**k_{ex} (s^{-1})**	**$\Delta\omega p_1 p_2$**
Ile [7]	4000 ± 1000	30000 ± 10000
Ile [11]	4000 ± 1000	20000 ± 10000
Ile [13]	4000 ± 2000	---
Ile [23]	9000 ± 2000	70000 ± 20000
LV [21]	---	---
LV [25]	4000 ± 800	20000 ± 4000
LV [33]	---	---
LV [39]	5000 ± 2000	50000 ± 20000
LV [43]	3000 ± 700	40000 ± 12000
LV [53]	5000 ± 2000	---
LV [57]	4000 ± 2000	30000 ± 10000
LV [59]	---	---
LV [65]	7000 ± 700	90000 ± 20000
LV [73]	6000 ± 1000	40000 ± 10000
LV [99]	9000 ± 2000	90000 ± 40000
LV [111]	7000 ± 1000	100000 ± 20000
LV [113]	6000 ± 2000	80000 ± 40000
LV [115]	---	---
LV [119]	6000 ± 2000	100000 ± 50000
LV [121]	6000 ± 1000	40000 ± 10000

3.3.2 Hydrogen-Deuterium Exchange Results

The dimer interface in tdTomato is important for fluorescence [22], however its precise role is not understood. To further explore the role of the dimer interface, solvent accessibility and conformational exchange were studied using hydrogen-deuterium exchange experiments performed on tdTomato, mCherry and mRojoB. Representative data showing the relative peak volumes as a funcion of time after exchange for fast, intermediate and slow exchangers in mCherry and mRojoB are shown in Figure 3.13. Fast and intermediate exchangers are shown in Figure 3.13 for tdTomato, as well, however, no slow exchangers were detected for tdTomato. The peak volumes were normalized to the peak volume after 1.5 hours of exchange, or the first point plotted.

The results from the HDX experiments were useful in determining global differences in solvent accessibility and in conformational exchange among the RFPs studied. The HDX results show a much larger

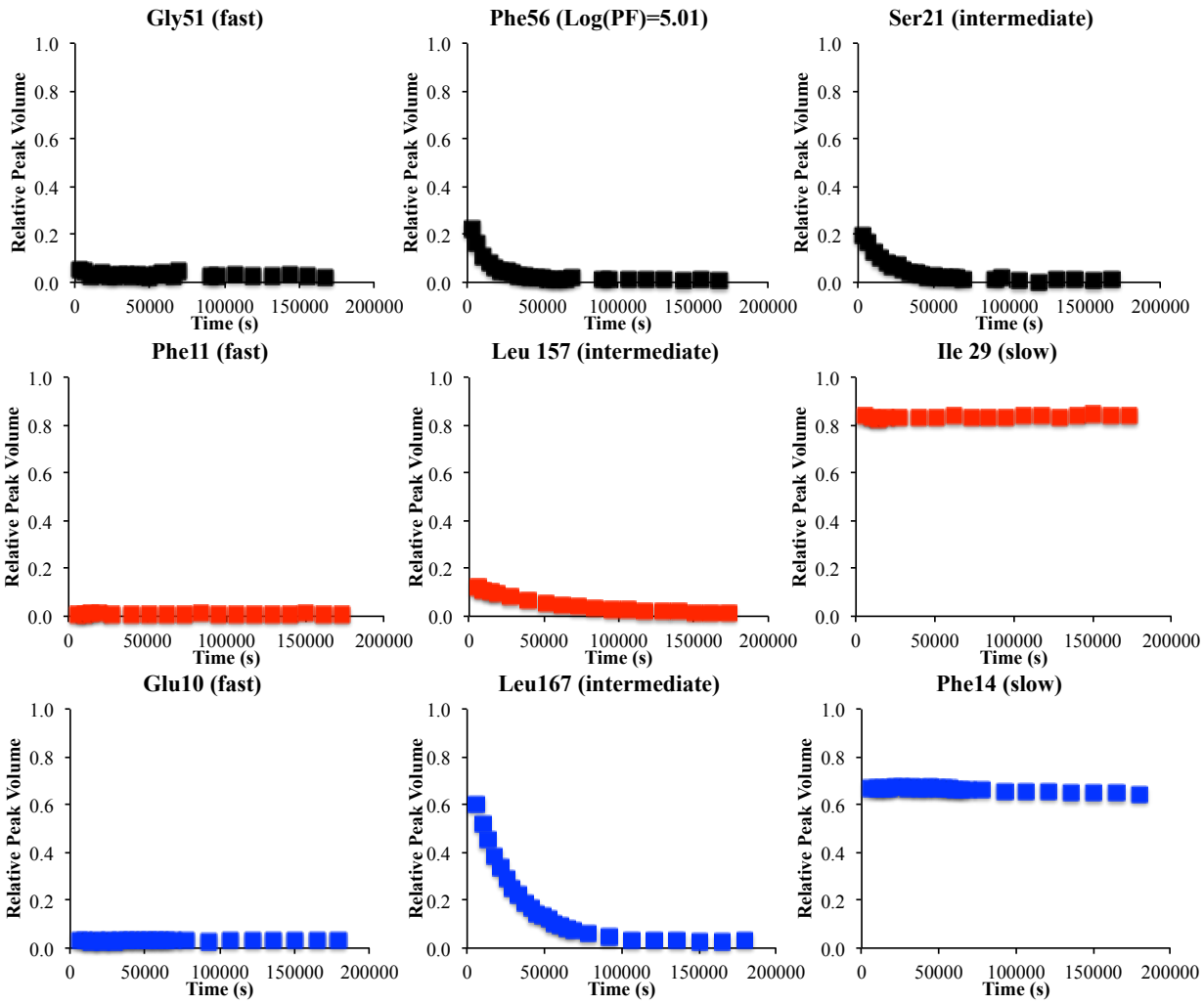

Figure 3.13: Representative data for the HDX of tdTomato (black), mCherry (red) and mRojoB (blue) are shown. The relative peak volumes versus time after exchange are plotted and normalized to the peak volume in the spectra collected before exchange. Data for fast, intermediate and slow exchangers are shown. (Data were not plotted before 1.5 hours after exchange.)

% of fast exchanging amides (61%) in tdTomato than either mCherry (21%) or mRojoB (35%). Whereas tdTomato had no slowly exchanging amides, the monomeric RFPs, mCherry and mRojoB, had 7% and 5%, respectively. The % of expected amide resonances in the spectra prior to buffer exchange of tdTomato, mCherry, and mRojoB were 88%, 86%, and 92%, respectively, and thus, data from missing peaks could not fully account for the observed differences.

Exchange rate constants, k_{ex}, between 10^{-7} s^{-1} and 10^{-4} s^{-1} were measured for the amides that were neither fast nor slow exchangers. For assigned backbone amide protons, the rate constants were used to calculate protection factors (PF), or the ratio of the observed exchange rate constant to that for the same amide proton in an unstructured polypeptide [224]. The PF describes the degree of protection provided by the secondary and tertiary structural elements. The PFs for the assigned residues in the 3 RFPs ranged from $< 10^3$ to $> 10^8$ (Table C.4). PFs could only be calculated for the assigned amides, thus, Figure 3.14 shows a histogram of the range of k_{ex} for both assigned and unassigned amide protons in the 3 RFPs, excluding the fast and slow exchangers. k_{ex} values with associated errors larger than 50% were excluded from the histogram.

Since data collected during the first 2 days were used to calculate the k_{ex}, it was important that the proteins were stable over this time. Overlay of spectra collected before exchange and after 2 days of exchange show only 2, 3, and 4 new peaks in the spectra of mCherry, mRojoB, and tdTomato respectively (Figure 3.15).

3.3.3 Absorption Spectra Changes Post Incubation at 37°C in D_2O

10-Week Incubation

Chromophore modification affects absorption and emission wavelengths which would complicate interpretation of fluorescence data when using FPs to study live cells. Therefore chromophore resistance to covalent modification is an important property. To further assess structural perturbations to the chromophore, absorption spectra for tdTomato, mCherry and mRojoB were collected before and after the 10-13 week incubation at 37°C in D_2O. The 2 or 3 major peaks in each absorption spectra were assigned. Aromatic side chains absorb at 280 nm. The fully mature and deprotonated chromophores of tdTomato and mCherry

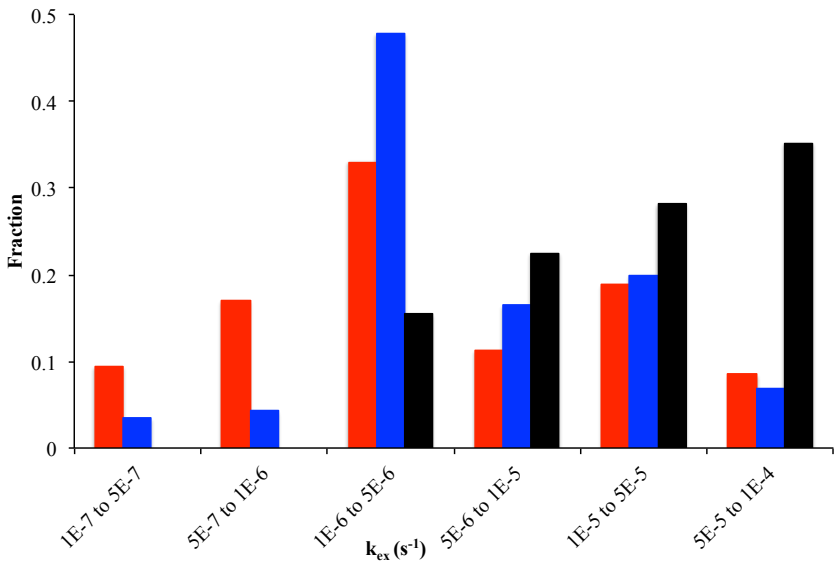

Figure 3.14: The histogram of HDX k_{ex} values for both assigned and unassigned residues for mCherry (red), mRojoB (blue) and tdTomato (black). These data include amides for which the error in k_{ex} was less than 50% and do not include fast or slow exchangers. Data was input for 73 residues for tdTomato, 106 residues for mCherry, and 115 residues in mRojoB. The monomeric RFPs have more amide protons with smaller valued k_{ex}, and tdTomato has more amide protons with larger valued k_{ex}.

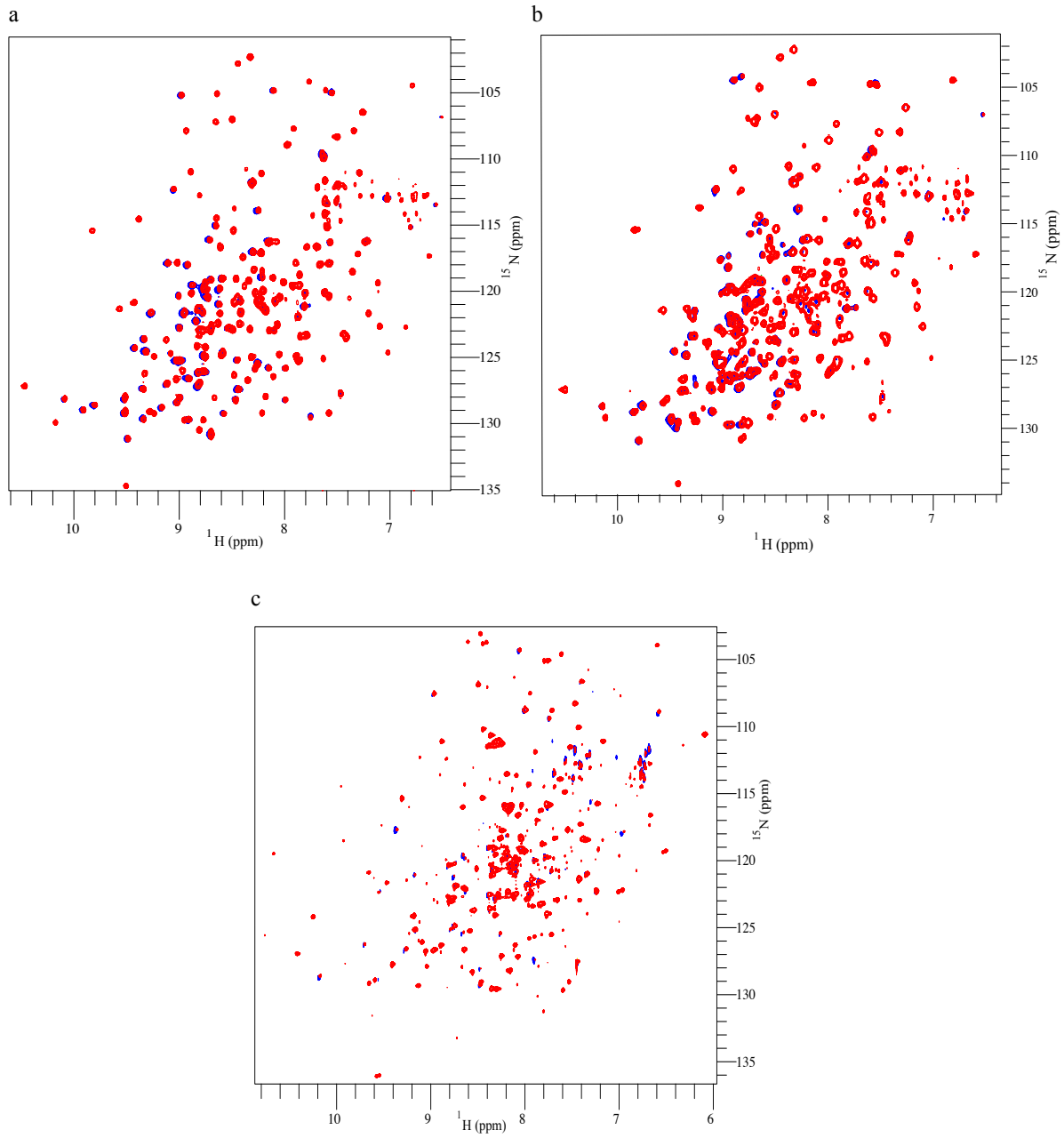

Figure 3.15: ^{1}H-^{15}N HSQC TROSY overlay before exchange and after ≈2 days of incubation at 37°C for mCherry (a), mRojoB (b), tdTomato (c). Most tdTomato residues have exchanged after 2 days of incubation, but notably, several amino groups from asparagine and glutamine side chains are not exchanged after 2 days (c).

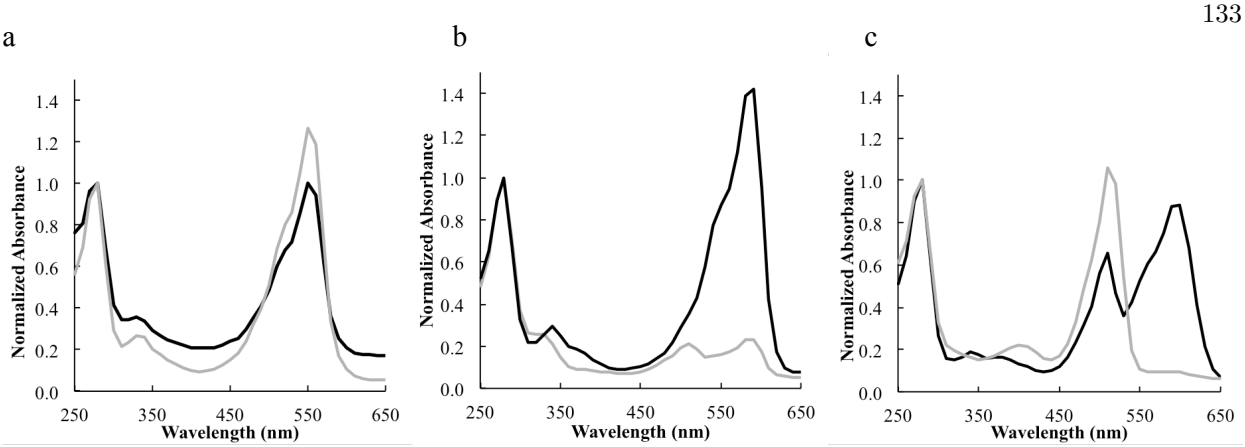

Figure 3.16: The absorption spectra of tdTomato (a), mCherry (b), and mRojoB (c) before exchange (black) and after (grey) incubation in D_2O at 37°C for 10 weeks. The absorption spectrum for mCherry was collected after thirteen weeks at 37°C, whereas the other 2 were collected after 10 weeks of incubation.

absorb at 550 and 587 nm, respectively. The mature chromophore of mRojoB absorbs at 600 nm, and an immature green form of the chromophore absorbs at 500 nm [25] (Figure 3.16). Due to the change in the ratio of the peak intensity for the mature and immature chromophores of mCherry and mRojoB, the spectra were not normalized to the absorption peak from the mature chromophores but rather the peak at 280 nm. The concentration, and thus absorption at 280 nm, of oxidized DTT increased during the 10-week experiment, thereby precluding comparison of individual peak intensities before and after incubation. The absorption spectrum for tdTomato remains largely unchanged after incubation at 37°C, but those for mCherry and mRojoB change after incubation (Figure 3.16). The ratio of the absorption from the mature (587 and 600 nm) and immature chromophores (500 nm) in the samples of mCherry and mRojoB decreased by 75% and 93% after 13 and 10 weeks respectively (Figure 3.16).

2-Day Incubation

Changes to the chromophores of tdTomato, mCherry and mRojoB during the first 2 days of incubation in deuterated buffer at 37°C were assessed using absorption spectroscopy. NMR data from the first 2 days of following buffer exchange were used to determine the exchange rate constants, thus it was important that the proteins were stable during that time. Changes were noted in the absorption spectra from before and after 10 weeks of incubation in deuterated buffer at 37°C (Figure 3.16). To determine whether these changes were pronounced after only 2 days of incubation in deuterated buffer at 37°C, a second set of absorption

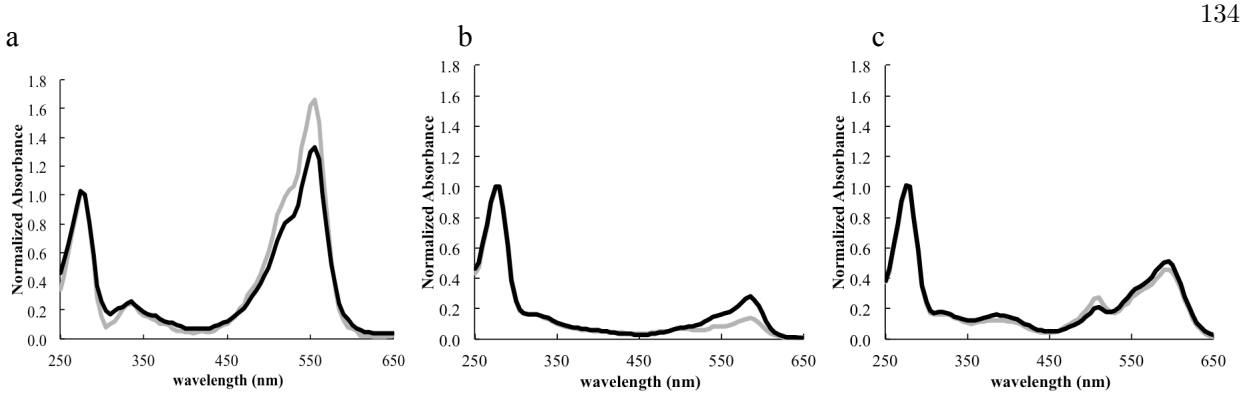

Figure 3.17: The absorption spectra of tdTomato (a), mCherry (b), and mRojoB (c) approximately 5 minutes after exchange into deuterated buffer (black) and after (grey) incubation in deuterated buffer at 37°CC for 2 days. The plots are normalized so that the absorption at 280 nm is 1 for each spectrum. Due to covalent modification of the chromophores of mCherry and mRojoB during the course of the experiment, the spectra were not normalized to the absorption peak from the chromophores, however, the concentration of oxidized DTT, and thus absorption at 280 nm, increased during the 2 day experiment.

spectra were collected on RFPs incubated in deuterated buffer at 37°C for only 2 days. As in the 10-week experiment described previously, due to change peak intensity ratios, the spectra were not normalized to the absorption peak from the mature chromophores but rather the peak at 280 nm. The increased concentration of oxidized DTT, and thus absorption at 280 nm [227], precludes comparison of individual peak intensities before and after incubation. After 2 days of incubation, the ratio of the absorption from the mature (587 and 600 nm) and immature (500 nm) chromophores in the samples of mCherry and mRojoB decreased by 50 and 30%, respectively (Figure 3.17). No such change occurred in the absorption spectra of tdTomato (Figure 3.17).

3.3.4 Fluorescence Quenching with Acrylamide Results

One of the roles of the FP protein matrix is to shield the chromophore from fluorescence quenchers in the solvent. Fluorescent quenchers, if capable of penetrating the β-barrel, could promote non-radiative relaxation of the excited state chromophore, thus decreasing fluorescence quantum yield. To test for exposure of the interior of the RFPs to solvent, acrylamide-induced fluorescence quenching experiments were performed [43,219]. Results of a previous study suggested that while the chromophore of the wild-type tetramer, DsRed, was the most protected from quenching by acrylamide, that dimer2 was more susceptible to quenching than

the monomer, mRFP1. Whether the dimer interface in tdTomato plays a role in solvent occlusion was tested by measuring fluorescence quenching of the dimer, tdTomato, and of the monomers, mCherry, mRaspberry and mRojoB. No chromophore fluorescence quenching was detected at acrylamide concentrations up to 2.5 M. To quantify quenching, Stern-Volmer constants, which compare fluorescence in the presence and absence of quencher, were determined. The Stern-Volmer constants (K_{sv}) for tryptophan fluorescence quenching are presented in Table 3.3 and Figure 3.18. Table 3.3 plots the ratio of fluorescence in the absence and presence of increasing concentrations of quencher, acrylamide. A positive correlation indicates fluorescence quenching is occurring, with the slope (the Stern-Volmer constant) indicating the efficiency of quenching.

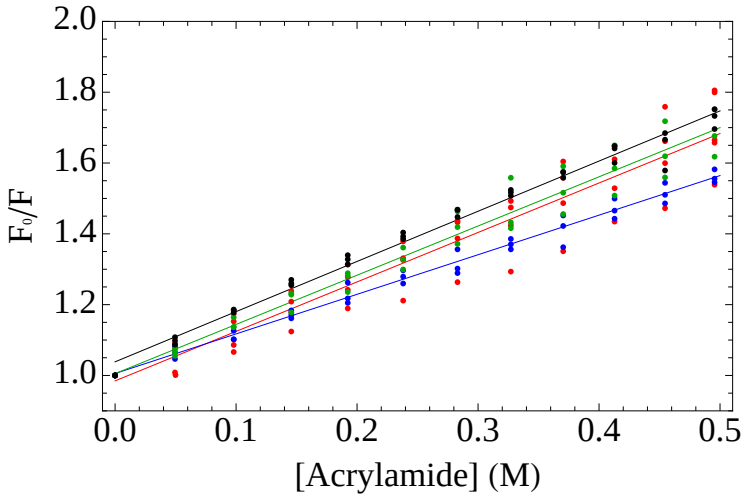

Figure 3.18: Stern-Volmer plots for the acrylamide-induced quenching of tryptophan fluorescence in td-Tomato (black), mCherry (red), mRojoB (blue), and mRaspberry (green).

Table 3.3: The Stern-Volmer constants for acrylamide quenching of the tryptophans in tdTomato, mCherry, mRaspberry and mRojoB.

protein	Tryptophan K_{sv}
mCherry	1.39±.06
mRojoB	1.12±.02
mRaspberry	1.41±.03
tdTomato	1.39±.03

3.4 Discussion

Relative to shorter wavelength FPs, RFPs are advantageous tools for studying multicellular organisms due to decreased scattering and autofluorescence when exciting with and detecting longer wavelengths, however, low quantum yields in currently available monomeric RFPs make them sub-optimal tools for studying low-copy proteins within cells. Currently available monomeric FPs used for tracking low-copy proteins within cells have higher quantum yields than most available monomeric RFPs. For example a YFP variant, Venus, which has a quantum yield of 0.63 [114] , has been used to monitor single copy expression of a membrane protein [228]. Many currently available and commonly used monomeric RFPs, such as mCherry, have quantum yields of less than 0.25. The cause of decreased quantum yields in monomeric relative to oligomeric RFPs is not fully understood. An improved understanding of the cause of the decrease in quantum yield is vital for the development of mRFPs that can be used to study low-copy proteins. Here several possible explanations for the decrease in quantum yield in monomeric RFPs compared to a dimeric variant were explored: solvent accessibility of the chromophore and the presence of interconverting populations. Solvent accessibility could allow fluorescence quenchers to promote non-radiative relaxation of the chromophore, and interconverting populations may signify the presence of a locally unfolded state with a lower quantum yield. Differences in solvent accessibility were studied using HDX, absorption spectroscopy, and fluorescence quenching experiments. Whether multiple interconverting populations exist was tested using NMR relaxation dispersion and HDX experiments.

3.4.1 NMR Relaxation Dispersion Results Indicate Local Differences in Conformational Exchange

More Experiments Necessary to Determine Whether Apparent Increase in Dynamics of Several Backbone Amides in mRojoB Explains Decreased Quantum Yield

Differences in conformational exchange might help explain the differences in quantum yields of mCherry, mRaspberry and mRojoB. Although μs-ms timescale dynamics are not fast enough to provide non-radiative relaxation pathways for the excited state chromophore, the detection of dynamics may be indicative of the

presence of dark state populations in solution. It is possible that the decreased quantum yields of mRaspberry and mRojoB relative to mCherry are due to increased populations in locally unfolded states that unfavorably alter the environment of the chromophore. This hypothesis would be supported by the absence of exchange in mCherry indicating a single population exists in solution. Functionally relevant protein side chain rotamerization [229], sub-global rearrangements [154], and loop flexibility [230] have been detected on the μs-ms timescale using NMR relaxation dispersion experiments. NMR relaxation dispersion experiments can detect conformational exchange if 1) the exchange is occurring on the μs-ms timescale, 2) there is a detectable (i.e. larger than the peak linewidth) chemical shift difference between the interconverting species, and 3) a significant population exists in each state (>0.5%) [155].

The results of NMR relaxation dispersion experiments performed on the backbone amides of mCherry, mRaspberry and mRojoB, revealed that conformational exchange was detected in similar %s of the backbone amides in mCherry, mRaspberry and mRojoB but in different residues. Dynamics were detected in threonine 41 in mRojoB that were not detected in the same assigned residue in the other 2 RFPs (Figure 3.19). (Again, it is important to note that lack of detection does not preclude the existence of dynamics, and therefore that exchange at residue 41 may also be occurring in mCherry and mRaspberry.) Additional differences may exist, however, since some of the residues displaying μs-ms dynamics in mCherry, mRaspberry and mRojoB were unassigned, and thus, not all of the locations of the residues displaying differences in dynamics are known. While residue 41 is distal (11 Å) from the chromophore, dynamics may perturb the environment of the chromophore through a transfer of kinetic energy between neighboring atoms, eventually reaching the chromophore and promoting a conformation with a low quantum yield.

Perhaps the different residues in which dynamics were detected in mRojoB are indicative of a different mechanism for exchange relative to mCherry or mRaspberry. The detected dynamics may be indicative of global conformation exchange which would likely effect the environment of the chromophore and thus the quantum yield. However, data at additional magnetic field strengths would need to be collected to confidently determine whether the relaxation dispersion profiles are better fit to residue-specific exchange or to a global exchange model. Previous studies have predicted global exchange based on detection of dispersion in <1% of the residues [231], supporting the idea that global exchange may be occurring in the monomeric RFPs

despite the small (≤ 5) % of residues in which exchange was detected.

The preliminary data presented here suggest a difference in dynamics among the three monomeric RFPs that may contribute to differences in quantum yields and that additional data should be collected in order to pursue RFPs with improved quantum yields. Dynamic residues in mRojoB could be targeted for mutation in attempt to stabilize one of the conformations. Because of the putative increased dynamics in residue 41 of mRojoB, this residue is a promising location to perform cite directed mutagenesis when developing new RFPs. If a mutant with increased the quantum yield were isolated, relaxation dispersion experiments performed at multiple fields could be used to determine whether one population were stabilized in this mutant relative to mRojoB. This strategy of targeting dynamic residues for mutation was used to develop a brighter CFP when a dynamic isoleucine residue on strand 7 of the β-barrel, which was thought to cause collisional quenching of the chromophore in one of its conformations, was mutated and resulted in a variant with improved the quantum yield [71]. Other CPMG relaxation dispersion studies probing the dynamics of protein mutants relative to their wild-type counterparts have shown functionally deleterious mutations to affect dynamics thereby further demonstrating the utility of this experimental technique for studying functionally disruptive protein mutations [231].

Differences in Dynamics of δ, δ, and γ ILV Methyl Groups on β-strands 8 and 10 may Provide Clues as to the Difference in Quantum Yields

Conformational exchange on the μs-ms timescale was detected in a larger % of ILV methyls in mRojoB (26%) than in mCherry (22%). If these dynamics were occurring according to a residue-specific rather than due to global exchange mechanism the larger % of methyl groups exchanging in mRojoB would more likely cause a disturbance in the environment of the chromophore and thus decrease the quantum yield. Due to lack of assignments, the locations of the dynamic methyls relative to the chromophore are unknown making it difficult to speculate as to whether dynamics are affecting the quantum yield. However, due to the excellent overlay of the peaks in the ^{1}H-^{13}C HMQC spectra of ^{1}H, ^{13}C methyl ILV labeled mRojoB and mCherry (Figure 3.22), comparison of resonances indicates different methyl groups display dynamics in each protein. In addition, once the assignments were made for either protein, many of them would be transferrable. Having assignments for these methyl groups could be very helpful in understanding which

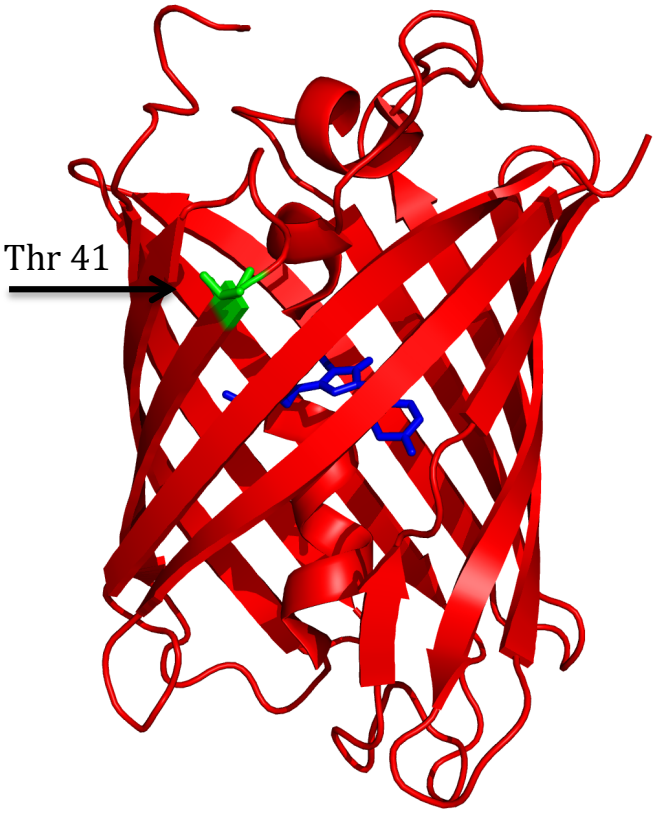

Figure 3.19: The crystal structure of mCherry used to depict, in green, backbone amide assigned in mCherry, mRaspberry, and mRojoB but in which μs-ms dynamics were only detected in the backbone amide of mRojoB. The chromophore is colored blue. Dynamics were detected using NMR relaxation dispersion experiments performed at 37°C.

parts of the protein were perturbed the most during the development of mRojoB from mCherry. Also, several ILV residues in mCherry, and mRojoB are located on strands 8 and 10 (Figures 3.20 and 3.21). Dynamics in a neighboring region, β-strand 7, of several FP variants have been proposed previously [66, 69]. In particular, a dynamic residue in strand 7 of structurally homologous CFP was targeted for mutation when developing a CFP with higher quantum yield [66]. Therefore, differences in dynamics in this region in mCherry and mRojoB may be affecting the relative quantum yields, and the assignment of the ILV methyl groups should be pursued. Again, even with assignments and therefore more structural information about the conformations between which the proteins are converting only speculations could be made as to whether dynamics are affecting the quantum yield. As proposed for the backbone amides, mutagenesis and additional relaxation dispersion experiments could be performed to further explore this issue.

3.4.2 Hydrogen-Deuterium Exchange Results Indicate tdTomato is More Prone to Local Unfolding than Monomeric RFPs

The development of RFP variants from wild-type tetramer, DsRed, generated monomeric red-shifted FPs at the expense of quantum yield. Whether protein dynamics were affected by this directed development process was further explored using hydrogen-deuterium exchange experiments, in particular, the effect the disruption of the dimer interface had on protein dynamics. NMR HDX experiments can be used to study protein local and global unfolding [43, 164–168] and solvent occlusion [169–173] to assess weather differences in local unfolding and solvent accessibility between RFP variants were contributing to differences in quantum yields. Protection of the chromophores from fluorescence quenchers in the solvent is an important role of the protein matrix surrounding the chromophore of FPs and may be affected by local unfolding events. The high quantum yield of tdTomato relative to monomeric RFPs was expected to be the product of a highly rigid protein, therefore it was also expected that tdTomato would have slow exchangers due to solvent occlusion by the dimer interface.

Local and global unfolding motions occur on a much slower timescale than that of fluorescence. The fastest measurable exchange rate constants of these are on the order of 10^{-4} s^{-1}, which is exceedingly slow compared to the timescale of fluorescence (10^{9} s^{-1}). Therefore local unfolding motions leading to HD

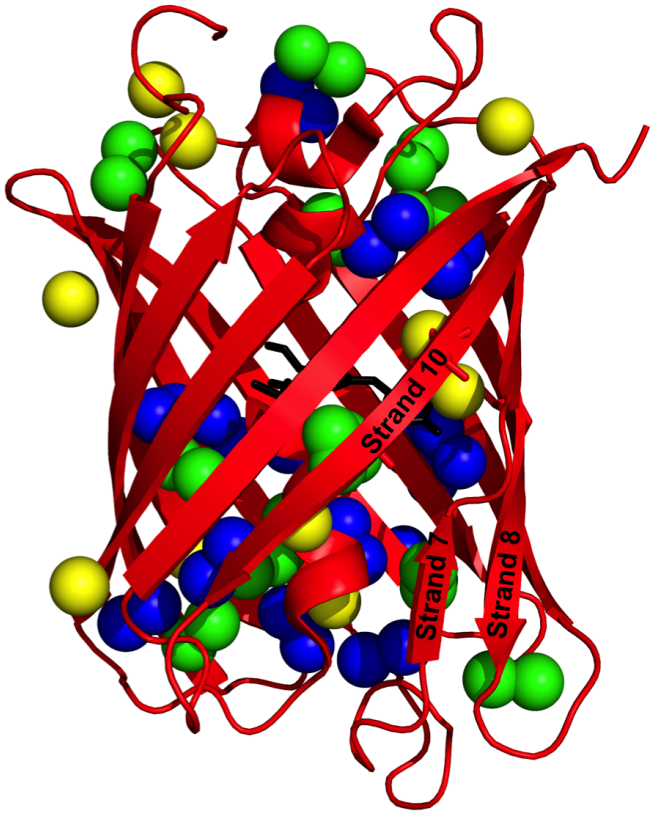

Figure 3.20: The δ isoleucine (yellow), δ leucine (green), and γ valine (blue) methyl groups are represented as balls on the crystal structure of mCherry. The chromophore is in black.

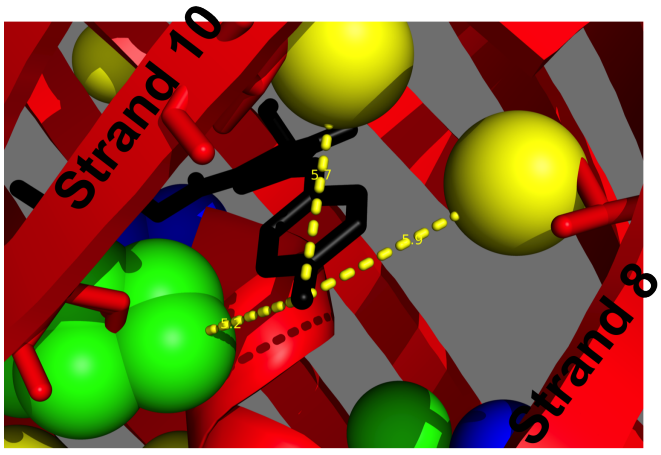

Figure 3.21: The δ methyl groups of isoleucine 161 and 197, and leucine 199 are near the chromophore (black) of mCherry. The δ isoleucine (yellow), δ leucine (green), and γ valine (blue) methyl groups are represented as balls on the crystal structure of mCherry. Several residues in strand 7 have been hidden to better see the chromophore. The yellow dashed lines are measurements from 2 δ isoleucine methyl group carbons (5.7 and 5.9 Å) and one leucine δ methyl group carbon (5.2 Å) to the chromophore tyrosine phenyl oxygen.

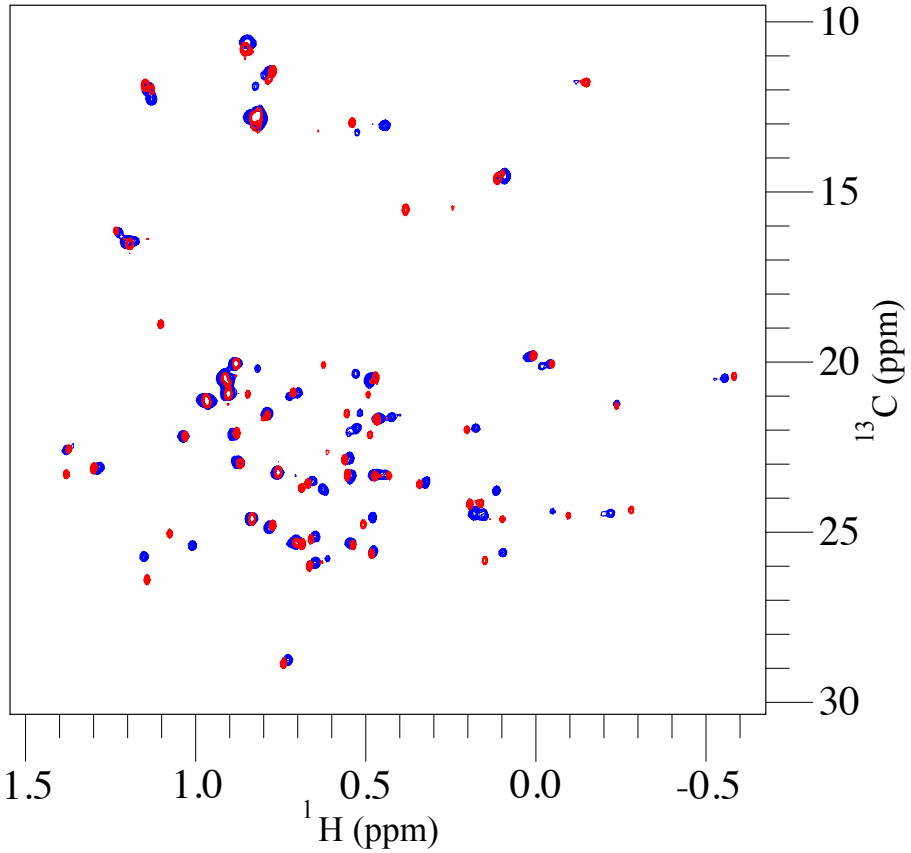

Figure 3.22: The overlay of ^{1}H-^{13}C ILV methyl-labeled mCherry (red) and mRojoB (blue) ^{1}H-^{13}C HMQC Spectra at 37°C.

exchange do not provide non-radiative relaxation pathways for an excited state chromophore. Yet differences in local unfolding as detected by HDX could provide clues about the relative quantum yields by indicating the relative populations of molecules in an unfolded (whether local or global) and therefore potentially non-fluorescent state. Previous studies on the locally unfolded states (unfolding intermediates) of GFP have found them to have decreased fluorescence quantum yield or to be non-fluorescent [71, 158, 165].

Proteins Remained Stable During Experiment

It was important that the protein remain stable during the course of the HDX experiment to measure accurate HD exchange rate constants. Upon inspection of the ^{1}H-^{15}N HSQC TROSY spectra collected during the course of the first 2 days of the experiment, the samples were deemed stable (Figure 3.15). Comparison of absorption spectra collected during the experiment was also used to assess the stability of the protein sample. The decrease in the ratio of absorbance from the mature chromophore to that at 280 nm for mCherry and mRojoB upon incubation at 37°C in D_2O was concerning at first, but was later rationalized as follows (Figures 3.16 and 3.17). The increase in concentration of oxidized DTT during the course of the experiment lead to an increase in the absorption at 280 nm and thus the decreased ratio of absorbance of the mature chromophore to that at 280 nm. The absorption at 280 nm of protein samples incubating in buffer containing 5 mM DTT at 37° for 2 days and diluted 100X into the same buffer, (which had been stored at 4°), also increased by 50% on average (data not shown) suggesting that the change in absorption at 280 nm can be attributed to the change in absorption from DTT. The increase in absorption from DTT is reasonable considering the concentration of and the relative extinction coefficients for oxidized (270 M^{-1} cm^{-1}, [227]) and reduced (110 M^{-1} cm^{-1}, [232]) DTT at 280 nm. However, the change in ratio of absorption at 500 to 600 nm, from the immature and mature chromophores respectively, suggest that even while the tertiary structure of the proteins are stable (as indicated by the stable NMR spectra), covalent modification of the chromophores of mCherry and mRojoB can still occur. In addition, the absorption spectra results show that the chromophore of tdTomato is more resistant to modification under the given conditions which suggests a different mechanism for modification.

Differences in HDX Suggest tdTomato most Prone to Local Unfolding

Exchange rate constants for the amide protons of tdTomato, mCherry and mRojoB ranged from too

fast to measure accurately with the experimental setup ($< 10^{-4}$ s^{-1}) to quite slow (10^{-8} s^{-1}, i.e. a half time for exchange of > 10 weeks). The protection factors measured were within the range of previously reported values for other proteins (Table C.4). However, the smallest measured protection factor was several orders of magnitude larger than the smallest reported protection factors which were measured for proteins in a molten globule state, indicating that the three RFPs studied here were well-folded proteins. The most striking result obtained from the NMR HDX experiments was the difference in %s of fast and slow exchangers. In contrast to the 2 monomeric RFPs, tdTomato has the largest % (61) fast exchangers and the smallest % (0) slow exchangers. This large % fast and lack of slow exchangers was also noted when the experiment was performed on a sample of tdTomato expressed in H_2O rather than D_2O, thereby negating the possibility that slow exchangers were missing from the data due to slow back-exchange from deuterons to protons prior to data collection. In addition, the large % fast exchangers in tdTomato cannot be accounted for by the presence of the linker between subunits, which only contains 12 residues. Although unassigned, presumably, these residues were fast exchangers as they are likely to be solvent exposed and not involved in hydrogen bonds. However the 12 residues account for fewer than 5% of the unique resonances detected in the NMR spectra and therefore cannot account for the 2-3 times larger % fast exchangers found in tdTomato relative to the monomers. These results suggest that tdTomato is more prone to local unfolding events than are the 2 monomeric RFPs. In addition, the presence of slowly exchanging peaks in the monomeric RFPs suggests that the unfolding pathway for the monomeric RFPs involves a stable intermediate that provides protection for some amide protons from contact with the solvent.

Small Fraction Locally Unfolded Does not Preclude a High Fluorescence Quantum Yield in tdTomato

The fluorescence quantum yield of tdTomato remains high, despite the fact that is more prone to local unfolding than the two monomers studied. This suggests either the locally unfolded states are still protecting the chromophore from solvent and holding it in a rigid state or that the fraction unfolded is small. Although tdTomato has the largest % fast exchangers, only a small population is in an unfolded state under the experimental conditions. The logic is as follows. Most proteins have been found to undergo hydrogen deuterium exchange primarily under the EX2 limit [166], including GFP [165]. (Refer to Chapter 1 for an introduction to HDX and the EX1 and EX2 exchange limits.) In the EX2 limit, the observed exchange

rate constant, k_{obs}, is equal to $K_{op} \times k_{int}$ where K_{op} is the equilibrium constant for the first half of the following reaction: RFP-$H_{closed} \Longleftrightarrow$ RFP-$H_{open} \Longrightarrow$ RFP-D_{open} with k_{op} and k_{cl} being the forward and reverse rate constants for the first reaction and k_{int} the exchange rate constant for the second. (No reverse arrow is displayed for the second half of the reaction due to the small concentration of protons relative to deuterons.) k_{int} is the intrinsic exchange rate constant for a proton in an unfolded peptide chain. RFP_{open} is an unfolded (be it locally or globally) form of the protein in which the amide proton of interest is exposed to, and able to exchange with, the solvent. In the EX2 limit of exchange, the protection factors are equal to the inverse of K_{op}. This is reflective of the requirement that conformational exchange to a locally unfolded state "de-protects" an amide hydrogen, thus allowing it to exchange with deuterons in the bulk solvent. In tdTomato, the smallest measured protection factor was $10^{3.89}$, leading to an equilibrium constant for the exposure of that proton to solvent of $\approx 1 \times 10^{-4}$ assuming the protein is exchanging under the EX2 limit and structural unfolding model for HDX [218]. This K_{op} is consistent with only a small population of locally unfolded protein at any given time. Even if this unfolded state were non-fluorescent, such a small fraction of the population would be non-fluorescent that it would only trivially affect the quantum yield of the overall population of molecules.

Rates of Exchange Affected by Solvent Accessibility and Hydrogen Bonding

Protection factors determined for mCherry and mRojoB ranged from $10^{3.7}$ to $10^{8.2}$, and many of the amide protons with smaller protection factors were in the loops and ends of the β-strands. The locations of the less protected amide protons in mCherry and mRojoB are mapped on the crystal structure of mCherry in Figures 3.23 and 3.24. Using Pymol [233], the possible carbonyl oxygen-amide proton hydrogen bonds within the crystal structure of mCherry were identified, thus enabling a more in depth analysis of the HDX data. Pymol emulates the criteria defined in the program DSSP, which include distance and angle constraints, to identify hydrogen bonds [234]. Figures 3.25 and 3.26 map the network of hydrogen bonds within the β-barrel as well as the protection factors for the residues of mCherry and mRojoB, respectively. Most residues with protection factors of less than 10^6 are either not involved in hydrogen bonds and/or are located at in loops or in regions of random coil. These amide hydrogens would be expected to exchange rapidly. The lower protection factors of these amide protons may be attributed to increased solvent exposure, lack of hydrogen

bonding, and/or increased dynamics in these regions. However, several of the least protected amide hydrogens in mCherry are involved in hydrogen bonds according to the crystal structure; for example residues 32, 50, 102, 126, 127, 156, 157, 170 and 177. Most of these residues are at the ends of β-strands, and so the hydrogen bonds in the crystal structure predicted by Pymol may not exist or be fluctuating (lacking hydrogen bonds and therefore more dynamic) in the solution structure, thus providing less protection. Residues 32 and 177 are in the middle of β-strands 2 and 9 respectively making it less likely that local unfolding events are allowing for exchange at residues 32 and 177 relative to the other residues mentioned. However, residues 32 and 177 have protection factors of $\geq 10^{5.7}$ and so are at the well-protected limit of residues highlighted here as "less-protected".

Analysis of the HDX data using the crystal structures and considering the hydrogen bonding patterns indicates the importance of both solvent exposure and hydrogen bonding in hydrogen exchange rates. Most amide hydrogens have protection factors of $> 10^6$ when the residue is involved in a hydrogen bond as predicted by Pymol. Yet residues located between strands 3 and 4 which comprise regions of random coil and the internal α-helix, many of which are not predicted to form hydrogen bonds, range from fast to slow exchangers (Figure 3.23). Table 3.4 lists the residues' solvent exposure, indicate the hydrogen bonding status and display relative protection factors. Of these amide protons, those buried in the interior of the protein are slow to exchange in the presence of a hydrogen bond (residues 60, 72 and 86). Intuitively, the residues lacking hydrogen bonds that are exposed to solvent are generally faster to exchange (residues 58 and 59). Residues 57, 84 and 85, however, are slow to exchange despite being solvent exposed, consistent with their amide hydrogen bonds providing protection from exchange. Buried residue 83 does not participate in a hydrogen bond and has a protection factor of $< 10^6$, indicating that either it gains little protection from lack of solvent exposure, that protein dynamics are transiently exposing it to the solvent, or that the solution structure differs from the crystal structure. These results suggest that hydrogen bonds offer more protection from exchange than lack of solvent exposure and therefore support the local unfolding model for HDX rather than the penetration model. However, buried residue 71 is slower to exchange despite lacking a hydrogen bond thus confirming the importance of both solvent exposure and hydrogen bonding in hydrogen exchange rates. Exposed residue 82 is hydrogen bonded but is still faster to exchange, thus demonstrating the presence

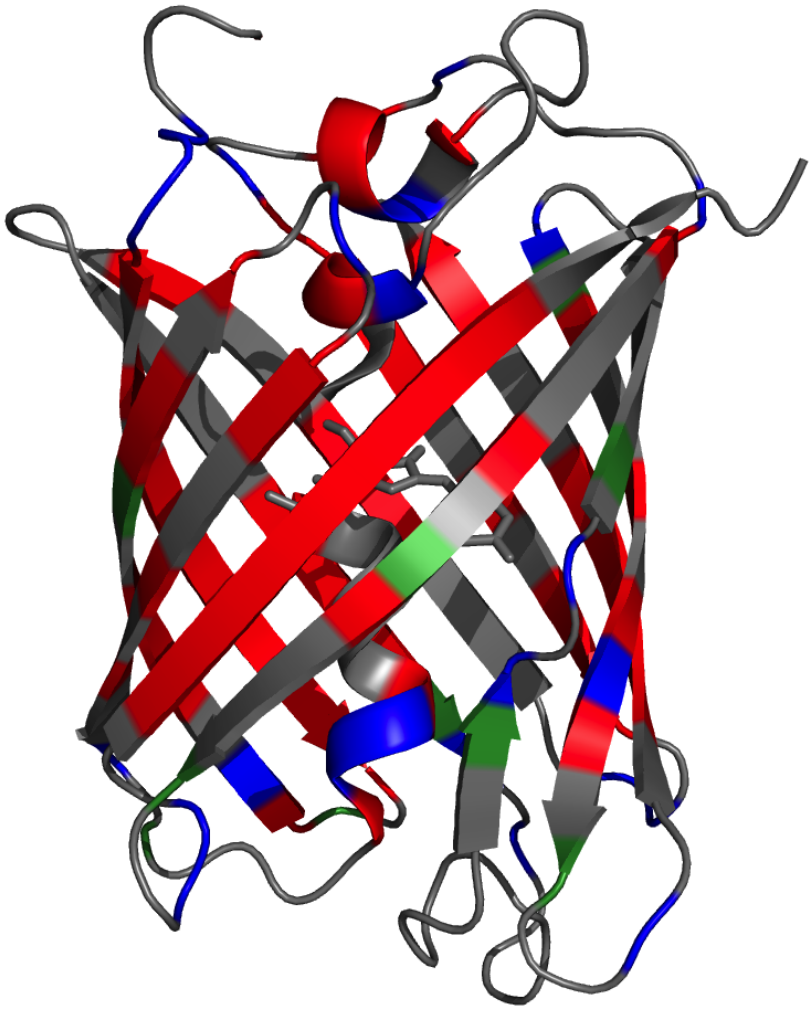

Figure 3.23: The faster exchangers in mCherry are colored blue and green. Backbone amides with protection factors $\leq 10^5$ are colored blue. Backbone amides with $10^5 < PF < 10^6$ are colored green. Backbone amides with protection factors $\geq 10^6$ are colored red. Grey residues do not have a calculated protection factor, either due to lack of assignment or an exchange rate constant error >10%.

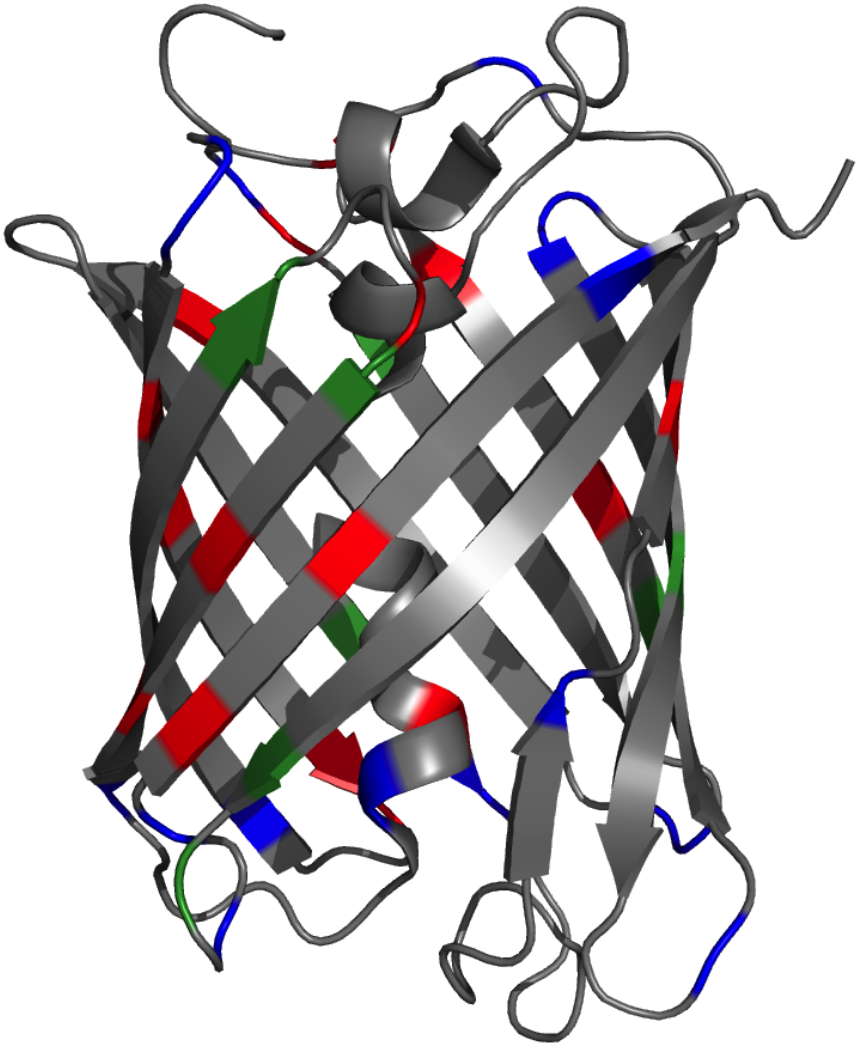

Figure 3.24: The faster exchangers in mRojoB are colored blue and green. Backbone amides with protection factors $\leq 10^5$ are colored blue. Backbone amides with $10^5 < PF < 10^6$ are colored green. Backbone amides with protection factors $\geq 10^6$ are colored red. Grey residues do not have a calculated protection factor, either due to lack of assignment or an exchange rate constant error >10%.

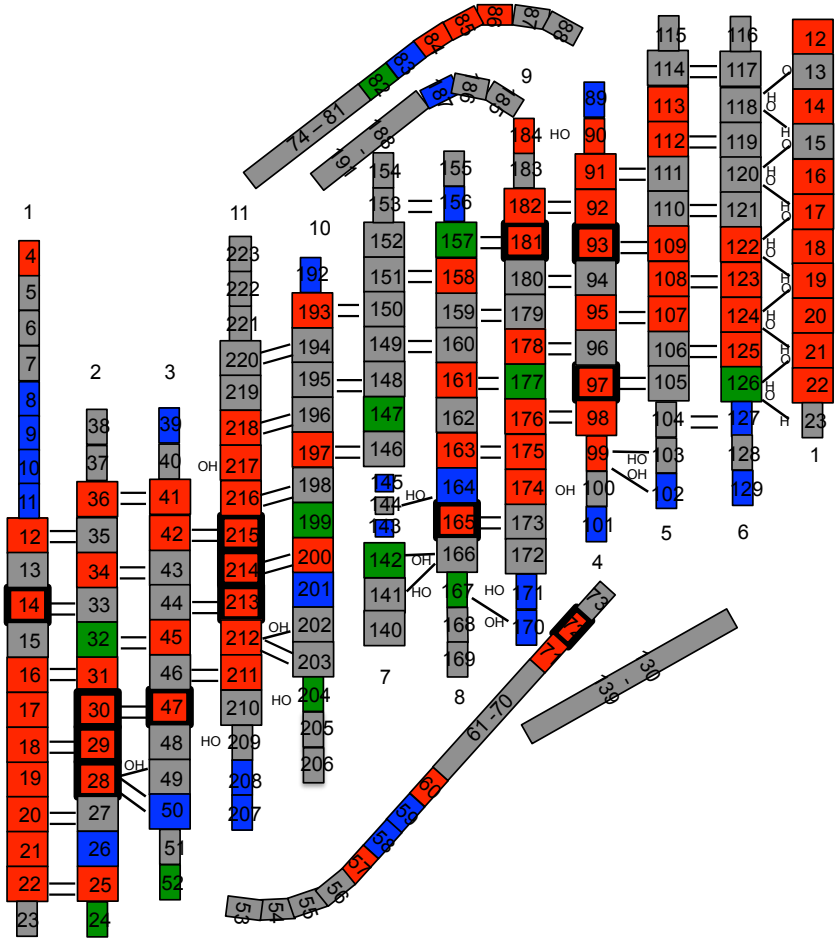

Figure 3.25: The protection factors and hydrogen bonds were mapped onto a topology diagram for mCherry. The faster exchangers in mCherry are colored blue and green. Backbone amides with protection factors $\leq 10^5$ are colored blue. Backbone amides with $10^5 < PF < 10^6$ are colored green. Backbone amides with protection factors $\geq 10^6$ are colored red. Grey residues do not have a calculated protection factor, either due to lack of assignment or an exchange rate constant error >10%. Two black lines indicate two hydrogen bonds between residues. One black line indicates one H-bond between residues and is accompanied by the letters H and O to denote which residue is contributing the amide proton or carbonyl oxygen, respectively, to the H-bond. Squares represent individual residues in the β-barrel, while rectangles represent residues in loops, α-helices, or random coils. Residues 143-145 are an exception as they are shown as small squares but are located in the bulge in strand 7. Bold black outlines indicate slow exchangers. The strand number is given either directly below or above each β-strand.

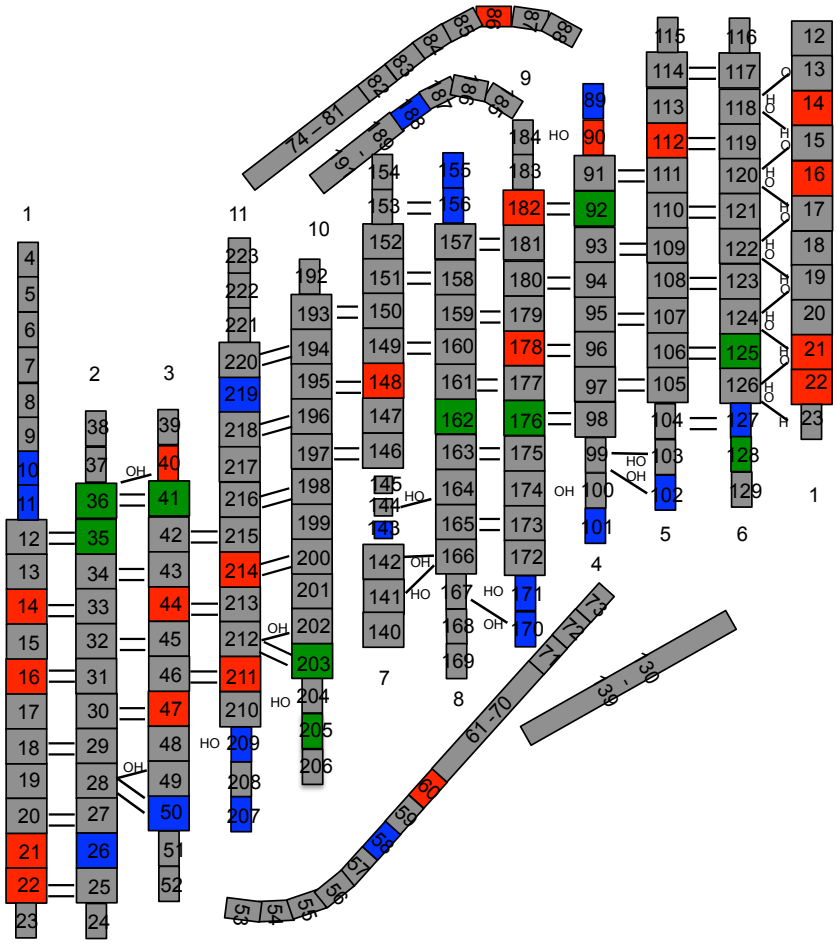

Figure 3.26: The protection factors and hydrogen bonds were mapped onto a topology diagram for mRojoB. The faster exchangers in mRojoB are colored blue and green. Backbone amides with protection factors $\leq 10^5$ are colored blue. Backbone amides with 10^5<PF<10^6 are colored green. Backbone amides with protection factors $\geq 10^6$ are colored red. Grey residues do not have a calculated protection factor, either due to lack of assignment or an exchange rate constant error >10%. Two black lines indicate two hydrogen bonds between residues. One black line indicates one H-bond between residues and is accompanied by the letters H and O to denote which residue is contributing the amide proton or carbonyl oxygen, respectively, to the H-bond. Squares represent individual residues in the β-barrel, while rectangles represent residues in loops, α-helices, or random coils. Residues 143-145 are an exception as they are shown as small squares but are located in the bulge in strand 7. The strand number is given either directly below or above each β-strand.

Table 3.4: HDX Dependence on Solvent Exposure and Hydrogen Bonding[a]

	H-bonded	No H-bond
Exposed	**82** **57,84,85**	**58,59**
Buried	**86** **60,72**	**83** **71**

[a]Hydrogen bonds were predicted by Pymol, as were their solvent accessibilities. Blue indicates a protection factor of $< 10^6$, and red a protection factor of $> 10^6$.

of local unfolding events necessary for the amide proton of residue 82 to exchange with deuteron from the solvent. However, since the solution structure may be slightly different than the crystal structure, additional insight into the importance of solvent exposure and hydrogen bonding for protection from exchange could be gained from solving the solution structure.

Similarities with GFP Suggest Fast Exchange in Strands 7-10 Does Not Preclude a High Quantum Yield

The results of the HDX experiments revealed some similarities between monomeric RFPs and a GFP variant. In each protein, smaller protection factors were found near the gap in the β-barrel between strands 7 and 10. This increase in the inter-strand distance between strands 7 and 10 of the β-barrel is seen in the crystal structures of mCherry, mRojoA and other FPs and likely accounts for the increased rates of exchange either due to increase solvent exposure, lack of hydrogen bonding, or increased dynamics. In mCherry, the amide hydrogens of residues 142, 143, 145, 147, 164, 167, 199, 201 and 204 are some of the least protected, with protection factors of less than 10^6, and are located in strands 7-10 thus supporting the idea that this is a region of increased dynamics in the β-barrel. Perhaps dynamics reposition the amide hydrogens such that they readily exchange with deuterons in the solvent. This putative region of increased dynamics in strands 7 and 10 may contribute to decreased quantum yields in monomeric RFPs by allowing conformational exchange to a conformation in which the chromophore is not held in a rigid and planar environment. Similar to the results of the HDX study on mCherry, a previous HDX study on a GFP variant also found that amide protons in β-strands 7 and 10 have lower protection factors compared to the rest of the β-barrel [163]. The HDX data were used to generate potential models for stable intermediates in the unfolding pathway for the GFP variant. The proposed intermediates were locally unfolded at strands 7-10, 7-9, or 7-8 [165]. The

unfolding of strands 7-10 would certainly disrupt the environment of the chromophore, as inward facing side chains from residues on strands 7-10 surround the chromophore. Therefore, one would expect this locally unfolded intermediate to have a different quantum yield from the fully folded state, an idea supported by previous studies of GFP denaturation [165]. Yet, the HDX data for the GFP variant, which has a high quantum yield of 0.8, also indicate elevated dynamics in strands 7-10, suggesting that increased flexibility near the gap between strands 7 and 10 do not preclude a high quantum yield. Thus, flexibility in the region of strands 7-10 may not be contributing to decreased quantum yields of the monomeric RFPs. Instead, since each of the less-protected residues near the gap between strands 7 and 10 is exposed to solvent as determined using the "show surface" feature of Pymol, the increased rates of exchange could be simply be due to solvent exposure and lack of hydrogen bonds rather than increased dynamics that would perturb the environment of the chromophore and decrease quantum yield.

Both the monomeric RFPs and the GFP variant were found to contain slow exchangers which retain at least 50% of their original peak volume after 10 weeks of exchange. Forty (17%) of the amide protons were found to be slow exchangers in an HDX study performed previously on the GFP variant [163, 165] whereas 16 (7%) and 12 (5%) amide protons were slow exchangers in mCherry and mRojoB respectively. The larger % of slow exchangers in GFP suggests that the energy barrier for global unfolding is higher in the GFP variant than it is in mCherry or mRojoB, and as a result, more protons in the GFP variant are highly protected from solvent. It could also indicate that the unfolded intermediate that provides protection for these slowest exchangers is structured differently for GFP and the RFPs studied here. These interpretations stem from the idea that the slowly exchanging amide protons are most likely exchanging during a global unfolding event [165]. The slowest exchanging residues in GFP were on one face of the β-barrel in strands 1, and 4-6 with four additional slow exchangers in strand 11 [165]. This is in contrast to the location of the slowest exchanger in mCherry, which reside mostly on strands 2, 4 and 11 3.25. This difference in location for the slowest exchangers suggests a difference in the structure of a locally unfolded intermediate. These locally unfolded intermediates may have relatively little bearing on the relative quantum yields since such a small fraction is locally unfolded at any given time. However, the difference may be reflective of different folding pathways.

mRojoB Undergoes More Local Unfolding than mCherry

The results of the HDX experiment indicate that the 2 monomeric red fluorescent proteins, mCherry and mRojoB, which differ by only 5 amino acids, undergo different degrees of local unfolding as well although the difference is modest. mRojoB has a larger % fast exchangers (35%) than mCherry (21%) and a smaller % slow exchangers (5% compared to 7%). Although the structure of mRojoB has not yet been solved, the crystal structures of mCherry and mRojoA (only 2 residues different from mRojoB), overlay with an RMSD of less than 0.3 Å. Thus, provided the difference in crystal and solution structures are small, a difference in structure should not account for this difference in HDX, but rather, increased local unfolding may contribute to the difference in % fast exchangers. However, as discussed in Chapter 2, the difference in NMR spectra suggest there may be difference in the solution structures of mRFPs, despite similar crystal structures. The determination of the solution structure of the RFPs studied here would help determine whether differences in exchange rates were due to differences in dynamics or differences in structure.

Residues involved in hydrogen bonding must undergo local unfolding events in order to exchange with the solvent, as the hydrogen bonds must break for exchange to occur. Of the residues analyzed in figures 3.25 and 3.26, mRojoB has a larger fraction of faster-to-exchange amides, (protection factors $< 10^6$), involved in hydrogen bonds (12/43 or 28% versus 13/104 or 13%) supporting the conclusion that mRojoB undergoes a larger degree of local unfolding relative to mCherry. This destabilization of the fully folded state relative to the local unfolded states occurred during the development of mRojoB from mCherry, perhaps due to the approach used to generate mRojoB which focused solely on increasing the wavelength of emission. The lack of selective pressure to maintain or improve thermostability may have lead to a decrease in this property.

Threonine 41 is of interest as differences in both HDX (Table C.4) and relaxation dispersion experiments were detected when comparing mRojoB and mCherry (Figure 3.19). Threonine 41 is less protected in mRojoB (PF = $10^{5.74}$) compared with mCherry (PF = $10^{6.37}$) (Table C.4). The relaxation dispersion experiment indicated the presence of μs-ms timescale dynamics at residue 41 in mRojoB but not in mCherry (although this may be due to factors other than lack of exchange, as noted previously) (Figure 3.19). Furthermore, the crystal structure of mRojoA (only 2 residues different from mRojoB) shows a slight deviation from that of mCherry near threonine 41. The crystal structure of mRojoA was solved as a tetramer [25].

In one of the 4 subunits of mRojoA, β-strand 2 terminates one residue earlier than in the other 3 subunits. The second β-strand in mCherry and 3 out of the 4 subunits of the tetrameric crystal structure of mRojoA have 12 residues and terminate with arginine 36 (Figure 3.27). However, in one subunit of the mRojoA crystal structure strand 2 only has 11 residues and terminates with histidine 35. This might indicate that the C-terminal end of strand 2 in mRojoA (and possibly in mRojoB as well) populates more than one conformation in solution. It is also interesting that threonine 41 was mutated in mOrange, which differs from mCherry by only 4 residues, but has more than a quantum yield 3 times larger than that of mCherry [23]. These results suggest a structural element or dynamics near threonine 41 influences quantum yield. The apparent increase in flexibility in mRojoB relative to mCherry at threonine 41 provides good incentive to target this amino acid for mutation given that mCherry has a higher quantum yield than mRojoB. Perhaps this region of the protein is important for fluorescence, and was perturbed with negative consequences when developing mRojoB from mCherry.

Globally Folded State Stabilized During Directed Development

The higher propensity for locally unfolded states in the dimer relative to the monomers was unexpected given that interfaces are known to stabilize the tertiary structure of proteins [170, 235–237] and that a stable interface may occlude solvent. The apparent decrease in local unfolding in the monomeric RFPs provides insight into the effect directed development had on RFP dynamics. The data suggest that directed development may have decreased the propensity for locally unfolded states in the monomers relative to the wild-type tetramer. This decrease in locally unfolded states in the monomers was unexpected as monomeric RFPs have lower quantum yields than the tetrameric and dimeric RFPs. However, as discussed previously, the population of locally unfolded states in tdTomato appears low, less than 1%, and therefore may not significantly alter the quantum yield in solution. However, during directed development of the first monomeric RFP, the population of locally or globally unfolded protein may have increased drastically therefore significantly reducing the quantum yield. In fact the first monomer, mRFP0.1, was only negligently fluorescent [22]. The directed development of monomeric RFPs first required the disruption of the AB interface of wild-type tetrameric DsRed to produce the dimeric RFP, dimer2. Post dimerization, approximately 90% of the wild-type quantum yield was rescued by 6 compensatory mutations. The subsequent disruption

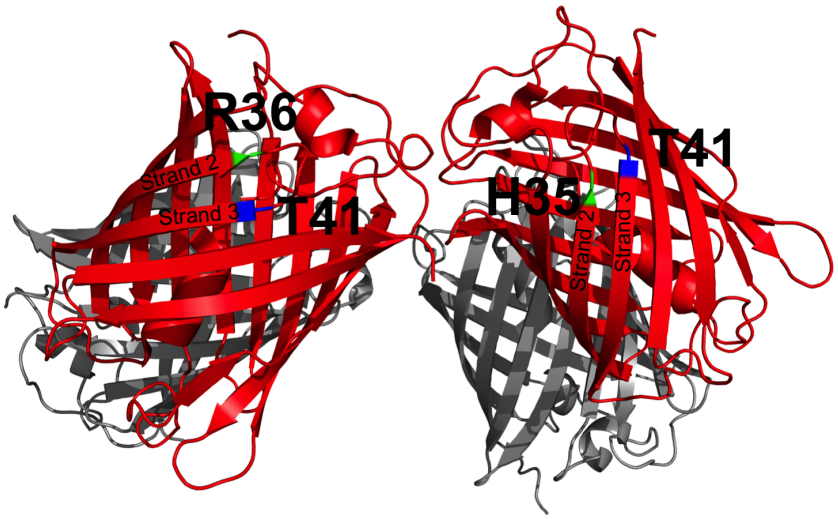

Figure 3.27: The crystal structure of mRojoA was solved as a tetramer [25], and in 3 out of the 4 subunits, strand 2 has 12 residues. However, in one of the subunits strand 2 terminates at histidine 35 (green) rather than arginine 36 (green). Threonine 41 (blue) is in the neighboring β-strand, strand 3. Differences in the crystal structure among subunits may be indicative of flexibility in this region in the protein.

of the residual AC interface in dimer2 required more mutations (11) than did the AB interface (3) and resulted in a weakly fluorescent monomeric RFP, mRFP0.1, for which a quantum yield was not reported. The nearly complete loss of fluorescence after disruption of the residual dimer interface indicates its importance for fluorescence quantum yield. Eight compensatory mutations were required to recover fluorescence of the monomer mRFP1, but only 36% of fluorescence quantum yield was recovered in mRFP1 relative to dimer2 and only 30% relative to wild-type DsRed [22]. mCherry was subsequently developed from mRFP1 and mRojoB from mCherry. While quantum yield increased during the development of mRFP1 from mRFP0.1, the data indicate another physical property may have been affected as well; the propensity for local unfolding.

During directed development the stability of the globally folded state relative to locally unfolded states of monomeric RFPs appears to have increased relative to the dimer tdTomato on the timescale of local unfolding. One might therefore predict that the first monomer, mRFP0.1, which had an almost negligible quantum yield, would have a larger % fast exchangers than tdTomato due to the loss of the AC interface. Such a result would support the idea that post disruption of both the AC and AB interfaces of DsRed, the RFP directed development process produced a more globally folded monomeric RFP. Although the degree of local unfolding detected in tdTomato seems not to significantly impact its quantum yield, the population of locally unfolded and thus non-fluorescent protein in original monomer may have been more significant. Therefore subsequently developed monomers with decreased local unfolded states may have been unintentionally selected for due to enhanced quantum yields relative to the original monomer. Thus, one explanation for the regain of fluorescence after monomerization is that a stabilization of the globally folded state of protein was achieved during the development of monomeric RFPs. The proposed stabilization that occurred during directed development of monomeric RFPs may have partially compensated for the loss of the AC interface which is known to be important for fluorescence quantum yield.

3.4.3 Fluorescence Quenching Results Do Not Indicate Dimer Interface Increased Protection from Acrylamide Relative to Monomers

While the exact role of the AC interface in upholding a high fluorescence quantum yield is unknown, proposed roles include providing interactions between subunits that rigidify the structure and/or increase

the global stability of the protein. The interface in tdTomato contains residues whose side chains form contacts with the chromophore, so the disruption of the interface may have affected chromophore packing and planarity. In tdTomato, potentially stabilizing interactions with the opposing subunit may rigidfy residues near the chromophore and decrease non-radiative relaxation pathways relative to monomeric RFPs. It has also been suggested that the dimer interface in dimer2, the non-covalently linked precursor to tdTomato, may play a role in shielding the interior of the protein from fluorescence quenchers [41]. The proposed shielding role of the interface was tested using acrylamide fluorescence quenching studies. Fluorescence quenching was monitored for the tryptophans and chromophore of tdTomato, mCherry, mRojoB and mRaspberry. Differences in susceptibility to acrylamide-induced quenching suggests differences in solvent accessibility, in particular near the chromophore. All 4 proteins contain the same chromophore and 3 tryptophans, 2 of which lie very near to the gap between strands 7 and 10 (Figure 3.3). Smaller quenching constants in tdTomato than in the monomers would indicate less contact with solvent, however, the results showed that the tryptophans of tdTomato are not more protected relative to those in the monomers (Figure 3.18 and Table 3.3). The chromophores of all 4 proteins are well protected as no measurable chromophore fluorescence quenching was observed. Previously, very low Stern-Volmer constants were also measured for the quenching of the chromophores of wild-type DsRed, dimer2 and mRFP1 [41], and GFP [91], consistent with the results of the experiment performed here on tdTomato, mCherry, mRaspberry and mRojoB. These results are consistent with the chromophores being well shielded from fluorescence quenchers in the solvent.

Despite the presence of an interface, the tryptophans of tdTomato have a similar propensity for quenching by acrylamide as those of monomeric RFPs. This suggests that the role of the interface is not to occlude solvent and fluorescence quenchers. It is also possible that despite partial shielding by the interface, tdTomato is undergoing a large degree of unfolding which could expose its tryptophans to solvent, an interpretation that is consistent with the results of the HDX study. If this were the case, this would further support the idea that the degree of local unfolding in tdTomato is not detrimental to its quantum yield. Rather, the high quantum yield in tdTomato may be due to a high degree of rigidity on the ps-ns timescale. The dimer interface may promote ps-ns timescale rigidity in tdTomato, however conformation of this using NMR relaxation experiments would be technically difficult due to the unfavorable relaxation

properties of high molecular weight molecules. Yet another possible explanation for the similar levels of tryptophan quenching in tdTomato and the monomers despite the presence of the putatively shielding dimer interface is that the fluorescence lifetimes of the tryptophans differ among the 4 RFFs. Susceptibility to quenching depends on the fluorescence lifetime of the species being probed [64], thus it is possible that despite solvent occlusion provided by the dimer interface, elevated fluorescence lifetimes lead to similar levels of quenching in tdTomato compared to the monomers. Thus the balance between solvent occlusion and increased fluorescence lifetimes could result in similar Stern-Volmer constants for tryptophan quenching in tdTomato and the monomeric RFPs. This is not an unreasonable hypothesis as the chromophore lifetime for tdTomato is larger (3.4 ns) than that of mCherry (1.5 ns) [238], although the relative lifetimes of the tryptophans haven't been measured. If this second interpretation of the data were correct, the idea that the the role of the dimer interface provides the chromophore protection from fluorescence quenchers in the solvent would still be plausible.

3.4.4 Concluding Thoughts on the Effect of Directed Development on the Dynamics of RFP Variants

The data presented in this work provide valuable insight into the effect RFP directed development had on protein dynamics over several different timescales. Figure 3.28 depicts the development of RFPs from the wild-type RFP and summarizes the differences in dynamics observed using NMR spectroscopy. These results demonstrate that directed development affected the dynamics of RFP variants. The NMR relaxation data showed restricted internal ps-ns dynamics for the backbone amides of monomeric RFPs on average, as well as for the chromophore tyrosine C $^{\beta}$, however, internal dynamics were detected for a larger % of the backbone amides in mRojoB (see Figures 2.16, 2.17, and 2.18). The data suggest that the decreased quantum yield in mRojoB may be attributable to increased ps-ns dynamics. However, perhaps more relevant than the average backbone amide order parameter are the residue-specific dynamics. Collisional quenching due to a single amino acid side chain has been cited as a cause for decreased quantum yield in a CFP variant [71], yet unfortunately, some backbone amides near the chromophore were not assigned in mRaspberry and mRojoB. Increased dynamics in these unassigned residues of mRaspberry and mRojoB relative to mCherry may be

accounting for their decreased quantum yields, and therefore, this study would benefit from traditional assignment of mRaspberry and mRojoB. Alternatively, ps-ns timescale dynamics in side chains closer to the chromophore may be perturbing the environment of the chromophore, and therefore, probing side chain dynamics may be more fruitful in addressing functionally relevant differences in dynamics. In addition, the definition of a "rigid" backbone amide (having an S^2 $\geq$0.8) may not be stringent enough when analyzing fluorescent proteins. Perhaps, the dynamics present in a backbone amide with an S^2 of 0.8 are enough to promote non-radiative relaxation.

In this work, the most dramatic difference in dynamics detected was increased local unfolded in tdTomato relative to the monomers suggested by the HDX data (Figure 3.14). This difference indicates global stabilization occurred post monomerization, potentially to aid in fluorescence recovery after the loss of the AC interface. However, the stabilized globally folded state may have locked the monomers in a conformation with a low quantum yield. A previous study demonstrating decreased planarity of the chromophores of the mFruits relative to the wild-type DsRed supports this model [31]. The determination of the solution structures of these RFPs would provide additional valuable insight into these different possibilities.

The conformational exchange occurring in tdTomato may demonstrate the importance of slow timescale flexibility for quantum yield in tdTomato. Assuming the same conformations (with differing fluorescent quantum yields) are present in solution for both tdTomato and the monomeric RFPs, the conformation with the higher quantum yield may be favored in tdTomato. This conformation may be one in which interactions between subunits rigidify the chromophore on the ps-ns timescale. The result of the lack of interface and the associated putative rigidifying interactions in the monomers may be a low quantum yield. Under this assumption, through directed development reforming a dimer interface may result in a globally stabilized and rigidified dimeric RFP with a high quantum yield (Figure 3.28). Overall, the results of the NMR relaxation, relaxation dispersion, HDX, and quenching experiments demonstrate that the directed development of RFPs affected protein dynamics, and that the complexity of the factors affecting the photophysics of FPs merit additional exploration.

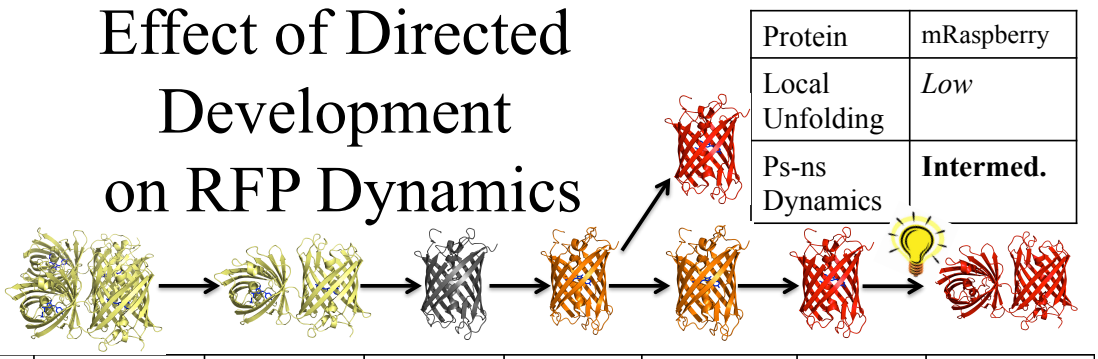

Protein	DsRed	tdTomato	mRFP0.1	mRFP1.0	mCherry	mRojoB	New Dimer
Local Unfolding	*Intermed.*	**Intermed.**	*High*	*Low*	**Low**	**Low**	*Intermed.*
ps-ns Dynamics	*Low*	*Low*	*High*	*Intermed.*	**Intermed.**	**High**	*Low*

Figure 3.28: The tandem dimer, tdTomato was developed from the wild-type tetrameric RFP, DsRed. Monomeric red-shifted RFPs were subsequently developed at the expense of quantum yield. The relative propensities for local unfolding and degree of ps-ns dynamics, influenced by the process of directed development, are depicted in the table where the measured values are in bold and the predicted values are in italics. Since no new RFP was developed from mRaspberry, it is shown in a separate branch. Although tdTomato and mRFP0.1 were developed from dimer2, dimer2 and tdTomato differ only by a 12 amino acid linker between subunits, and so tdTomato is shown in the progression of related RFPs. The ribbon diagrams are from the crystal structures of DsRed and mCherry, colored to indicate the wavelength of fluorescence. mRFP0.1 was non-fluorescent.

Bibliography

[1] H. Dubois, "Fonction photogénic des pyrophores," Compt. ren. soc. biol., vol. 37, pp. 559–562, 1885.

[2] O. Shimomura, F. Johnson, and Y. O. Saiga, "Extraction , Purification and Properties of Aequorin , a Bioluminescent Protein from the Luminous," Journal of Cell Comp Physiol, pp. 223–239, 1962.

[3] O. Shimomura and F. H. Johnson, "Peroxidized coelenterazine, the active group in the photoprotein aequorin.," Proceedings of the National Academy of Sciences of the United States of America, vol. 75, pp. 2611–5, June 1978.

[4] D. C. Prasher, V. K. Eckenrode, W. W. Ward, F. G. Prendergast, and M. J. Cormier, "Primary structure of the Aequorea victoria green-fluorescent protein," Gene, vol. 111, pp. 229–233, 1992.

[5] M. Chalfie, Y. Tu, G. Euskirchen, W. W. Ward, and D. Prasher, "Green fluorescent protein as a marker gene expression," Science, vol. 263, pp. 802–805, Oct. 1994.

[6] R. M. Wachter, J. L. Watkins, and H. Kim, "Mechanistic diversity of red fluorescence acquisition by GFP-like proteins.," Biochemistry, vol. 49, pp. 7417–27, Sept. 2010.

[7] S. F. Field, M. Y. Bulina, I. V. Kelmanson, J. P. Bielawski, and M. V. Matz, "Adaptive evolution of multicolored fluorescent proteins in reef-building corals.," Journal of molecular evolution, vol. 62, pp. 332–9, Mar. 2006.

[8] R. Heim, D. C. Prasher, and R. Y. Tsien, "Wavelength mutations and posttranslational autoxidation of green fluorescent protein.," Proceedings of the National Academy of Sciences of the United States of America, vol. 91, pp. 12501–4, Dec. 1994.

[9] M. Ormo, A. B. Cubitt, K. Kallio, L. A. Gross, R. Y. Tsien, and S. J. Remington, "Crystal structure of the Aequorea victoria green fluorescent protein.," Science (New York, N.Y.), vol. 273, pp. 1392–5, Sept. 1996.

[10] R. M. Wachter, B. a. King, R. Heim, K. Kallio, R. Y. Tsien, S. G. Boxer, and S. J. Remington, "Crystal structure and photodynamic behavior of the blue emission variant Y66H/Y145F of green fluorescent protein.," Biochemistry, vol. 36, pp. 9759–65, Aug. 1997.

[11] R. Y. Tsien, "The green fluorescent protein.," Annual review of biochemistry, vol. 67, pp. 509–44, Jan. 1998.

[12] N. C. Shaner, M. Z. Lin, M. R. Mckeown, P. A. Steinbach, K. L. Hazelwood, M. W. Davidson, and R. Y. Tsien, "Improving the photostability of bright monomeric orange and red fluorescent proteins," Nature Methods, vol. 5, no. 6, pp. 545–551, 2008.

[13] D. Yarbrough, R. M. Wachter, K. Kallio, M. V. Matz, and S. J. Remington, "Refined crystal structure of DsRed, a red fluorescent protein from coral, at 2.0-A resolution.," Proc. Natl. Acad. Sci. U.S.A, vol. 98, pp. 462–7, Jan. 2001.

[14] G.-J. Kremers, S. G. Gilbert, P. J. Cranfill, M. W. Davidson, and D. W. Piston, "Fluorescent proteins at a glance," Journal of Cell Science, vol. 124, pp. 2676–2676, July 2011.

[15] M. Iwasaka, J. Miyakoshi, and S. Ueno, "Optical absorbance of hemoglobin and red blood cell suspensions under magnetic fields," IEEE Transactions on Magnetics, vol. 37, pp. 2906–2908, July 2001.

[16] M. Z. Lin, M. R. McKeown, H.-L. Ng, T. a. Aguilera, N. C. Shaner, R. E. Campbell, S. R. Adams, L. a. Gross, W. Ma, T. Alber, and R. Y. Tsien, "Autofluorescent proteins with excitation in the optical window for intravital imaging in mammals.," Chemistry & biology, vol. 16, pp. 1169–79, Nov. 2009.

[17] K. V. Rajapopalan and P. Handler, "The Absorption Spectra of Iron-Flavoproteins," The Journal of Biological Chemistry, vol. 239, no. 5, 1964.

[18] G. N. Stamatas, M. Southall, and N. Kollias, "In vivo monitoring of cutaneous edema using spectral imaging in the visible and near infrared.," The Journal of investigative dermatology, vol. 126, pp. 1753–60, Aug. 2006.

[19] B. J. Tromberg, N. Shah, R. Lanning, a. Cerussi, J. Espinoza, T. Pham, L. Svaasand, and J. Butler, "Non-invasive in vivo characterization of breast tumors using photon migration spectroscopy.," Neoplasia (New York, N.Y.), vol. 2, no. 1-2, pp. 26–40, 2000.

[20] M. V. Matz, a. F. Fradkov, Y. a. Labas, a. P. Savitsky, a. G. Zaraisky, M. L. Markelov, and S. a. Lukyanov, "Fluorescent proteins from nonbioluminescent Anthozoa species.," Nature biotechnology, vol. 17, pp. 969–73, Oct. 1999.

[21] E. M. Merzlyak, J. Goedhart, D. Shcherbo, M. E. Bulina, A. S. Shcheglov, A. F. Fradkov, A. Gaintzeva, K. A. Lukyanov, S. Lukyanov, T. W. J. Gadella, and D. M. Chudakov, "Bright monomeric red fluorescent protein with an extended fluorescence lifetime," Nature Methods, vol. 4, no. 7, pp. 555–557, 2007.

[22] R. E. Campbell, O. Tour, A. E. Palmer, P. A. Steinbach, G. S. Baird, D. A. Zacharias, and R. Y. Tsien, "A monomeric red fluorescent protein," Proc. Natl. Acad. Sci. U.S.A, vol. 99, pp. 7877–82, June 2002.

[23] N. C. Shaner, R. E. Campbell, P. a. Steinbach, B. N. G. Giepmans, A. E. Palmer, and R. Y. Tsien, "Improved monomeric red, orange and yellow fluorescent proteins derived from Discosoma sp. red fluorescent protein.," Nature biotechnology, vol. 22, pp. 1567–72, Dec. 2004.

[24] L. Wang, W. C. Jackson, P. a. Steinbach, and R. Y. Tsien, "Evolution of new nonantibody proteins via iterative somatic hypermutation.," Proc. Natl. Acad. Sci. U.S.A, vol. 101, pp. 16745–9, Nov. 2004.

[25] R. Chica, M. M. Moore, B. D. Allen, and S. L. Mayo, "Generation of longer emission wavelength red fluorescent proteins using computationally designed libraries.," Proc. Natl. Acad. Sci. U.S.A, vol. 107, pp. 20257–62, Nov. 2010.

[26] L. Wang, W. C. Jackson, P. a. Steinbach, and R. Y. Tsien, "Evolution of new nonantibody proteins via iterative somatic hypermutation.," Proceedings of the National Academy of Sciences of the United States of America, vol. 101, pp. 16745–9, Nov. 2004.

[27] J. L. Lubbeck, K. M. Dean, H. Ma, A. E. Palmer, and R. Jimenez, "Microfluidic flow cytometer for quantifying photobleaching of fluorescent proteins in cells.," Analytical chemistry, vol. 84, pp. 3929–37, May 2012.

[28] L. M. Davis, J. L. Lubbeck, K. M. Dean, A. E. Palmer, and R. Jimenez, "Microfluidic cell sorter for use in developing red fluorescent proteins with improved photostability.," Lab on a chip, vol. 13, pp. 2320–7, June 2013.

[29] L. a. Gross, G. S. Baird, R. C. Hoffman, K. K. Baldridge, and R. Y. Tsien, "The structure of the chromophore within DsRed, a red fluorescent protein from coral.," Proceedings of the National Academy of Sciences of the United States of America, vol. 97, pp. 11990–5, Oct. 2000.

[30] V. V. Verkhusha, D. M. Chudakov, N. G. Gurskaya, S. Lukyanov, and K. A. Lukyanov, "Common Pathway for the Red Chromophore Formation in Fluorescent Proteins and Chromoproteins," Chemistry and Biology, vol. 11, pp. 845–854, 2004.

[31] X. Shu, N. C. Shaner, C. A. Yarbrough, R. Y. Tsien, and S. J. Remington, "Novel Chromophores and Buried Charges Control Color in mFruits," Biochemistry, vol. 45, no. 32, 2006.

[32] J. E. McCombs and A. E. Palmer, "Measuring calcium dynamics in living cells with genetically encodable calcium indicators.," Methods (San Diego, Calif.), vol. 46, pp. 152–9, Nov. 2008.

[33] D. M. Chudakov, M. V. Matz, S. Lukyanov, and K. A. Lukyanov, "Fluorescent Proteins and Their Applications in Imaging Living Cells and Tissues," Physiol. Rev., vol. 90, pp. 1103–1163, 2010.

[34] A. Crameri, E. A. Whitehorn, E. Tate, and W. P. Stemmer, "Improved Green fluorescent protein by molecular evolution using DNA Shuffling," Nature biotechnology, vol. 14, pp. 315–319, 1996.

[35] L. Tian, S. A. Hires, T. Mao, D. Huber, M. E. Chiappe, S. H. Chalasani, L. Petreanu, J. Akerboom, S. a. McKinney, E. R. Schreiter, C. I. Bargmann, V. Jayaraman, K. Svoboda, and L. L. Looger, "Imaging neural activity in worms, flies and mice with improved GCaMP calcium indicators.," Nature methods, vol. 6, pp. 875–81, Dec. 2009.

[36] K. Truong and M. Ikura, "The use of FRET imaging microscopy to detect protein protein interactions and protein conformational changes in vivo Kevin Truong and Mitsuhiko Ikura *," Biopyhsical methods, vol. 11, pp. 573–578, 2001.

[37] D. J. Wallace, S. Meyer, S. Astori, Y. Yang, M. Bausen, A. E. Palmer, R. Y. Tsien, R. Sprengel, J. N. D. Kerr, W. Denk, and M. T. Hasan, "Single-spike detection in vitro and in vivo with a genetic Ca 2 + sensor," Nature, vol. 5, no. 9, pp. 797–804, 2008.

[38] G. S. Harms, L. Cognet, P. H. Lommerse, G. a. Blab, and T. Schmidt, "Autofluorescent proteins in single-molecule research: applications to live cell imaging microscopy.," Biophysical journal, vol. 80, pp. 2396–408, May 2001.

[39] S. Kredel, K. Nienhaus, F. Oswald, M. Wolff, S. Ivanchenko, F. Cymer, A. Jeromin, F. J. Michel, K.-D. Spindler, R. Heilker, G. U. Nienhaus, and J. Wiedenmann, "Optimized and far-red-emitting variants of fluorescent protein eqFP611.," Chemistry & biology, vol. 15, pp. 224–33, Mar. 2008.

[40] V. V. Verkhusha, I. M. Kuznetsova, O. V. Stepanenko, A. G. Zaraisky, M. M. Shavlovsky, K. K. Turoverov, and V. N. Uversky, "Accelerated Publications High Stability of Discosoma DsRed As Compared to Aequorea EGFP," Biochem., pp. 7879–7884, 2003.

[41] O. V. Stepanenko, V. V. Verkhusha, V. I. Kazakov, M. M. Shavlovsky, I. M. Kuznetsova, V. N. Uversky, and K. K. Turoverov, "Comparative Studies on the Structure and Stability of Fluorescent Proteins EGFP, zFP506, mRFP1, "dimer2", and DsRed1," Biochemistry, vol. 43, pp. 14913–14923, 2004.

[42] J. Cavanagh, W. J. Fairbrother, I. Palmer, A. G., M. Rance, and N. J. Skelton, Protein NMR Spectroscopy: Principles and Practice. San Diego, CA: Academic Press, 2nd ed., 2007.

[43] S. W. Englander and N. R. Kallenbach, "Hydrogen exchange and structural dynamics of proteins and nucleic acids.," Nov. 1983.

[44] R. Englman and J. Jortner, "The energy gap law for radiationless transitions in large molecules," Molecular Physics, vol. 18, no. 2, pp. 145–164, 1970.

[45] W. a. Wassam and E. C. Lim, "Proximity effect in radiationless transitions," The Journal of Chemical Physics, vol. 68, no. 2, p. 433, 1978.

[46] A. D. Kummer, C. Kompa, H. Lossau, F. Pollinger-dammer, M. E. Michel-beyerle, C. M. Silva, E. J. Bylina, W. J. Coleman, M. M. Yang, and D. C. Youvan, "Dramatic reduction in fluorescence quantum yield in mutants of Green Fluorescent Protein due to fast internal conversion 1," Chemical Physics, vol. 237, pp. 183–193, 1998.

[47] M. L. Quillin, D. M. Anstrom, X. Shu, S. O'Leary, K. Kallio, D. M. Chudakov, and S. J. Remington, "Kindling fluorescent protein from Anemonia sulcata: dark-state structure at 1.38 A resolution.," Biochemistry, vol. 44, pp. 5774–87, Apr. 2005.

[48] P. G. Wilmann, J. Petersen, A. Pettikiriarachchi, A. M. Buckle, S. C. Smith, S. Olsen, M. a. Perugini, R. J. Devenish, M. Prescott, and J. Rossjohn, "The 2.1A crystal structure of the far-red fluorescent protein HcRed: inherent conformational flexibility of the chromophore.," Journal of molecular biology, vol. 349, pp. 223–37, May 2005.

[49] S. L. Maddalo and M. Zimmer, "The role of the protein matrix in green fluorescent protein fluorescence.," Photochemistry and photobiology, vol. 82, no. 2, pp. 367–72, 2006.

[50] A. P. Demchenko, Advanced Fluorescence Reporters in Chemistry and Biology Vol. 1. Springer, 2010.

[51] M. Vengris, I. H. M. V. Stokkum, X. He, A. F. Bell, P. J. Tonge, R. V. Grondelle, and D. S. Larsen, "Ultrafast Excited and Ground-State Dynamics of the Green Fluorescent Protein Chromophore in Solution," J. Phys. Chem. A, vol. 31, no. 0, pp. 4587–4598, 2004.

[52] M. Andresen, A. C. Stiel, S. Trowitzsch, G. Weber, C. Eggeling, M. C. Wahl, S. W. Hell, and S. Jakobs, "Structural basis for reversible photoswitching in Dronpa.," Proceedings of the National Academy of Sciences of the United States of America, vol. 104, pp. 13005–9, Aug. 2007.

[53] S. Diego and L. Jolla, "Shedding light on the dark and weakly fluorescent states of green," PNAS, vol. 96, no. May, pp. 6177–6182, 1999.

[54] H. Niwa, S. Inouye, T. Hirano, T. Matsuno, S. Kojima, M. Kubota, M. Ohashi, and F. I. Tsuji, "Chemical nature of the light emitter of the Aequorea green fluorescent protein.," Proc. Natl. Acad. Sci. U.S.A, vol. 93, pp. 13617–22, Nov. 1996.

[55] E. A. Pozzi, L. R. Schwall, R. Jimenez, and J. M. Weber, "Pressure-Induced Changes in the Fluorescence Behavior of Red Fluorescent Proteins.," The journal of physical chemistry. B, Aug. 2012.

[56] O. V. Stepanenko, O. V. Stepanenko, I. M. Kuznetsova, V. V. Verkhusha, and K. K. Turoverov, "Beta-Barrel Scaffold of Fluorescent Proteins : Folding , Stability and Role in Chromophore Formation," International Review of Cell and Molecular Biology, vol. 302, pp. 221–278, 2013.

[57] T. B. Mcananey, W. Zeng, C. F. E. Doe, N. Bhanji, S. Wakelin, D. S. Pearson, P. Abbyad, X. Shi, S. G. Boxer, and C. R. Bagshaw, "Protonation , Photobleaching , and Photoactivation of Yellow Fluorescent Protein," Biochem., pp. 5510–5524, 2005.

[58] J. J. van Thor, G. Zanetti, K. L. Ronayne, and M. Towrie, "Structural events in the photocycle of green fluorescent protein.," The journal of physical chemistry. B, vol. 109, pp. 16099–108, Aug. 2005.

[59] J. N. Henderson, H.-W. Ai, R. E. Campbell, and S. J. Remington, "Structural basis for reversible photobleaching of a green fluorescent protein homologue.," Proc. Natl. Acad. Sci. U.S.A, vol. 104, pp. 6672–7, Apr. 2007.

[60] L. V. Schäfer, G. Groenhof, M. Boggio-Pasqua, M. a. Robb, and H. Grubmüller, "Chromophore protonation state controls photoswitching of the fluoroprotein asFP595.," PLoS computational biology, vol. 4, p. e1000034, Mar. 2008.

[61] S. Pletnev, F. V. Subach, Z. Dauter, A. Wlodawer, and V. V. Verkhusha, "A structural basis for reversible photoswitching of absorbance spectra in red fluorescent protein rsTagRFP.," Journal of molecular biology, vol. 417, pp. 144–51, Mar. 2012.

[62] H. Mizuno, T. K. Mal, M. Wälchli, A. Kikuchi, T. Fukano, R. Ando, J. Jeyakanthan, J. Taka, Y. Shiro, M. Ikura, and A. Miyawaki, "Light-dependent regulation of structural flexibility in a photochromic fluorescent protein.," Proceedings of the National Academy of Sciences of the United States of America, vol. 105, pp. 9227–32, July 2008.

[63] F. V. Subach and V. V. Verkhusha, "Chromophore transformations in red fluorescent proteins.," Chemical reviews, vol. 112, pp. 4308–27, July 2012.

[64] J. R. Lakowicz, Principles of Fluorescence Spectroscopy. New York: Springer, 2006.

[65] K. Henzler-Wildman and D. Kern, "Dynamic personalities of proteins.," Nature, vol. 450, pp. 964–72, Dec. 2007.

[66] J. Goedhart, D. von Stetten, M. Noirclerc-Savoye, M. Lelimousin, L. Joosen, M. a. Hink, L. van Weeren, T. W. J. Gadella, and A. Royant, "Structure-guided evolution of cyan fluorescent proteins towards a quantum yield of 93%.," Nature communications, vol. 3, p. 751, Jan. 2012.

[67] S. Pletnev, D. Shcherbo, D. M. Chudakov, N. Pletneva, E. M. Merzlyak, A. Wlodawer, Z. Dauter, and V. Pletnev, "A crystallographic study of bright far-red fluorescent protein mKate reveals pH-induced cis-trans isomerization of the chromophore.," The Journal of biological chemistry, vol. 283, pp. 28980–7, Oct. 2008.

[68] A. D. Laurent, V. a. Mironov, P. P. Chapagain, A. V. Nemukhin, and A. I. Krylov, "Exploring Structural and Optical Properties of Fluorescent Proteins by Squeezing: Modeling High-Pressure Effects on the mStrawberry and mCherry Red Fluorescent Proteins.," The journal of physical chemistry. B, vol. 116, pp. 12426–40, Oct. 2012.

[69] P. P. Chapagain, C. K. Regmi, and W. Castillo, "Fluorescent protein barrel fluctuations and oxygen diffusion pathways in mCherry.," The Journal of chemical physics, vol. 135, p. 235101, Dec. 2011.

[70] F. Khan, I. Kuprov, T. D. Craggs, P. J. Hore, and S. E. Jackson, "19F NMR studies of the native and denatured states of green fluorescent protein.," Journal of the American Chemical Society, vol. 128, pp. 10729–37, Aug. 2006.

[71] M. H. J. Seifert, D. Ksiazek, M. K. Azim, P. Smialowski, N. Budisa, and T. a. Holak, "Slow exchange in the chromophore of a green fluorescent protein variant.," Journal of the American Chemical Society, vol. 124, pp. 7932–42, July 2002.

[72] M. Noirclerc-savoye, C. Lazareno-saez, B. Paetzold, S. L. Vot, R. Chazal, P. Macheboeuf, M. J. Field, D. Bourgeois, and A. Royant, "Intrinsic Dynamics in ECFP and Cerulean Control Fluorescence Quantum Yield," Biochem., vol. 48, pp. 10038–10046, 2009.

[73] D. Mandal, T. Tahara, and S. R. Meech, "Excited-State Dynamics in the Green Fluorescent Protein Chromophore," The Journal of Physical Chemistry B, vol. 108, pp. 1102–1108, Jan. 2004.

[74] M. H. J. Seifert, J. Georgescu, D. Ksiazek, P. Smialowski, T. Rehm, B. Steipe, and T. A. Holak, "Backbone Dynamics of Green Fluorescent Protein and the Effect of Histidine 148," Biochem., no. 10, pp. 2500–2512, 2003.

[75] U. Haupts, S. Maiti, P. Schwille, and W. W. Webb, "Dynamics of fluorescence fluctuations in green fluorescent," Biophysics, vol. 95, no. November, pp. 13573–13578, 1998.

[76] M. Chattoraj, B. a. King, G. U. Bublitz, and S. G. Boxer, "Ultra-fast excited state dynamics in green fluorescent protein: multiple states and proton transfer.," Proceedings of the National Academy of Sciences of the United States of America, vol. 93, pp. 8362–7, Aug. 1996.

[77] C. M. Megley, L. a. Dickson, S. L. Maddalo, G. J. Chandler, and M. Zimmer, "Photophysics and dihedral freedom of the chromophore in yellow, blue, and green fluorescent protein.," The journal of physical chemistry. B, vol. 113, pp. 302–8, Jan. 2009.

[78] H. Mizuno, T. K. Mal, M. Wälchli, T. Fukano, M. Ikura, and A. Miyawaki, "Molecular basis of photochromism of a fluorescent protein revealed by direct 13C detection under laser illumination.," Journal of biomolecular NMR, vol. 48, pp. 237–46, Dec. 2010.

[79] M. Andresen, M. C. Wahl, A. C. Stiel, F. Gräter, L. V. Schäfer, S. Trowitzsch, G. Weber, C. Eggeling, H. Grubmüller, S. W. Hell, and S. Jakobs, "Structure and mechanism of the reversible photoswitch of a fluorescent protein.," Proc. Natl. Acad. Sci. U.S.A, vol. 102, pp. 13070–4, Sept. 2005.

[80] R. Battistutta, a. Negro, and G. Zanotti, "Crystal structure and refolding properties of the mutant F99S/M153T/V163A of the green fluorescent protein.," Proteins, vol. 41, pp. 429–37, Dec. 2000.

[81] D. Bourgeois, A. Regis-faro, and V. Adam, "Biochemical Society Annual Symposium No . 79 Photoactivated structural dynamics of fluorescent proteins," Biochem. Soc. Trans., pp. 531–538, 2012.

[82] K. Brejc, T. K. Sixma, P. a. Kitts, S. R. Kain, R. Y. Tsien, M. Ormö, and S. J. Remington, "Structural basis for dual excitation and photoisomerization of the Aequorea victoria green fluorescent protein.," Proceedings of the National Academy of Sciences of the United States of America, vol. 94, pp. 2306–11, Mar. 1997.

[83] D. B. Calhoun, J. M. Vanderkooi, G. R. Holtom, and S. W. Englander, "Protein fluorescence quenching by small molecules: protein penetration versus solvent exposure.," Proteins, vol. 1, pp. 109–15, Oct. 1986.

[84] W. Downey and N. Nijegorodov, "The Influence of Planarity and Rigidity on the Absorption and Fluorescence Parameters and Intersystem Crossing Rate Constant in Aromatic Molecules," Journal of Physical Chemistry, vol. 98, pp. 5639–5643, 1994.

[85] C. Fang, R. R. Frontiera, R. Tran, and R. Mathies, "Mapping GFP structure evolution during proton transfer with femtosecond Raman spectroscopy.," Nature, vol. 462, pp. 200–4, Nov. 2009.

[86] A. R. Faro, P. Carpentier, G. Jonasson, G. Pompidor, D. Arcizet, I. Demachy, and D. Bourgeois, "Low-Temperature Chromophore Isomerization Reveals the," JACS, vol. 133, pp. 16362–16365, 2011.

[87] H. Fukuda, M. Arai, and K. Kuwajima, "Folding of green fluorescent protein and the cycle3 mutant.," Biochemistry, vol. 39, pp. 12025–32, Oct. 2000.

[88] L. Greenbaum, C. Rothmann, R. Lavie, and Z. Malik, "Green fluorescent protein photobleaching: a model for protein damage by endogenous and exogenous singlet oxygen.," Biological chemistry, vol. 381, pp. 1251–8, Dec. 2000.

[89] X. He, A. F. Bell, and P. J. Tonge, "Ground state isomerization of a model green fluorescent protein chromophore," FEBS Letters, vol. 549, pp. 35–38, Aug. 2003.

[90] a. a. Heikal, S. T. Hess, G. S. Baird, R. Y. Tsien, and W. W. Webb, "Molecular spectroscopy and dynamics of intrinsically fluorescent proteins: coral red (dsRed) and yellow (Citrine).," Proc. Natl. Acad. Sci. U.S.A, vol. 97, pp. 11996–2001, Oct. 2000.

[91] K. Jung, J. Park, P.-j. Maeng, and H. Kim, "Fluorescence Quenching of Green Fluorescent Protein during Denaturation by Guanidine," Bulletin of the Korean Chemical Society, vol. 26, no. 3, pp. 413–417, 2005.

[92] C. Kiss, J. Temirov, L. Chasteen, G. S. Waldo, and A. R. M. Bradbury, "Directed evolution of an extremely stable fluorescent protein.," Protein engineering, design & selection : PEDS, vol. 22, pp. 313–23, May 2009.

[93] K. Mauring, J. Deich, F. I. Rosell, T. B. McAnaney, W. E. Moerner, and S. G. Boxer, "Enhancement of the fluorescence of the blue fluorescent proteins by high pressure or low temperature.," The journal of physical chemistry. B, vol. 109, pp. 12976–81, July 2005.

[94] I. B. Nielsen, S. Boyé-Péronne, M. O. a. El Ghazaly, M. B. Kristensen, S. Brøndsted Nielsen, and L. H. Andersen, "Absorption spectra of photoactive yellow protein chromophores in vacuum.," Biophysical journal, vol. 89, pp. 2597–604, Oct. 2005.

[95] J. Petersen, P. G. Wilmann, T. Beddoe, A. J. Oakley, R. J. Devenish, M. Prescott, and J. Rossjohn, "The 2.0-A crystal structure of eqFP611, a far red fluorescent protein from the sea anemone Entacmaea quadricolor.," The Journal of biological chemistry, vol. 278, pp. 44626–31, Nov. 2003.

[96] K. D. Piatkevich, E. N. Efremenko, V. V. Verkhusha, and S. D. Varfolomeev, "Red fluorescent proteins and their properties," Russian Chemical Reviews, vol. 79, pp. 243–258, May 2010.

[97] M. Prescott, M. Ling, T. Beddoe, A. J. Oakley, S. Dove, O. Hoegh-Guldberg, R. J. Devenish, and J. Rossjohn, "The 2.2 A crystal structure of a pocilloporin pigment reveals a nonplanar chromophore conformation.," Structure (London, England : 1993), vol. 11, pp. 275–84, Mar. 2003.

[98] O. V. Stepanenko, O. V. Stepanenko, I. M. Kuznetsova, V. V. Verkhusha, and K. K. Turoverov, "Structural Perturbation of Superfolder GFP in the Presence of Guanidine Thiocyanate," Spectroscopy: An International Journal, vol. 27, no. 5-6, pp. 381–386, 2012.

[99] A. C. Stiel, S. Trowitzsch, G. Weber, M. Andresen, C. Eggeling, S. W. Hell, S. Jakobs, and M. C. Wahl, "1.8 A bright-state structure of the reversibly switchable fluorescent protein Dronpa guides the generation of fast switching variants.," The Biochemical journal, vol. 402, pp. 35–42, Feb. 2007.

[100] D. Stoner-Ma, A. a. Jaye, K. L. Ronayne, J. Nappa, S. R. Meech, and P. J. Tonge, "An alternate proton acceptor for excited-state proton transfer in green fluorescent protein: rewiring GFP.," Journal of the American Chemical Society, vol. 130, pp. 1227–35, Jan. 2008.

[101] K. Turcic, A. Pettikiriarachchi, J. Battad, P. G. Wilmann, J. Rossjohn, S. G. Dove, R. J. Devenish, and M. Prescott, "Amino acid substitutions around the chromophore of the chromoprotein Rtms5 influence polypeptide cleavage.," Biochemical and biophysical research communications, vol. 340, pp. 1139–43, Feb. 2006.

[102] V. V. Verkhusha, N. A. Akovbian, E. N. Efremenko, S. D. Varfolomeyev, and P. V. Vrzheshch, "Kinetic analysis of maturation and denaturation of DsRed, a coral-derived red fluorescent protein.," Biochemistry. Biokhimiia, vol. 66, pp. 1342–51, Dec. 2001.

[103] A. a. Voityuk, A. D. Kummer, M.-E. Michel-Beyerle, and N. Rösch, "Absorption spectra of the GFP chromophore in solution: comparison of theoretical and experimental results," Chemical Physics, vol. 269, pp. 83–91, July 2001.

[104] D. C. Loos, S. Habuchi, C. Flors, J.-I. Hotta, J. Wiedenmann, G. U. Nienhaus, and J. Hofkens, "Photoconversion in the red fluorescent protein from the sea anemone Entacmaea quadricolor: is cis-trans isomerization involved?," Journal of the American Chemical Society, vol. 128, pp. 6270–1, May 2006.

[105] L. V. Schäfer, G. Groenhof, A. R. Klingen, G. M. Ullmann, M. Boggio-Pasqua, M. a. Robb, and H. Grubmüller, "Photoswitching of the fluorescent protein asFP595: mechanism, proton pathways, and absorption spectra.," Angewandte Chemie (International ed. in English), vol. 46, pp. 530–6, Jan. 2007.

[106] T. a. Schüttrigkeit, T. V. Feilitzsch, C. K. Kompa, K. a. Lukyanov, A. P. Savitsky, A. a. Voityuk, and M. E. Michel-Beyerle, "Femtosecond study of light-induced fluorescence increase of the dark chromoprotein asFP595," Chemical Physics, vol. 323, pp. 149–160, Apr. 2006.

[107] P. Carpentier, S. Violot, L. Blanchoin, and D. Bourgeois, "Structural basis for the phototoxicity of the fluorescent protein KillerRed.," FEBS letters, vol. 583, pp. 2839–42, Sept. 2009.

[108] A. Choudhary, K. J. Kamer, and R. T. Raines, "A conserved interaction with the chromophore of fluorescent proteins.," Protein science : a publication of the Protein Society, vol. 21, pp. 171–7, Feb. 2012.

[109] G. N. J. Phillips, "Structure and dynamics of green fluorescent protein," Proteins, vol. 7, pp. 821–827, 1997.

[110] F. Yang, L. G. Moss, and G. N. Phillips, "The molecular structure of green fluorescent protein.," Nature biotechnology, vol. 14, pp. 1246–51, Oct. 1996.

[111] N. M. Webber, K. L. Litvinenko, and S. R. Meech, "Radiationless Relaxation in a Synthetic Analogue of the Green Fluorescent Protein Chromophore," J. Phys. Chem. B, vol. 105, pp. 8036–8039, 2001.

[112] J. Goedhart, L. van Weeren, M. a. Hink, N. O. E. Vischer, K. Jalink, and T. W. J. Gadella, "Bright cyan fluorescent protein variants identified by fluorescence lifetime screening.," Nature methods, vol. 7, pp. 137–9, Feb. 2010.

[113] R. Heim and R. Y. Tsien, "Engineering green fluorescent protein for improved brightness, longer wavelengths and fluorescence resonance energy transfer.," Current biology : CB, vol. 6, pp. 178–82, Feb. 1996.

[114] G.-J. Kremers, J. Goedhart, E. B. van Munster, and T. W. J. Gadella, "Cyan and yellow super fluorescent proteins with improved brightness, protein folding, and FRET Förster radius.," Biochemistry, vol. 45, pp. 6570–80, May 2006.

[115] M. a. Rizzo, G. H. Springer, B. Granada, and D. W. Piston, "An improved cyan fluorescent protein variant useful for FRET.," Nature biotechnology, vol. 22, pp. 445–9, Apr. 2004.

[116] M. L. Markwardt, G.-J. Kremers, C. a. Kraft, K. Ray, P. J. C. Cranfill, K. a. Wilson, R. N. Day, R. M. Wachter, M. W. Davidson, and M. a. Rizzo, "An improved cerulean fluorescent protein with enhanced brightness and reduced reversible photoswitching.," PloS one, vol. 6, p. e17896, Jan. 2011.

[117] M. Mandel, M. Akke, and G. Palmer, "Backbone dynamics of Escherichia coli ribonuclease HI: correlations with structure and function in an active enzyme.," Journal of molecular biology, vol. 246, pp. 144–63, Feb. 1995.

[118] J. H. Bae, M. Rubini, G. Jung, G. Wiegand, M. H. Seifert, K. M. Azim, J.-S. Kim, A. Zumbusch, T. A. Holak, L. Moroder, R. Huber, and N. Budisa, "Expansion of the Genetic Code Enables Design of a Novel Gold Class of Green Fluorescent Proteins," J. Mol. Biol., vol. 328, 2003.

[119] A. Fredj, H. Pasquier, I. Demachy, G. Jonasson, B. Levy, V. Derrien, Y. Bousmah, G. Manoussaris, F. Wien, J. Ridard, M. Erard, and F. Merola, "The single T65S mutation generates brighter cyan fluorescent proteins with increased photostability and pH insensitivity.," PloS one, vol. 7, p. e49149, Jan. 2012.

[120] M. E. Martin, F. Negri, and M. Olivucci, "Origin, nature, and fate of the fluorescent state of the green fluorescent protein chromophore at the CASPT2//CASSCF resolution.," Journal of the American Chemical Society, vol. 126, pp. 5452–64, May 2004.

[121] T. a. Larsen, a. J. Olson, and D. S. Goodsell, "Morphology of protein-protein interfaces.," Structure, vol. 6, pp. 421–7, Apr. 1998.

[122] A. Kumar, R. R. Ernst, and K. Wüthrich, "A two-dimensional nuclear Overhauser enhancement (2D NOE) experiment for the elucidation of complete proton-proton cross-relaxation networks in biological macromolecules.," Biochemical and biophysical research communications, vol. 95, pp. 1–6, July 1980.

[123] L. E. Kay, M. Ikura, R. Tschudin, and A. Bax, "Three-dimensional triple-resonance NMR Spectroscopy of isotopically enriched proteins.," Journal of magnetic resonance, vol. 89, pp. 496–514, Dec. 1990.

[124] N. R. Nirmala and G. Wagner, "Measurement of 13C Relaxation Times in Proteins by Two-Dimensional Heteronuclear 1H-13C Correlation Spectroscopy," JACS, vol. 14329, no. 2, pp. 7557–7558, 1988.

[125] N. Nirmala and G. Wagner, "Measurement of 13C spin-spin relaxation times by two-dimensional heteronuclear 1H-13C correlation spectroscopy," Journal of Magnetic Resonance, vol. 82, pp. 659–661, May 1989.

[126] L. E. Kay, D. a. Torchia, and A. Bax, "Backbone dynamics of proteins as studied by 15N inverse detected heteronuclear NMR spectroscopy: application to staphylococcal nuclease.," Biochem., vol. 28, pp. 8972–9, Dec. 1989.

[127] M. J. Stone, W. J. Fairbrother, a. G. Palmer, J. Reizer, M. H. Saier, and P. E. Wright, "Backbone dynamics of the Bacillus subtilis glucose permease IIA domain determined from 15N NMR relaxation measurements.," Biochemistry, vol. 31, pp. 4394–406, May 1992.

[128] D. M. Schneider, M. J. Dellwo, and a. J. Wand, "Fast internal main-chain dynamics of human ubiquitin.," Biochemistry, vol. 31, pp. 3645–52, Apr. 1992.

[129] V. a. Jarymowycz and M. J. Stone, "Fast time scale dynamics of protein backbones: NMR relaxation methods, applications, and functional consequences.," Chemical reviews, vol. 106, pp. 1624–71, May 2006.

[130] G. S. Rule and K. T. Hitchens, Fundamentals of Protein NMR Spectroscopy, vol. 5 of Focus on Structural Biology. Dordrecht: Springer, 2006.

[131] M. H. Levitt, Spin Dynamics. Southampton: John Wiley & Sons, 2001.

[132] O. Jardetzky and G. C. K. Roberts, NMR in Molecular Biology. New York: Academic Press, 1981.

[133] M. P. Williamson, Modern Magnetic Resonance. Dordrecht: Springer, 2008.

[134] T. D. W. Claridge, High-Resolution NMR Techniques in Organic Chemistry, vol. 19 of Tetrahedron Organic Chemistry Series. Oxford: Elsevier, 2009.

[135] G. Lipari and A. Szabo, "Model-free approach to the interpretation of nuclear magnetic resonance relaxation in macromolecules. 1. Theory and range of validity," Journal of the American Chemical Society, vol. 104, pp. 4546–4559, Aug. 1982.

[136] P. Dosset, J. C. Hus, M. Blackledge, and D. Marion, "Efficient analysis of macromolecular rotational diffusion from heteronuclear relaxation data.," Journal of biomolecular NMR, vol. 16, pp. 23–8, Jan. 2000.

[137] A. Abragam, The Principles of Nuclear Magnetism, vol. 29. Oxford: Oxford Science Publications, 1961.

[138] Y. Hiyama, C.-h. Niu, J. V. Silverton, and A. Bavoso, "Determination of 15N Chemical Shift Tensor via 15N-2H Dipolar Coupling in Boc-glycylglycyl[15N]glycine Benzyl Ester," J. Am. Chem. Soc., vol. 110, no. 4, pp. 2378–2383, 1988.

[139] G. Barbato, M. Ikura, L. E. Kay, R. W. Pastor, and A. Bax, "Backbone Dynamics of Calmodulin Studied by 15N Relaxation Using Inverse Detected Two-Dimensional NMR Spectroscopy: The Central Helix Is Flexible," Biochem., vol. 31, pp. 5269–5278, 1992.

[140] F. Cordier, M. Caffrey, B. Brutscher, M. a. Cusanovich, D. Marion, and M. Blackledge, "Solution structure, rotational diffusion anisotropy and local backbone dynamics of Rhodobacter capsulatus cytochrome c2.," Journal of molecular biology, vol. 281, pp. 341–61, Aug. 1998.

[141] K. Henzler-Wildman, M. Lei, V. Thai, S. J. Kerns, M. Karplus, and D. Kern, "A hierarchy of timescales in protein dynamics is linked to enzyme catalysis.," Nature, vol. 450, pp. 913–6, Dec. 2007.

[142] A. K. Gardino, J. Villali, A. Kivenson, M. Lei, C. F. Liu, P. Steindel, E. Z. Eisenmesser, W. Labeikovsky, M. Wolf-Watz, M. W. Clarkson, and D. Kern, "Transient non-native hydrogen bonds promote activation of a signaling protein.," Cell, vol. 139, pp. 1109–18, Dec. 2009.

[143] M. Wolf-Watz, V. Thai, K. Henzler-Wildman, G. Hadjipavlou, E. Z. Eisenmesser, and D. Kern, "Linkage between dynamics and catalysis in a thermophilic-mesophilic enzyme pair.," Nature structural & molecular biology, vol. 11, pp. 945–9, Oct. 2004.

[144] H. Y. Carr and E. M. Purcell, "Effects of Diffusion on Free Precession in Nuclear Magnetic Resonance Experiments," Phys. Rev., vol. 94, no. 3, 1954.

[145] S. Meiboom and D. Gill, "Modified Spin-Echo Method for Measuring Nuclear Relaxation Times," Review of Scientific Instruments, vol. 29, no. 8, p. 688, 1958.

[146] M. Akke and A. G. Palmer, "Monitoring Macromolecular Motions on Microsecond to Millisecond Time Scales by R 1G -R 1 Constant Relaxation Time NMR Spectroscopy," JACS, vol. 118, no. 9, pp. 911–912, 1996.

[147] F. a. Mulder, P. J. van Tilborg, R. Kaptein, and R. Boelens, "Microsecond time scale dynamics in the RXR DNA-binding domain from a combination of spin-echo and off-resonance rotating frame relaxation measurements.," Journal of biomolecular NMR, vol. 13, pp. 275–88, Mar. 1999.

[148] J. P. Loria, M. Rance, and A. G. I. Palmer, "A Relaxation-Compensated Carr-Purcell-Meiboom-Gill Sequence for Characterizing Chemical Exchange by NMR Spectroscopy," JACS, vol. 121, no. 16, pp. 2331–2332, 1999.

[149] R. Ishima, J. M. Louis, and D. A. Torchia, "Transverse 13C Relaxation of CHD2 Methyl Isotopmers To Detect Slow Conformational Changes of Protein Side Chains," JACS, no. 18, pp. 11589–11590, 1999.

[150] N. R. Skrynnikov, F. a. Mulder, B. Hon, F. W. Dahlquist, and L. E. Kay, "Probing slow time scale dynamics at methyl-containing side chains in proteins by relaxation dispersion NMR measurements: application to methionine residues in a cavity mutant of T4 lysozyme.," Journal of the American Chemical Society, vol. 123, pp. 4556–66, May 2001.

[151] D. M. Korzhnev, K. Kloiber, V. Kanelis, V. Tugarinov, and L. E. Kay, "Probing slow dynamics in high molecular weight proteins by methyl-TROSY NMR spectroscopy: application to a 723-residue enzyme.," Journal of the American Chemical Society, vol. 126, pp. 3964–73, Mar. 2004.

[152] A. J. Wand, "Dynamic activation of protein function : A view emerging from NMR spectroscopy," Nature, vol. 8, no. 11, 2001.

[153] E. Z. Eisenmesser, O. Millet, W. Labeikovsky, D. M. Korzhnev, M. Wolf-Watz, D. a. Bosco, J. J. Skalicky, L. E. Kay, and D. Kern, "Intrinsic dynamics of an enzyme underlies catalysis.," Nature, vol. 438, pp. 117–21, Nov. 2005.

[154] D. M. Korzhnev, T. L. Religa, W. Banachewicz, A. R. Fersht, and L. E. Kay, "A transient and low-populated protein-folding intermediate at atomic resolution.," Science, vol. 329, pp. 1312–6, Sept. 2010.

[155] A. J. Baldwin and L. E. Kay, "NMR spectroscopy brings invisible protein states into focus.," Nature chemical biology, vol. 5, pp. 808–14, Nov. 2009.

[156] B. Ma, S. Kumar, C. J. Tsai, and R. Nussinov, "Folding funnels and binding mechanisms.," Protein engineering, vol. 12, pp. 713–20, Sept. 1999.

[157] R. Ishima and D. a. Torchia, "Protein dynamics from NMR.," Nature structural biology, vol. 7, pp. 740–3, Sept. 2000.

[158] S. Enoki, K. Saeki, K. Maki, and K. Kuwajima, "Acid denaturation and refolding of green fluorescent protein.," Biochemistry, vol. 43, pp. 14238–48, Nov. 2004.

[159] H. Iwai, a. Lingel, and a. Pluckthun, "Cyclic green fluorescent protein produced in vivo using an artificially split PI-PfuI intein from Pyrococcus furiosus.," The Journal of biological chemistry, vol. 276, pp. 16548–54, May 2001.

[160] J. S. Merkel and L. Regan, "Modulating protein folding rates in vivo and in vitro by side-chain interactions between the parallel beta strands of green fluorescent protein.," Sept. 2000.

[161] P. V. Vrzheshch, N. A. Akovbian, S. D. Varfolomeyev, and V. V. Verkhusha, "Denaturation and partial renaturation of a tightly tetramerized DsRed protein under mildly acidic conditions.," FEBS letters, vol. 487, pp. 203–8, Dec. 2000.

[162] J. Wiehler, J. von Hummel, and B. Steipe, "Mutants of Discosoma red fluorescent protein with a GFP-like chromophore.," FEBS letters, vol. 487, pp. 384–9, Jan. 2001.

[163] J.-R. Huang, S.-T. D. Hsu, J. Christodoulou, and S. E. Jackson, "The extremely slow-exchanging core and acid-denatured state of green fluorescent protein.," HFSP journal, vol. 2, pp. 378–87, Dec. 2008.

[164] Y. Bai, J. S. Milne, L. Mayne, and S. W. Englander, "Protein stability parameters measured by hydrogen exchange.," Proteins, vol. 20, pp. 4–14, Sept. 1994.

[165] J. Huang, T. D. Craggs, J. Christodoulou, and S. E. Jackson, "Stable intermediate states and high energy barriers in the unfolding of GFP.," Journal of molecular biology, vol. 370, pp. 356–71, July 2007.

[166] E. Rennella, A. Corazza, F. Fogolari, P. Viglino, S. Giorgetti, M. Stoppini, V. Bellotti, and G. Esposito, "Equilibrium unfolding thermodynamics of beta2-microglobulin analyzed through native-state H/D exchange.," Biophysical journal, vol. 96, pp. 169–79, Jan. 2009.

[167] E. J. Fuentes and J. Wand, "Local dynamics and stability of apocytochrome b562 examined by hydrogen exchange.," Biochemistry, vol. 37, pp. 3687–98, Mar. 1998.

[168] H. J. Dyson and P. E. Wright, "Unfolded proteins and protein folding studied by NMR.," Chemical reviews, vol. 104, pp. 3607–22, Aug. 2004.

[169] J. Mandell, A. Falick, and E. Komives, "Identification of protein protein interfaces by decreased amide," PNAS, vol. 95, no. December, pp. 14705–14710, 1998.

[170] S. G. Codreanu, L. C. Thompson, D. L. Hachey, H. W. Dirr, and R. N. Armstrong, "Influence of the Dimer Interface on Glutathione Transferase Structure and Dynamics Revealed by Amide H / D Exchange Mass Spectrometry ," Biochem., vol. 44, no. 5, pp. 10605–10612, 2005.

[171] D. H. P. Low, V. Frecer, A. Le Saux, G. A. Srinivasan, B. Ho, J. Chen, and J. L. Ding, "Molecular interfaces of the galactose-binding protein Tectonin domains in host-pathogen interaction.," The Journal of biological chemistry, vol. 285, pp. 9898–907, Mar. 2010.

[172] V. a. Roberts, M. E. Pique, S. Hsu, S. Li, G. Slupphaug, R. P. Rambo, J. W. Jamison, T. Liu, J. H. Lee, J. a. Tainer, L. F. Ten Eyck, and V. L. Woods, "Combining H/D exchange mass spectroscopy and computational docking reveals extended DNA-binding surface on uracil-DNA glycosylase.," Nucleic acids research, vol. 40, pp. 6070–81, July 2012.

[173] B. Zhou, J. Zhang, S. Liu, S. Reddy, F. Wang, and Z.-Y. Zhang, "Mapping ERK2-MKP3 binding interfaces by hydrogen/deuterium exchange mass spectrometry.," The Journal of biological chemistry, vol. 281, pp. 38834–44, Dec. 2006.

[174] Y. Bai, T. R. Sosnick, L. Mayne, and S. W. Englander, "Protein folding intermediates: native-state hydrogen exchange.," Science (New York, N.Y.), vol. 269, pp. 192–7, July 1995.

[175] M. M. G. Krishna, L. Hoang, Y. Lin, and S. W. Englander, "Hydrogen exchange methods to study protein folding.," Methods (San Diego, Calif.), vol. 34, pp. 51–64, Sept. 2004.

[176] A. L. Norris and E. H. Serpersu, "NMR detected hydrogen-deuterium exchange reveals differential dynamics of antibiotic- and nucleotide-bound aminoglycoside phosphotransferase 3'-IIIa.," Journal of the American Chemical Society, vol. 131, pp. 8587–94, June 2009.

[177] M. A. Liebert, R. A. Garcia, D. Pantazatos, and F. J. Villarreal, "Investigating Protein-Ligand Interactions," Assay and Drug Development Technologies, vol. 2, no. 1, 2004.

[178] G. S. Anand, D. Law, J. G. Mandell, A. N. Snead, I. Tsigelny, S. S. Taylor, L. F. T. Eyck, and E. A. Komives, "Identification of the protein kinase A regulatory R1alpha-catalytic subunit interface by amide H/D exchange and protein docking," PNAS, vol. 100, no. 23, pp. 13264–13269, 2003.

[179] A. T. Alexandrescu, S. A. Dames, and R. Wiltscheck, "A fragment of staphylococcal nuclease with an OB-fold structure shows hydrogen-exchange protection factors in the range reported for "molten globules".," Protein science : a publication of the Protein Society, vol. 5, pp. 1942–6, Sept. 1996.

[180] M. F. Jeng, S. W. Englander, G. Elöve, J. Wand, and H. Roder, "Structural description of acid-denatured cytochrome c by hydrogen exchange and 2D NMR.," Biochem., vol. 29, pp. 10433–7, Nov. 1990.

[181] Y. Hamuro, S. J. Coales, M. R. Southern, J. F. Nemeth-cawley, D. D. Stranz, and P. R. Griffin, "Rapid Analysis of Protein Structure and Dynamics by Hydrogen/Deuterium Exchange Mass Spectrometry," Journal of Biomolecular Techniques, vol. 14, no. 3, pp. 171–182, 2003.

[182] L. S. Mullins, C. N. Pace, and F. M. Raushel, "Conformational stability of ribonuclease T1 determined by hydrogen-deuterium exchange," Protein Science, vol. 6, pp. 1387–1395, 1997.

[183] D. Waugh, "Genetic tools for selective labeling of proteins with alpha 15N amino acids," Journal of biomolecular NMR, vol. 8, pp. 184–192, 1996.

[184] D. Muchmore, L. McIntosh, C. Russell, D. E. Anderson, and F. Dahlquist, "Expression and nitrogen-15 labeling of proteins for proton and nitrogen-15 nuclear magnetic resonance," Methods in enzymology, vol. 177, pp. 44–73, 1989.

[185] A. Bahrami, A. H. Assadi, J. L. Markley, and H. R. Eghbalnia, "Probabilistic interaction network of evidence algorithm and its application to complete labeling of peak lists from protein NMR spectroscopy.," PLoS computational biology, vol. 5, p. e1000307, Mar. 2009.

[186] F. Delaglio, S. Grzesiek, G. W. Vuister, G. Zhu, J. Pfeifer, and A. Bax, "NMRPipe: a multidimensional spectral processing system based on UNIX pipes.," Journal of biomolecular NMR, vol. 6, pp. 277–93, Nov. 1995.

[187] W. F. Vranken, W. Boucher, T. J. Stevens, R. H. Fogh, A. Pajon, M. Llinas, E. L. Ulrich, J. L. Markley, J. Ionides, and E. D. Laue, "The CCPN data model for NMR spectroscopy: development of a software pipeline.," Proteins, vol. 59, pp. 687–96, July 2005.

[188] A. G. Palmer, M. Ranee, and P. E. Wright, "Intramolecular Motions of a Zinc Finger DNA-Binding Domain from Xfin Characterized by Proton-Detected Natural Abundance 13C Heteronuclear NMR Spectroscopy," JACS, vol. 11, no. 12, 1991.

[189] T. a. Walton, C. M. Sandoval, C. A. Fowler, A. Pardi, and M. C. Sousa, "The cavity-chaperone Skp protects its substrate from aggregation but allows independent folding of substrate domains.," Proc. Natl. Acad. Sci. U.S.A, vol. 106, pp. 1772–7, Feb. 2009.

[190] H. H. Ku, "Notes on the Use of Propagation of Error Formulas," Journal of Research of the National Bureau of Standards, vol. 79, no. 4, pp. 75–79, 1966.

[191] V. B. Chen, W. B. Arendall, J. J. Headd, D. a. Keedy, R. M. Immormino, G. J. Kapral, L. W. Murray, J. S. Richardson, and D. C. Richardson, "MolProbity: all-atom structure validation for macromolecular crystallography.," Acta crystallographica. Section D, Biological crystallography, vol. 66, pp. 12–21, Jan. 2010.

[192] S. Norton, "Studies of Individual Natural Abundance Spectroscopy Carbon Sites of Proteins in Solution by Carbon 13 Nuclear Magnetic Resonance," J. Biol. Chem., vol. 250, no. 16, pp. 6368–6380, 1975.

[193] M. Ramirez-Alvarado, V. a. Daragan, L. Serrano, and K. H. Mayo, "Motional dynamics of residues in a beta-hairpin peptide measured by 13C-NMR relaxation.," Protein science : a publication of the Protein Society, vol. 7, pp. 720–9, Mar. 1998.

[194] D. J. Wilbur, R. S. Norton, a. O. Clouse, R. Addleman, and a. Allerhand, "Determination of rotational correlation times of proteins in solution from carbon-13 spin-lattice relaxation measurements. Effect of magnetic field strength and anisotropic rotation.," Journal of the American Chemical Society, vol. 98, pp. 8250–4, Dec. 1976.

[195] S. Rumpel, A. Razeto, C. M. Pillar, V. Vijayan, A. Taylor, K. Giller, M. S. Gilmore, S. Becker, and M. Zweckstetter, "Structure and DNA-binding properties of the cytolysin regulator CylR2 from Enterococcus faecalis.," The EMBO journal, vol. 23, pp. 3632–42, Sept. 2004.

[196] J. G. Kempf, J.-Y. Jung, C. Ragain, N. S. Sampson, and J. P. Loria, "Dynamic requirements for a functional protein hinge.," Journal of molecular biology, vol. 368, pp. 131–49, Apr. 2007.

[197] X. Huang, I. M. S. de Vera, A. M. Veloro, J. R. Rocca, C. Simmerling, B. M. Dunn, and G. E. Fanucci, "Backbone (1)H, (13)C, and (15)N chemical shift assignment for HIV-1 protease subtypes and multi-drug resistant variant MDR 769.," Biomolecular NMR assignments, pp. 13–16, July 2012.

[198] D. Ma, N. R. Brandon, T. Cui, V. Bondarenko, C. Canlas, J. S. Johansson, P. Tang, and Y. Xu, "Four-alpha-helix bundle with designed anesthetic binding pockets. Part I: structural and dynamical analyses.," Biophysical journal, vol. 94, pp. 4454–63, June 2008.

[199] L. Pecqueur, B. D'Autréaux, J. Dupuy, Y. Nicolet, L. Jacquamet, B. Brutscher, I. Michaud-Soret, and B. Bersch, "Structural changes of Escherichia coli ferric uptake regulator during metal-dependent dimerization and activation explored by NMR and X-ray crystallography.," The Journal of biological chemistry, vol. 281, pp. 21286–95, July 2006.

[200] N. Tjandra, S. E. Feller, R. W. Pastor, and A. Bax, "Rotational Diffusion Anisotropy of Human Ubiquitin from NMR Relaxation," JACS, no. 12, pp. 12562–12566, 1995.

[201] K. Sikic, S. Tomic, and O. Carugo, "Systematic comparison of crystal and NMR protein structures deposited in the protein data bank.," The open biochemistry journal, vol. 4, pp. 83–95, Jan. 2010.

[202] D. S. Wishart, M. S. Watson, R. F. Boyko, and B. D. Sykes, "Automated 1H and 13C chemical shift prediction using the BioMagResBank.," Journal of biomolecular NMR, vol. 10, pp. 329–36, Dec. 1997.

[203] C. J. Langmead and B. R. Donald, "High-throughput 3D structural homology detection via NMR resonance assignment.," Proceedings / IEEE Computational Systems Bioinformatics Conference, CSB. IEEE Computational Systems Bioinformatics Conference, pp. 278–89, Jan. 2004.

[204] Y. Akdogan, J. Reichenwallner, and D. Hinderberger, "Evidence for water-tuned structural differences in proteins: an approach emphasizing variations in local hydrophilicity.," PloS one, vol. 7, p. e45681, Jan. 2012.

[205] V. D. A. Silva, M. T. Cargnelutti, G. M. Giesel, L. C. Palmieri, R. Q. Monteiro, H. Verli, and L. M. T. R. Lima, "Structure and behavior of human α-thrombin upon ligand recognition: thermodynamic and molecular dynamics studies.," PloS one, vol. 6, p. e24735, Jan. 2011.

[206] B. C. Lechtenberg, D. J. D. Johnson, S. M. V. Freund, and J. a. Huntington, "NMR resonance assignments of thrombin reveal the conformational and dynamic effects of ligation.," Proceedings of the National Academy of Sciences of the United States of America, vol. 107, pp. 14087–92, Aug. 2010.

[207] B. Wu, T. Skarina, A. Yee, M.-C. Jobin, R. Dileo, A. Semesi, C. Fares, A. Lemak, B. K. Coombes, C. H. Arrowsmith, A. U. Singer, and A. Savchenko, "NleG Type 3 effectors from enterohaemorrhagic Escherichia coli are U-Box E3 ubiquitin ligases.," PLoS pathogens, vol. 6, p. e1000960, Jan. 2010.

[208] J. J. Kwan, E. Smirnova, S. Khazai, F. Evanics, K. L. Maxwell, and L. W. Donaldson, "The Solution Structures of Two Prophage Homologues of the Bacteriophage λ Ea8.5 Protein Reveal a Newly Discovered Hybrid Homeodomain/Zinc-Finger Fold.," Biochemistry, pp. 3612–3614, May 2013.

[209] T. C. Bjorndahl, L. C. Andrew, V. Semenchenko, and D. S. Wishart, "NMR solution structures of the apo and peptide-inhibited human rhinovirus 3C protease (Serotype 14): structural and dynamic comparison.," Biochemistry, vol. 46, pp. 12945–58, Nov. 2007.

[210] A. Canales-Mayordomo, R. Fayos, J. Angulo, R. Ojeda, M. Martín-Pastor, P. M. Nieto, M. Martín-Lomas, R. Lozano, G. Giménez-Gallego, and J. Jiménez-Barbero, "Backbone dynamics of a biologically active human FGF-1 monomer, complexed to a hexasaccharide heparin-analogue, by 15N NMR relaxation methods.," Journal of biomolecular NMR, vol. 35, pp. 225–39, Aug. 2006.

[211] Y. Wen, J. Li, M. Xiong, Y. Peng, W. Yao, J. Hong, and D. Lin, "Solution structure and dynamics of the I214V mutant of the rabbit prion protein.," PloS one, vol. 5, p. e13273, Jan. 2010.

[212] P. Rossi, G. V. T. Swapna, Y. J. Huang, J. M. Aramini, C. Anklin, K. Conover, K. Hamilton, R. Xiao, T. B. Acton, A. Ertekin, J. K. Everett, and G. T. Montelione, "A microscale protein NMR sample screening pipeline.," Journal of biomolecular NMR, vol. 46, pp. 11–22, Jan. 2010.

[213] N. V. Brilliantov and V. P. Denisov, "GENERALIZED STOKES-EINSTEIN-DEBYE RELATION FOR CHARGED BROWNIAN PARTICLES IN SOLUTION," Physica A, vol. 175, pp. 293–304, 1991.

[214] T. Sugiki, C. Yoshiura, Y. Kofuku, T. Ueda, I. Shimada, and H. Takahashi, "High-throughput screening of optimal solution conditions for structural biological studies by fluorescence correlation spectroscopy.," Protein science : a publication of the Protein Society, vol. 18, pp. 1115–20, May 2009.

[215] D. Doddrell, "Theory of Nuclear Overhauser Enhancement and 13C-1H Dipolar Relaxation in Proton-Decoupled Carbon-13 NMR Spectra of Macromolecules," The Journal of Chemical Physics, vol. 56, no. 7, p. 3683, 1972.

[216] A. Bazzi, L. Zargarian, F. Chaminade, H. De Rocquigny, B. René, Y. Mély, P. Fossé, and O. Mauffret, "Intrinsic Nucleic Acid Dynamics Modulates HIV-1 Nucleocapsid Protein Binding to Its Targets," PLoS ONE, vol. 7, p. e38905, June 2012.

[217] V. Tugarinov and L. E. Kay, "A 2H NMR relaxation experiment for the measurement of the time scale of methyl side-chain dynamics in large proteins.," Journal of the American Chemical Society, vol. 128, pp. 12484–9, Sept. 2006.

[218] S. W. Englander and N. R. Kallenbach, "Hydrogen exchange and structural dynamics of proteins and nucleic acids.," Quarterly reviews of biophysics, vol. 16, pp. 521–655, Nov. 1983.

[219] M. R. Eftink and C. a. Ghiron, "Exposure of tryptophanyl residues in proteins. Quantitative determination by fluorescence quenching studies.," Biochemistry, vol. 15, pp. 672–80, Feb. 1976.

[220] A. M. Ruschak and L. E. Kay, "Methyl groups as probes of supra-molecular structure, dynamics and function.," Journal of biomolecular NMR, vol. 46, pp. 75–87, Jan. 2010.

[221] H. Beach, R. Cole, M. L. Gill, and J. P. Loria, "Conservation of mus-ms enzyme motions in the apo- and substrate-mimicked state.," Journal of the American Chemical Society, vol. 127, pp. 9167–76, June 2005.

[222] D. J. Ruben and G. Bodenhausen, "Natural Abundance Nitrogen-15 NMR by Enhanced Heteronuclear Spectroscopy," Chemical Physical Letters, vol. 69, no. 1, 1980.

[223] P. Schanda, H. Van Melckebeke, and B. Brutscher, "Speeding up three-dimensional protein NMR experiments to a few minutes.," Journal of the American Chemical Society, vol. 128, pp. 9042–3, July 2006.

[224] Y. Bai, J. S. Milne, L. Mayne, and S. W. Englander, "Primary structure effects on peptide group hydrogen exchange.," Proteins, vol. 17, pp. 75–86, Sept. 1993.

[225] G. P. Connelly, Y. Bai, M. F. Jeng, and S. W. Englander, "Isotope effects in peptide group hydrogen exchange.," Proteins, vol. 17, pp. 87–92, Sept. 1993.

[226] R. S. Molday, S. W. Englander, and R. G. Kallen, "Primary structure effects on peptide group hydrogen exchange.," Biochemistry, vol. 11, pp. 150–8, Jan. 1972.

[227] S. r. Klitgaard, M. T. Neves-Petersen, and S. B. Petersen, "Quenchers induce wavelength dependence on protein fluorescence lifetimes.," Journal of fluorescence, vol. 16, pp. 595–609, July 2006.

[228] J. Yu, J. Xiao, X. Ren, K. Lao, and X. S. Xie, "Probing gene expression in live cells, one protein molecule at a time.," Science (New York, N.Y.), vol. 311, pp. 1600–3, Mar. 2006.

[229] M. a. S. Hass, D. F. Hansen, H. E. M. Christensen, J. J. Led, and L. E. Kay, "Characterization of conformational exchange of a histidine side chain: protonation, rotamerization, and tautomerization of His61 in plastocyanin from Anabaena variabilis.," Journal of the American Chemical Society, vol. 130, pp. 8460–70, July 2008.

[230] I. R. Kleckner and M. P. Foster, "An introduction to NMR-based approaches for measuring protein dynamics.," Biochimica et biophysica acta, vol. 1814, pp. 942–68, Aug. 2011.

[231] F. Bahna, B. Honig, L. Shapiro, G. Arthur, Y. Li, N. L. Altorelli, and A. G. Palmer, "Mechanism of E-cadherin dimerization probed by NMR relaxation dispersion.," PNAS, vol. 062270, Oct. 2013.

[232] J.-M. Zen, A. S. Kumar, J.-C. Chen, K. Jayachithra, K. Balamurugan, and D.-H. Chin, "Electrocatalytic cyclization of dithiothreitol on a chemically modified electrode by analogy with protein action," The Analyst, vol. 126, no. 8, pp. 1409–1413, 2001.

[233] "The PyMOL Molecular Graphics System," 2009.

[234] W. Kabsch and C. Sander, "Dictionary of protein secondary structure: pattern recognition of hydrogen-bonded and geometrical features.," Biopolymers, vol. 22, pp. 2577–637, Dec. 1983.

[235] S. Akanuma, T. Matsuba, E. Ueno, N. Umeda, and A. Yamagishi, "Mimicking the evolution of a thermally stable monomeric four-helix bundle by fusion of four identical single-helix peptides.," Journal of biochemistry, vol. 147, pp. 371–9, Mar. 2010.

[236] L. Regan and W. F. DeGrado, "Characterization of a helical protein designed from rst principles..pdf," Science, vol. 241, 1988.

[237] S. Tanaka, S. Igarashi, S. Ferri, and K. Sode, "Increasing stability of water-soluble PQQ glucose dehydrogenase by increasing hydrophobic interaction at dimeric interface.," BMC biochemistry, vol. 6, p. 1, Jan. 2005.

[238] A. T. N. Kumar, E. Chung, S. B. Raymond, J. a. J. M. van de Water, K. Shah, D. Fukumura, R. K. Jain, B. J. Bacskai, and D. a. Boas, "Feasibility of in vivo imaging of fluorescent proteins using lifetime contrast.," Optics letters, vol. 34, pp. 2066–8, July 2009.

[239] R. Hiller, Z. H. Zhou, M. W. Adams, and S. W. Englander, "Stability and dynamics in a hyperthermophilic protein with melting temperature close to 200 degrees C.," Proceedings of the National Academy of Sciences of the United States of America, vol. 94, pp. 11329–32, Oct. 1997.

[240] C. N. Pace, "Determination and analysis of urea and guanidine hydrochloride denaturation curves.," Jan. 1986.

[241] E. Bornberg-Bauer and H. S. Chan, "Modeling evolutionary landscapes: mutational stability, topology, and superfunnels in sequence space.," Proceedings of the National Academy of Sciences of the United States of America, vol. 96, pp. 10689–94, Sept. 1999.

[242] B. W. Matthews, H. Nicholson, and W. J. Becktel, "Enhanced protein thermostability from site-directed mutations that decrease the entropy of unfolding.," Proc. Natl. Acad. Sci. U.S.A, vol. 84, pp. 6663–7, Oct. 1987.

[243] J.-D. Pédelacq, S. Cabantous, T. Tran, T. C. Terwilliger, and G. S. Waldo, "Engineering and characterization of a superfolder green fluorescent protein.," Nature biotechnology, vol. 24, pp. 79–88, Jan. 2006.

[244] M. S. Lawrence, K. J. Phillips, and D. R. Liu, "Supercharging proteins can impart unusual resilience.," Journal of the American Chemical Society, vol. 129, pp. 10110–2, Aug. 2007.

[245] G. S. Baird, D. A. Zacharias, and R. Y. Tsien, "Biochemistry, mutagenesis, and oligomerization of DsRed, a red fluorescent protein from coral.," Proc. Natl. Acad. Sci. U.S.A, vol. 97, pp. 11984–9, Oct. 2000.

[246] B. Peelle, T. L. Gururaja, D. G. Payan, and D. C. Anderson, "Characterization and use of green fluorescent proteins from Renilla mulleri and Ptilosarcus guernyi for the human cell display of functional peptides.," Journal of protein chemistry, vol. 20, pp. 507–19, Aug. 2001.

[247] K. M. Alkaabi, A. Yafea, and S. S. AShraf, "Effect of pH on Thermal- and Chemical-Induced Denaturation of GFP," Applied Biochemistry and Biotechnology, vol. 126, pp. 149–156, 2005.

[248] W. W. Ward and S. H. Bokman, "Reversible denaturation of Aequorea green-fluorescent protein: physical separation and characterization of the renatured protein.," Biochem., vol. 21, pp. 4535–40, Oct. 1982.

[249] J. M. Louis, Y. Zhang, J. M. Sayer, Y.-F. Wang, R. W. Harrison, and I. T. Weber, "The L76V drug resistance mutation decreases the dimer stability and rate of autoprocessing of HIV-1 protease by reducing internal hydrophobic contacts.," Biochemistry, vol. 50, pp. 4786–95, May 2011.

[250] S. Bershtein, W. Wu, and E. I. Shakhnovich, "Soluble oligomerization provides a beneficial fitness effect on destabilizing mutations," PNAS, vol. 109, no. 13, pp. 4857–4862, 2012.

[251] P. D. Dixit and S. Maslov, "Evolutionary capacitance and control of protein stability in protein-protein interaction networks.," PLoS computational biology, vol. 9, p. e1003023, Apr. 2013.

[252] N. C. Shaner, M. Z. Lin, M. R. McKeown, P. a. Steinbach, K. L. Hazelwood, M. W. Davidson, and R. Y. Tsien, "Improving the photostability of bright monomeric orange and red fluorescent proteins.," Nature methods, vol. 5, pp. 545–51, June 2008.

[253] D. H. A. Corrêa and C. H. I. Ramos, "The use of circular dichroism spectroscopy to study protein folding , form and function," African Journal of Biochemistry Research, vol. 3, no. 5, pp. 164–173, 2009.

[254] A. Abdul-Gader, A. J. Miles, and B. a. Wallace, "A reference dataset for the analyses of membrane protein secondary structures and transmembrane residues using circular dichroism spectroscopy.," Bioinformatics (Oxford, England), vol. 27, pp. 1630–6, June 2011.

[255] S. M. Kelly, T. J. Jess, and N. C. Price, "How to study proteins by circular dichroism.," Biochimica et biophysica acta, vol. 1751, pp. 119–39, Aug. 2005.

[256] F. Cava, M. A. de Pedro, E. Blas-Galindo, G. S. Waldo, L. F. Westblade, and J. Berenguer, "Expression and use of superfolder green fluorescent protein at high temperatures in vivo: a tool to study extreme thermophile biology.," Environmental microbiology, vol. 10, pp. 605–13, Mar. 2008.

[257] W. Research Inc., "Mathematica," 2010.

[258] N. V. Visser, M. A. Hink, J. Willem, G. N. M. V. D. Krogt, and A. J. W. G. Visser, "Circular dichroism spectroscopy of Fluorescent proteins," FEBS letters, vol. 521, pp. 31–35, 2002.

[259] K. P. Kent, L. M. Oltrogge, and S. G. Boxer, "Synthetic control of green fluorescent protein.," Journal of the American Chemical Society, vol. 131, pp. 15988–9, Nov. 2009.

[260] M. N. Boyden and S. a. Asher, "UV Raman studies of peptide conformation demonstrate that betanova does not cooperatively unfold.," Biochemistry, vol. 40, pp. 13723–7, Nov. 2001.

[261] S. Akanuma and A. Yamagishi, "Experimental evidence for the existence of a stable half-barrel subdomain in the (beta/alpha)8-barrel fold.," Journal of molecular biology, vol. 382, pp. 458–66, Oct. 2008.

[262] A. Miyawaki, D. M. Shcherbakova, and V. V. Verkhusha, "Red fluorescent proteins: chromophore formation and cellular applications.," Current opinion in structural biology, vol. 22, pp. 679–88, Oct. 2012.

[263] O. M. Subach, V. N. Malashkevich, W. D. Zencheck, S. Kateryna, K. D. Piatkevich, S. C. Almo, and V. V. Verkhusha, "Structural characterization of acylimine-containing blue and red chromophores in mTagBFP and TagRFP fluorescent proteins," Chem. Biol., vol. 17, no. 4, pp. 333–341, 2010.

[264] E. Kauffmann, N. C. Darnton, R. H. Austin, C. Batt, and K. Gerwert, "Lifetimes of intermediates in the beta -sheet to alpha -helix transition of beta -lactoglobulin by using a diffusional IR mixer.," Proceedings of the National Academy of Sciences of the United States of America, vol. 98, pp. 6646–9, June 2001.

[265] L. F. Drummy, D. M. Phillips, M. O. Stone, B. L. Farmer, and R. R. Naik, "Thermally Induced α-Helix to β-Sheet Transition in Regenerated Silk Fibers and Films," Biomacromolecules, pp. 3328–3333, 2005.

[266] H. Mizuno, T. K. Mal, K. I. Tong, R. Ando, T. Furuta, M. Ikura, and A. Miyawaki, "Photo-induced peptide cleavage in the green-to-red conversion of a fluorescent protein.," Molecular cell, vol. 12, pp. 1051–8, Oct. 2003.

[267] V. V. Verkhusha and K. A. Lukyanov, "The molecular properties and applications of Anthozoa fluorescent proteins and chromoproteins.," Nature biotechnology, vol. 22, pp. 289–96, Mar. 2004.

[268] G. N. J. Phillips, "Structure and dynamics of green fluorescent protein," Proteins, pp. 821–827, 1997.

Appendix A

NMR Spectra Collected and Parameters

Table A.1: ^{15}N NMR relaxation experimental parameters

Protein	**0.6mM 15N mCherry**
Buffer conditions	20mM Tris pH=7, 50mM NaCl, 0.15mM TSP, 10%D2O
Sample conditions	37°C
Spectrometer	Inova600
Sequence	•gNhsqc.c TROSY, T1='y' relaxT=0, 20ms, 40ms, 80ms, 100ms, 200ms, 400ms, 800ms, 1000ms •gNhsqc.c decoupled, T1rho='y' relaxT=0ms, 10ms, 20ms, 30ms, 50ms, 80ms, 120ms, 160ms, 200ms, 300ms •N15NOE_lek_pfg_sel_enh.c
Date	Sample made April 26 2011, Experiments Run August 25 2011
File Locations	T1: Data/Fluorescent_Proteins/mCherry/relaxation/15N_T1_T2/NT1 T1rho: Data/Fluorescent_Proteins/mCherry/relaxation/15N_T1_T2/NT1rho NOE: Data/Fluorescent_Proteins/mCherry/relaxation/HNhetNOE_data

Protein	**0.8mM 15N mRojoB**
Buffer conditions	20mM Tris pH=7, 50mM NaCl, 5mM DTT, 0.15mM TSP, 10%D2O
Sample conditions	37°C
Spectrometer	Inova600
Sequence	•gNhsqc.c TROSY, T1='y' relaxT=0, 20ms, 40ms(2x), 80ms, 100ms, 200ms(2x), 800ms, 1000ms, 1600ms •gNhsqc.c deoupled, T1rho='y' relaxT=0ms, 10ms, 20ms (2x), 30ms, 50ms, 80ms, 120ms, 160ms, 200ms (2x), 300ms •N15NOE_lek_pfg_sel_enh.c
Date	Sample made June 2011 (or Feb 2012), Experiments run September 2, 2011 (and March 2012)
File Names	15NmRojoB_NT1_09022011.fid 15NmRojoB_NT1rho_09022011.fid 15NmRojoB_hetNOE_satON_laj_03292012.fid 15NmRojoB_hetNOE_satoff_laj_03292012.fid

Protein	**0.5mM 15N mRaspberry**
Buffer conditions	20mM Tris pH=7, 50mM NaCl, 5mM DTT, 0.15mM TSP, 10%D2O
Sample conditions	37°C
Spectrometer	Inova600
Sequence	•gNhsqc.c TROSY, T1='y' relaxT=0, 20ms, 40ms, 80ms, 100ms, 200ms(2x), 800ms, 1000ms, 1600ms •gNhsqc.c deoupled, T1rho='y' relaxT=0ms, 10ms, 20ms, 30ms, 40ms, 50ms, 80ms, 120ms, 160ms, 200ms, 300ms •g_NNOE.c
Date	Sample made June 2011, Experiments run January 2013
File Names	15NmRaspberry_gNhsqc_T1_relaxTarray_01072013.fid 15NmRaspberry_gNhsqc_T1rho_relaxT0_01032013.fid 15NmRaspberry_gNhsqc_T1rho_relaxTarray_01032013.fid 15NmRaspberry_g_NNOE_satOFF_01072013.fid 15NmRaspberry_g_NNOE_satON_01072013.fid

Table A.2: ^{13}C NMR relaxation experimental parameters

Protein	0.6mM **13C-beta-Tyr mCherry**
Buffer conditions	20mM d-11 Tris pH=7, 50mM NaCl, 0.15mM TSP, 100%D2O
Sample conditions	37C
Spectrometer	Inova600
Sequence	•gCT1T2.c TROSY, T1='y' relaxT=0, 20ms, 40ms, 80ms, 100ms, 200ms, 400ms, 800ms, 1000ms •C13T1rho_trosy_lek_randomsat_600c.c TROSY, relaxT=0ms, 1ms, 2ms, 3ms, 4ms, 5ms, 7ms, 9ms, 13ms, 17ms, 20ms •gHChetNOE.c
Date	Sample made 7/2011, Experiments run 8/2011 and 4/2012
File Locations	**T1:** Data/Fluorescent_Proteins/mCherry/relaxation/13C_relaxation/ T1_T2_T1rho/13C_beta_Tyr_CT19cells_mCherry_T1_08022011.fid **T1rho:** Data/Fluorescent_Proteins/mCherry/relaxation/13C_relaxation/ T1_T2_T1rho/13C_beta_Tyr_CT19cells_mCherry_T1rho_08092011.fid **NOE:** Data/Fluorescent_Proteins/mCherry/relaxation/13C_relaxation/ 13C_beta_Tyr_CT19cells_mCherry_hetNOE_presat_08092011.fid, 13C_beta_Tyr_CT19cells_mCherry_hetNOE_08092011.fid 13C_beta_Tyr_CT19cells_mCherry_HChetNOE_NOSat_04142012.fid 13C_beta_Tyr_CT19cells_mCherry_HChetNOE_Sat_04142012.fid

Protein	1mM **13C-beta-Tyr mRojoB**
Buffer conditions	20mM d-11 Tris pH=7, 50mM NaCl, 0.15mM TSP, 100%D2O
Sample conditions	37C
Spectrometer	Inova600
Sequence	•gCT1T2_trosy_working.c T1='y' relaxT=0, 100ms, 200ms(2x), 400ms, 600ms, 800ms, 1000ms •gCT1T2_trosy_working.c T2='y' relaxT=0ms, 2ms, 4ms, 6ms, 8ms, 10ms, 14ms •gHChetNOE.c
Date	Sample made 9/2011, Experiments run 10/11
File Locations	**T1:** Data/Fluorescent_Proteins/mRojoB/13C/13C_relaxation/ T1_T2_hetNOE_600MHz/13C_T1/10192011_CT1_mRojoB_data **T1rho:** Data/Fluorescent_Proteins/mRojoB/13C/13C_relaxation/ T1_T2_hetNOE_600MHz/13C_T2/10102011_CT2_experiment **NOE:** Data/Fluorescent_Proteins/mRojoB/13C/13C_relaxation/ T1_T2_hetNOE_600MHz/13C_beta_Tyr_mRojoB_gHChetNOE_ Presat_short2_Sample2_10262011.fid/sum.ft2, 13C_beta_Tyr_mRojoB_gHChetNOE_noPresat_ Sample2_10262011.fid

Protein	0.85mM **13C-beta-Tyr mRaspberry**
Buffer conditions	20mM d-11Tris pH=7, 50mM NaCl, 5mM DTT, 0.15mM TSP, 100%D2O
Sample conditions	37C
Spectrometer	Inova800
Sequence	•gCT1T2_trosy_working, T1='y' relaxT=0, 100ms, 200ms, 300ms, 400ms, 600ms(2x), 800ms, 1000ms, 1200ms, •gCT1T2_trosy_working, T2='y' relaxT=2ms, 4ms(2x), 6ms, 8ms, 10ms, 16ms, 20ms •gHChetNOE.c
Date	Sample made 10/2011, Experiments run 10/2011 and 4/2012
File Locations:	**T1:** Data/Fluorescent_Proteins/mRaspberry/CT1 **T2:** Data/Fluorescent_Proteins/mRaspberry/CT2 **NOE:**13C_beta_Tyr_mRaspberry_gHChetNOE_presat_10252011.fid, 13C_beta_Tyr_mRaspberry_gHChetNOE_NOpresat_10252011.fid 13C_beta_Tyr_mRaspberry_gHChetNOE_NOpresat_04092012.fid 13C_beta_Tyr_mRaspberry_gHChetNOE_presat_04092012.fid

Table A.3: ^{15}N NMR relaxation dispersion experimental parameters

Protein	0.5mM **15N mCherry**
Buffer conditions	20mM Tris pH=7, 50mM NaCl, 0.15mM TSP, 5mM DTT, 10%D2O
Sample conditions	37°C
Spectrometer	Inova800
Sequence	•N15_CPMG_Rex_NH_trosy_lek_600.c, time_T2=0.02s, ncyc=0,20,3,19,5,18,16,7,14,9,12,10
Date	Protein made 12/2011 experiments run 04/2012
File Locations	Data/Fluorescent_Proteins/mCherry/relaxation/

Protein	0.5mM **15N mRojoB**
Buffer conditions	20mM Tris pH=7, 50mM NaCl, 5mM DTT, 0.15mM TSP, 10%D2O
Sample conditions	37°C
Spectrometer	Inova800
Sequence	•N15_CPMG_Rex_NH_trosy_lek_600.c, time_T2=0.02s, ncyc=0,20,3,19,5,18,16,7,14,9,12,10
Date	Protein made 02/2012, experiments run 04/2012
File Locations	Data/Fluorescent_Proteins/mRojoB/15N_relaxation/15N_CPMG

Protein	0.5mM **15N mRaspberry**
Buffer conditions	20mM Tris pH=7, 50mM NaCl, 5mM DTT, 0.15mM TSP, 10%D2O
Sample conditions	37°C
Spectrometer	Inova800
Sequence	•N15_CPMG_Rex_NH_trosy_lek_600.c, time_T2=0.02s, ncyc=0,20,3,19,5,18,16,7,14,9,12,10
Date	Protein made 06/2011, experiments run 04/2012
File Locations	Data/Fluorescent_Proteins/mRaspberry/N15_relaxation/

Table A.4: ^{1}H^{13}C ILV methyl NMR relaxation dispersion experimental parameters

Protein	0.2mM **1H13C ILV methyl 2H15N mCherry**
Buffer conditions	20mM d-11 Tris pH=7, 50mM NaCl, 0.15mM TSP, 5mM DTT, 100%D2O
Sample conditions	37C
Spectrometer	Inova800
Sequence	•hmqc_CH3_exchange_bigprotein_800_lek_v4.c, time_T2=0.04s, ncyc_cp=0,1,40,2,30,3,20,4,15,5,10
Date	Protein made 11/2011 experiment run 11/2011
File Locations	Data/Fluorescent_Proteins/mCherry/ILV

Protein	0.2mM **1H13C ILV methyl 2H15N mRojoB**
Buffer conditions	20mM d-11 Tris pH=7, 50mM NaCl, 5mM DTT, 0.15mM TSP, 100%D2O
Sample conditions	37C
Spectrometer	Inova800
Sequence	•hmqc_CH3_exchange_bigprotein_800_lek_v4.c, time_T2=0.04s, ncyc_cp=0,1,40,2,30,3,20,4,15,5,10
Date	Protein expressed 11/2011, experiments run 12/2011
File Locations	Data/Fluorescent_Proteins/mRojoB/13C/13C_relaxation/ILV_CPMG

Table A.5: Relevant spectral parameters for a subset of the NMR collected.[a]

Experiment	B_0	Temp.	pH	np	ni/ni2	sw	sw1/sw2	nt	tof	dof/dof2	d1	Conc.	Buffer	Label	File Name	Pulse Sequence	Other
mCherry Assignments																	
mCherry 1H15N HSQC TROSY	800	25°C	7	4096	200	13020.8	2844.4	20	-269	/1583	1.7	0.6 mM	SB	1H15N	gNhsqc_mCherry_25C_pH7_050311.fid	gNhsqc.c	
mCherry 1H15N HSQC TROSY	800	25°C	8	4096	200	13020.8	2844.4	20	-261	/1583	1.7	0.6 mM	SB	1H15N	gNhsqc_mCherry_25C_042811.fid	gNhsqc.c	
mCherry 1H15N HSQC TROSY	800	30°C	7	4096	200	13020.8	2844.4	20	-269	/1583	1.7	0.6 mM	SB	1H15N	gNhsqc_mCherry_30C_pH7_050411.fid	gNhsqc.c	
mCherry 1H15N HSQC TROSY	800	30°C	8	4096	200	13020.8	2844.4	20	-261	/1583	1.7	0.6 mM	SB	1H15N	gNhsqc_mCherry_30C_042811.fid	gNhsqc.c	
mCherry 1H15N HSQC TROSY	800	35°C	7	4096	200	13020.8	2844.4	20	-269	/1583	1.7	0.6 mM	SB	1H15N	gNhsqc_mCherry_35C_pH7_050411.fid	gNhsqc.c	
mCherry 1H15N HSQC TROSY	800	35°C	8	4096	200	13020.8	2844.4	20	-261	/1583	1.7	0.6 mM	SB	1H15N	gNhsqc_mCherry_35C_042711.fid	gNhsqc.c	
mCherry HNCO TROSY	600	30°C	7	2048	53/53	11990	3770/1944	12	-250	12744/1756	1.5	0.6 mM	SB	1H13C15N	13C15NmCherry_gHNCO_05132011.fid	ghn_co.c	
mCherry HNCACB TROSY	800	30°C	7	4096	48/48	11261	12000/2500	16	-272	-10338/1759	1.6	0.6 mM	SB	1H13C15N	13C15NmCherry_hncacb_05182011.fid	ghn_cacb.c	
mCherry CBCA(CO)NH TROSY	800	30°C	7	4096	42/42	11261	12000/2500	32	-261	-10338/1759	1.6	0.6 mM	SB	1H13C15N	13C15NmCherry_f1f2f3_gcbcaconh_05272011.fid	gcbca_co_nh.c	
mCherry 1H-1H NOESY 1H15N HSQC	600	30°C	7	2048	104/40	11990	7400/2000	8	-243	/1730	1.5	0.6 mM	SB	1H15N	15NmCherry_gnoesyNhsqc_mix250_07152011.fi	gnoesyNhsqc.c	
1H15N HSQC																	
mRojoB 1H15 HSQC TROSY	600	30°C	7	2048	152	11990	2000	24	-243	/1730	1.7	0.8 mM	SB	1H15N	15NmRojoB_gNhsqc_laj_06092011.fid	gNhsqc.c	
mRaspberry 1H15N HSQC TROSY	600	30°C	7	2048	144	11990	2000	40	-243	/1730	1.7	0.5 mM	SB	1H15N	15NmRaspberry_gNhsqc_laj_06082011.fid	gNhsqc.c	

Table A.5: Continued from previous page

Experiment	B_0	Temp.	pH	np	ni/ni2	sw	sw1/sw2	nt	tof	dof/dof2	d1	Conc.	Buffer	Label	File Name	Pulse Sequence	Other
tdTomato 1H15N HSQC TROSY	800	37°C	7	4096	128	13020	3084	8	-269	/1730	1.7	0.6 mM	SB	2H15N, 1H14N Ala	2H15NtdTomato_1H14Nala_TT_B4_Nhsqc_1H_afterFilter_10112012.fid	gNhsqc.c	
mRojoA 1H15 HSQC TROSY	600	30°C	7	2048	160	11990	2000	40	-243	/1730	1.7	0.5 mM	SB	1H15N	15NmRojoA_gNhsqc_laj_06072011.fid	gNhsqc.c	
mRouge 1H15 HSQC TROSY	600	30°C	7	2048	152	11990	2000	103	-245	/1730	1.7	0.2 mM	SB	1H15N	15NmRouge_GFP_gNhsqc_laj_06082011.fid	gNhsqc.c	
GFP 1H15 HSQC TROSY	600	35°C	8	2048	180	11990	2000	56	-240	/1730	2	0.5 mM	a*	1H15N	eGFP_gNhsqc_ni180_nt56_02212011laj.fid	gNhsqc.c	
13C																	
mCherry 1H12C Carbon HSQC	600	30°C	7	2048	128	11990	6000	16	-243	-8396	1.5	0.6 mM	SB	1H15N	15NmCherry_gChsqc_arom_07182011.fid	gChsqc.c	tCH=0.0018, lambda=0.0016,arom='y'
mCherry 1H13C HSQC	600	30°C	7	2048	128	11990	21000	8	-250	-8396	1.5	0.6 mM	SB	1H13C15N	13C15NmCherry_gChsqc_05132011.fid	gChsqc.c	tCH=0.00145, lambda=0.0013, arom='y'
mCherry 1H13C TYR HSQC (dseq=wurst140)	600	30°C	7	2048	128	11990	6000	16	-230	-8396	1.5	0.6 mM	b*	1H13C Tyr C-beta	13C_beta_Tyr_CT19cells_mCherry_gChsqc_arom_07182011.fid	gChsqc.c	tCH=0.00145, lambda=0.0013, arom='y'
mCherry 1H13C TYR 1D Carbon HDEC	800	30°C	7	130048	---	50000	---	7000	-2500	---	1	0.6 mM	b*	1H13C Tyr C-beta	Carbon_decoupling_13C_beta_Tyr_mCherry_07132011.fid	s2pul.c	Decoupling during detection
mCherry 1H13C TYR 1D Carbon No HDEC	800	30°C	7	130048	---	50000	---	7000	-2500	---	1	0.6 mM	b*	1H13C Tyr C-beta	Carbon_NOdecoupling_13C_beta_Tyr_mCherry_07132011.fid	s2pul.c	No decoupling during detection
mRojoB 1H13C TYR HSQC	600	37°C	7	2048	128	11990	6000	16	-226	-5955	1.5	1 mM	b*	1H13C Tyr C-beta	13C_beta_Tyr_mRojoB_gChsqc_arom_09162011.fid	gChsqc.c	tCH=0.00145, lambda=0.0013,arom='y'
mRojoB 1H13C TYR HSQC No HDEC	600	37°C	7	2048	128	11990	6000	64	-226	-5955	1.5	1 mM	b*	1H13C Tyr C-beta	13C_beta_Tyr_mRojoB_gChsqc_arom_noHdec_09192011.fid	gChsqc.c	tCH=0.00145, lambda=0.0013,arom='y'
mRaspberry 1H13C TYR HSQC	800	37°C	7	2048	64	11261	8000	16	-287	-9532	1.5	0.9 mM	b*	1H13C Tyr C-beta	13C_beta_Tyr_mRaspberry_gChsqc_arom_10252011.fid	gChsqc.c	tCH=0.00145, lambda=0.0016,arom='y'

Table A.5: Continued from previous page

Experiment	B_0	Temp.	pH	np	ni/ni2	sw	sw1/sw2	nt	tof	dof/dof2	d1	Conc.	Buffer	Label	File Name	Pulse Sequence	Other
15N Relaxation																	
mCherry 1H15N T1 (TROSY)	600	37°C	7	2048	128	11990	2120	16	-240	/1802	1.5	0.6 mM	SB	1H15N	15NmCherry_NT1_relaxT0_08172011.fid	gNhsqc.c	relaxT arrayed, T1='y'
mCherry 1H15N T1ρ (decoupled)	600	37°C	7	2048	128	11990	2120	32	-240	/1802	1.5	0.6 mM	SB	1H15N	15NmCherry_NT1rho_relaxT0_08192011.fid	gNhsqc.c	relaxT arrayed, T1rho='y'
mCherry 1H15N HETNOE presat (decoupled)	600	37°C	7	1024	128	90001	2120	48	-239	/1802	1.5	0.6 mM	SB	1H15N	15NmCherry_HNhetNOE_presat_08252011.fid	N15NOE_lek_pfg_sel_enh.c	ncyc 600, tpwrnoe=41
mCherry 1H15N HETNOE reference (decoupled)	600	37°C	7	1024	128	90001	2120	48	-239	/1802	1.5	0.6 mM	SB	1H15N	15NmCherry_HNhetNOE_NOpresat_08252011.fid	N15NOE_lek_pfg_sel_enh.c	ncyc600 and tpwrnoe=-16
mRaspberry 1H15N T1 (TROSY)	600	37°C	7	2048	128	11990	2120	16	-222	/1215	1.7	0.7 mM	SB	1H15N	15NmRaspberry_gNhsqc_T1_relaxTarray_01072013.fid	gNhsqc.c	relaxT arrayed, T1='y'
mRaspberry 1H15N T1ρ (decoupled)	600	37°C	7	2048	128	11990	2120	16	-222	/1215	1.7	0.7 mM	SB	1H15N	15NmRaspberry_gNhsqc_T1rho_relaxTarray_01032013.fid	gNhsqc.c	relaxT arrayed, T1rho='y'
mRaspberry 1H15N T2 (decoupled)	600	37°C	7	2048	128	11990	2120	16	-222	/1215	1.7	0.7 mM	SB	1H15N	15NmRaspberry_gNhsqc_T2_relaxTarray_01032013.fid	gNhsqc.c	relaxT arrayed, T2='y'
mRaspberry 1H15N HETNOE presat (decoupled)	600	37°C	7	4096	128	11259	2120	128	-222	/1215	3	0.7 mM	SB	1H15N	15NmRaspberry_g_NNOE_satON_01072013.fid	g_NNOE.c	ncyc=500, tpwrnoe=55, relaxT=3
mRaspberry 1H15N HETNOE reference (decoupled)	600	37°C	7	4096	128	11259	2120	128	-222	/1215	3	0.7 mM	SB	1H15N	15NmRaspberry_g_NNOE_satOFF_01072013.fid	g_NNOE.c	ncyc=500, tpwrnoe=55, relaxT=0
mRaspberry 1H15N T1 (TROSY)	800	37°C	7	2048	128	11261	2844	16	-267	/1583	1.5	0.5 mM	SB	1H15N	15NmRaspberry_NT1_relaxT0_01052012.fid	gNT1T2.c	relaxT arrayed, T1='y'

Table A.5: Continued from previous page

Experiment	B_0	Temp.	pH	np	ni/ni2	sw	sw1/sw2	nt	tof	dof/dof2	d1	Conc.	Buffer	Label	File Name	Pulse Sequence	Other
mRaspberry 1H13C HETNOE presat (duplicate)	800	37°C	7	2048	128	12019	8000	88	-286	8552	3	0.9 mM	b*	1H13C Tyr C-beta	13C_beta_Tyr_mRaspberry_gHChetNOE_presat_04092012.fid	gHChetNOE.c	Hsat_flg='y', sattime=3
mRaspberry 1H13C HETNOE reference (duplicate)	800	37°C	7	2048	128	12019	8000	88	-286	8552	3	0.9 mM	b*	1H13C Tyr C-beta	13C_beta_Tyr_mRaspberry_gHChetNOE_NOpresat_04092012.fid	gHChetNOE.c	Hsat_flg='n', sattime=3
mRasberry 1H13C TYR T1 TROSY (glycerol)	800	37°C	7	2048	64	12019	8000	32	-287	8552	1.2	0.9 mM	c*	1H13C Tyr C-beta	13C_beta_Tyr_mRaspberry_gCT1T2_trosy_working_T1_relaxT0ms_10272011.fid	gCT1T2_trosy_working.c	relaxT arrayed, T1='y', taua=taub=0.0015
mRaspberry 1H13C TYR T2 TROSY (glycerol)	800	37°C	7	2048	64	12019	8000	32	-305	8552	1.2	0.9 mM	c*	1H13C Tyr C-beta	13C_beta_Tyr_mRaspberry_glycerol_gCT1T2_trosy_working_T2_0ms_10292011.fid	gCT1T2_trosy_working.c	relaxT arrayed, T2='y', taua=taub=0.0015
mRojoB 1H13C TYR T1 TROSY	600	37°C	7	2048	64	12019	6000	192	-227	7616	1.2	1 mM	b*	1H13C Tyr C-beta	13C_beta_Tyr_mRojoB_gCT1T2_trosy_working_T1_0_10192011.fid	gCT1T2_trosy_working.c	relaxT arrayed, T1='y', taua=taub=0.0015
mRojoB 1H13C TYR T2 TROSY	600	37°C	7	2048	64	11990	6000	64	-227	7616	1.2	1 mM	b*	1H13C Tyr C-beta	13C_beta_Tyr_mRojoB_gCT1T2_trosy_working_T2_relaxT0_Sample2_10112011.fid	gCT1T2_trosy_working.c	relaxT arrayed, T2='y', taua=taub=0.0015
mRojoB 1H13C HETNOE presat1	600	37°C	7	2048	64	11990	6000	200	-227	7616	1.2	1 mM	b*	1H13C Tyr C-beta	13C_beta_Tyr_mRojoB_gHChetNOE_Presat_short_Sample2_10262011.fid	gHChetNOE.c	Hsat_flg='y', sattime=3
mRojoB 1H13C HETNOE presat2 (added to 1)	600	37°C	7	2048	64	11990	6000	216	-227	7616	1.2	1 mM	b*	1H13C Tyr C-beta	13C_beta_Tyr_mRojoB_gHChetNOE_Presat_short2_Sample2_10262011.fid	gHChetNOE.c	Hsat_flg='y', sattime=3
mRojoB 1H13C HETNOE reference	600	37°C	7	2048	64	12004	6000	416	-226	7616	3	1 mM	b*	1H13C Tyr C-beta	13C_beta_Tyr_mRojoB_gHChetNOE_noPresat_Sample2_10262011.fid	gHChetNOE.c	Hsat_flg='n', sattime=3

Table A.5: Continued from previous page

Experiment	B_0	Temp.	pH	np	ni/ni2	sw	sw1/sw2	nt	tof	dof/dof2	d1	Conc.	Buffer	Label	File Name	Pulse Sequence	Other
mCherry 1H13C TYR T1ρ TROSY	600	37°C	7	2048	128	11256	6000	32	-227	7616	1.5	0.6 mM	b*	1H13C Tyr C-beta	13C_beta_Tyr_CT19cells_mCherry_T1rho_08092011.fid	C13T1rho_trosy_lek_randomsat_600c.c	relaxT arrayed, taua=taub=0.0016
mCherry 1H13C HETNOE presat	600	37°C	7	2048	128	11990	6000	128	-227	7616	3	0.6 mM	b*	1H13C Tyr C-beta	13C_beta_Tyr_CT19cells_mCherry_hetNOE_presat_08092011.fid	gHChetNOE.c	Hsat_flg='y', sattime=3
mCherry 1H13C HETNOE reference	600	37°C	7	2048	128	11990	6000	128	-227	7616	3	0.6 mM	b*	1H13C Tyr C-beta	13C_beta_Tyr_CT19cells_mCherry_hetNOE_08092011.fid	gHChetNOE.c	Hsat_flg='n', sattime=3
mCherry 1H13C HETNOE presat (duplicate)	600	37°C	7	4096	128	12001	6000	192	-227	7616	3	0.6 mM	b*	1H13C Tyr C-beta	13C_beta_Tyr_CT19cells_mCherry_HChetNOE_Sat_04142012.fid	gHChetNOE.c	Hsat_flg='y', sattime=3
mCherry 1H13C HETNOE reference (duplicate)	600	37°C	7	4096	128	12001	6000	192	-227	7616	3	0.6 mM	b*	1H13C Tyr C-beta	13C_beta_Tyr_CT19cells_mCherry_HChetNOE_NOSat_04142012.fid	gHChetNOE.c	Hsat_flg='n', sattime=3
mRasberry 1H13C TYR T1 TROSY	800	37°C	7	2048	64	12019	8000	32	-287	8552	1.2	0.9 mM	b*	1H13C Tyr C-beta	13C_beta_Tyr_mRaspberry_gCT1T2_trosy_working_T1_relaxT0ms_10272011.fid	gCT1T2_trosy_working.c	relaxT arrayed, T1='y', taua=taub=0.0015
mRaspberry 1H13C TYR T2 TROSY	800	37°C	7	2048	64	12019	8000	32	-287	8552	1.2	0.9 mM	b*	1H13C Tyr C-beta	13C_beta_Tyr_mRaspberry_gCT1T2_trosy_working_T2_relaxT0ms_10282011.fid	gCT1T2_trosy_working.c	relaxT arrayed, T2='y', taua=taub=0.0015
mRaspberry 1H13C HETNOE presat	800	37°C	7	2048	128	12019	8000	88	-287	8552	3	0.9 mM	b*	1H13C Tyr C-beta	13C_beta_Tyr_mRaspberry_gHChetNOE_presat_10252011.fid	gHChetNOE.c	Hsat_flg='y', sattime=3
mRaspberry 1H13C HETNOE reference	800	37°C	7	2048	128	12019	8000	88	-287	8552	3	0.9 mM	b*	1H13C Tyr C-beta	13C_beta_Tyr_mRaspberry_gHChetNOE_NOpresat_10252011.fid	gHChetNOE.c	Hsat_flg='n', sattime=3

Table A.5: Continued from previous page

Experiment	B_0	Temp.	pH	np	ni/ni2	sw	sw1/sw2	nt	tof	dof/dof2	d1	Conc.	Buffer	Label	File Name	Pulse Sequence	Other
mRaspberry 1H13C HETNOE presat (duplicate)	800	37°C	7	2048	128	12019	8000	88	-286	8552	3	0.9 mM	b*	1H13C Tyr C-beta	13C_beta_Tyr_mRaspberry_gHChetNOE_presat_04092012.fid	gHChetNOE.c	Hsat_flg='y', sattime=3
mRaspberry 1H13C HETNOE reference (duplicate)	800	37°C	7	2048	128	12019	8000	88	-286	8552	3	0.9 mM	b*	1H13C Tyr C-beta	13C_beta_Tyr_mRaspberry_gHChetNOE_NOpresat_04092012.fid	gHChetNOE.c	Hsat_flg='n', sattime=3
mRasberry 1H13C TYR T1 TROSY (glycerol)	800	37°C	7	2048	64	12019	8000	32	-287	8552	1.2	0.9 mM	c*	1H13C Tyr C-beta	13C_beta_Tyr_mRaspberry_gCT1T2_trosy_working_T1_relaxT0ms_10272011.fid	gCT1T2_trosy_working.c	relaxT arrayed, T1='y', taua=taub=0.0015
mRaspberry 1H13C TYR T2 TROSY (glycerol)	800	37°C	7	2048	64	12019	8000	32	-305	8552	1.2	0.9 mM	c*	1H13C Tyr C-beta	13C_beta_Tyr_mRaspberry_glycerol_gCT1T2_trosy_working_T2_0ms_10292011.fid	gCT1T2_trosy_working.c	relaxT arrayed, T2='y', taua=taub=0.0015
mRojoB 1H13C TYR T1 TROSY	600	37°C	7	2048	64	12019	6000	192	-227	7616	1.2	1 mM	b*	1H13C Tyr C-beta	13C_beta_Tyr_mRojoB_gCT1T2_trosy_working_T1_0_10192011.fid	gCT1T2_trosy_working.c	relaxT arrayed, T1='y', taua=taub=0.0015
mRojoB 1H13C TYR T2 TROSY	600	37°C	7	2048	64	11990	6000	64	-227	7616	1.2	1 mM	b*	1H13C Tyr C-beta	13C_beta_Tyr_mRojoB_gCT1T2_trosy_working_T2_relaxT0_Sample2_10112011.fid	gCT1T2_trosy_working.c	relaxT arrayed, T2='y', taua=taub=0.0015
mRojoB 1H13C HETNOE presat1	600	37°C	7	2048	64	11990	6000	200	-227	7616	1.2	1 mM	b*	1H13C Tyr C-beta	13C_beta_Tyr_mRojoB_gHChetNOE_Presat_short_Sample2_10262011.fid	gHChetNOE.c	Hsat_flg='y', sattime=3
mRojoB 1H13C HETNOE presat2 (added to 1)	600	37°C	7	2048	64	11990	6000	216	-227	7616	1.2	1 mM	b*	1H13C Tyr C-beta	13C_beta_Tyr_mRojoB_gHChetNOE_Presat_short2_Sample2_10262011.fid	gHChetNOE.c	Hsat_flg='y', sattime=3
mRojoB 1H13C HETNOE reference	600	37°C	7	2048	64	12004	6000	416	-226	7616	3	1 mM	b*	1H13C Tyr C-beta	13C_beta_Tyr_mRojoB_gHChetNOE_noPresat_Sample2_10262011.fid	gHChetNOE.c	Hsat_flg='n', sattime=3

Table A.5: Continued from previous page

Experiment	B_0	Temp.	pH	np	ni/ni2	sw	sw1/sw2	nt	tof	dof/dof2	d1	Conc.	Buffer	Label	File Name	Pulse Sequence	Other
15N Relaxation Dispersion																	
mCherry 1H15N CPMG Relaxation Dispersion	800	37°C	7	4096	128	15060	2844	16	-268	/1583	1.7	0.5 mM	SB	1H15N	N15_CPMG_Rex_NH_trosy_lek_600_15NmCherry_37C_04062012.fid	N15_CPMG_Rex_NH_trosy_lek_600.c	array ncyc
mRaspberry 1H15N CPMG Relaxation Dispersion	800	37°C	7	4096	96	15060	2844	16	-268	/1583	1.7	0.5 mM	SB	1H15N	15N_CPMG_mRaspberry_04112012.fid	N15_CPMG_Rex_NH_trosy_lek_600.c	array ncyc
mRojoB 1H15N CPMG Relaxation Dispersion	800	37°C	7	4096	128	15060	2844	16	-267	/1583	1.7	0.5 mM	SB	1H15N	15NmRojoB_15N_CPMG_array_ncyc_04052012.fid	N15_CPMG_Rex_NH_trosy_lek_600.c	array ncyc
13C ILV HMQC																	
mCherry 1H13C ILV HMQC	800	37°C	7	4096	128	20161	5430	80	-269	-15162	1.5	0.2 mM	d*	2H15N, 1H13C ILV	Chmqc_ILV_mCherry_11172011.fid	hmqc_c13_800_methyl_lek.c	
mRojoB 1H13C ILV HMQC	800	37°C	7	2048	64	10080	5430	16	-270	-15162	1.5	0.2 mM	d*	2H15N, 1H13C ILV	Chmqc_mRojoB_ILV_11302011.fid	hmqc_c13_800_methyl_lek.c	
13C Relaxation Dispersion																	
mCherry 1H13C ILV HMQC Relaxation Dispersion (Ile)	800	37°C	7	2048	72	12019	5500	24	-271	-16906	1.7	0.2 mM	d*	2H15N, 1H13C ILV	CPMG_ILV_Ile_mCherry_11302011.fid	hmqc_CH3_exchange_bigprotein_800_lek_v4.c	array ncyc_cp
mCherry 1H13C ILV HMQC Relaxation Dispersion (Leu Val)	800	37°C	7	2048	72	12019	5500	24	-271	-16906	1.7	0.2 mM	d*	2H15N, 1H13C ILV	CPMG_ILV_LeuVal_mCherry_11282011.fid	hmqc_CH3_exchange_bigprotein_800_lek_v4.c	array ncyc_cp

Table A.5: Continued from previous page

Experiment	B_0	Temp.	pH	np	ni/ni2	sw	sw1/sw2	nt	tof	dof/dof2	d1	Conc.	Buffer	Label	File Name	Pulse Sequence	Other
mRojoB 1H13C ILV HMQC Relaxation Dispersion (Ile)	800	37°C	7	2048	72	12019	5500	24	-271	-16906	1.7	0.2 mM	d*	2H15N, 1H13C ILV	CPMG_Ile_mRojoB_ILV_12022011.fid	hmqc_CH3_exchange_bigprotein_800_lek_v4.c	array ncyc_cp
mRojoB 1H13C ILV HMQC Relaxation Dispersion (Leu Val)	800	37°C	7	2048	72	12019	5500	24	-270	-14897	1.7	0.2 mM	d*	2H15N, 1H13C ILV	CPMG_LeuVal_mRojoB_ILV_12012011.fid	hmqc_CH3_exchange_bigprotein_800_lek_v4.c	array ncyc_cp
mCherry Tyrosine C-beta Relaxation Dispersion	600	37°C	7	4096	128	18002	6000	40	-226	7617	1.4	0.6 mM	b*	1H13C Tyr C-beta	13C_beta_Tyr_CT19cells_mCherry_13C_CPMG_Rex_ncyc0_timeT2_20ms_45C_07272011.fid	13C_CPMG_Rex_CH_trosy_lek_600v2.c	ncyc=0,1,20
HDX																	
mCherry 1H15N BEST HSQC TROSY (series)	800	37°C	7									0.6 mM	e*	1H15N	Folder: HDX_Dec2011	best_Nhsqc_trosy.c	See HDX table
mRojoB 1H15N BEST HSQC TROSY (series)	800	37°C	7									0.6 mM	e*	1H15N	Folder: HDX	best_Nhsqc_trosy.c	See HDX table
tdTomato 2H15N, 1H14N ala, HSQC TROSY (series)	800	37°C	7									0.6 mM	e*	2H15N, 1H14N Ala	Folder: HDX_deuterated_1HAla	gNhsqc.c	See HDX table

[a]The standard buffer used for the experiments were 20 mM Tris, 50 mM NaCl, 5 mM DTT, 0.15 mM TSP and 10% D_2O except when noted with a letter and asterisk. a* GFP HSQC Buffer: 50 mM Tris, 100 mM NaCl, 5 mM DTT, 0.15 mM TSP, 10% D_2O. b* All samples ^{13}C-labeled at Tyrosine C beta: 20 mM d-11 Tris, 50 mM NaCl, 0.15 mM TSP, >99% D_2O. c* Samples of mRaspberry used for glycerol experiments were in standard buffer with 20% v/v d-8 glycerol. (Two ^{13}C T_1 and T_2NMR relaxation experiments performed on mRaspberry were also in the presence of 20% v/v d-8 glycerol as noted in the Experiment column of the table.) d* The ILV labeled samples were in 20 mM d-11 Tris, 50 mM NaCl, 0.15 mM TSP, 10% D_2O. e* The samples used for hydrogen deuterium exchange experiments were in standard buffer with >99% D_2O

Table A.6: NMR spectra collected for the hydrogen-deuterium exchange experiments.[a]

Spectrum	Seconds from Start of Experiment
tdTomato	
2H15NtdTomato_1H14Nala_TT_Nhsqc_1stAfterExchange_10122012.fid	1317
2H15NtdTomato_1H14Nala_TT_Nhsqc_2ndAfterExchange_10122012.fid	2277
2H15NtdTomato_1H14Nala_TT_Nhsqc_3rdAfterExchange_10122012.fid	3237
2H15NtdTomato_1H14Nala_TT_Nhsqc_4thAfterExchange_10122012.fid	4197
2H15NtdTomato_1H14Nala_TT_Nhsqc_5thAfterExchange_10122012.fid	5157
sum4_7	**5637**
2H15NtdTomato_1H14Nala_TT_Nhsqc_6thAfterExchange_10122012.fid	6117
2H15NtdTomato_1H14Nala_TT_Nhsqc_7thAfterExchange_10122012.fid	7077
2H15NtdTomato_1H14Nala_TT_Nhsqc_8thAfterExchange_10122012.fid	8037
15N2HtdTomato_1H14Nala_TT_Nhsqc_1H_001.fid	**10656**
15N2HtdTomato_1H14Nala_TT_Nhsqc_1H_002.fid	**14570**
15N2HtdTomato_1H14Nala_TT_Nhsqc_1H_003.fid	**18484**
15N2HtdTomato_1H14Nala_TT_Nhsqc_1H_004.fid	**22398**
15N2HtdTomato_1H14Nala_TT_Nhsqc_1H_005.fid	**26312**
15N2HtdTomato_1H14Nala_TT_Nhsqc_1H_006.fid	**30226**
15N2HtdTomato_1H14Nala_TT_Nhsqc_1H_007.fid	**34140**
15N2HtdTomato_1H14Nala_TT_Nhsqc_1H_008.fid	**38054**
15N2HtdTomato_1H14Nala_TT_Nhsqc_1H_009.fid	**41968**
15N2HtdTomato_1H14Nala_TT_Nhsqc_1H_010.fid	**45882**
15N2HtdTomato_1H14Nala_TT_Nhsqc_1H_011.fid	**49796**
15N2HtdTomato_1H14Nala_TT_Nhsqc_1H_012.fid	**53710**
15N2HtdTomato_1H14Nala_TT_Nhsqc_1H_013.fid	**57624**
15N2HtdTomato_1H14Nala_TT_Nhsqc_1H_014.fid	**61538**
15N2HtdTomato_1H14Nala_TT_Nhsqc_1H_015.fid	**65452**
15N2HtdTomato_1H14Nala_TT_Nhsqc_1H_016.fid	**69366**
15N2HtdTomato_1H14Nala_TT_Nhsqc_3H_001.fid	**90102**
15N2HtdTomato_1H14Nala_TT_Nhsqc_3H_002.fid	**94817**
15N2HtdTomato_1H14Nala_TT_Nhsqc_3H_003.fid	**106936**
15N2HtdTomato_1H14Nala_TT_Nhsqc_3H_004.fid	**119055**
15N2HtdTomato_1H14Nala_TT_Nhsqc_3H_005.fid	**131174**
15N2HtdTomato_1H14Nala_TT_Nhsqc_3H_006.fid	**143293**
15N2HtdTomato_1H14Nala_TT_Nhsqc_3H_007.fid	**155412**
15N2HtdTomato_1H14Nala_TT_Nhsqc_3H_008.fid	**167531**
15N2HtdTomato_1H14Nala_TT_Nhsqc_1H_10242012.fid	**1041070**
15N2HtdTomato_1H14Nala_TT_Nhsqc_1H_11082012.fid	**2334780**
15N2HtdTomato_1H14Nala_TT_Nhsqc_1H_12192013.fid	**5900830**

Table A.6: Continued from previous page

Spectrum	Seconds from Start of Experiment
mCherry	
best_Nhsqc_trosy_1st_exchange_15NmCherry_nt4_12082011.fid	675
best_Nhsqc_trosy_2nd_exchange_15NmCherry_nt4_12082011.fid	843
best_Nhsqc_trosy_3rd_exchange_15NmCherry_nt4_12082011.fid	1011
best_Nhsqc_trosy_4th_exchange_15NmCherry_nt4_12082011.fid	1179
best_Nhsqc_trosy_5th_exchange_15NmCherry_nt8_12082011.fid	1428
best_Nhsqc_trosy_6th_exchange_15NmCherry_nt8_12082011.fid	1758
best_Nhsqc_trosy_7th_exchange_15NmCherry_nt8_12082011.fid	2088
best_Nhsqc_trosy_8th_exchange_15NmCherry_nt8_12082011.fid	2418
best_Nhsqc_trosy_9th_exchange_15NmCherry_nt16_12082011.fid	2908
best_Nhsqc_trosy_10th_exchange_15NmCherry_nt16_12082011.fid	3561
best_Nhsqc_trosy_11th_exchange_15NmCherry_nt32_12082011.fid	4539
best_Nhsqc_trosy_12th_exchange_15NmCherry_nt32_12082011.fid	5839
sum11th_12th_13th_exchange_nt96equiv_12212011.ft2	**5839**
best_Nhsqc_trosy_13th_exchange_15NmCherry_nt32_12082011.fid	7139
best_Nhsqc_trosy_14th_exchange_15NmCherry_nt96_12082011.fid	**9734**
15NmCherry_12082011_besthsqc_1H_001.fid	**14195**
15NmCherry_12082011_besthsqc_1H_array_001.fid	**19235**
15NmCherry_12082011_besthsqc_1H_array2_001.fid	**27650**
15NmCherry_12082011_besthsqc_3H001.fid	**36363**
15NmCherry_12082011_besthsqc_3H002.fid	**47451**
15NmCherry_12082011_besthsqc_3H003.fid	**58539**
15NmCherry_12082011_besthsqc_3H004.fid	**69627**
15NmCherry_12082011_besthsqc_3H005.fid	**80715**
15NmCherry_12082011_besthsqc_3H006.fid	**91803**
15NmCherry_12082011_besthsqc_3H007.fid	**102891**
15NmCherry_12082011_besthsqc_3H008.fid	**113979**
15NmCherry_12082011_besthsqc_3H009.fid	**125067**
15NmCherry_12082011_besthsqc_3H010.fid	**136155**
15NmCherry_12082011_besthsqc_3H011.fid	**147243**
15NmCherry_12082011_besthsqc_3H012.fid	**158331**
15NmCherry_12082011_besthsqc_3H013.fid	**169419**
15NmCherry_12082011_besthsqc_3H014.fid	**180507**
15NmCherry_12082011_besthsqc_3H015.fid	**191595**
15NmCherry_12082011_besthsqc_3H016.fid	**202683**
15NmCherry_12082011_besthsqc_3H017.fid	**213771**
15NmCherry_12082011_besthsqc_3H018.fid	**224859**
15NmCherry_12082011_besthsqc_3H019.fid	**235947**
15NmCherry_12082011_besthsqc_3H020.fid	**247035**

Table A.6: Continued from previous page

Spectrum	Seconds from Start of Experiment
mCherry (continued)	
15NmCherry_12082011_besthsqc_3H021.fid	**258123**
15NmCherry_12082011_besthsqc_3H022.fid	**269211**
15NmCherry_12082011_besthsqc_3H023.fid	**280299**
15NmCherry_12082011_besthsqc_3H024.fid	**291387**
15NmCherry_12082011_besthsqc_3H025.fid	**302475**
15NmCherry_12082011_besthsqc_3H026.fid	**313563**
15NmCherry_12082011_besthsqc_3H027.fid	**501905**
15NmCherry_12082011_besthsqc_3H028_12202011.fid	**1018426**
15NmCherry_12082011_besthsqc_3H029_12292011.fid	**1798115**
15NmCherry_12082011_besthsqc_3H030_01052012.fid	**2406858**
15NmCherry_12082011_besthsqc_1H031_01272012.fid	**4326292**
15NmCherry_12082011_besthsqc_1H032_02162012.fid	**6032052**
mRojoB	
15NmRojoB_1st_after_exchange_nt4_02162012.fid	667
15NmRojoB_2nd_after_exchange_nt4_02162012.fid	850
15NmRojoB_3rd_after_exchange_nt4_02162012.fid	1033
15NmRojoB_4th_after_exchange_nt4_02162012.fid	1216
15NmRojoB_5th_after_exchange_nt8_02162012.fid	1478
15NmRojoB_6th_after_exchange_nt8_02162012.fid	1822
15NmRojoB_7th_after_exchange_nt8_02162012.fid	2166
15NmRojoB_8th_after_exchange_nt8_02162012.fid	2510
15NmRojoB_9th_after_exchange_nt16_02162012.fid	3017
15NmRojoB_10th_after_exchange_nt16_02162012.fid	3685
15NmRojoB_11th_after_exchange_nt32_02162012.fid	4677
15NmRojoB_12th_after_exchange_nt32_02162012.fid	5991
sum11th_12th_13th_exchange_nt96equiv_mRojoB.ft2	**5991**
15NmRojoB_13th_after_exchange_nt32_02162012.fid	7306
15NmRojoB_besthsqc_nt96_1H_001.fid	**9974**
15NmRojoB_besthsqc_nt96_1H_002.fid	**13877**
15NmRojoB_besthsqc_nt96_1H_003.fid	**17780**
15NmRojoB_besthsqc_nt96_1H_004.fid	**21683**
15NmRojoB_besthsqc_nt96_1H_005.fid	**25586**
15NmRojoB_besthsqc_nt96_1H_006.fid	**29489**
15NmRojoB_besthsqc_nt96_1H_007.fid	**33392**
15NmRojoB_besthsqc_nt96_1H_008.fid	**37295**
15NmRojoB_besthsqc_nt96_1H_009.fid	**41198**
15NmRojoB_besthsqc_nt96_1H_010.fid	**45101**

Table A.6: Continued from previous page

Spectrum	Seconds from Start of Experiment
mRojoB (continued)	
15NmRojoB_besthsqc_nt96_1H_011.fid	**49004**
15NmRojoB_besthsqc_nt96_1H_012.fid	**52907**
15NmRojoB_besthsqc_nt96_1H_013.fid	**56810**
15NmRojoB_besthsqc_nt96_1H_014.fid	**60713**
15NmRojoB_besthsqc_nt96_1H_015.fid	**64616**
15NmRojoB_besthsqc_nt96_1H_016.fid	**68519**
15NmRojoB_besthsq_nt96_4H_001.fid	**77757**
15NmRojoB_besthsq_nt96_4H_002.fid	**92299**
15NmRojoB_besthsq_nt96_4H_003.fid	**106841**
15NmRojoB_besthsq_nt96_4H_004.fid	**121383**
15NmRojoB_besthsq_nt96_4H_005.fid	**135925**
15NmRojoB_besthsq_nt96_4H_006.fid	**150467**
15NmRojoB_besthsq_nt96_4H_007.fid	**165009**
15NmRojoB_besthsq_nt96_4H_008.fid	**179551**
15NmRojoB_besthsq_nt96_4H_009.fid	**194093**
15NmRojoB_besthsq_nt96_4H_010.fid	**208635**
15NmRojoB_besthsq_nt96_4H_011.fid	**223177**
15NmRojoB_besthsq_nt96_4H_012.fid	**237719**
15NmRojoB_besthsq_nt96_4H_013.fid	**252261**
15NmRojoB_besthsq_nt96_4H_014.fid	**266803**
15NmRojoB_besthsq_nt96_4H_015.fid	**281345**
15NmRojoB_besthsq_nt96_4H_016.fid	**295887**
15NmRojoB_besthsq_nt96_4H_017.fid	**310429**
15NmRojoB_besthsq_nt96_4H_018.fid	**324971**
15NmRojoB_besthsqc_nt96_02232012.fid	**591446**
15NmRojoB_besthsqc_nt96_03022012.fid	**1197798**
15NmRojoB_besthsqc_nt96_03292012.fid	**3531609**
15NmRojoB_besthsqc_nt96_04262012.fid	**5954721**

[a] Bold spectra were collected with nt=96. Data were collected at 37°C.

Appendix B

NMR Strip Plots for mCherry Assignments

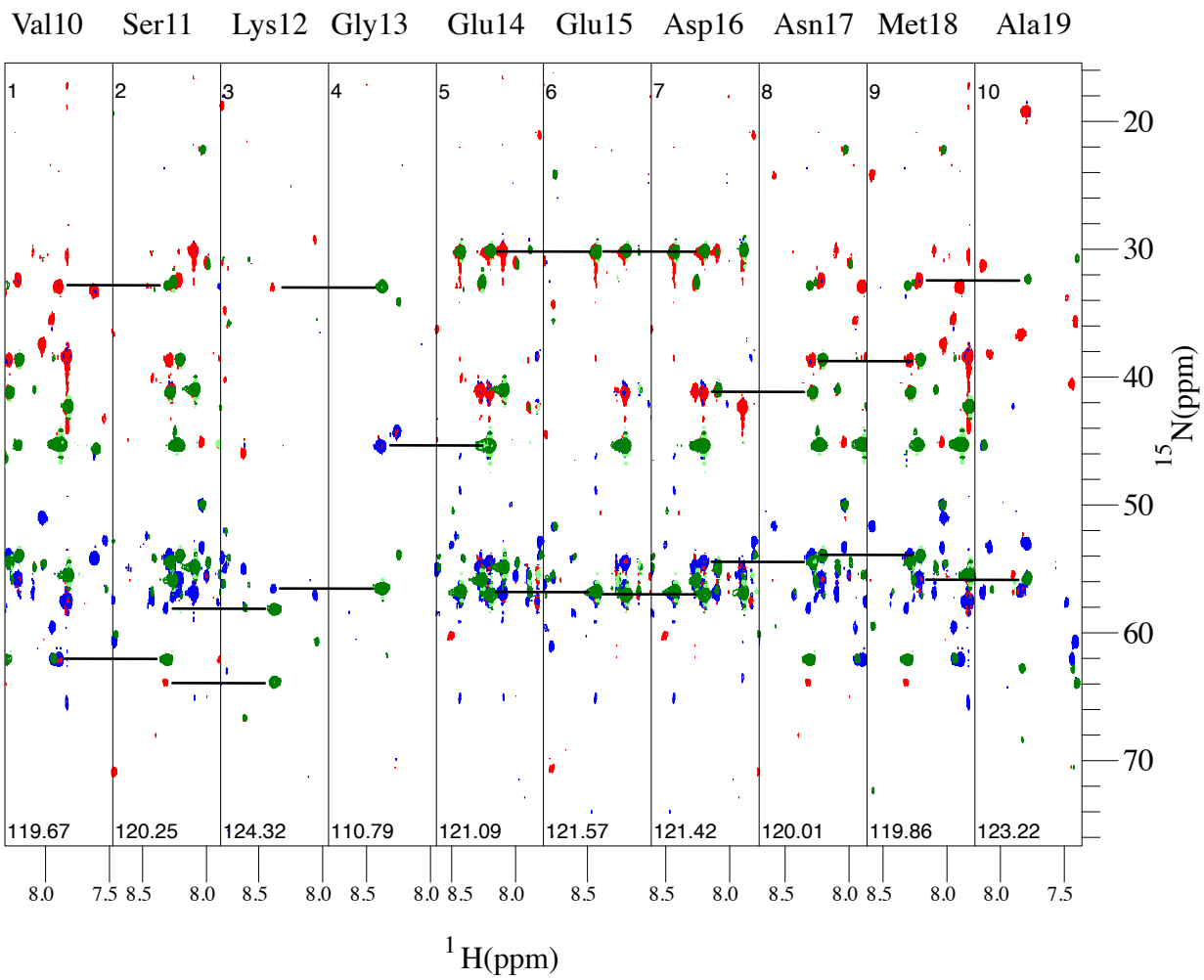

Figure B.1: Continued on following page

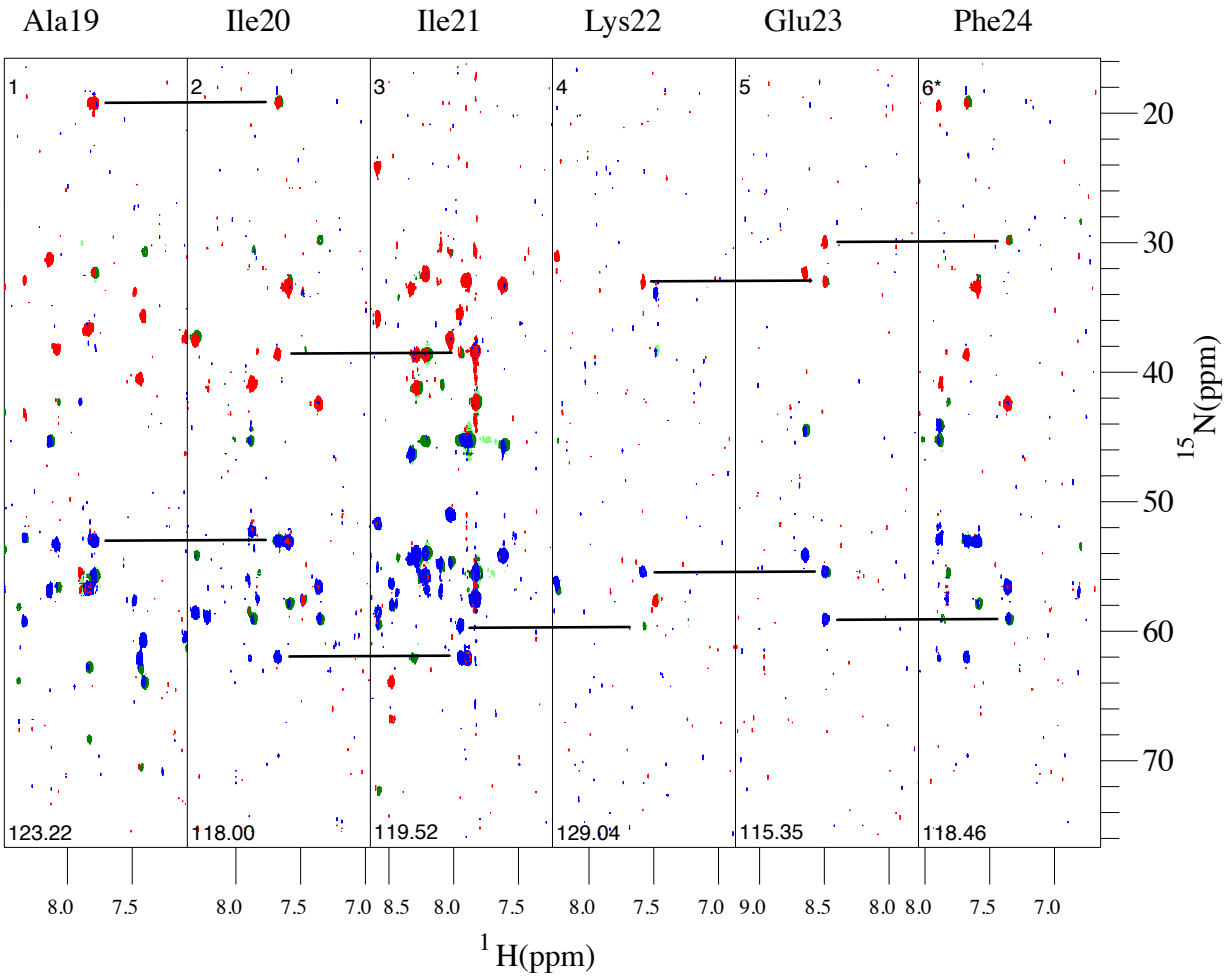

Figure B.2: Continued on following page

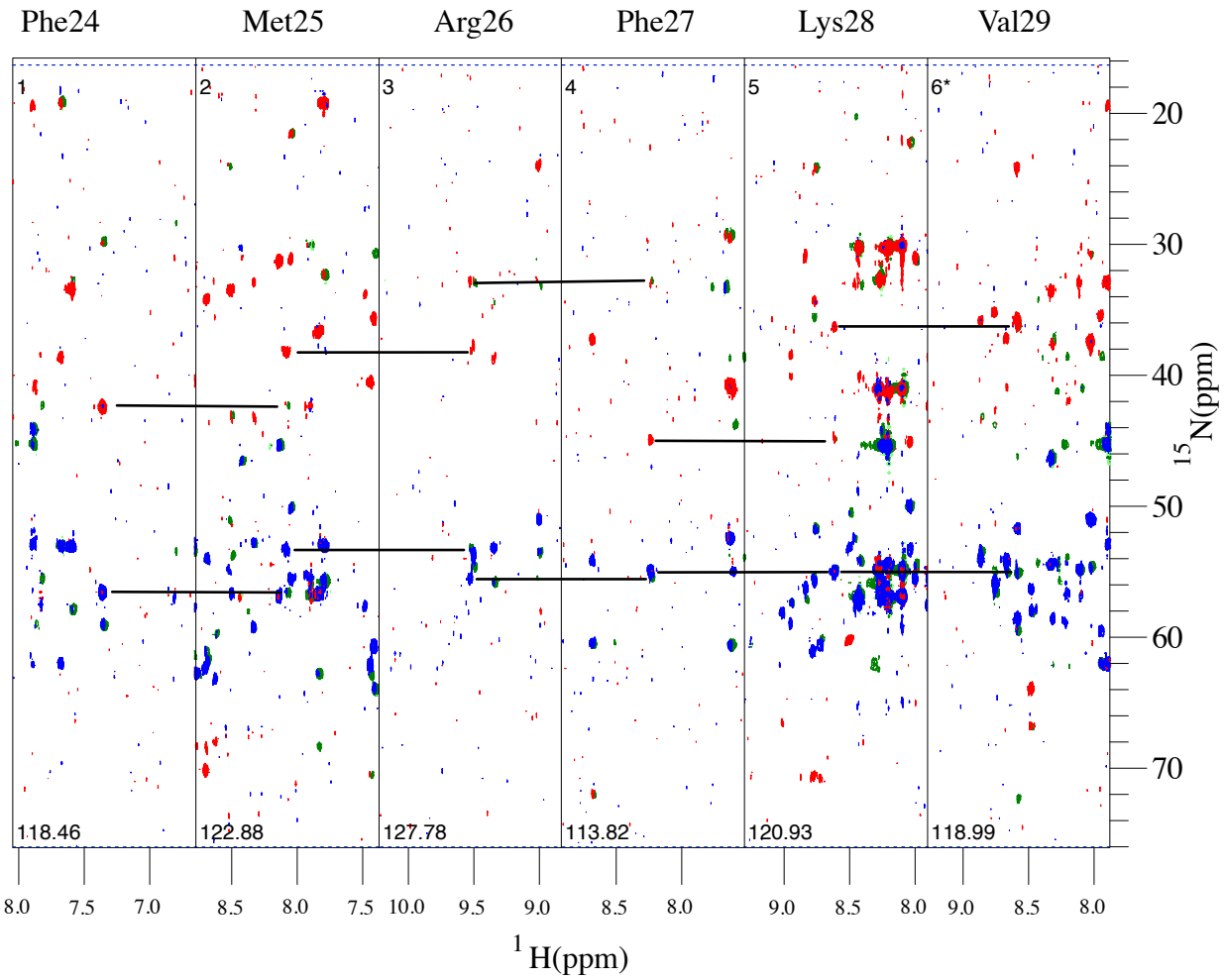

Figure B.3: Continued on following page

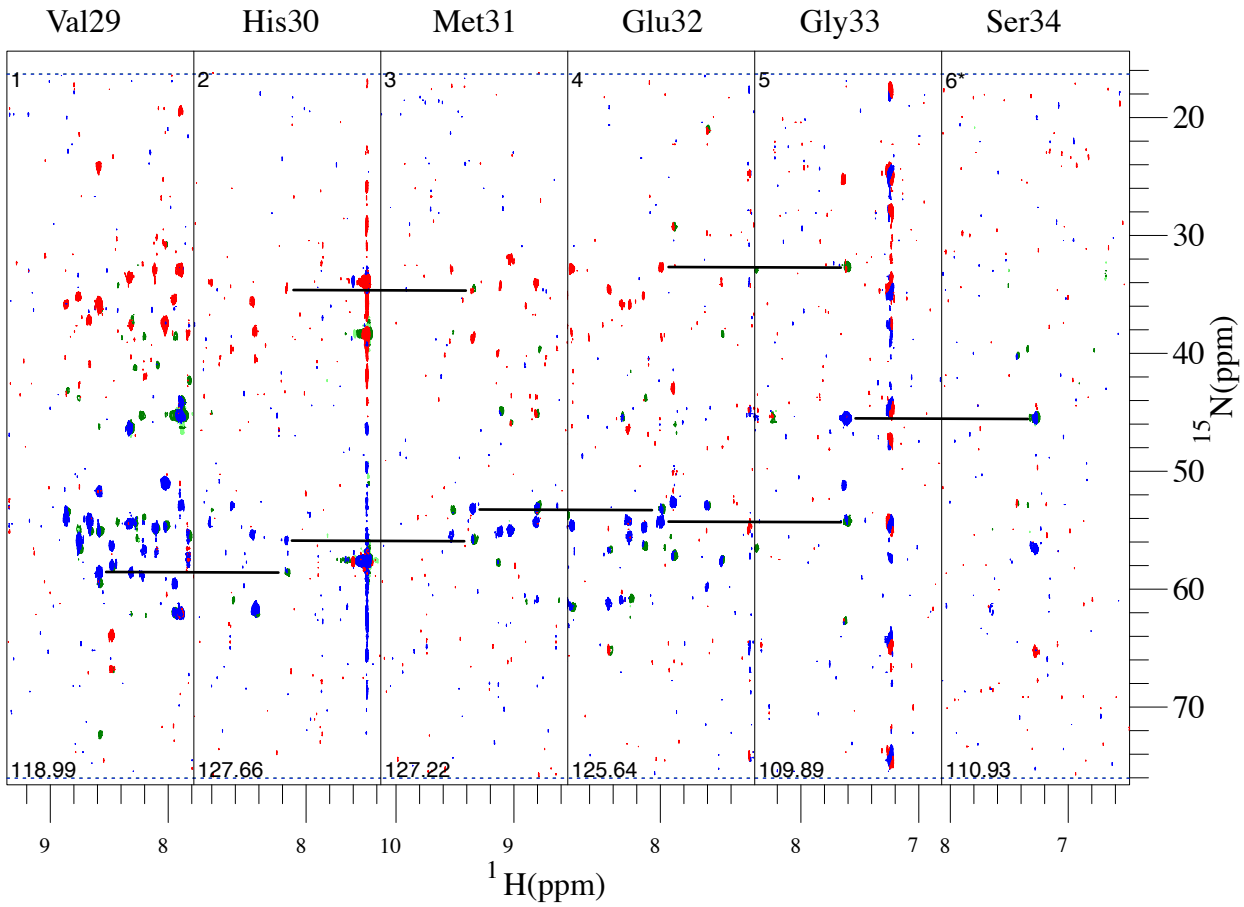

Figure B.4: Continued on following page

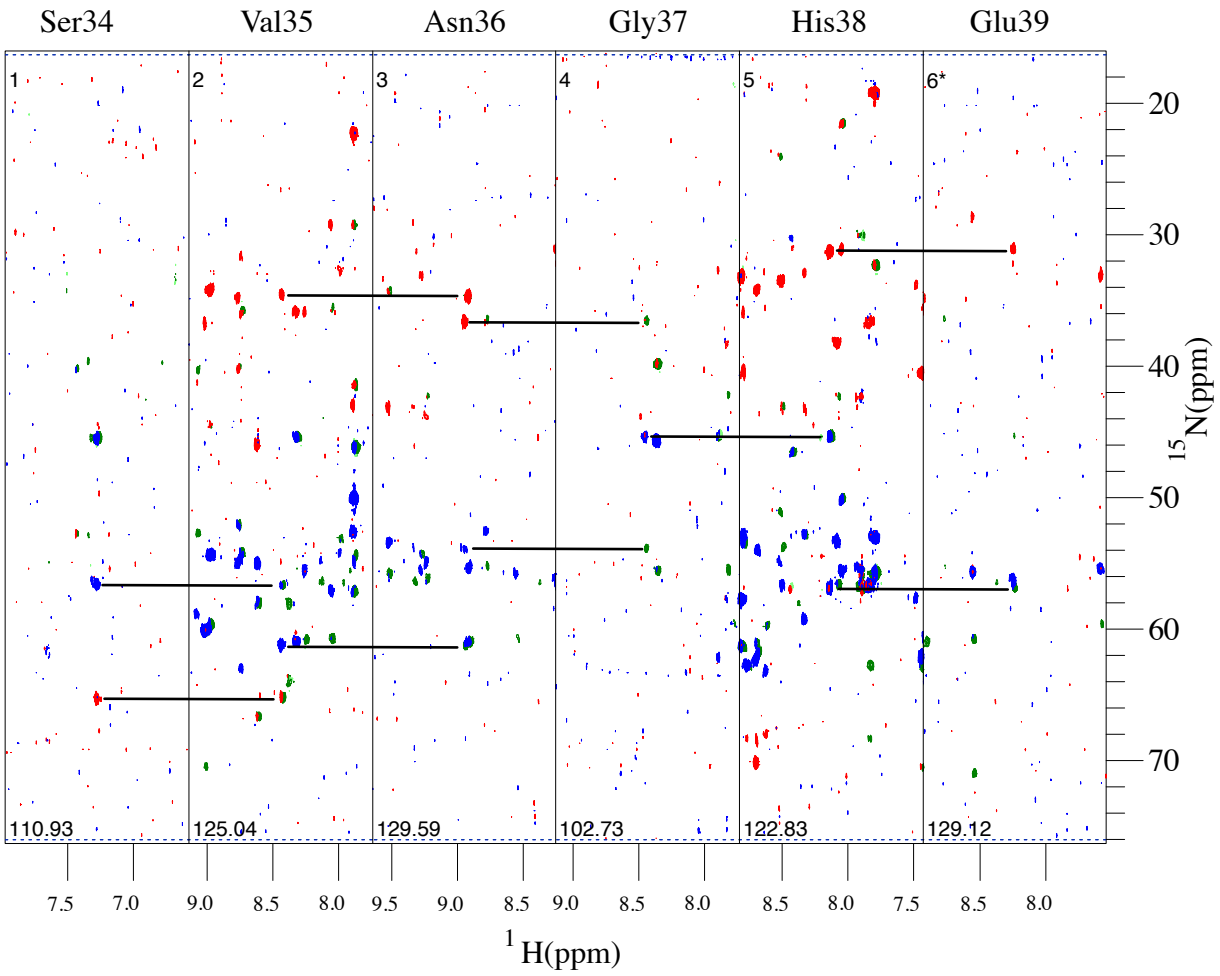

Figure B.5: Continued on following page

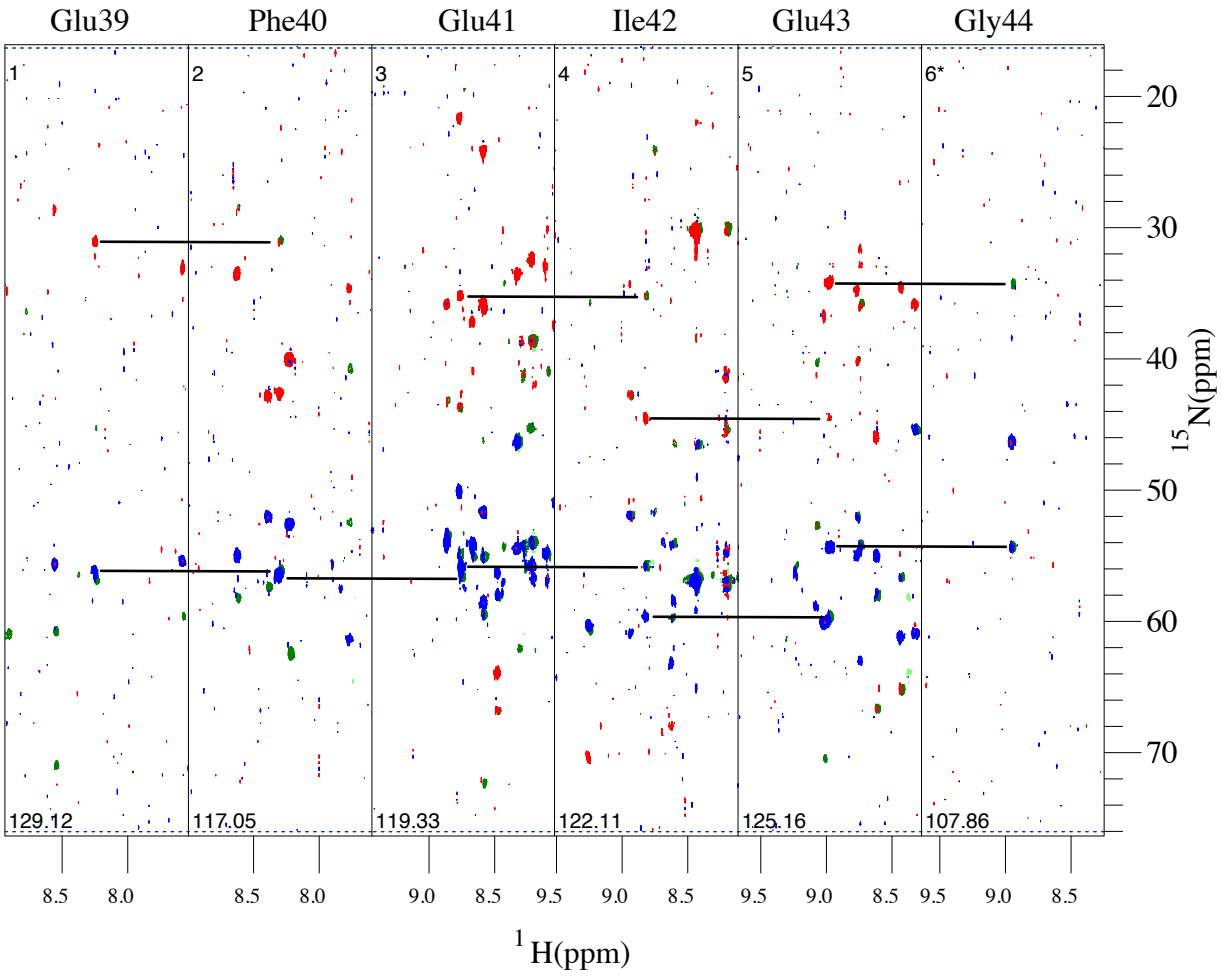

Figure B.6: Continued on following page

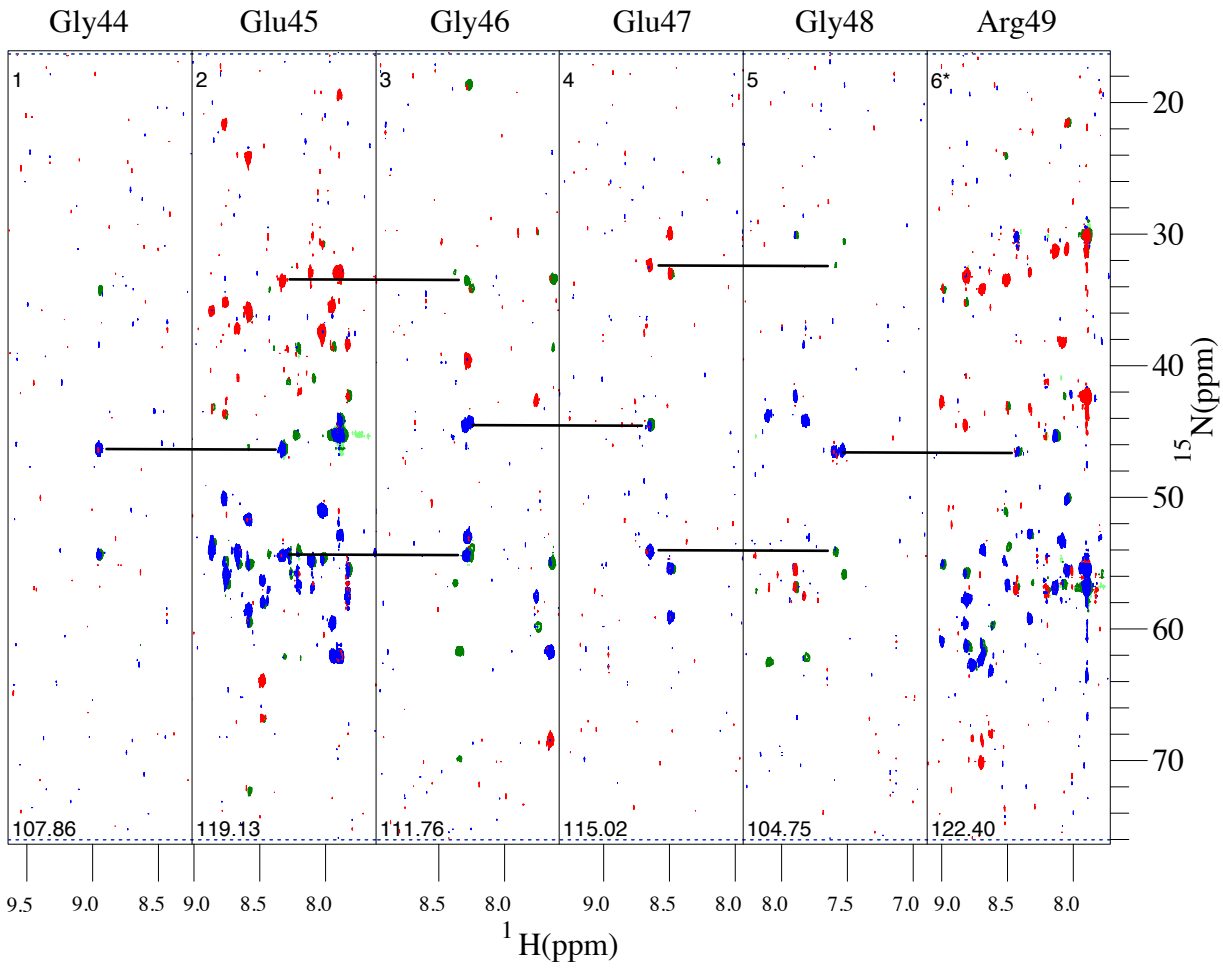

Figure B.7: Continued on following page

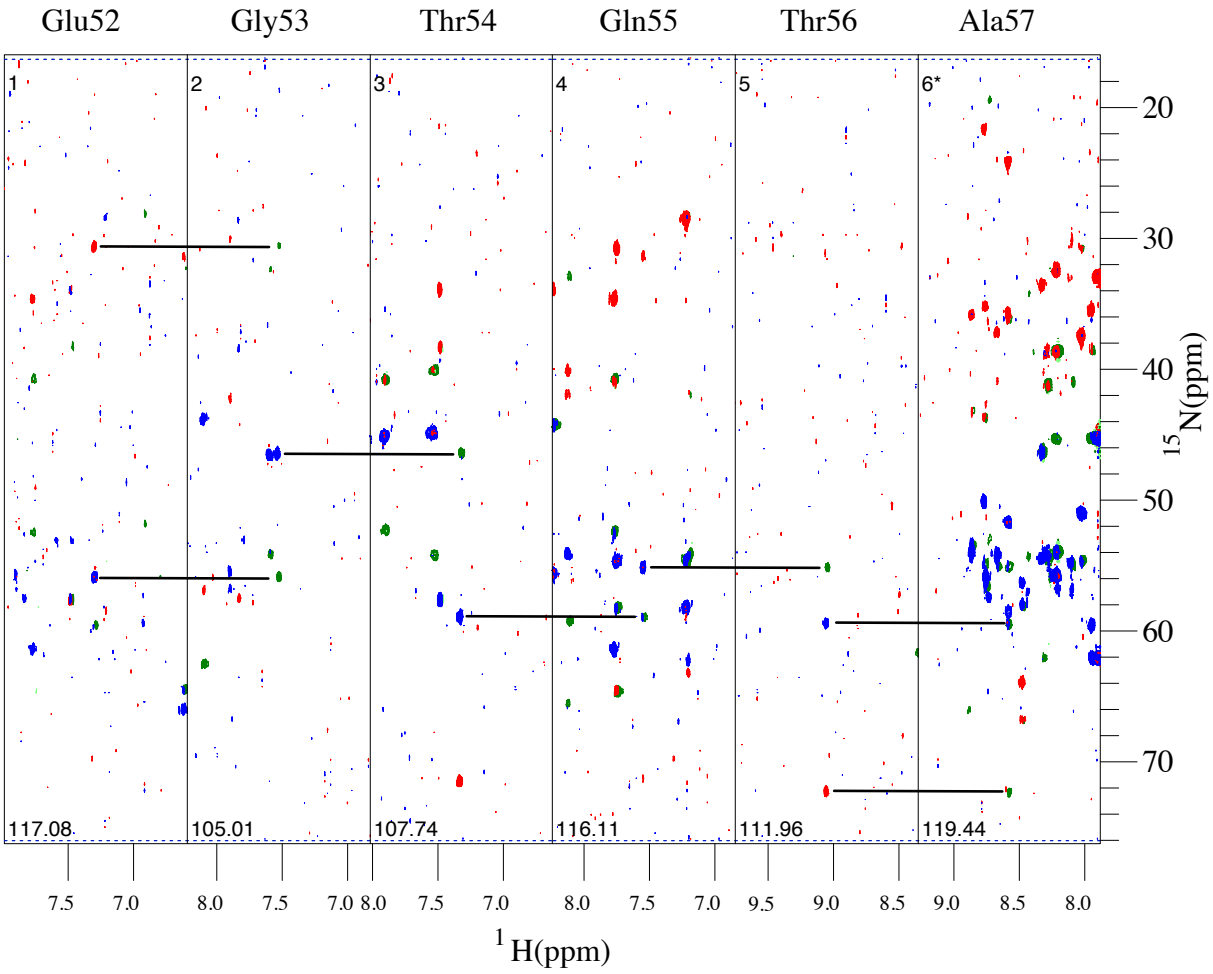

Figure B.8: Continued on following page

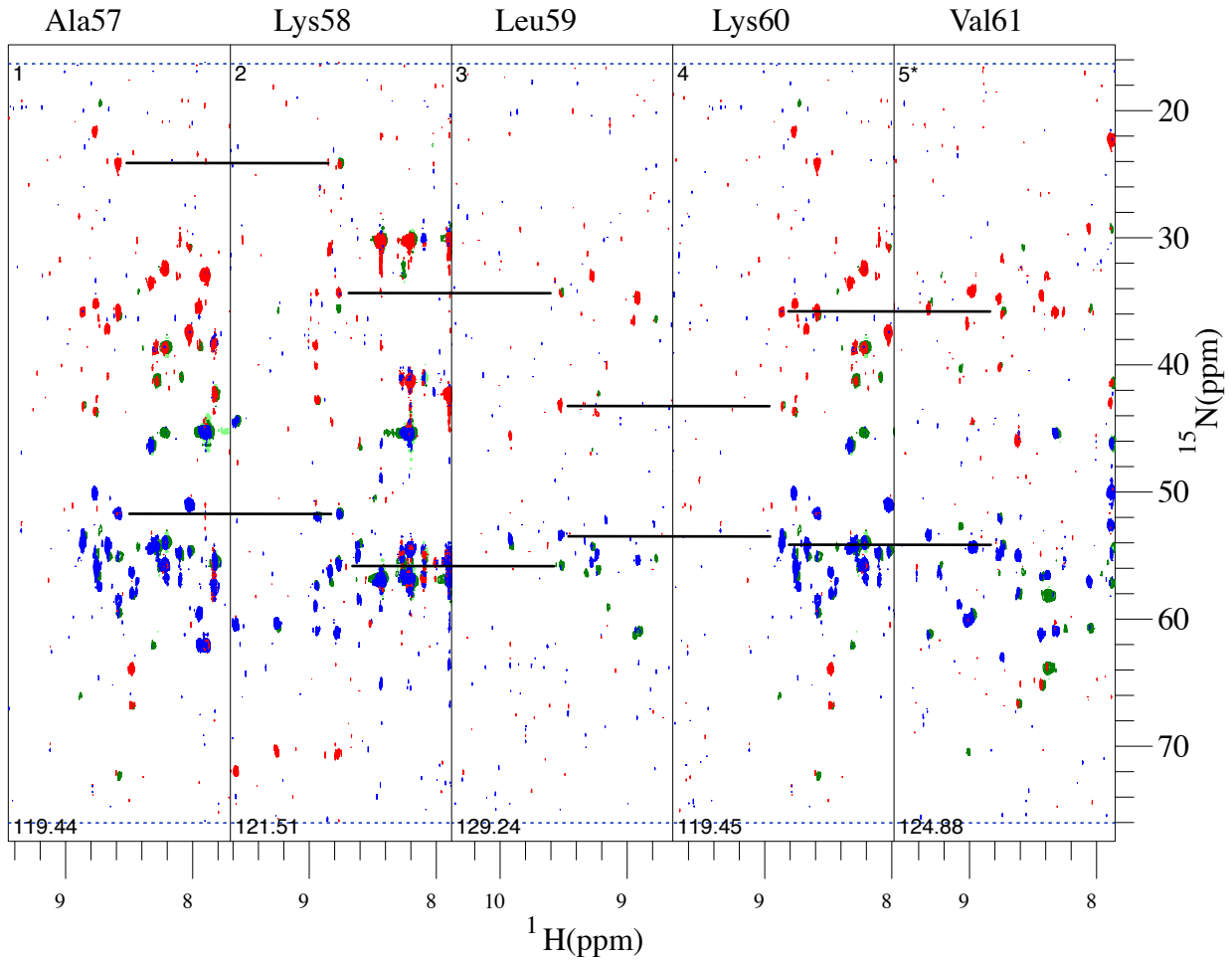

Figure B.9: Continued on following page

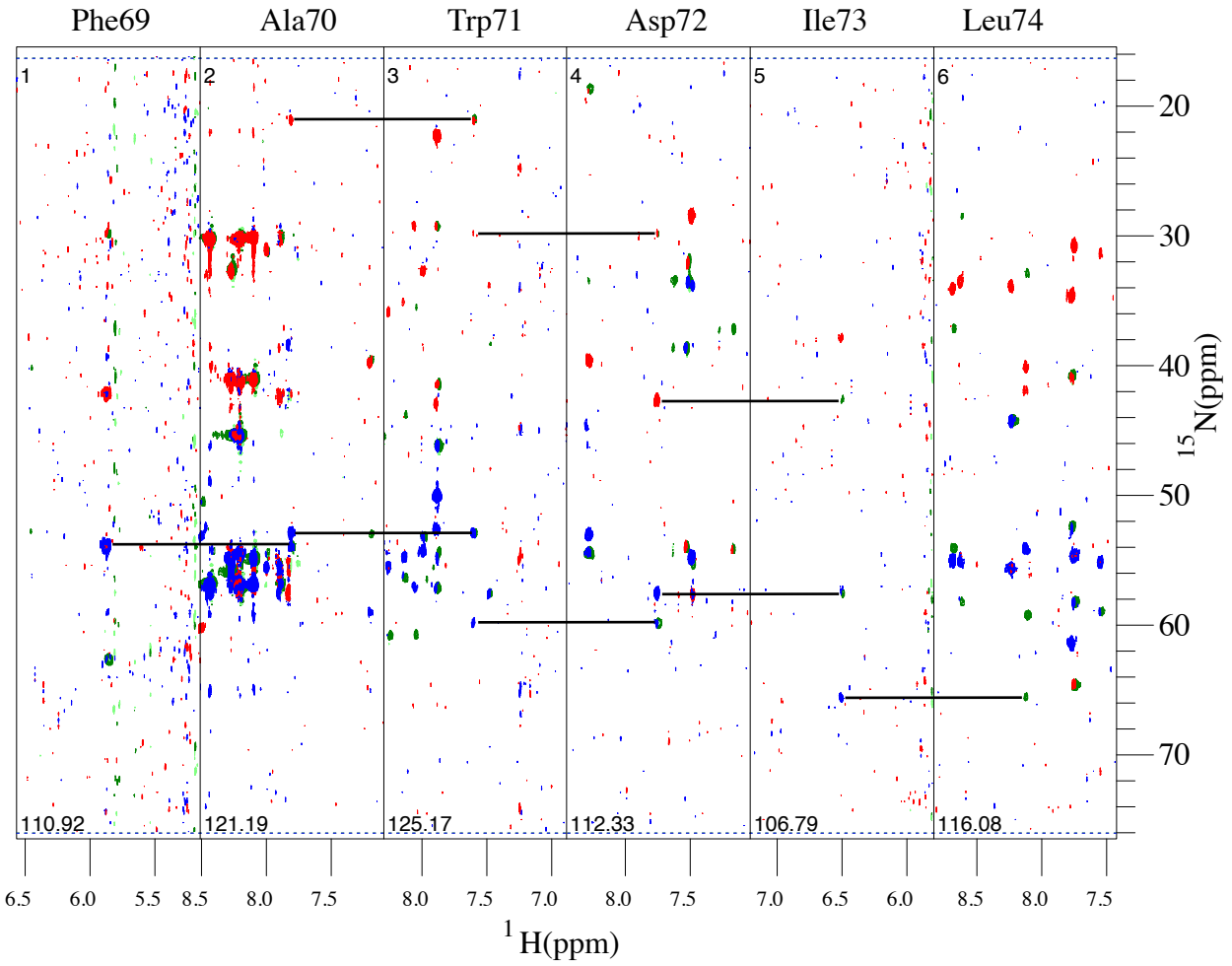

Figure B.10: Continued on following page

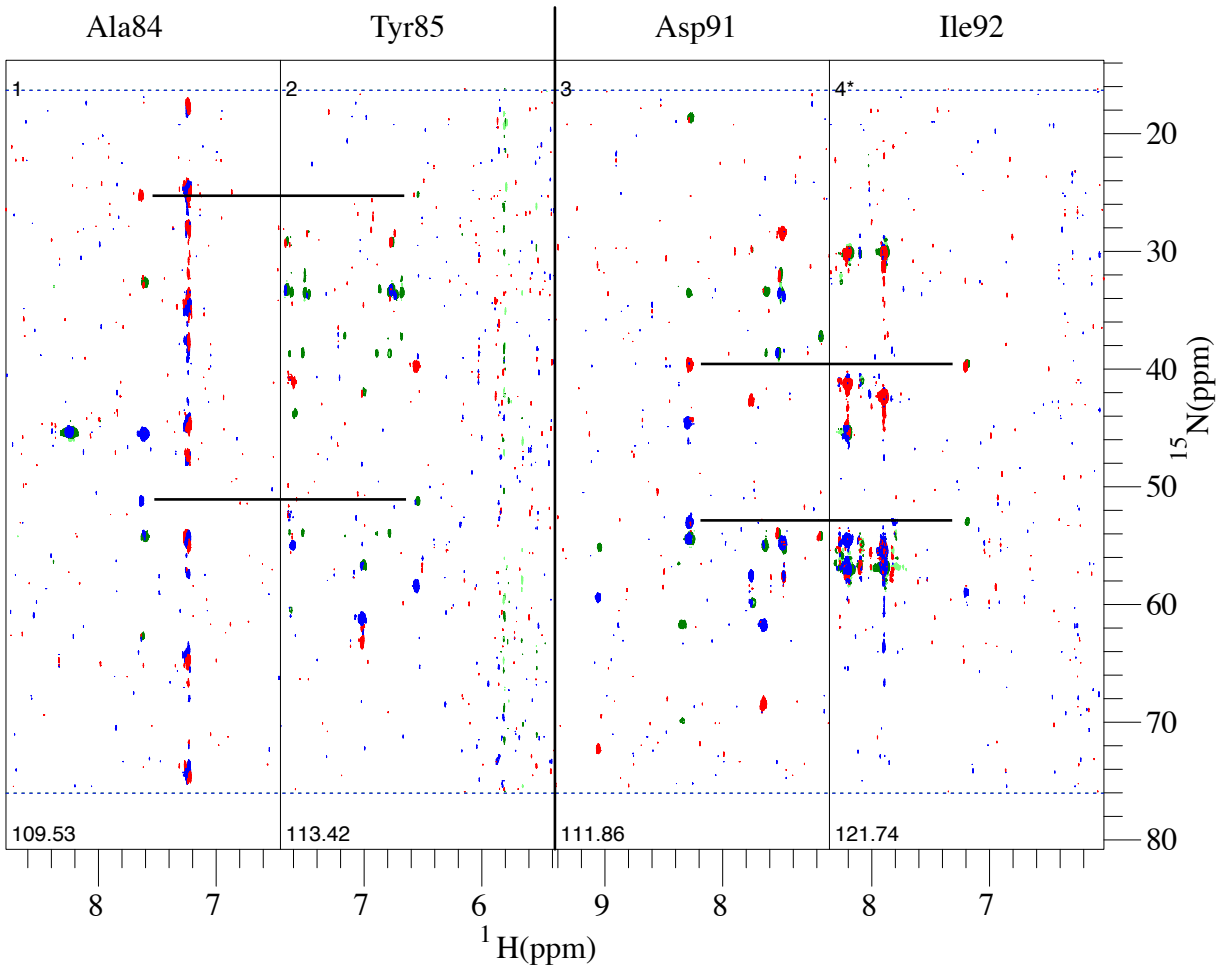

Figure B.11: Continued on following page

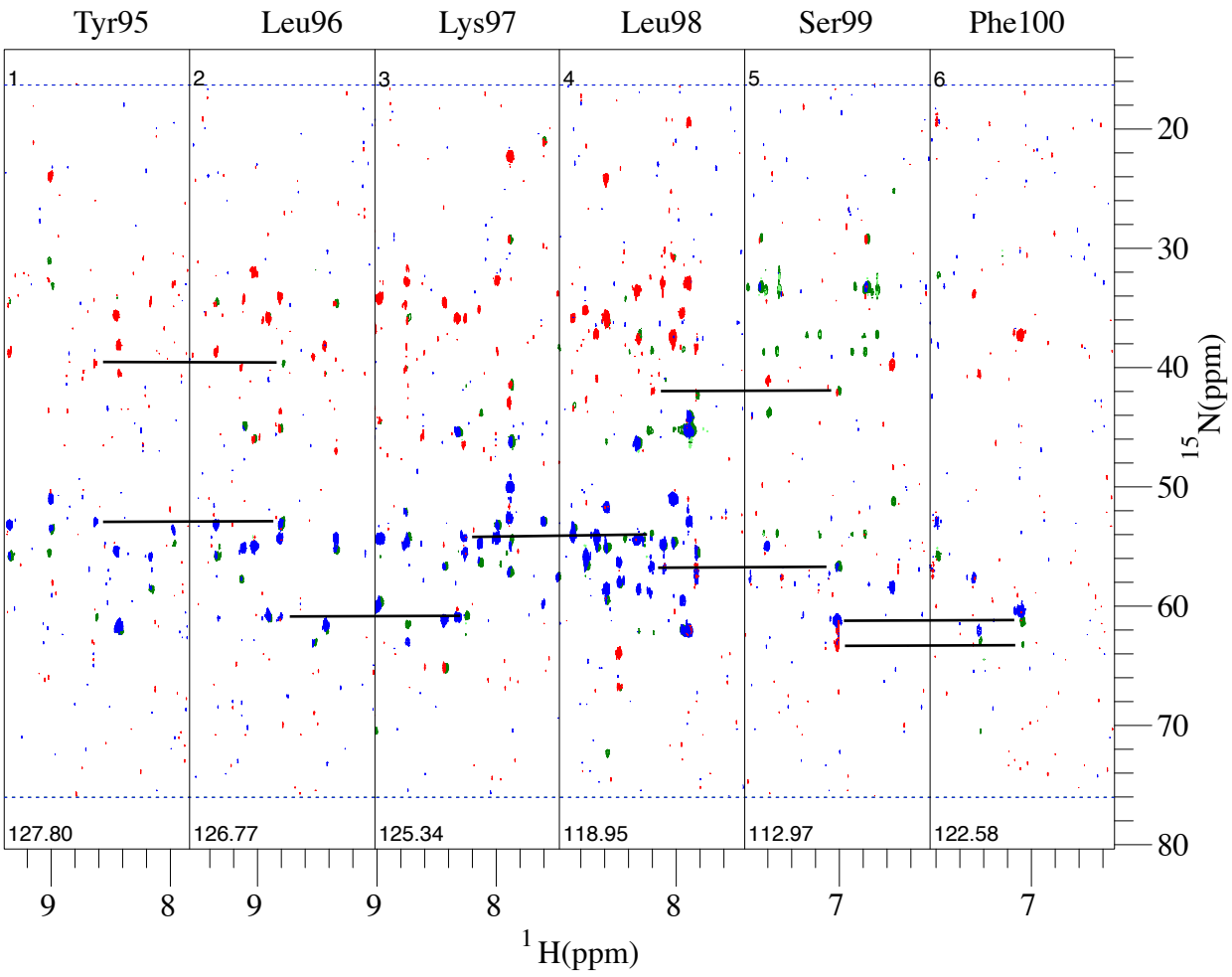

Figure B.12: Continued on following page

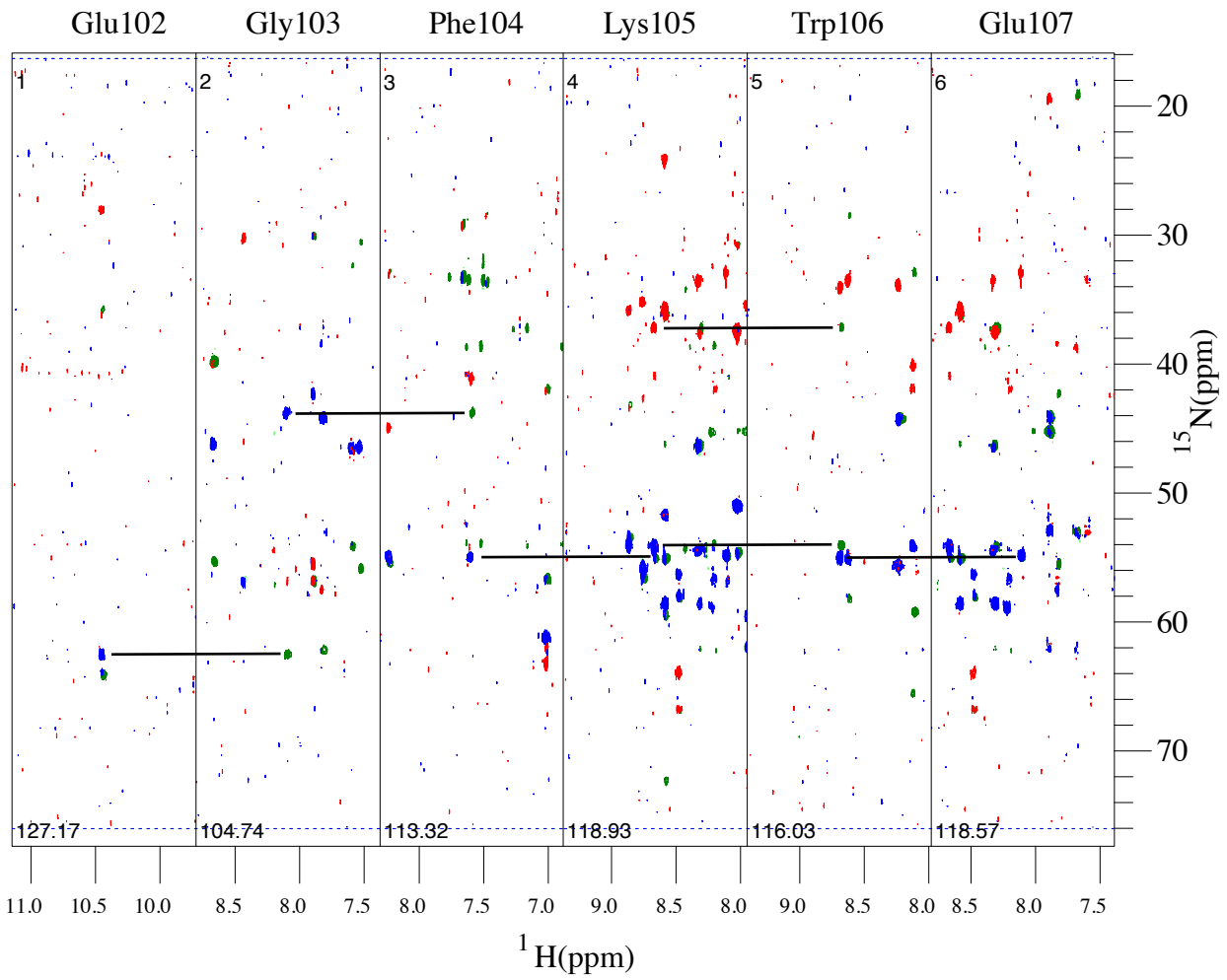

Figure B.13: Continued on following page

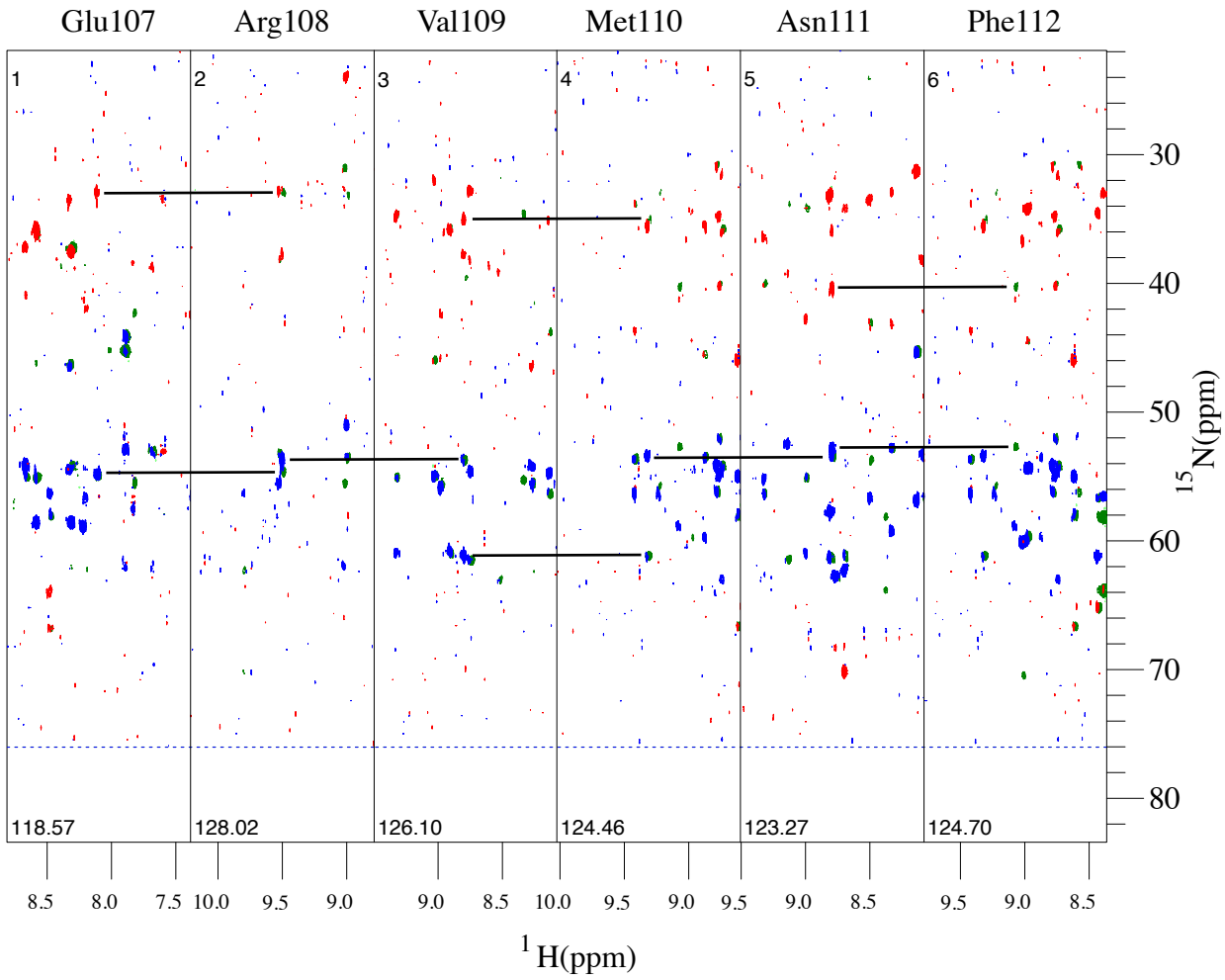

Figure B.14: Continued on following page

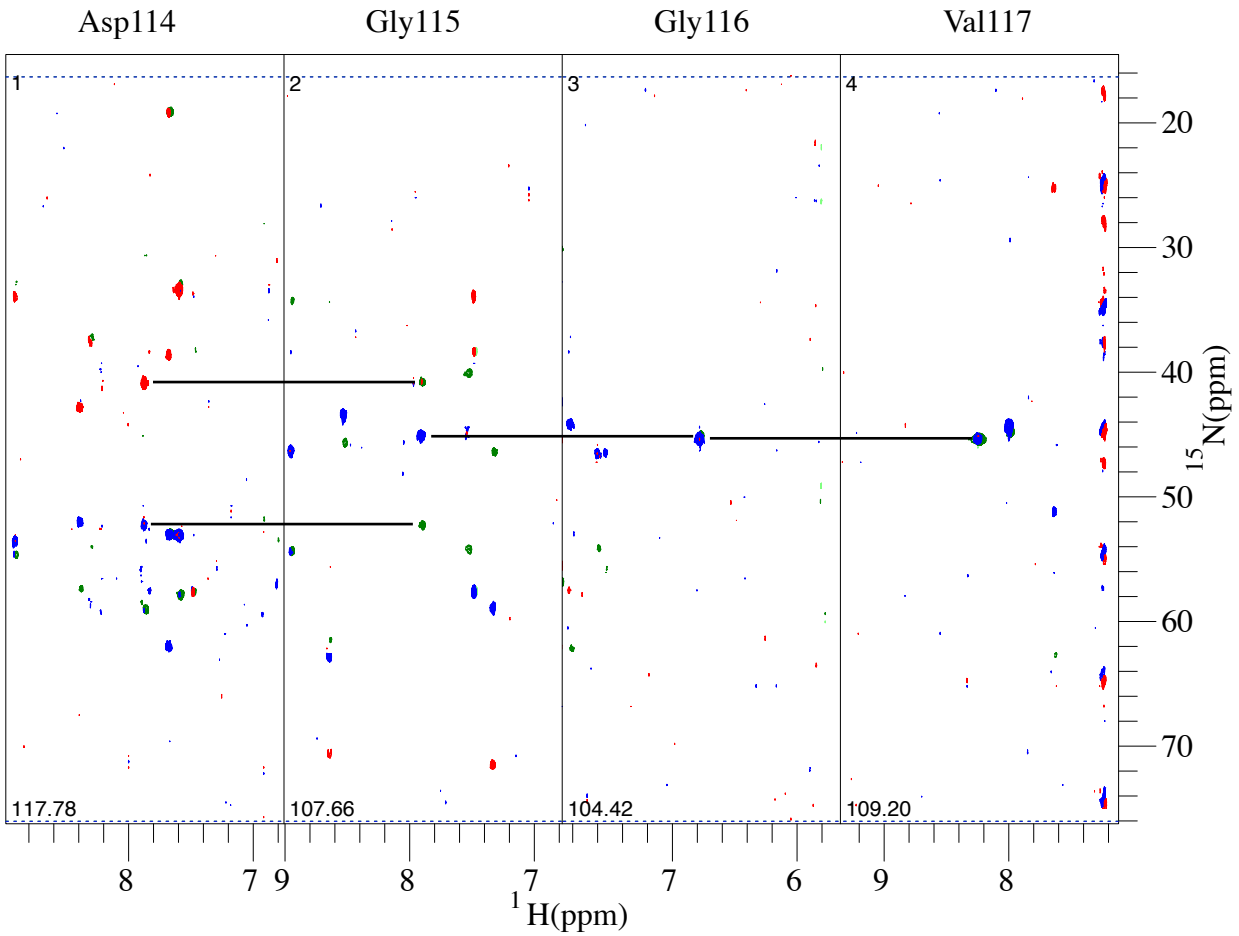

Figure B.15: Continued on following page

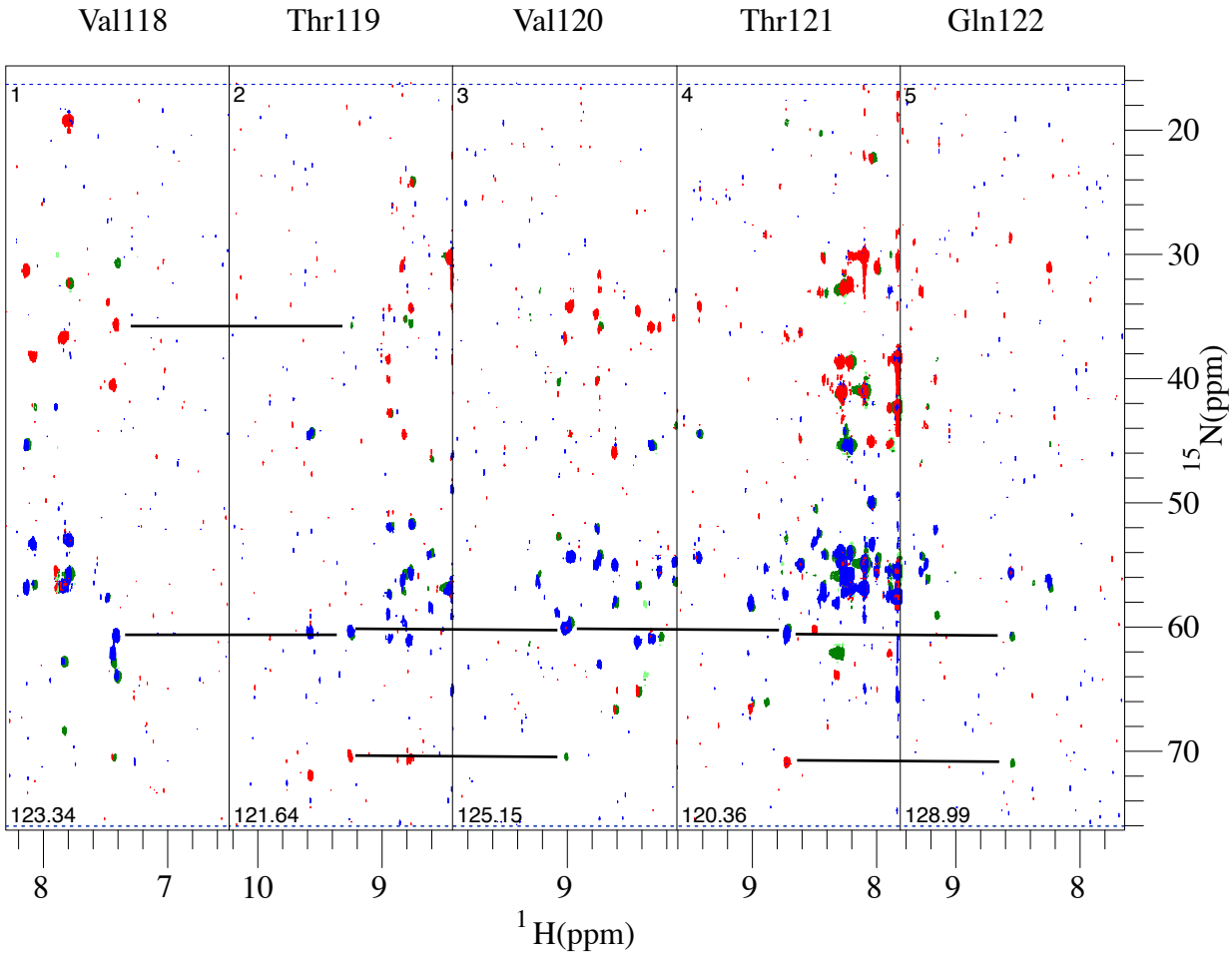

Figure B.16: Continued on following page

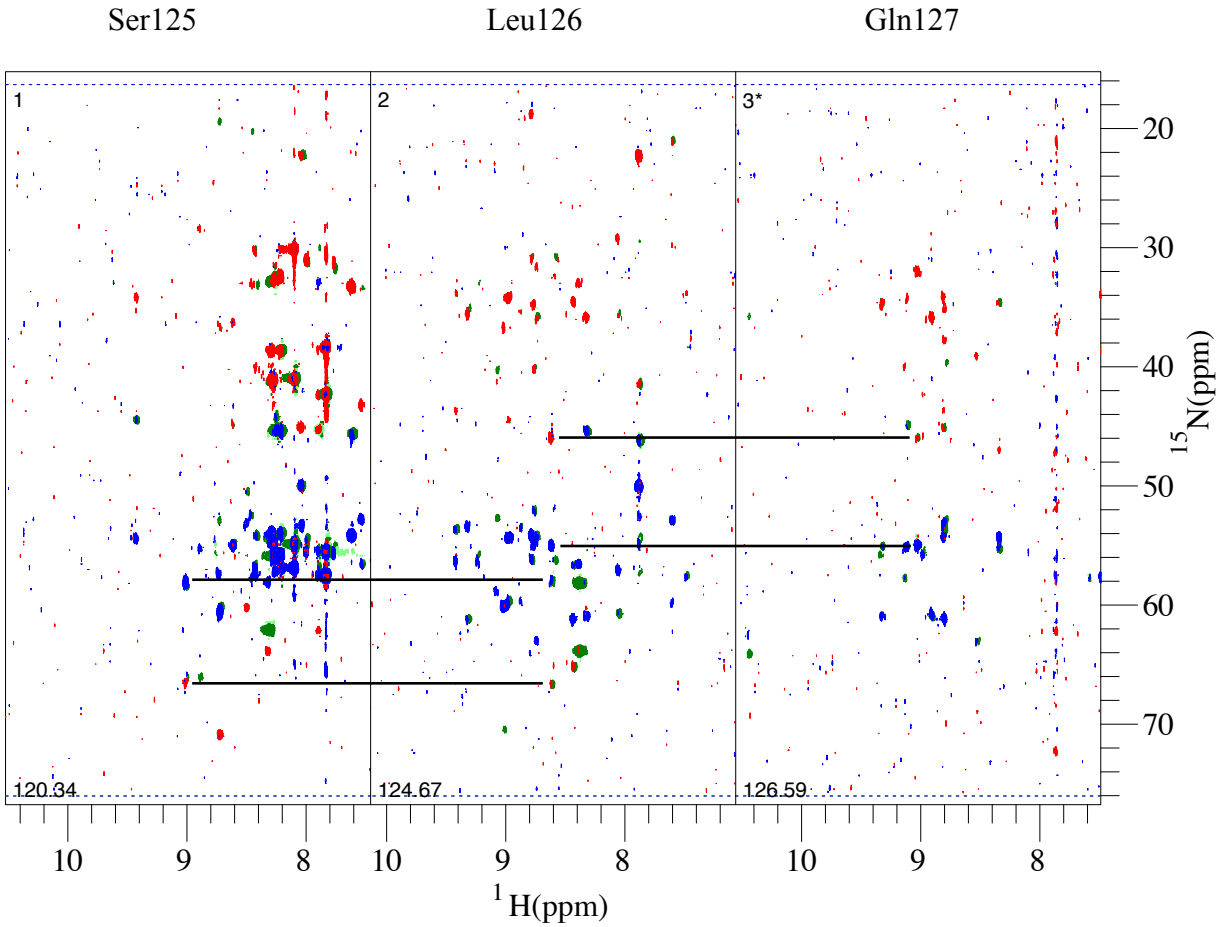

Figure B.17: Continued on following page

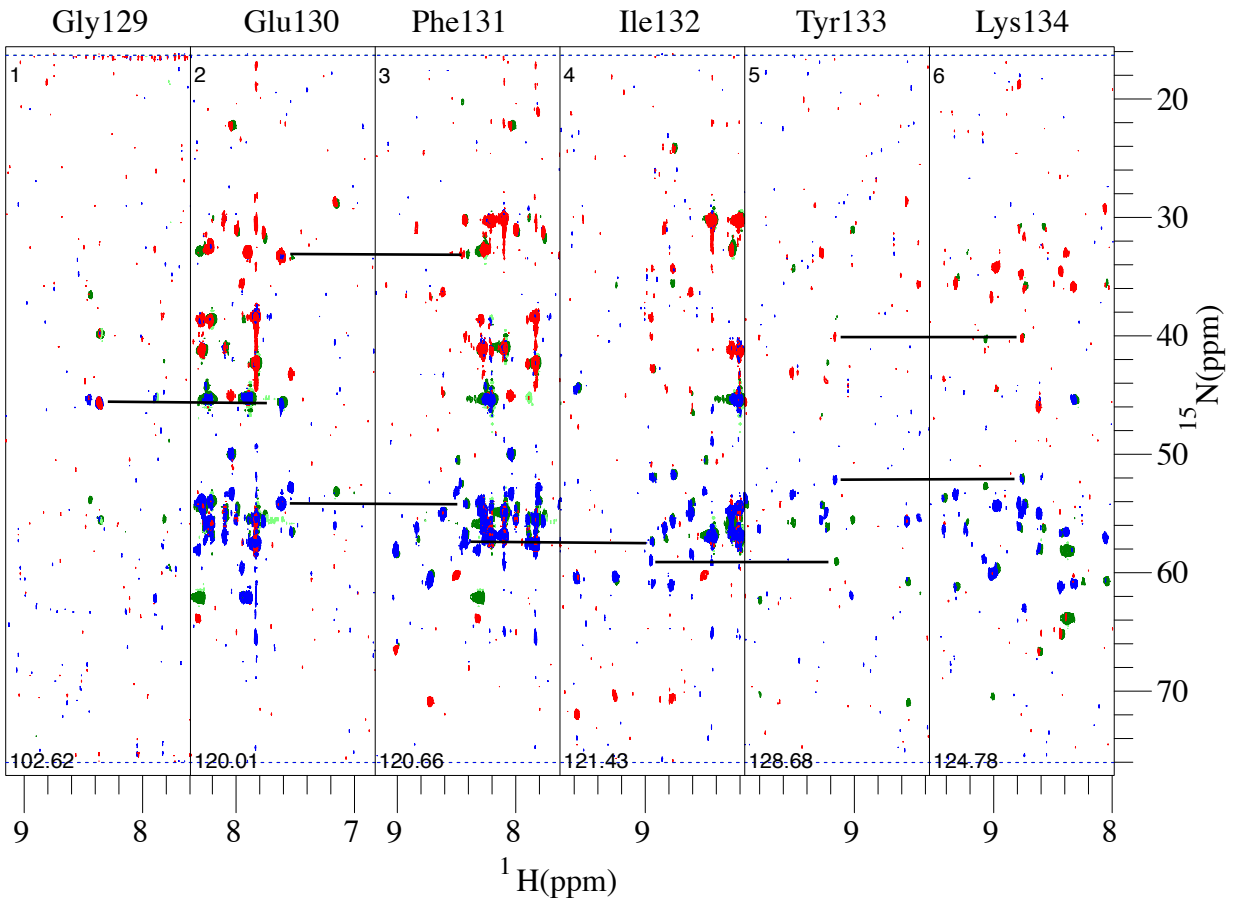

Figure B.18: Continued on following page

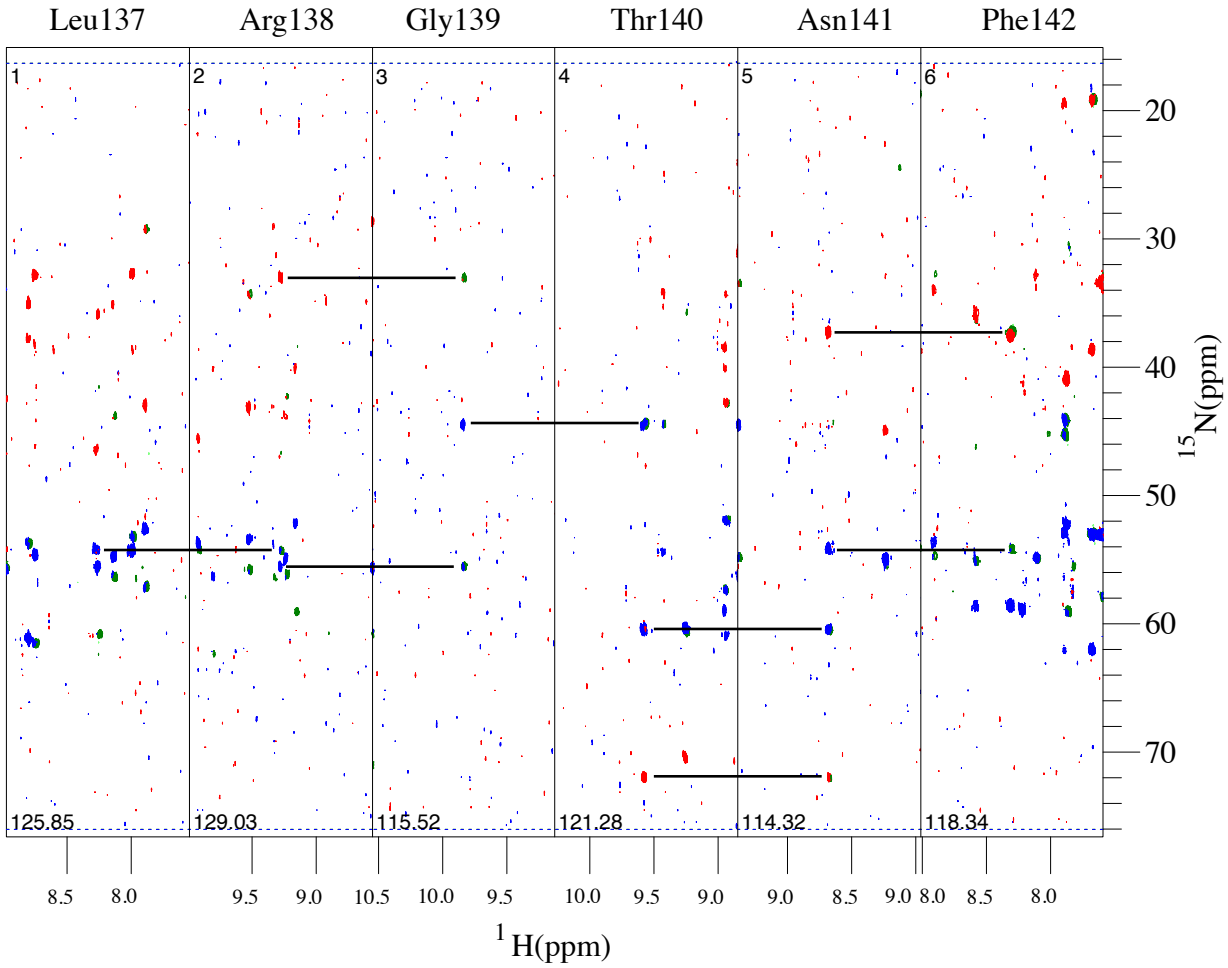

Figure B.19: Continued on following page

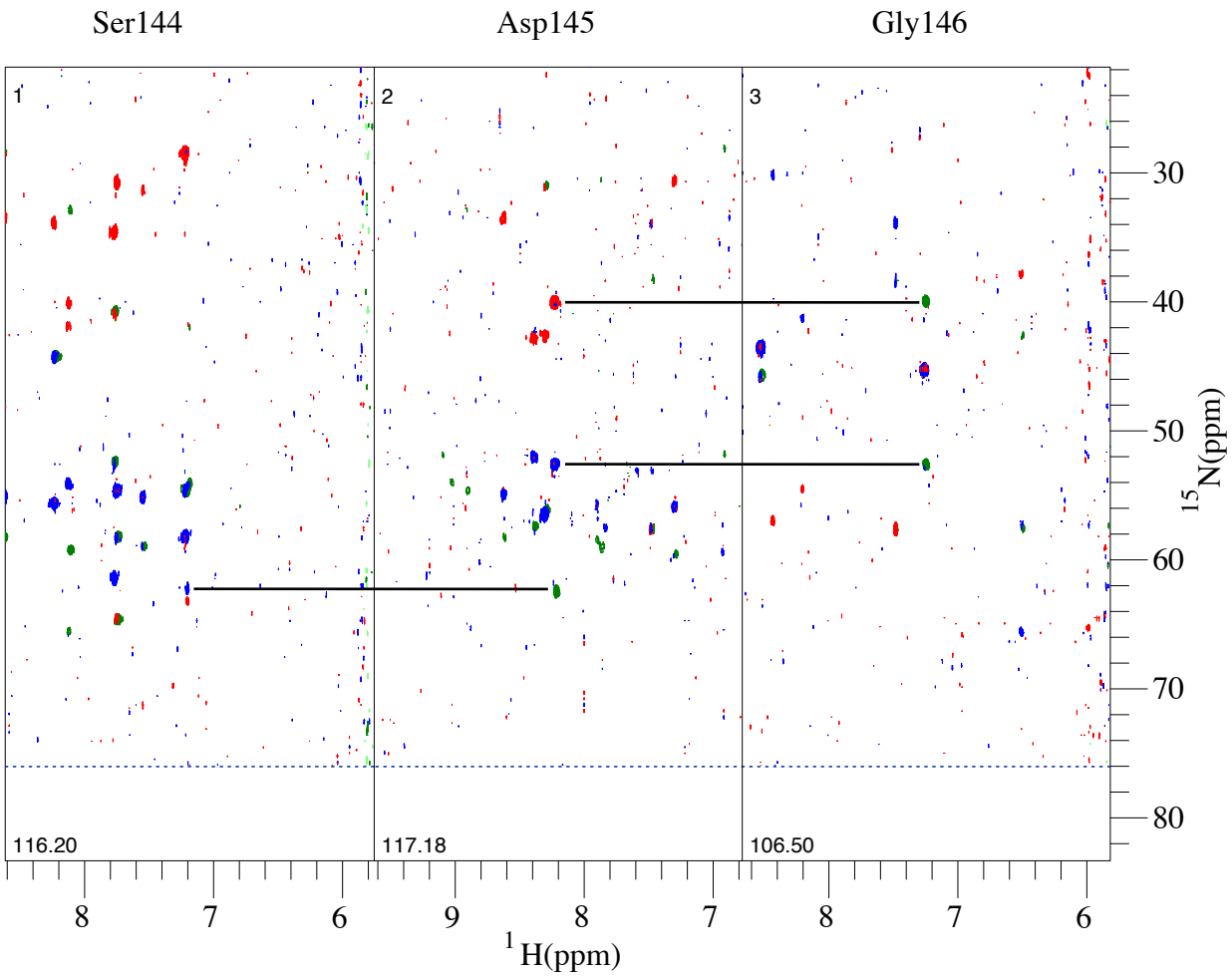

Figure B.20: Continued on following page

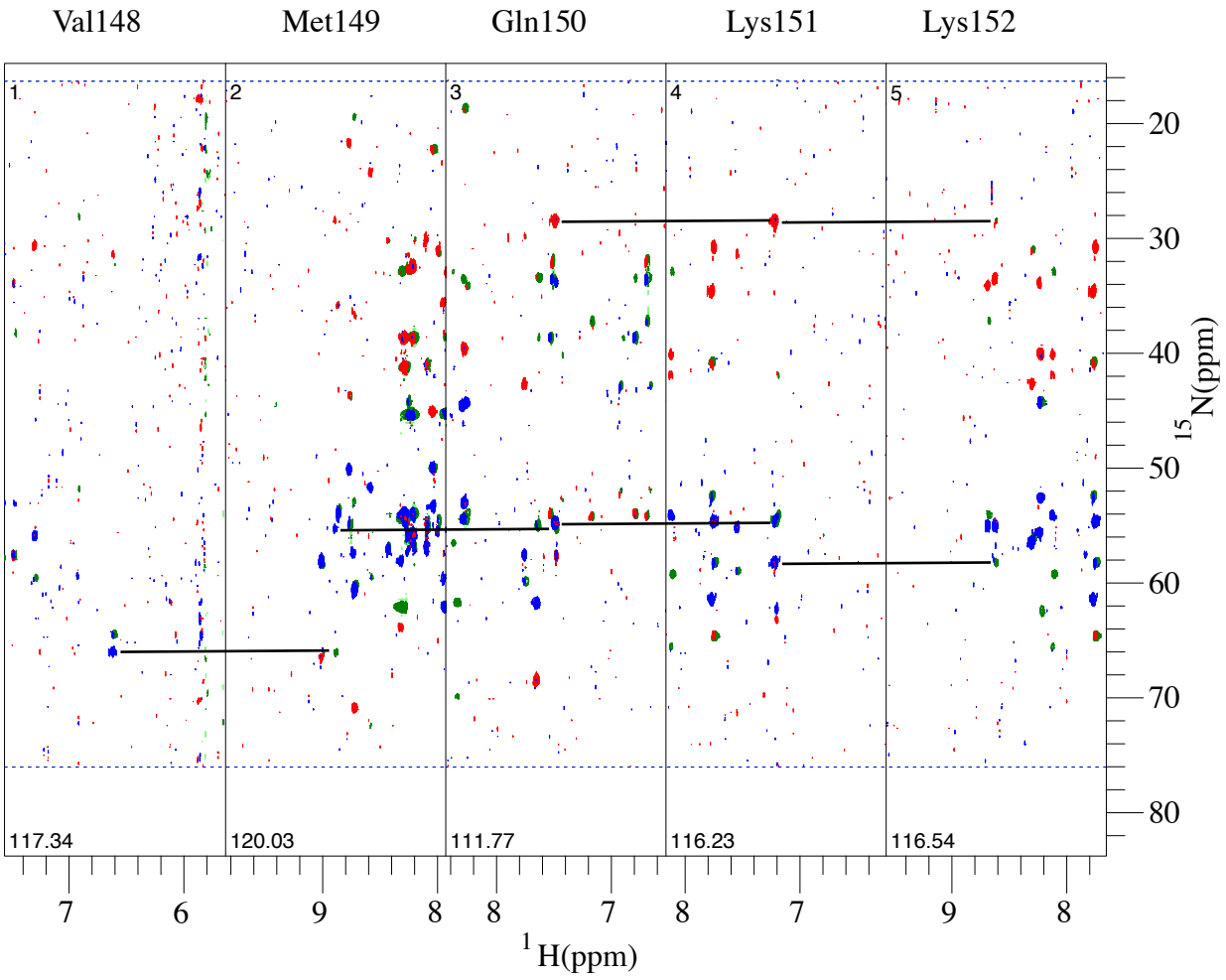

Figure B.21: Continued on following page

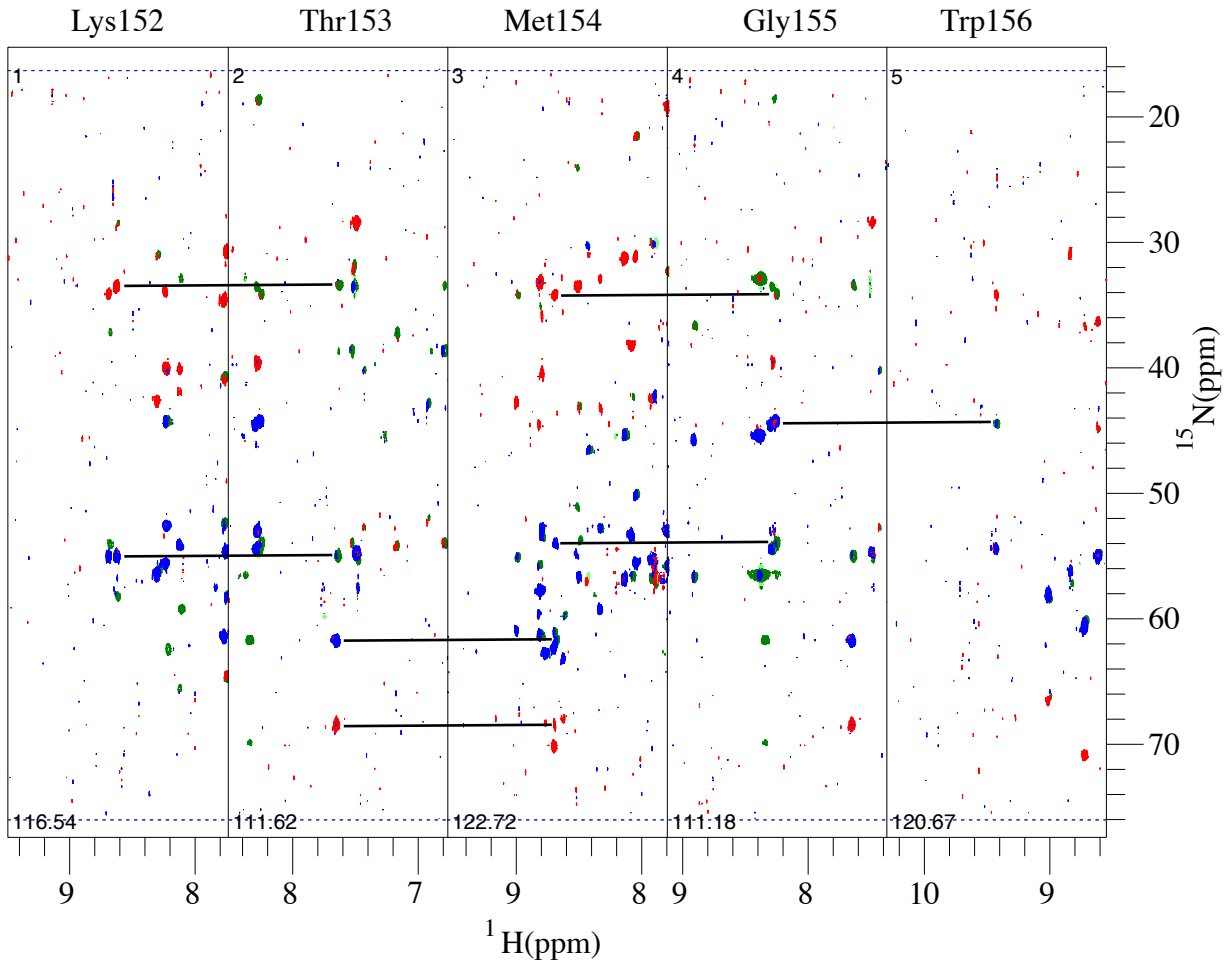

Figure B.22: Continued on following page

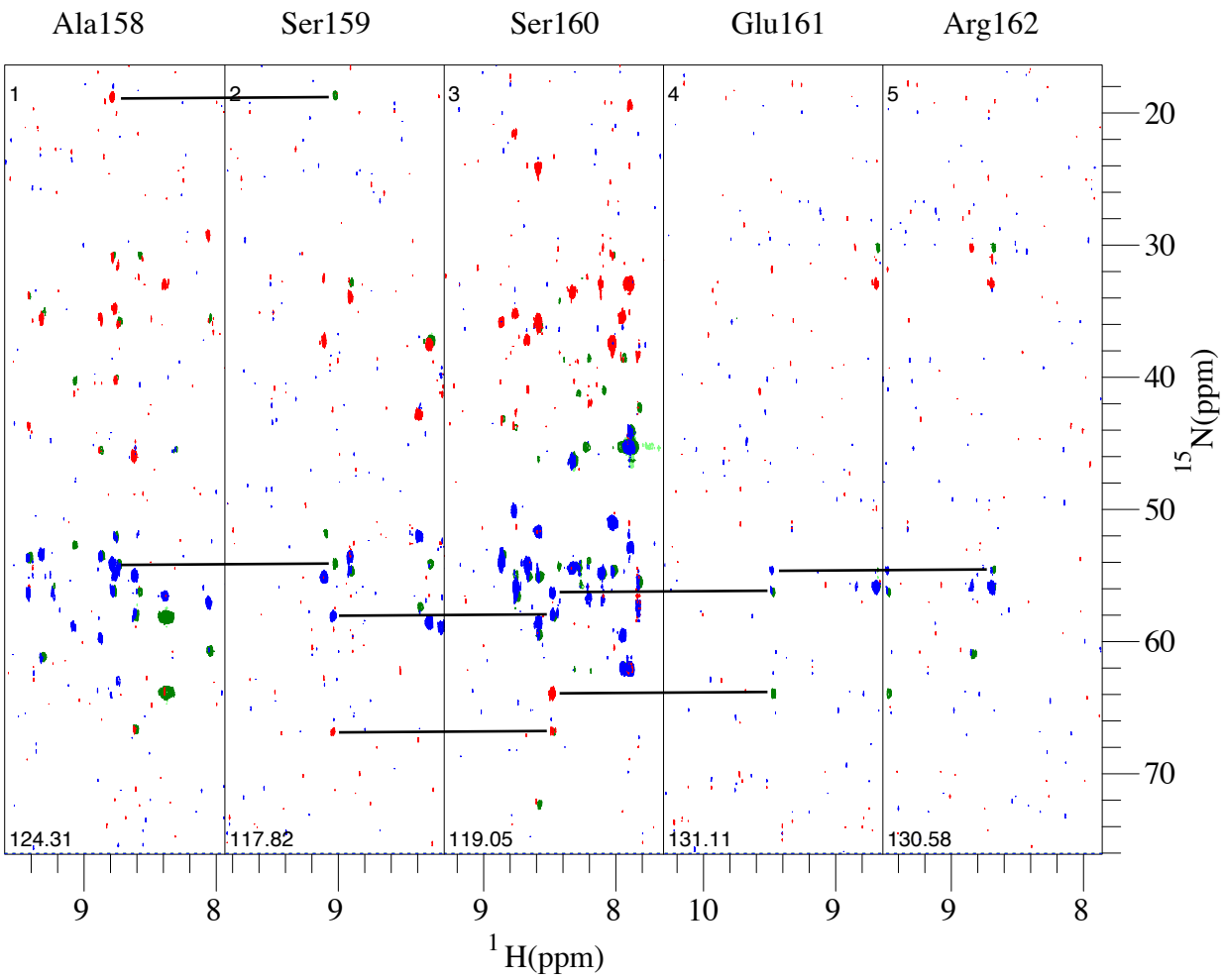

Figure B.23: Continued on following page

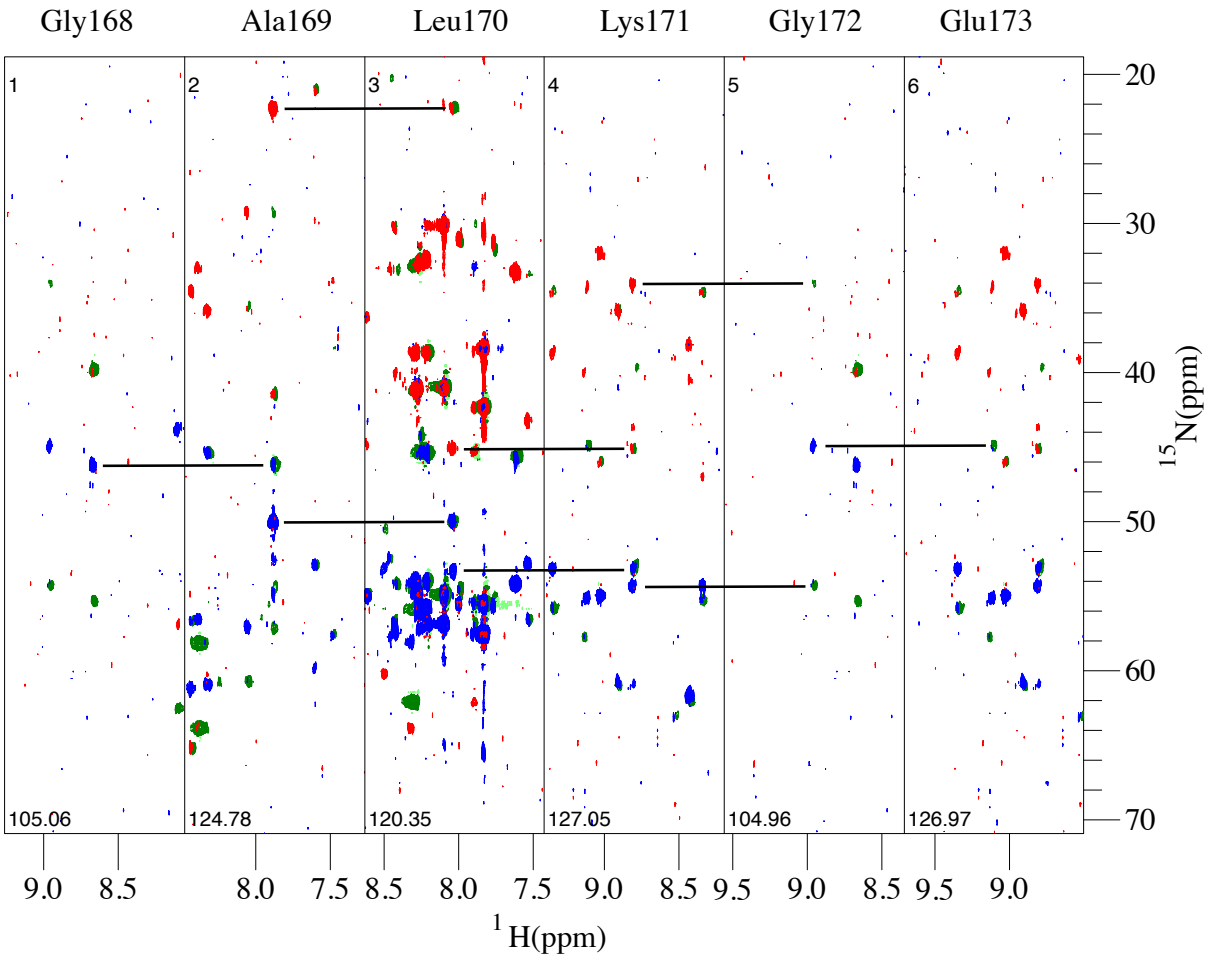

Figure B.24: Continued on following page

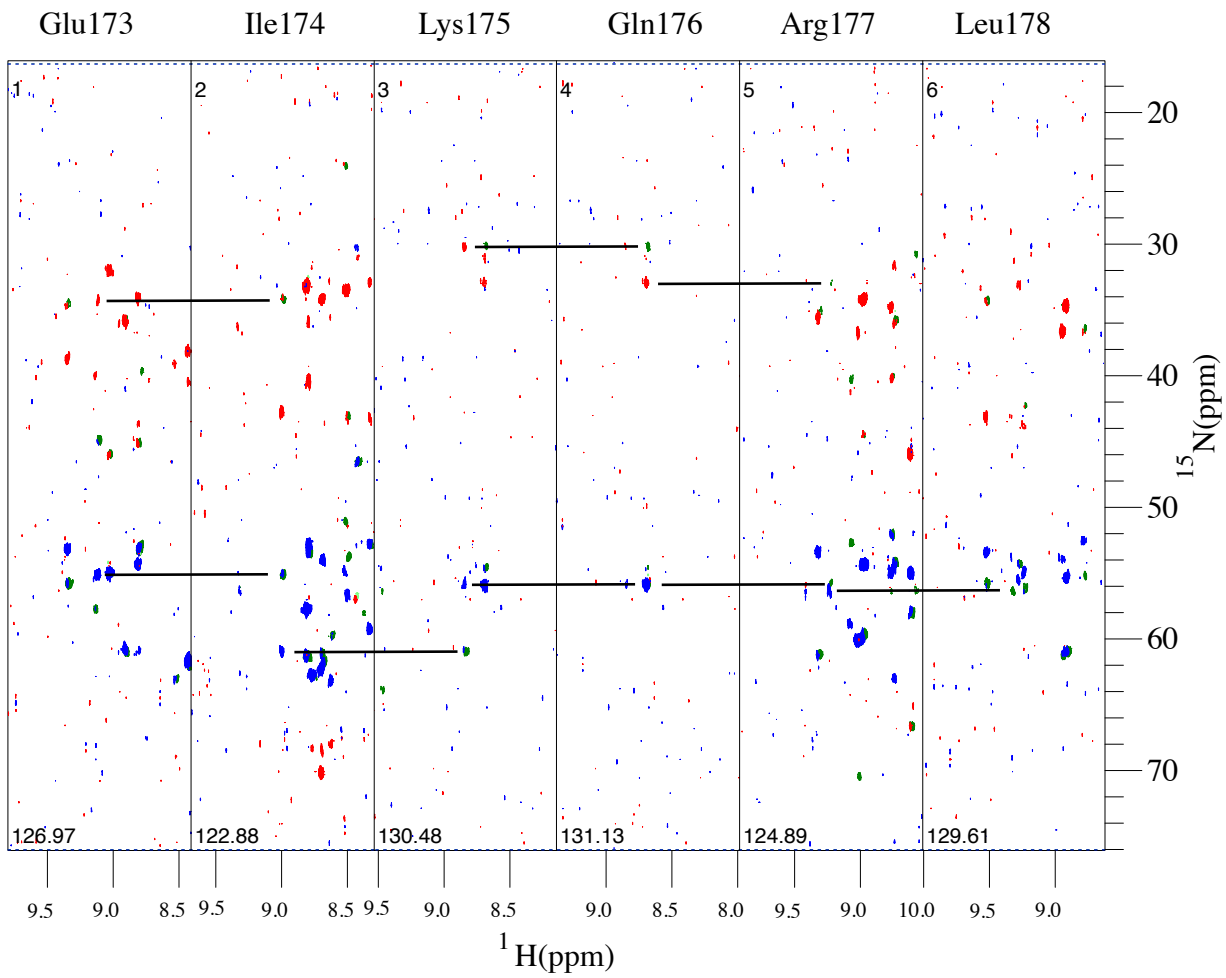

Figure B.25: Continued on following page

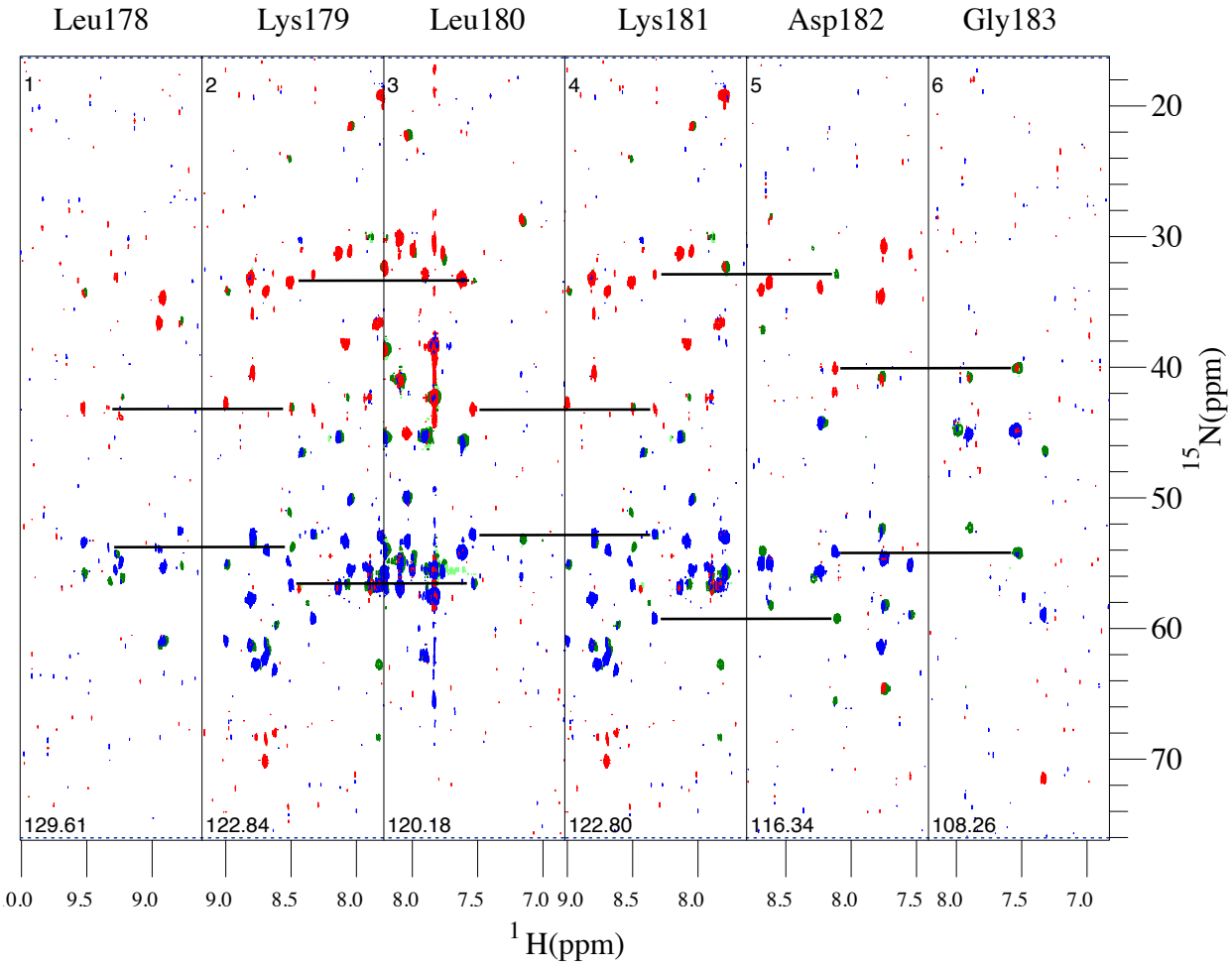

Figure B.26: Continued on following page

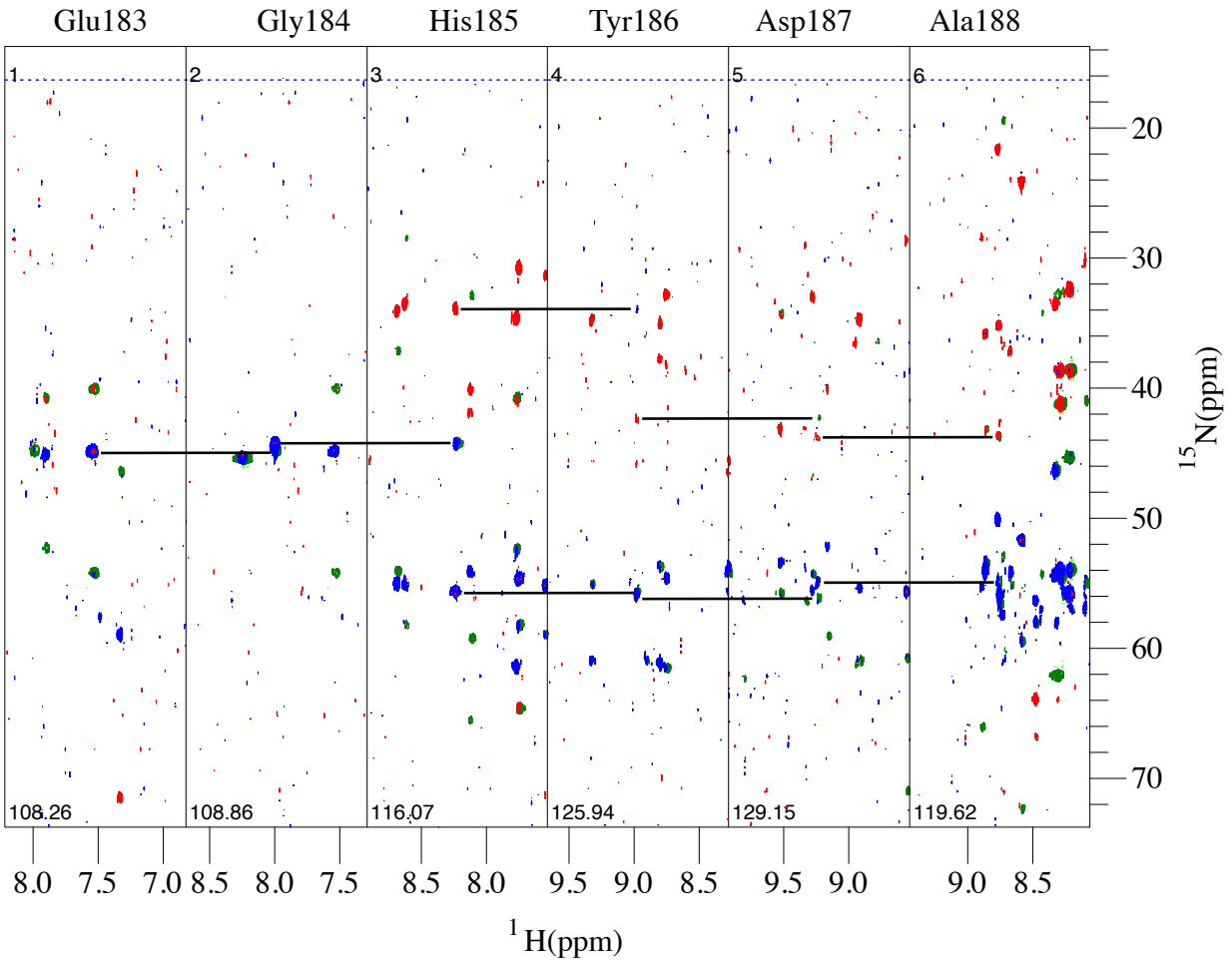

Figure B.27: Continued on following page

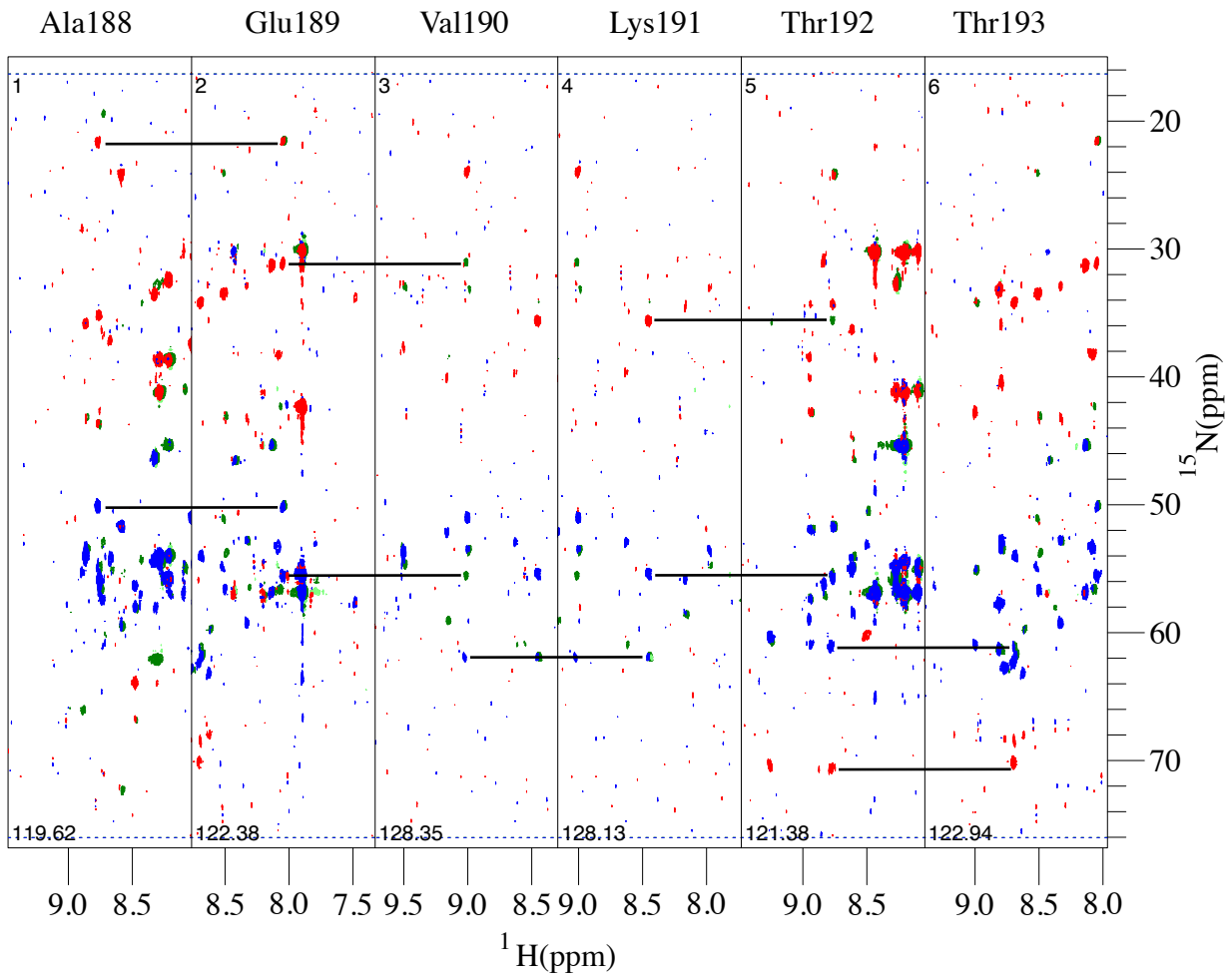

Figure B.28: Continued on following page

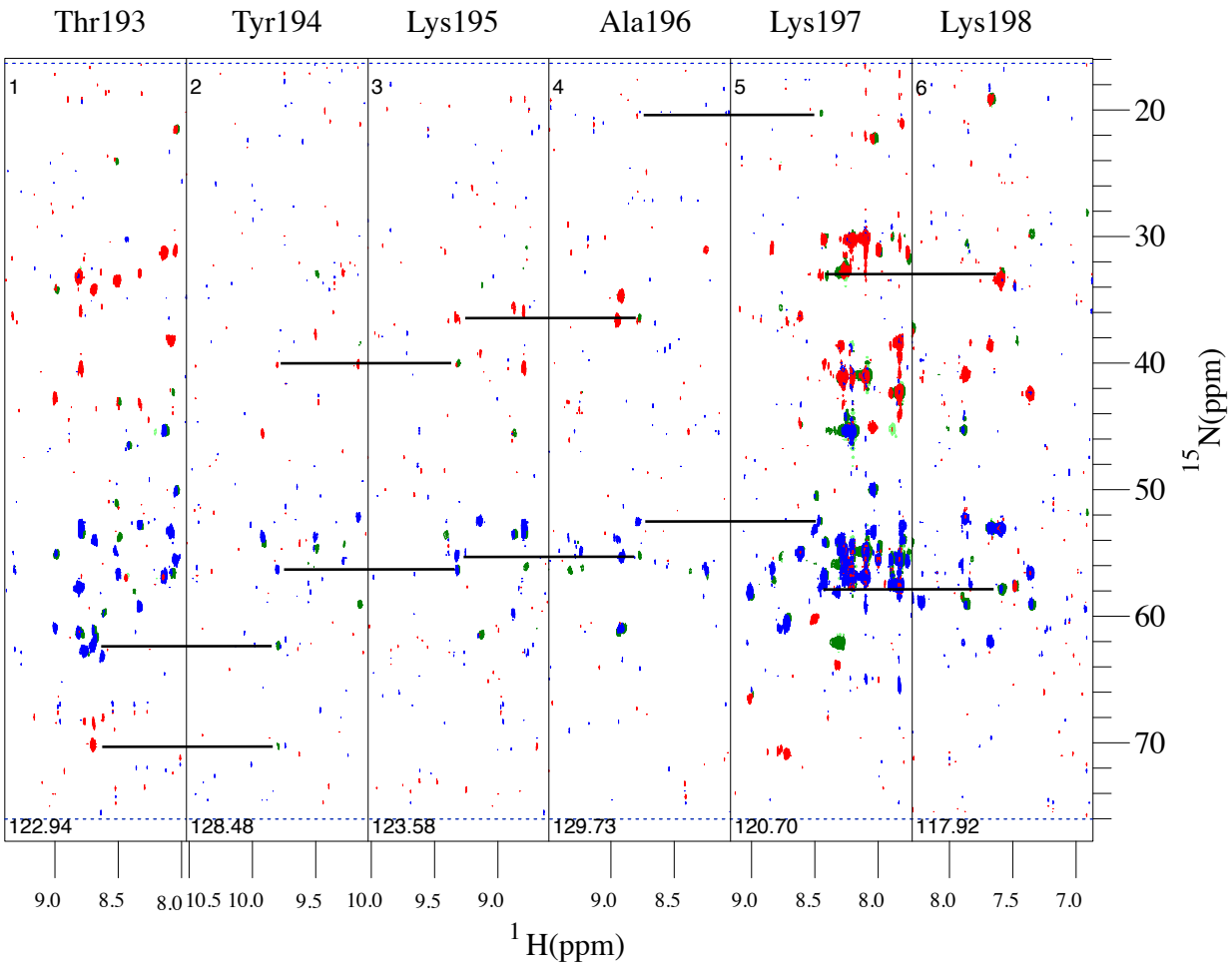

Figure B.29: Continued on following page

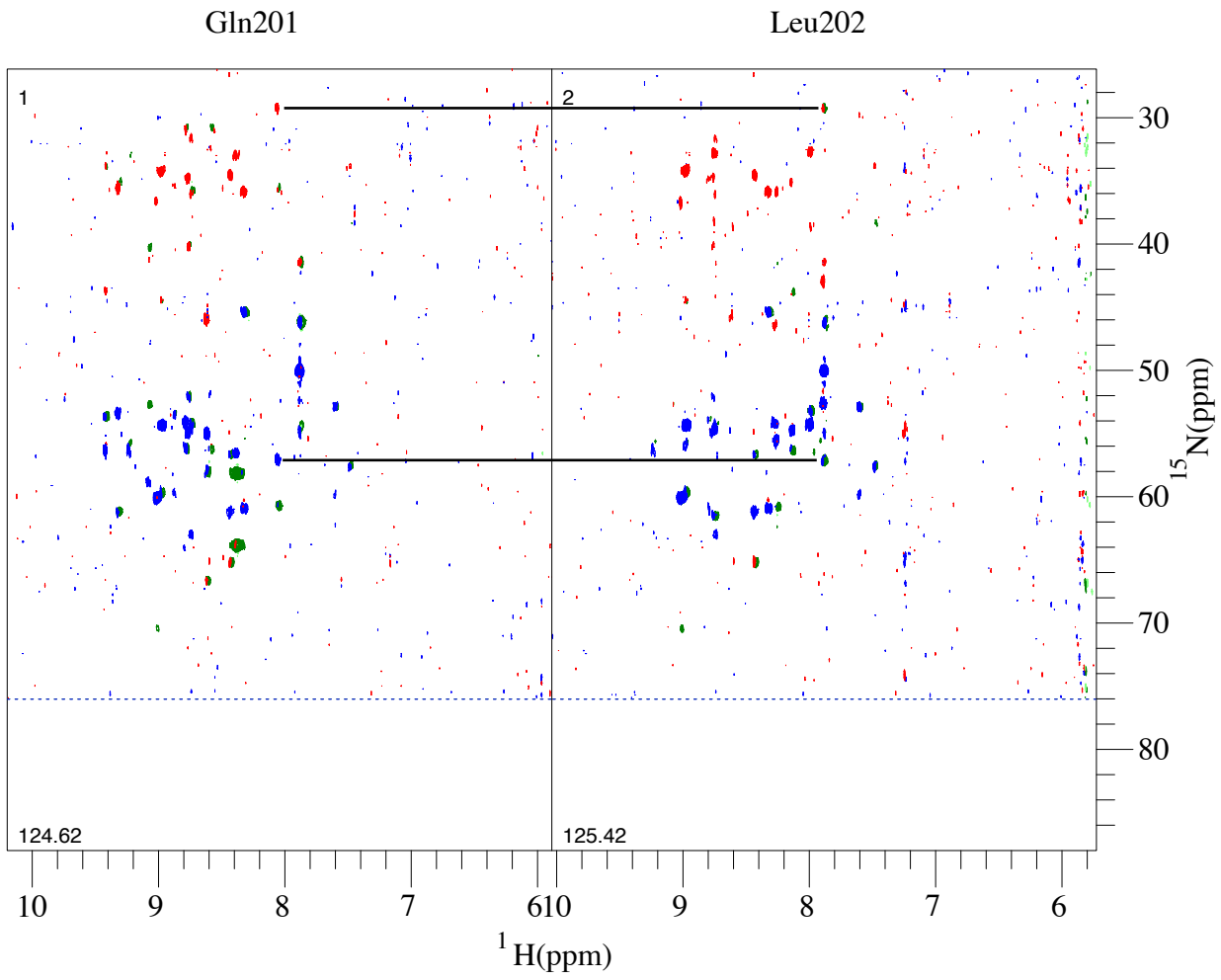

Figure B.30: Continued on following page

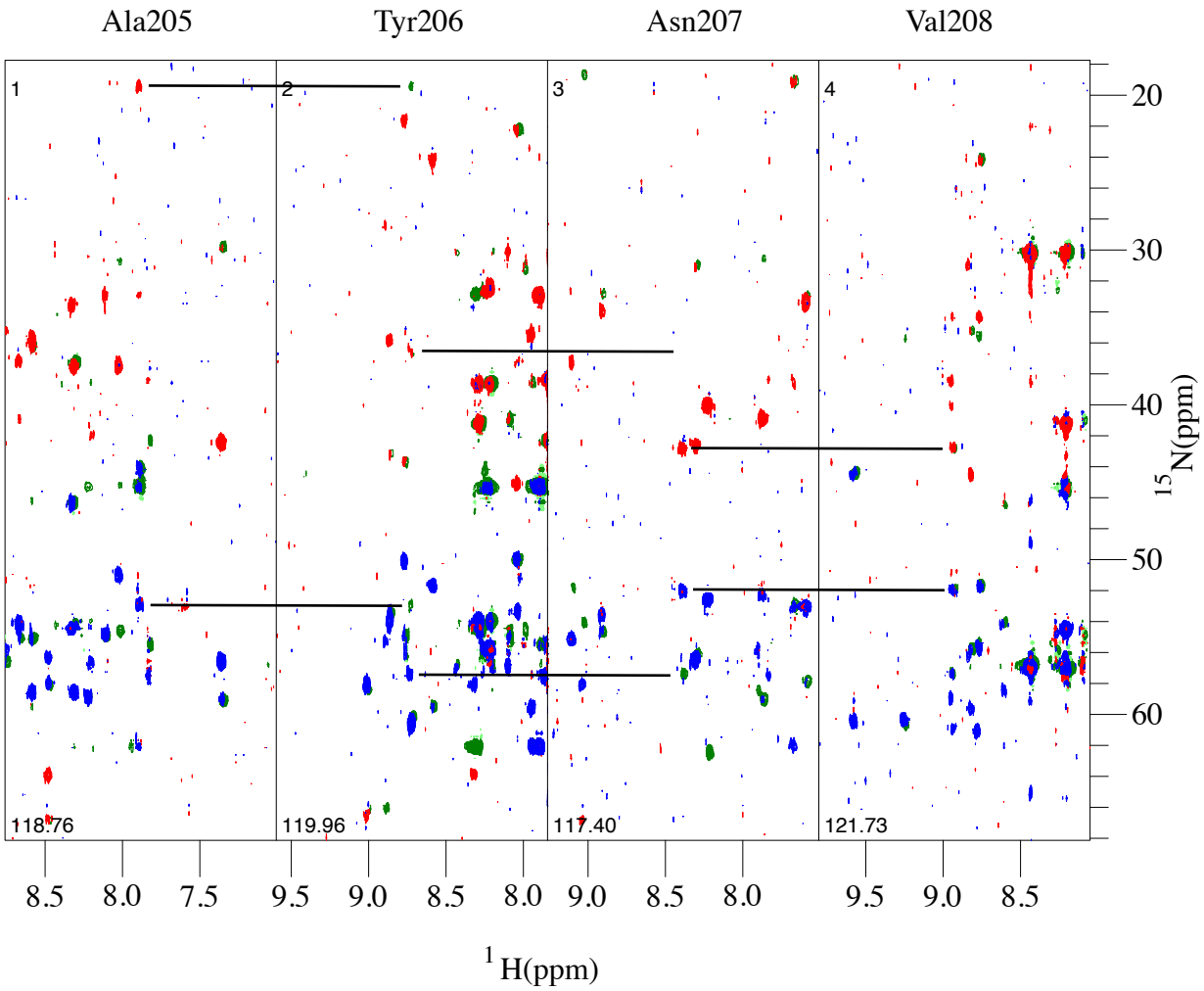

Figure B.31: Continued on following page

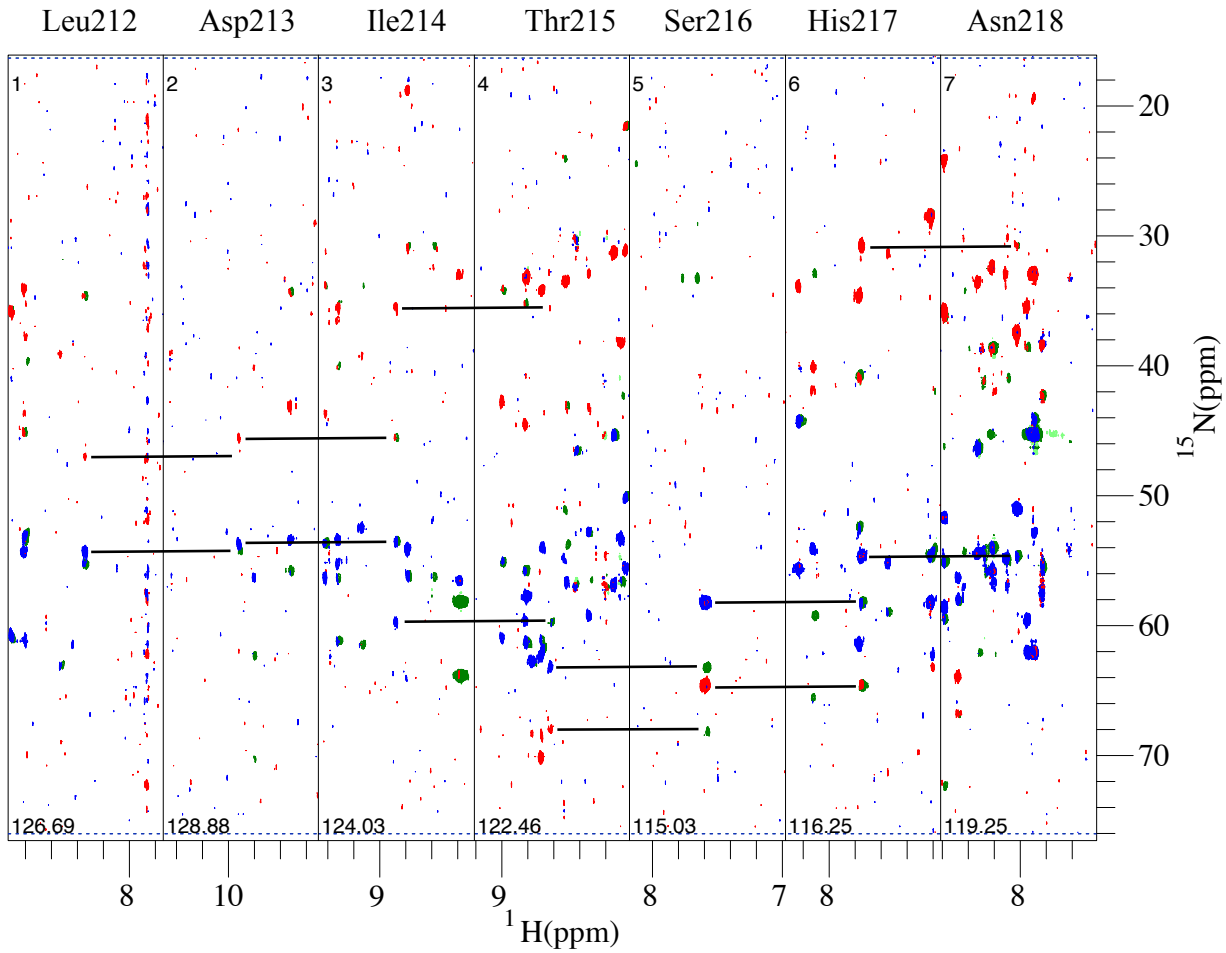

Figure B.32: Continued on following page

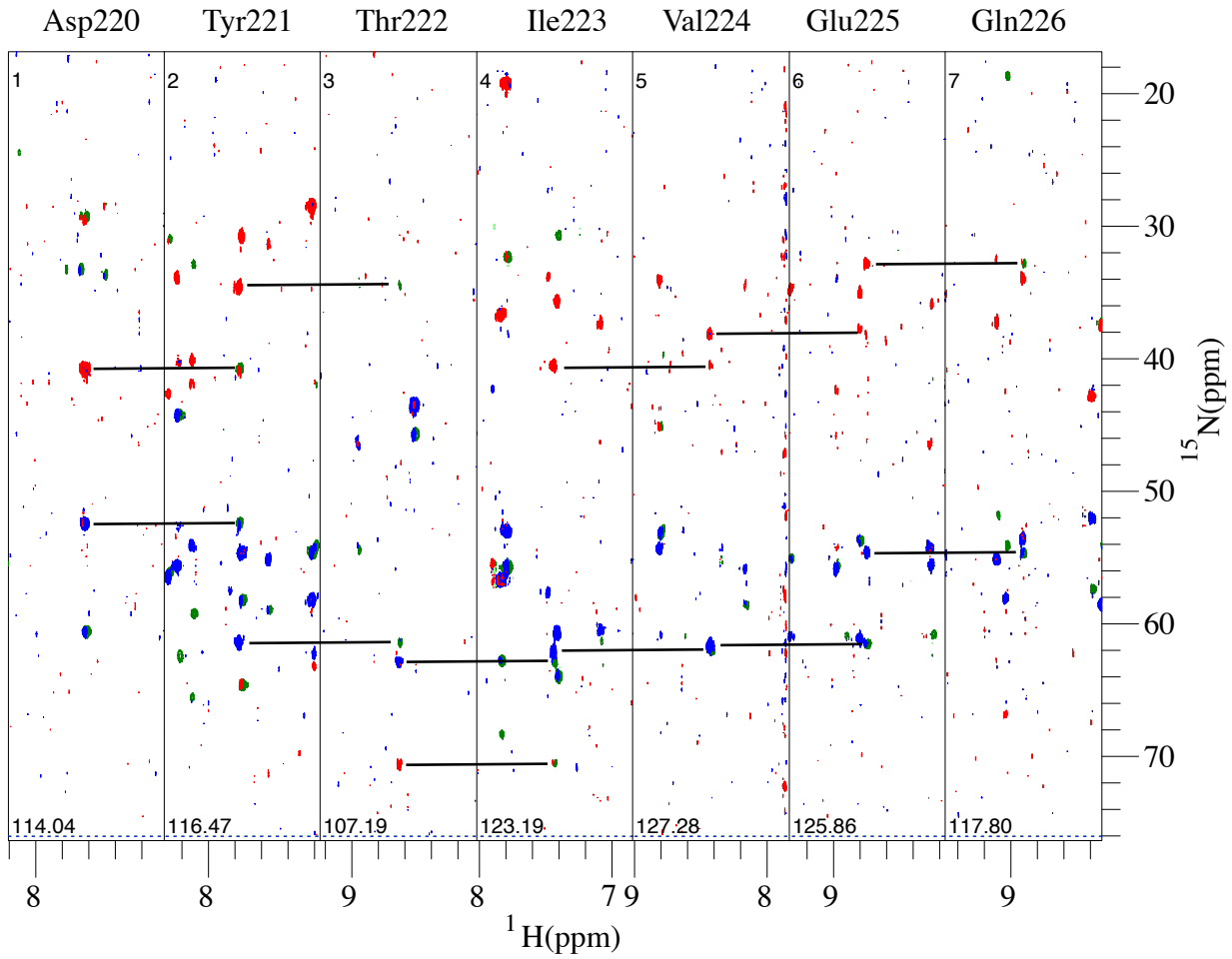

Figure B.33: Continued on following page

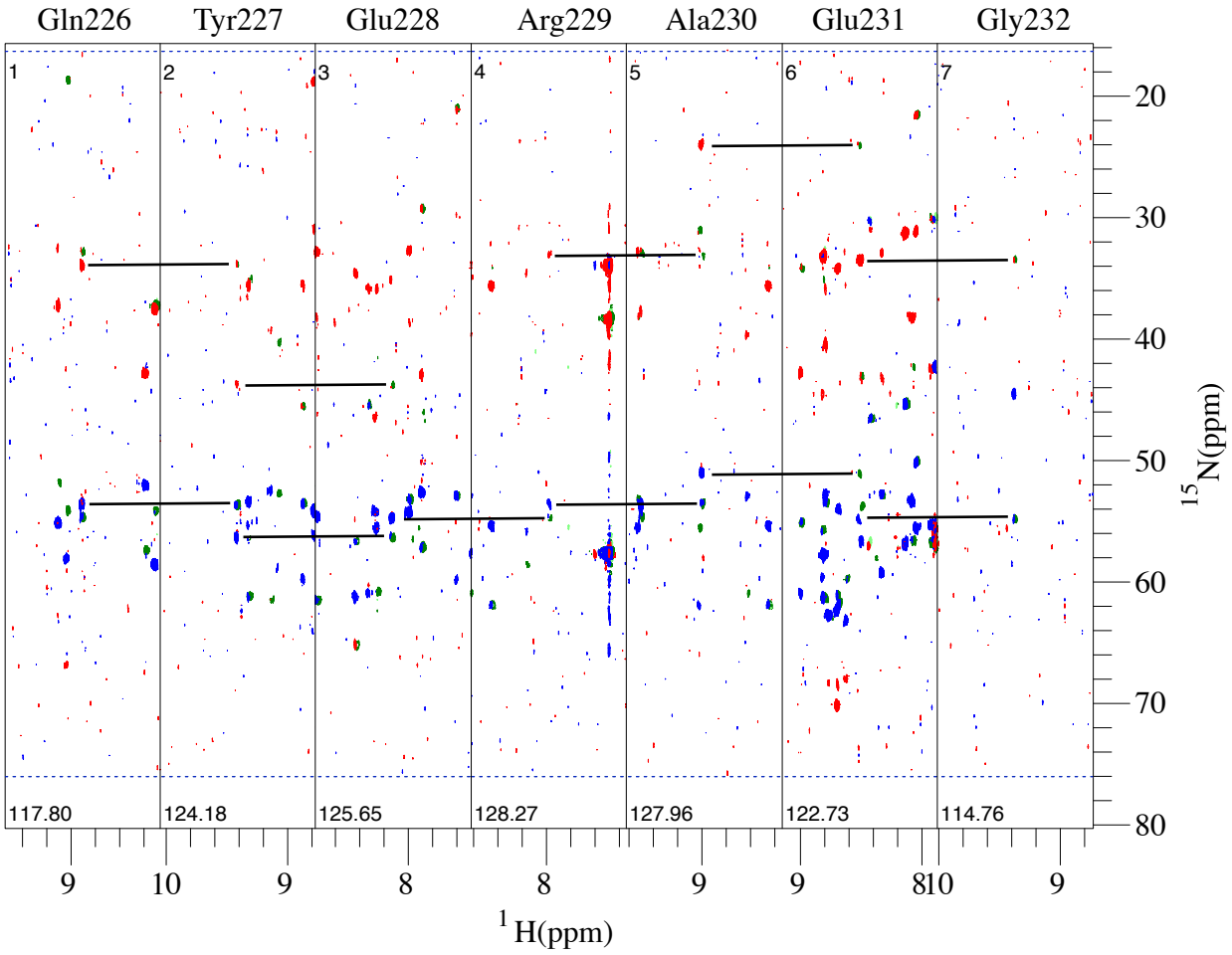

Figure B.34: Continued on following page

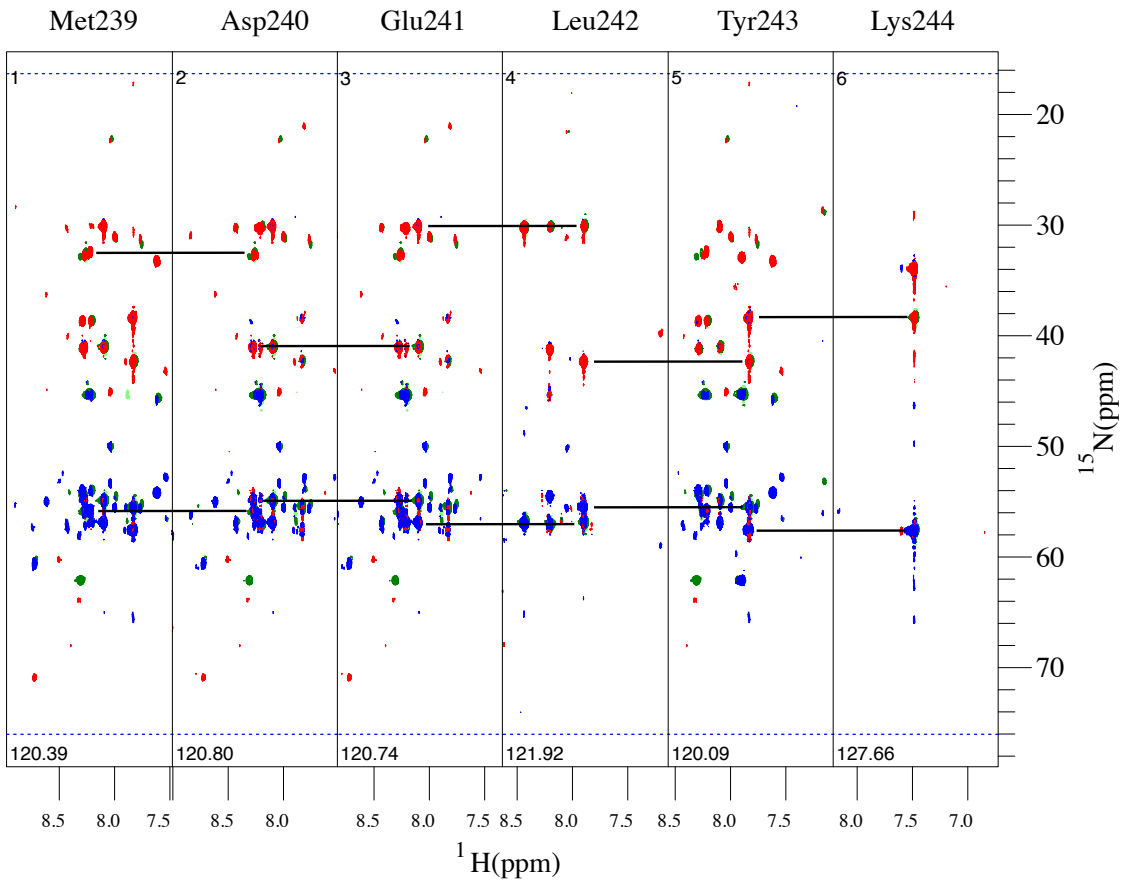

Figure B.34: The strip plots show the connectivity for residues of mCherry at 30°. The blue and red peaks are the C^{α}s and C^{β}s detected in the HNCACB spectrum, respectively. The CBCA(CO)NH spectrum is in green. Black lines connect the C^{α}s and C^{β}s in the HNCACB and CHBCA(CO)NH spectra for the the backbone amides of residue i and i+1. The residue number (using the plasmid number rather than the pdb number, see methods) and type are indicated at the top of each strip. The nitrogren chemical shifts are noted at the bottom of each strip. The dashed lines at the bottom and top of each strip mark the edges of the spectrum in the carbon dimension. The strip number is indicated at the top of each strip.

Appendix C

NMR Assignment Tables and Backbone Amide Order parameters

Table C.1: NMR backbone amide NH assignments for mCherry at 30°C.[a]

mCherry (30°C)			
PDB	plasmid	1H (ppm)	15N (ppm)
	10Val	7.93	119.74
	11Ser	**8.35**	**120.49**
	12Lys	8.42	124.54
	13Gly	8.42	110.93
1	**14Glu**	**8.25**	**121.27**
2	**15Glu**	**8.47**	**121.73**
3	16Asp	8.24	121.59
4	17Asn	8.33	120.24
5	18Met	8.25	120.07
6	19Ala	7.83	123.40
7	20Ile	7.71	118.14
8	21Ile	7.98	119.68
9	22Lys	7.62	129.30
10	23Glu	8.53	115.51
11	24Phe	7.39	118.61
12	25Met	8.12	123.05
13	26Arg	9.56	127.95
14	27Phe	8.27	113.97
15	28Lys	8.65	121.08
16	29Val	8.62	119.10
17	30His	8.20	127.86
18	31Met	9.38	127.43
19	32Glu	8.02	125.89
20	33Gly	7.65	110.02
21	34Ser	7.31	111.09
22	35Val	8.47	125.30
23	36Asn	8.98	130.00
24	37Gly	8.48	102.88
25	**38His**	**8.17**	**123.03**
26	**39Glu**	**8.28**	**129.33**
27	40Phe	8.34	117.13
28	41Glu	8.79	119.46
29	42Ile	8.86	122.31
30	43Glu	9.01	125.32
31	44Gly	8.99	107.98
32	**45Glu**	**8.36**	**119.36**
33	**46Gly**	**8.33**	**111.86**
34	47Glu	8.68	115.19
35	48Gly	7.63	104.86

Table C.1: Continued from previous page

(continued) mCherry 30°C			
PDB	plasmid	1H (ppm)	15N (ppm)
36	49Arg	8.46	122.56
39	52Glu	7.33	117.29
40	53Gly	7.57	105.16
41	54Thr	7.37	107.89
42	55Gln	7.58	116.33
43	56Thr	9.09	112.15
44	57Ala	8.62	119.64
45	58Lys	8.80	121.65
46	59Leu	9.56	129.39
47	60Lys	8.90	119.63
48	61Val	8.78	125.04
49	62Thr	8.80	123.07
50	63Lys	7.87	123.54
51	64Gly	8.95	111.05
52	65Gly	8.56	107.18
56	69Phe	5.90	111.09
57	70Ala	7.84	121.28
58	71Trp	7.64	125.35
59	72Asp	7.79	112.39
60	73Ile	6.54	106.90
61	74Leu	8.17	116.25
71	84Ala	7.67	109.66
72	85Tyr	6.59	113.60
78	91Asp	8.31	111.97
79	**92Ile**	**7.24**	**121.90**
82	95Tyr	8.66	128.04
83	96Leu	8.83	126.97
84	**97Lys**	**8.29**	**125.63**
85	98Leu	8.23	119.10
86	99Ser	7.05	113.16
87	100Phe	7.12	122.78
89	102Glu	10.48	127.33
90	103Gly	8.14	104.94
91	104Phe	7.64	113.51
92	105Lys	8.70	119.20
93	106Trp	8.72	116.19
94	107Glu	8.15	119.07
95	108Arg	9.54	128.14
96	109Val	8.84	126.29

Table C.1: Continued from previous page

(continued) mCherry 30°C			
PDB	plasmid	1H (ppm)	15N (ppm)
97	110Met	9.35	124.68
98	111Asn	8.83	123.39
99	112Phe	9.12	124.90
101	114Asp	7.91	118.05
102	115Gly	7.94	107.83
103	116Gly	6.81	104.56
104	117Val	8.28	109.39
106	119Thr	9.29	121.78
107	120Val	9.05	125.34
108	121Thr	8.76	120.50
109	122Gln	8.59	129.20
112	125Ser	9.04	120.51
113	126Leu	8.66	124.92
114	127Gln	9.07	126.80
116	129Gly	8.40	102.39
117	130Glu	7.66	120.23
118	131Phe	8.46	120.85
119	132Ile	8.98	121.61
120	133Tyr	9.20	128.85
121	134Lys	8.79	125.02
124	137Leu	8.31	126.05
125	138Arg	9.32	129.26
126	139Gly	9.88	115.68
127	140Thr	9.61	121.47
128	141Asn	8.72	114.50
129	142Phe	8.35	118.55
131	144Ser	7.24	116.32
132	145Asp	8.26	117.22
133	146Gly	7.29	106.62
135	148Val	6.65	117.47
136	149Met	8.93	120.23
137	150Gln	7.52	111.95
138	151Lys	7.25	116.42
139	**152Lys**	**8.66**	**116.78**
140	153Thr	7.69	111.79
141	154Met	8.72	122.90
142	155Gly	8.30	111.30
143	156Trp	9.46	120.86
145	158Ala	8.82	124.43

Table C.1: Continued from previous page

(continued) mCherry 30°C			
PDB	plasmid	1H (ppm)	15N (ppm)
146	159Ser	9.07	118.00
147	160Ser	8.51	119.29
148	161Glu	9.51	131.31
149	162Arg	8.72	130.81
155	168Gly	8.71	105.20
156	169Ala	7.92	125.01
157	170Leu	8.08	120.55
158	171Lys	8.85	127.19
159	172Gly	8.99	105.09
160	173Glu	9.15	127.14
161	174Ile	9.03	122.96
162	175Lys	8.88	130.76
163	176Gln	8.73	131.26
164	177Arg	9.27	125.11
165	178Leu	9.37	129.79
166	179Lys	8.54	122.98
167	180Leu	7.57	120.39
168	181Lys	8.36	123.06
169	182Asp	8.16	116.47
170	183Gly	7.57	108.41
172	185His	8.27	116.23
171	184Gly	8.00	108.94
173	**186Tyr**	**9.01**	**126.20**
174	187Asp	9.27	129.36
175	188Ala	8.80	119.80
176	189Glu	8.08	122.62
177	190Val	9.06	128.56
178	191Lys	8.49	128.35
179	192Thr	8.81	121.47
180	193Thr	8.73	123.08
181	194Tyr	9.84	128.75
182	195Lys	9.36	123.73
183	196Ala	8.82	130.00
184	197Lys	8.49	120.85
185	198Lys	7.63	118.10
188	201Gln	8.09	124.78
189	202Leu	7.92	125.61
192	205Ala	7.93	118.90
193	206Tyr	8.77	120.12

Table C.1: Continued from previous page

(continued) mCherry 30°C			
PDB	plasmid	1H (ppm)	15N (ppm)
194	207Asn	8.43	117.54
195	208Val	8.97	121.84
199	212Leu	8.38	126.85
200	213Asp	9.95	129.07
201	214Ile	8.91	124.25
202	215Thr	8.66	122.66
203	216Ser	7.62	115.20
204	217His	7.79	116.39
205	218Asn	8.06	119.46
207	220Asp	7.67	114.22
208	221Tyr	7.80	116.60
209	222Thr	8.68	107.33
210	223Ile	7.48	123.34
211	224Val	8.46	127.49
212	225Glu	8.79	126.05
213	226Gln	8.95	117.98
214	227Tyr	9.45	124.42
215	228Glu	8.17	125.89
216	229Arg	8.01	128.40
217	230Ala	9.04	128.20
218	231Glu	8.56	122.84
219	232Gly	9.41	114.74
226	239Met	8.29	120.65
227	**240Asp**	**8.31**	**120.97**
228	241Glu	8.13	120.93
229	242Leu	7.93	122.09
230	243Tyr	7.86	120.29
231	244Lys	7.52	127.85

mCherry (37°C)			
PDB	plasmid	1H (ppm)	15N (ppm)
	13Gly	8.45	111.26
1	14Glu	8.16	121.35
2	15Glu	8.41	121.74
3	16Asp	8.18	121.64
4	17Asn	8.26	120.18
5	18Met	8.19	120.16
6	19Ala	7.79	123.44

Table C.1: Continued from previous page

(continued) mCherry (37°C)			
PDB	plasmid	1H (ppm)	15N (ppm)
7	20Ile	7.66	118.05
8	21Ile	7.93	119.81
9	22Lys	7.58	129.38
10	23Glu	8.48	115.59
11	24Phe	7.36	118.74
12	25Met	8.12	123.14
13	26Arg	9.52	128.09
14	27Phe	8.25	114.10
15	28Lys	8.63	121.14
16	29Val	8.60	119.23
17	30His	8.19	127.87
18	31Met	9.37	127.63
19	32Glu	8.01	126.02
20	33Gly	7.62	110.05
21	34Ser	7.30	111.22
22	35Val	8.44	125.35
23	36Asn	8.96	129.97
24	37Gly	8.45	102.97
25	38His	8.14	123.08
26	39Glu	8.23	129.41
27	40Phe	8.30	117.24
28	41Glu	8.76	119.66
29	42Ile	8.84	122.55
30	43Glu	9.00	125.54
31	44Gly	8.94	108.09
32	45Glu	8.35	119.45
33	46Gly	8.31	111.93
34	47Glu	8.66	115.26
35	48Gly	7.62	105.02
36	49Arg	8.44	122.69
39	52Glu	7.31	117.41
40	53Gly	7.56	105.19
41	54Thr	7.35	108.07
42	55Gln	7.57	116.48
43	56Thr	9.06	112.47
44	57Ala	8.63	120.02
45	58Lys	8.79	121.85
46	59Leu	9.52	129.34
47	60Lys	8.88	119.76

Table C.1: Continued from previous page

(continued) mCherry (37°C)			
PDB	plasmid	1H (ppm)	15N (ppm)
48	61Val	8.76	125.17
49	62Thr	8.79	123.13
50	63Lys	7.86	123.57
51	64Gly	8.89	111.16
52	65Gly	8.51	107.26
56	69Phe	5.89	111.24
57	70Ala	7.82	121.35
58	71Trp	7.64	125.26
59	72Asp	7.68	112.30
60	73Ile	6.52	107.08
71	84Ala	7.65	109.86
72	85Tyr	6.57	113.68
78	91Asp	8.30	112.12
79	92Ile	7.22	121.93
82	95Tyr	8.68	128.26
83	96Leu	8.82	127.16
84	97Lys	8.26	125.74
85	98Leu	8.22	119.19
86	99Ser	7.03	113.23
87	100Phe	7.10	122.86
89	102Glu	10.47	127.39
90	103Gly	8.11	105.02
91	104Phe	7.59	113.58
92	105Lys	8.71	119.33
93	106Trp	8.72	116.33
94	107Glu	8.11	119.20
95	108Arg	9.52	128.34
96	109Val	8.83	126.38
97	110Met	9.32	124.74
98	111Asn	8.81	123.48
99	112Phe	9.09	124.92
101	114Asp	7.91	118.09
102	115Gly	7.92	107.87
103	116Gly	6.80	104.67
106	119Thr	9.27	121.78
107	120Val	9.03	125.41
108	121Thr	8.73	120.74
109	122Gln	8.59	129.53
112	125Ser	9.01	120.54

Table C.2: The backbone amide assignments transferred to the ^{1}H-^{15}N HSQC TROSY spectra of mCherry, mRaspberry, mRojoB and tdTomato at 37°C from the ^{1}H-^{15}N HSQC TROSY spectra of mCherry at 30°C.

(continued) mCherry (37°C)			
PDB	plasmid	1H (ppm)	15N (ppm)
113	126Leu	8.61	125.04
114	127Gln	9.03	126.87
116	129Gly	8.33	102.53
117	130Glu	7.63	120.26
118	131Phe	8.43	120.89
119	132Ile	8.96	121.71
120	133Tyr	9.17	128.94
121	134Lys	8.78	125.12
124	137Leu	8.29	126.08
125	138Arg	9.29	129.26
126	139Gly	9.82	115.61
127	140Thr	9.57	121.54
128	141Asn	8.65	114.68
129	142Phe	8.29	118.57
132	145Asp	8.23	117.30
133	146Gly	7.26	106.67
135	148Val	6.64	117.54
136	149Met	8.89	120.36
137	150Gln	7.51	112.14
139	152Lys	8.61	116.84
140	153Thr	7.59	111.67
141	154Met	8.69	122.80
142	155Gly	8.21	111.27
143	156Trp	9.43	120.99
145	158Ala	8.75	124.42
146	159Ser	9.02	118.04
147	160Ser	8.46	119.27
148	161Glu	9.49	131.34
149	162Arg	8.71	130.94
155	168Gly	8.64	105.30
156	169Ala	7.90	125.12
157	170Leu	8.05	120.61
158	171Lys	8.83	127.31
159	172Gly	8.99	105.41
160	173Glu	9.13	127.22
161	174Ile	9.00	123.02
162	175Lys	8.81	130.72
163	176Gln	8.71	131.16
164	177Arg	9.25	125.11

Table C.2: Continued from previous page

(continued) mCherry (37°C)			
PDB	plasmid	1H (ppm)	15N (ppm)
165	178Leu	9.35	129.83
166	179Lys	8.51	123.15
167	180Leu	7.56	120.56
168	181Lys	8.33	123.00
170	183Gly	7.54	108.44
171	184Gly	8.00	109.07
172	185His	8.21	116.17
173	186Tyr	8.97	126.27
174	187Asp	9.24	129.49
175	188Ala	8.78	119.99
176	189Glu	8.07	122.74
177	190Val	9.03	128.59
178	191Lys	8.47	128.41
180	193Thr	8.71	123.21
181	194Tyr	9.80	128.79
182	195Lys	9.34	123.80
183	196Ala	8.77	129.92
184	197Lys	8.47	120.88
185	198Lys	7.58	118.08
188	201Gln	8.05	124.99
189	202Leu	7.87	125.45
192	205Ala	7.87	118.94
193	206Tyr	8.78	120.41
194	207Asn	8.40	117.66
195	208Val	8.96	121.97
199	212Leu	8.35	126.96
200	213Asp	9.91	129.15
201	214Ile	8.83	124.31
202	215Thr	8.63	122.67
203	216Ser	7.60	115.25
204	217His	7.74	116.49
205	218Asn	8.05	119.55
207	220Asp	7.63	114.37
208	221Tyr	7.78	116.60
209	222Thr	8.66	107.39
210	223Ile	7.45	123.38
211	224Val	8.44	127.55
212	225Glu	8.76	126.29
213	226Gln	8.93	118.24

Table C.2: Continued from previous page

(continued) mCherry (37°C)			
PDB	plasmid	1H (ppm)	15N (ppm)
214	227Tyr	9.42	124.46
215	228Glu	8.16	126.03
216	229Arg	8.00	128.39
217	230Ala	9.00	128.26
218	231Glu	8.54	123.03
219	232Gly	9.39	114.75
226	239Met	8.25	120.77
227	240Asp	8.26	121.03
228	241Glu	8.09	120.91
229	242Leu	7.88	122.13
230	243Tyr	7.81	120.33
231	244Lys	7.47	127.93

mRasperry (37°C)			
PDB	plasmid	1H (ppm)	15N (ppm)
10	23Glu	8.43	115.63
11	24Phe	7.36	118.92
12	25Met	8.07	123.11
14	27Phe	8.23	114.14
18	31Met	9.35	127.62
25	38His	8.09	123.08
31	44Gly	8.96	108.61
34	47Glu	8.69	115.39
35	48Gly	7.62	104.89
39	52Glu	7.34	117.52
40	53Gly	7.51	105.16
41	54Thr	7.3	107.84
42	55Gln	7.53	116.35
43	56Thr	9.06	112.2
52	65Gly	8.47	107.3
56	69Phe	5.9	111.09
57	70Ala	7.75	121.35
58	71Trp	7.56	125.15
60	73Ile	6.49	107.68
79	92Ile	7.2	121.66
82	95Tyr	8.68	128.43
86	99Ser	7.05	113.21
87	100Phe	7.17	122.84
89	102Glu	10.42	127.51

Table C.2: Continued from previous page

(continued) mRasperry (37°C)			
PDB	plasmid	1H (ppm)	15N (ppm)
90	103Gly	8.06	105.07
93	106Trp	8.7	115.71
101	114Asp	7.89	118.08
102	115Gly	7.91	107.86
103	116Gly	6.8	104.62
109	122Gln	8.6	129.84
117	130Glu	7.62	120.22
126	139Gly	9.75	115.7
127	140Thr	9.59	121.83
128	141Asn	8.66	114.68
129	142Phe	8.34	118.66
133	146Gly	7.25	106.67
135	148Val	6.58	117.28
143	156Trp	9.45	120.62
156	169Ala	7.87	124.97
159	172Gly	8.95	105.1
162	175Lys	8.83	130.66
171	184Gly	8.02	109.55
176	189Glu	8.06	122.53
183	196Ala	8.75	129.95
188	201Gln	7.99	124.73
189	202Leu	7.86	125.47
192	205Ala	7.86	118.89
199	212Leu	8.38	127.22
203	216Ser	7.62	115.51
205	218Asn	8.01	119.46
207	220Asp	7.6	114.39
209	222Thr	8.64	107.29
210	223Ile	7.46	123.28
211	224Val	8.5	127.5
216	229Arg	8.04	128.26
219	232Gly	9.39	115.63

mRojoB (37°C)			
PDB	plasmid	1H (ppm)	15N (ppm)
	13Gly	8.46	111.26
1	14Glu	8.14	121.33
2	15Glu	8.41	121.74
3	16Asp	8.18	121.62

Table C.2: Continued from previous page

(continued) mRojoB (37°C)			
PDB	plasmid	1H (ppm)	15N (ppm)
4	17Asn	8.26	120.17
5	18Met	8.2	120.16
6	19Ala	7.79	123.38
9	22Lys	7.57	129.32
10	23Glu	8.49	115.6
11	24Phe	7.37	118.85
13	26Arg	9.53	128.07
14	27Phe	8.27	114.1
17	30His	8.13	128.1
21	34Ser	7.33	111.22
22	35Val	8.4	125.24
23	36Asn	8.97	130.11
24	37Gly	8.46	102.94
26	39Glu	8.3	129.52
34	47Glu	8.6	115.15
35	48Gly	7.6	104.99
39	52Glu	7.34	117.44
40	53Gly	7.54	105.01
41	54Thr	7.33	108.58
46	59Leu	9.48	129.3
50	63Lys	7.86	123.54
51	64Gly	8.9	111.15
56	69Phe	5.9	111.29
57	70Ala	7.82	121.42
58	71Trp	7.64	125.29
60	73Ile	6.53	107.3
86	99Ser	7.04	113.23
87	100Phe	7.1	122.77
89	102Glu	10.49	127.4
90	103Gly	8.15	104.88
91	104Phe	7.57	113.78
95	108Arg	9.56	128.35
97	110Met	9.34	124.85
99	112Phe	9.09	124.81
101	114Asp	7.89	118.03
102	115Gly	7.92	107.89
103	116Gly	6.83	104.73
109	122Gln	8.57	129.55
116	129Gly	8.33	102.5

Table C.2: Continued from previous page

(continued) mRojoB (37°C)			
PDB	plasmid	1H (ppm)	15N (ppm)
126	139Gly	9.81	115.66
127	140Thr	9.56	121.59
128	141Asp	8.65	114.66
132	145Asp	8.23	117.3
133	146Gly	7.26	106.66
135	148Val	6.6	117.44
137	150Gly	7.5	112.2
140	153Thr	7.61	111.63
155	168Gly	8.65	105.26
156	169Ala	7.92	125.19
157	170Leu	8.05	120.54
167	180Leu	7.53	120.56
168	181Lys	8.32	122.97
170	183Gly	7.59	108.38
171	184Gly	8.01	108.63
178	191Lys	8.5	128.51
181	194Tyr	9.76	128.56
183	196Ala	8.75	129.71
185	198Lys	7.59	118.1
188	201Gln	8.08	125.16
189	202Leu	7.92	125.5
192	205Ala	7.87	118.78
200	213Asp	9.84	129.01
203	216Ser	7.59	115.05
207	220Asp	7.64	114.36
210	223Ile	7.46	123.43
211	224Val	8.45	127.53
214	227Tyr	9.45	124.52
216	229Arg	8.06	128.35
219	232Gly	9.23	114.05
226	239Met	8.22	120.6
227	240Asp	8.26	121.09
228	241Glu	8.1	120.93
229	242Leu	7.88	122.19
230	243Tyr	7.82	120.36
231	244Lys	7.49	127.92

Table C.2: Continued from previous page

tdTomato (37°C)			
pdb	plasmid	1H (ppm)	15N (ppm)
9	22Lys	7.52	128.86
10	23Glu	8.45	115.32
21	34Ser	7.16	111.07
31	44Gly	9.00	107.57
36	49Arg	8.41	122.76
51	64Gly	8.87	111.02
52	65Gly	8.47	106.72
56	69Phe	6.08	110.56
60	73Ile	6.61	109.10
89	102Glu	10.42	126.94
90	103Gly	8.06	104.30
93	106Trp	8.69	116.02
102	115Gly	7.98	107.75
103	116Gly	6.63	104.16
168	181Lys	8.31	122.71
170	183Gly	7.45	108.26
171	184Gly	8.03	108.79
203	216Ser	7.57	114.87
207	220Asp	7.61	113.88
219	232Gly	9.34	115.56

[a]The NMR assignments and chemical shifts for the backbone amide hydrogen and nitrogen are given for mCherry at 30°C and 37°C, as well as for mRaspberry, mRojoB and tdTomato at 37°C. The assignments were confirmed manually, and bold assignments differed from the PINE predictions of $\geq$ 90% confidence.

Table C.3: The residue numbers, model, χ^2 value for model selection, ^{15}N amide order parameter, rotational correlation time for the internal motion, exchange rate constant, and second order parameter for mCherry, mRaspberry and mRojoB calculated using the model free formalism and the program Tensor2 [136].[a]

mCherry Residue	Model[b]	χ^2	S^2	τ_i (ns)	K_{ex} (s^{-1})	S_2^2 [c]
1	4	0.00	0.34±0.04	1.18±0.02	9.52±0.48	---
2	4	0.00	0.29±0.03	1.15±0.01	10.3±0.32	---
4	4	0.00	0.28±0.04	1.31±0.02	10.52±0.48	---
5	5	0.00	0.56±0.02	1.13±0.02	---	0.94±0.02
6	2	0.89	0.77±0.01	0.79±0.04	---	---
7	2	0.73	0.78±0.01	1.01±0.04	---	---
9	4	0.00	0.92±0.04	0.01±0.22	3.41±0.92	---
10	2	1.04	0.98±0.01	0.34±0.31	---	---
11	1	4.97	1±0.01	---	---	---
12	2	2.79	0.9±0.01	1.93±0.19	---	---
13	3	251.29	0.99±0	---	1.94±0	---
14	2	0.00	0.95±0.01	1.06±0.17	---	---
15	4	0.00	0.99±0.01	0.17±0.48	1.54±0.37	---
16	1	2.20	1±0.01	---	---	---
17	3	0.18	1±0.01	---	3.13±0.53	---
18	4	0.00	0.97±0.04	2.45±2.02	1.79±0.45	---
19	5	0.00	0.93±0.01	3.05±0.74	---	0.9±0.01
21	2	3.88	0.98±0.01	0.22±0.33	---	---
22	2	0.50	0.96±0.01	1.66±0.5	---	---
23	4	0.00	0.98±0.02	5.66±4.29	1.3±0.3	---
24	4	0.00	0.86±0.07	5.66±2.3	4.08±0.8	---
25	6(5)	7.76	1.01±0.01	0.11±0.51	---	0.98±0.01
26	6(4)	35.34	1±0.02	2.5±5.12	2.31±0.45	---
28	1	6.63	1±0.01	---	---	---
29	6(1)	8.32	1±0.01	---	---	---
31	2	2.94	0.87±0.02	0.03±0.01	---	---
32	1	4.78	1±0.01	---	---	---
33	5	0.00	0.92±0.01	1.76±0.15	---	0.96±0.01
34	4	0.00	0.97±0.01	0.23±0.21	2.32±0.29	---
35	4	0.00	0.96±0.04	0.06±0.51	1.44±0.86	---
36	2	0.02	0.9±0.01	0.05±0.01	---	---
39	4	0.00	0.89±0.01	0.02±0	2.79±0.42	---
40	4	0.00	0.94±0.02	0.06±0.12	2.36±0.62	---
41	4	0.00	0.95±0.03	0.04±0.23	1.86±0.64	---
42	1	7.84	1±0.01	---	---	---
44	1	1.43	0.97±0.01	---	---	---
45	4	0.00	0.96±0.02	0.09±0.37	1.38±0.48	---
47	2	0.71	0.97±0.01	0.06±0.47	---	---
50	5	0.00	0.93±0.01	0.88±0.12	---	0.9±0.01

Table C.3: Continued from previous page

mCherry continued						
Residue	Model[b]	χ^2	S^2	τ_i (ns)	K_{ex} (s^{-1})	S_2^2 [c]
51	4	0.00	0.93±0.03	1.93±0.75	1.59±0.63	---
52	6(4)	43.04	1±0.02	4.31±4.15	0.68±0.31	---
56	3	0.35	0.78±0.05	---	2.65±0.89	---
58	1	6.03	1±0.01	---	---	---
60	3	179.69	0.93±0	---	1.84±0	---
72	2	0.02	0.92±0.02	0.01±1.03	---	---
79	3	12.85	0.94±0	---	2.22±0	---
85	5	0.00	0.95±0.02	2.28±0.81	---	0.96±0.02
86	1	316.02	0.98±0	---	---	---
87	6(4)	37.53	1±0.03	12.32±64.79	1.95±0.39	---
89	4	0.00	0.91±0.03	3.58±1.16	3.24±0.44	---
90	2	0.64	0.99±0.01	0.31±0.5	---	---
92	2	0.02	1±0.01	0.38±1.64	---	---
93	6(4)	36.27	1±0.02	2.48±4.9	1.44±0.44	---
95	4	0.00	0.98±0.01	0.72±0.47	2.86±0.26	---
97	4	0.00	0.95±0.01	0.82±0.29	1.01±0.28	---
98	1	1.43	0.95±0.01	---	---	---
99	4	0.00	0.98±0.03	0.12±0.72	0.77±0.61	---
101	2	1.22	0.99±0.01	0.31±0.34	---	---
102	6(5)	11.77	0.94±0.03	12.94±4.22	---	1±0.01
103	4	0.00	0.98±0.01	1.23±0.62	2.31±0.37	---
106	6(4)	50.63	1±0.01	0.43±5.01	3.14±0.42	---
108	4	0.00	0.99±0.02	0.32±0.6	1.08±0.37	---
112	4	0.00	0.96±0.02	0.06±0.03	2.3±0.37	---
113	2	0.56	0.97±0.01	0.95±0.42	---	---
114	2	0.20	0.97±0.01	0.84±0.39	---	---
124	6(5)	1.47	0.91±0.04	12.94±3.98	---	0.96±0.02
125	4	0.00	0.96±0.03	1.81±1.16	2.85±0.53	---
126	4	0.00	0.98±0.01	0.05±0.34	1.34±0.39	---
127	3	4.42	1±0.02	---	1.36±0.69	---
128	2	76.26	0.96±0	12.94±0	---	---
129	6(4)	121.75	1±0.04	2.66±5.06	0.05±0.32	---
133	4	0.00	0.91±0.02	0.02±0	1.33±0.41	---
136	3	2.31	1±0.02	---	1.43±0.75	---
137	5	0.00	0.83±0.01	1.04±0.06	---	0.92±0.01
138	4	0.00	0.96±0.02	0.03±0.25	1.52±0.45	---
141	3	24.90	0.95±0	---	1.26±0	---
142	2	2.47	0.94±0.01	0.08±0.02	---	---
143	4	0.00	0.96±0.01	0.71±0.29	2.27±0.45	---

Table C.3: Continued from previous page

mCherry continued						
Residue	Model[b]	χ^2	S^2	τ_i(ns)	K_{ex} (s^{-1})	S_2^2 [c]
145	4	0.00	0.98±0.01	0.9±0.38	1.81±0.26	---
146	4	0.00	0.92±0.02	0.05±0.01	1.67±0.33	---
147	6(5)	18.37	0.94±0.02	12.94±3.95	---	0.98±0.01
148	4	0.00	0.97±0.01	0.11±0.06	2.35±0.37	---
155	4	0.00	0.92±0.04	1.38±0.67	1.41±0.62	---
156	2	0.63	0.97±0.01	0.15±0.15	---	---
161	2	0.03	0.94±0.01	2.09±0.33	---	---
162	4	0.00	0.97±0.01	2.49±1.12	1.05±0.46	---
164	4	0.00	0.9±0.03	0.01±0.01	1.59±0.59	---
165	4	0.00	0.97±0.01	1.44±0.76	2.55±0.4	---
167	2	2.04	0.96±0.01	0.26±0.19	---	---
168	4	0.00	0.91±0.01	1.7±0.21	0.87±0.28	---
170	2	2.78	0.93±0.01	1.26±0.16	---	---
172	6(4)	47.81	0.99±0.03	12.94±919.36	0.33±0.34	---
173	1	3.80	0.99±0.01	---	---	---
174	4	0.00	0.94±0.02	0.02±0.07	3.86±0.55	---
176	5	0.00	0.87±0.04	12.47±2.98	---	0.87±0.02
177	4	0.00	0.97±0.01	1.33±0.37	2.45±0.28	---
178	3	3.72	1±0.02	---	2.2±0.66	---
180	1	0.57	0.99±0.01	---	---	---
181	3	7.76	1±0.03	---	1.62±0.91	---
182	4	0.00	0.95±0.03	0.07±0.32	2.72±0.66	---
184	2	0.09	0.97±0.01	0.96±0.44	---	---
188	2	0.43	0.94±0.01	0.92±0.22	---	---
189	2	0.62	0.88±0.01	0.05±0.01	---	---
192	2	1.90	0.91±0.01	0.01±0	---	---
194	2	0.19	0.98±0.01	0.3±0.2	---	---
195	6(5)	6.98	0.97±0.02	12.94±37.7	---	0.99±0.01
199	3	13.13	0.99±0	---	0.08±0	---
200	1	3.29	1±0.01	---	---	---
201	2	0.24	0.97±0.01	0.06±0.58	---	---
202	4	0.00	0.98±0.01	0.44±0.31	0.71±0.3	---
203	4	0.00	0.93±0.03	0.05±0.12	1.4±0.62	---
204	6(4)	1.97	0.9±0.05	12.94±3.86	1.71±0.46	---
205	3	111.09	0.98±0	---	0.15±0	---
207	4	0.00	0.95±0.01	1.6±0.24	0.91±0.26	---
208	6(5)	51.18	0.99±0.02	12.94±1682.7	---	1.01±0.01
209	4	0.00	0.93±0.01	1.85±0.27	1.12±0.17	---
210	4	0.00	0.96±0.02	0.05±0.15	1.7±0.39	---

Table C.3: Continued from previous page

mCherry continued						
Residue	Model[b]	χ^2	S^2	τ_i (ns)	K_{ex} (s^{-1})	S_2^2 [c]
211	1	1.47	1±0.01	---	---	---
212	1	2.50	1±0.01	---	---	---
214	4	0.00	0.94±0.01	0.08±0.02	1.95±0.27	---
215	6(5)	0.02	0.91±0.03	12.94±3.88	---	0.94±0.01
216	2	2.76	0.94±0.03	0.03±0.37	---	---
217	6(4)	10.56	1±0.02	7.42±4.79	1.96±0.33	---
219	6(4)	17.17	0.98±0.01	12.94±172.68	0.76±0.29	---

mRaspberry Residue	Model[b]	χ^2	S^2	τ_i (ns)	K_{ex} (s^{-1})	S_2^2 [c]
10	6(5)	23.31	0.99±0.03	9.57±3.78	---	0.95±0.02
11	6(4)	122.09	1±0.05	8.62±24.1	0.53±0.4	---
12	1	4.49	0.98±0.01	---	---	1±0
14	6(5)	17.44	0.98±0.02	9.57±21.75	---	0.95±0.02
18	3	6.51	0.97±0	---	0.87±0	---
25	3	67.86	0.98±0	---	0.79±0	---
31	6(1)	8.05	0.9±0.01	---	---	---
34	3	39.68	0.96±0	---	0.73±0	---
35	6(4)	56.35	1±0.02	1.07±3.74	0.47±0.28	---
39	6(5)	36.13	0.86±0.05	9.57±2.86	---	0.98±0.02
40	3	35.53	0.99±0	---	0.29±0	---
41	6(4)	23.56	0.97±0.03	9.57±258.83	1±0.29	---
42	6(4)	44.27	0.96±0.04	9.57±127.25	0.63±0.38	---
43	3	10.59	0.99±0	---	0.38±0	---
52	6(4)	158.66	1±0.02	5.17±4.15	0.71±0.27	---
56	4	0	0.77±0.01	0.05±0	1.23±0.29	---
57	3	14.07	0.95±0	---	0.4±0	---
58	6(1)	7.14	0.97±0.02	---	---	---
60	6(4)	31.84	1±0.01	7.93±14.29	0.78±0.41	---
79	1	1.37	0.97±0.02	---	---	---
82	3	17.8	0.99±0	---	1.18±0	---
86	1	0.88	0.95±0.02	---	---	---
87	3	3.2	1±0.02	---	0.83±0.47	---
89	6(4)	41.47	1±0.07	2.71±3.6	1.37±0.79	---

Table C.3: Continued from previous page

mRaspberry continued						
Residue	Model[b]	χ^2	S^2	τ_i (ns)	K_{ex} (s^{-1})	S_2^2 [c]
90	1	0.65	0.98±0.01	---	---	---
101	6(4)	8.15	0.98±0.03	9.57±268.72	1.08±0.36	---
102	6(5)	25.31	1±0.01	9.57±390.7	---	1±0.01
103	6(4)	13.96	0.97±0.03	9.57±502.14	0.98±0.31	---
117	1	1.03	0.96±0.01	---	---	---
126	3	19.96	0.94±0	---	0.48±0	---
127	6(4)	52.11	1±0.02	1.86±3.78	0.38±0.26	---
128	6(5)	16.74	0.71±0.13	9.57±2.96	---	1.13±0.07
133	1	8.16	1±0.01	---	---	---
143	6(1)	11.49	0.99±0.01	---	---	---
156	2	0	0.97±0.02	1.88±1.35	---	---
159	6(4)	20.13	1±0.02	1.87±3.61	0.15±0.25	---
176	1	2.21	0.91±0.01	---	---	---
188	2	0.85	0.97±0.02	1.08±1.21	---	---
189	2	0.37	0.89±0.01	0.04±0.01	---	---
192	1	2.86	0.89±0.01	---	---	---
203	1	74.03	0.96±0	---	---	---
207	4	0	0.7±0.15	5.58±1.98	2±0.89	---
209	6(5)	22.73	0.86±0.04	9.57±2.71	---	1.06±0.03
219	1	1.56	1±0.01	---	---	---

mRojoB Residue	Model[b]	X^2	S^2	τ_i (ns)	K_{ex} (s^{-1})	S_2^2 [c]
1	4	0	0.22±0.04	0.8±0.02	4.32±0.41	---
2	4	0	0.24±0.03	0.94±0.02	4.5±0.28	---
4	4	0	0.3±0.01	1.42±0.04	7.74±0.19	---
5	5	0	0.44±0.01	1.2±0.03	---	0.85±0.01
6	5	0	0.62±0.01	1.11±0.04	---	0.85±0.01
9	3	8.12	0.84±0	---	0.95±0	---
10	1	3.16	0.88±0.01	---	---	---
11	3	0.25	0.85±0.03	---	3.43±0.6	---
13	5	0	0.97±0.01	1.54±4.34	---	0.92±0.01
14	1	2.85	0.9±0.01	---	---	---
17	1	1.36	0.88±0.01	---	---	---

Table C.3: Continued from previous page

mRojoB continued						
Residue	Model[b]	χ^2	S^2	τ_i (ns)	K_{ex} (s^{-1})	S_2^2 [c]
21	1	2.5	0.87±0.02	---	---	---
22	1	4	0.86±0.02	---	---	---
23	2	0.03	0.9±0.02	0.03±0.05	---	---
26	1	4.79	0.86±0.02	---	---	---
34	3	1.76	0.91±0.01	---	0.92±0.23	---
35	5	0	0.91±0.03	1.89±2.28	---	0.81±0.02
39	1	5.13	0.9±0.03	---	---	---
40	1	1.33	0.8±0.01	---	---	---
41	1	2.09	0.89±0.01	---	---	---
46	1	1.35	0.91±0	---	---	---
50	2	0.17	0.81±0.01	0.05±0.01	---	---
51	1	0.31	0.94±0.03	---	---	---
56	2	0.87	0.72±0.01	0.04±0.01	---	---
57	2	0.02	0.79±0.01	0.11±0.01	---	---
58	4	0	0.82±0.03	0.04±0.01	2.99±0.77	---
60	1	0.58	0.88±0.04	---	---	---
86	4	0	0.82±0.03	0.04±0.01	1.67±0.61	---
87	4	0	0.88±0.04	0.03±0.04	3.49±0.65	---
89	1	0.6	0.89±0.02	---	---	---
90	2	0	0.85±0.02	0.06±0.08	---	---
99	1	5.5	0.89±0.01	---	---	---
101	3	1.98	0.93±0.04	---	3.01±0.64	---
102	1	2.29	0.91±0.01	---	---	---
103	1	1.25	0.89±0.02	---	---	---
109	1	3.05	0.96±0.01	---	---	---
126	1	0.09	0.92±0.02	---	---	---
127	3	0.01	0.91±0.03	---	2.09±0.68	---
128	1	4.23	0.92±0.01	---	---	---
132	1	1.59	0.95±0	---	---	---
133	1	4.24	0.85±0.02	---	---	---
140	5	0	0.9±0.02	1.32±0.46	---	0.83±0.02
155	2	0.76	0.83±0.02	0.03±0.01	---	---
156	5	0	0.95±0.02	1.6±1.29	---	0.88±0.02
167	4	0	0.83±0.03	0.06±0.02	3.43±0.64	---
168	3	3.18	0.85±0.03	---	1.71±0.57	---
170	5	0	0.88±0.02	2.21±0.6	---	0.81±0.02
178	4	0	0.82±0.05	0.04±0.03	1.99±0.91	---
181	5	0	0.95±0.02	2.09±4.35	---	0.86±0.01
183	1	2.91	0.9±0.02	---	---	---

Table C.3: Continued from previous page

mRojoB continued						
Residue	Model[b]	χ^2	S^2	τ_i(ns)	K_{ex} (s^{-1})	S_2^2 [c]
188	4	0	0.79±0.04	0.04±0.01	3.14±0.7	---
189	2	1.15	0.81±0.01	0.04±0.01	---	---
192	4	0	0.77±0.02	0.02±0	2.23±0.43	---
196	1	4.08	0.88±0.01	---	---	---
200	1	0.42	0.91±0.01	---	---	---
203	3	4.07	0.8±0.03	---	2.47±0.51	---
207	2	0.4	0.88±0.01	0.02±0.01	---	---
210	4	0	0.84±0.03	0.03±0.01	1.65±0.63	---
211	1	4.3	0.88±0.01	---	---	---
214	1	4.27	0.91±0.02	---	---	---
216	1	2.25	0.94±0.02	---	---	---
219	1	2.56	0.91±0.03	---	---	---
222	5	0	0.37±0.02	0.84±0.03	---	0.85±0.02

[a] A '---' for τ_c, k_{ex}, or S_2^2 indicates the model used for that amide did not include these parameters, or that the error was larger than 100%.

[b] Models 1-5 were selected to fit the data for each amide (see Methods).

[c] For residues whose relaxation data fit best to model 5, two order parameters are reported, one for the faster internal motion, and one for the slower internal motion.

Table C.4: Hydrogen-deuterium exchange protection factors for mCherry, mRojoB, and tdTomato).[a]

Residue #	Protection Factor		
	mCherry	mRojoB	tdTomato
1	---	$<10^{5.09}$	---
2	$10^{7.18}$	$<10^{4.53}$	---
4	$10^{7.55}$	---	---
8	$<10^{3.68}$	---	---
9	$<10^{4.37}$	---	$<10^{4.37}$
10	$<10^{4.25}$	$<10^{4.25}$	$<10^{4.25}$
11	$<10^{4.25}$	$<10^{4.25}$	---
12	$10^{7.12}$	---	---
14	$>10^{8.1}$	$>10^{8.1}$	---
16	$10^{6.50}$	$10^{7.44}$	---
17	$10^{6.17}$	---	---
18	$10^{7.41}$	---	---
19	$10^{6.18}$	---	---
20	$10^{6.83}$	---	---
21	$10^{6.94}$	$10^{6.87}$	$10^{6.18}$
22	$10^{6.43}$	$10^{6.36}$	---
24	$<10^{5.22}$	$<10^{5.22}$	---
25	$10^{6.88}$	---	---
26	$<10^{4.25}$	$<10^{4.25}$	---
28	$>10^{7.67}$	---	---
29	$>10^{7.24}$	---	---
30	$>10^{7.38}$	---	---
31	$10^{7.27}$	---	$10^{6.19}$
32	$10^{5.70}$	---	---
34	$10^{6.96}$	---	---
35	---	$10^{5.85}$	---
36	$10^{6.24}$	$10^{5.97}$	---
39	$<10^{4.18}$	$<10^{4.18}$	---
40	---	$10^{7.05}$	---
41	$10^{6.37}$	$10^{5.74}$	---
42	$10^{7.58}$	---	---
44	---	$10^{7.37}$	---
45	$10^{6.76}$	---	---
47	$>10^{7.86}$	$10^{6.98}$	---
50	$<10^{4.8}$	$<10^{4.8}$	---
51	---	---	$<10^{5.02}$
52	$<10^{5.07}$	$<10^{5.07}$	$<10^{5.07}$
56	---	---	$10^{5.01}$
57	$10^{7.22}$	---	---
58	$<10^{4.23}$	$<10^{4.23}$	---
59	$<10^{4.23}$	---	---

Table C.4: Continued from previous page

Residue #	Protection Factor (continued)		
	mCherry	mRojoB	tdTomato
60	$10^{6.26}$	$10^{6.08}$	---
71	$10^{7.70}$	---	---
72	$>10^{7.84}$	---	---
73	$<10^{3.98}$	---	---
82	$10^{5.76}$	---	---
83	$<10^{4.11}$	---	---
84	$10^{7.41}$	---	---
85	$10^{6.65}$	---	---
86	$10^{7.46}$	$10^{6.89}$	---
89	$<10^{3.89}$	$<10^{3.89}$	$<10^{3.89}$
90	$10^{6.86}$	$10^{6.07}$	$10^{6.45}$
91	$10^{6.69}$	---	---
92	$10^{6.54}$	$10^{5.92}$	---
93	$>10^{8.12}$	---	$10^{5.53}$
95	$10^{7.48}$	---	---
97	$>10^{7.96}$	---	---
98	$10^{6.81}$	---	---
99	$10^{6.62}$	---	---
101	$<10^{4.19}$	$<10^{4.19}$	---
102	$<10^{4.73}$	$<10^{4.73}$	---
107	$<10^{7.61}$	---	---
108	$10^{7.11}$	---	---
109	$10^{7.21}$	---	---
112	$10^{8.15}$	$>10^{8.78}$	---
113	$10^{7.15}$	---	---
122	$10^{6.22}$	---	---
123	$10^{6.17}$	---	---
124	$10^{6.11}$	$10^{5.88}$	---
125	$10^{6.15}$	---	---
126	$<10^{5.12}$	$<10^{5.12}$	---
127	$<10^{4.74}$	$<10^{4.74}$	---
128	---	$<10^{5.33}$	---
129	$<10^{4.72}$	---	---
142	$<10^{5.01}$	---	---
143	$<10^{4.3}$	$<10^{4.3}$	--
145	$<10^{4.49}$	---	---
147	$<10^{5.31}$	---	---
148	---	$10^{6.93}$	---
155	---	$<10^{4.73}$	---
156	$<10^{4.81}$	$<10^{4.81}$	---
157	$10^{5.60}$	---	---
158	$10^{6.99}$	---	---
161	$10^{6.40}$	---	---

Table C.4: Continued from previous page

Residue #	Protection Factor (continued)		
	mCherry	mRojoB	tdTomato
162	---	$10^{5.65}$	---
163	$10^{7.05}$	---	---
164	$<10^{4.91}$	---	---
165	$>10^{7.76}$	---	---
167	$10^{5.40}$	$10^{5.32}$	---
168	---	---	$<10^{4.39}$
170	$<10^{4.73}$	$<10^{4.73}$	$<10^{4.73}$
171	$<10^{5.07}$	$<10^{5.07}$	$<10^{5.07}$
174	$10^{6.40}$	---	---
175	$10^{7.14}$	---	---
176	$10^{6.04}$	$10^{5.96}$	---
177	$10^{5.77}$	---	---
178	$10^{6.42}$	$10^{6.58}$	---
181	$>10^{8.1}$	---	---
182	$10^{7.11}$	$10^{6.61}$	---
184	$10^{6.49}$	---	---
187	$<10^{3.69}$	---	---
188	---	$<10^{4.56}$	---
192	$<10^{4.81}$	---	---
193	$10^{6.94}$	---	---
197	$10^{6.37}$	---	---
199	$10^{5.42}$	---	---
200	$10^{7.17}$	---	---
201	$10^{3.73}$	---	---
203	---	$<10^{5.21}$	$<10^{5.21}$
204	$<10^{5.22}$	---	---
205	---	$<10^{5.52}$	---
207	$<10^{4.19}$	$<10^{4.19}$	$<10^{4.19}$
208	$<10^{4.19}$	---	---
209	---	$<10^{4.62}$	---
211	$10^{6.91}$	$10^{6.45}$	---
212	$10^{6.83}$	---	---
213	$>10^{8.1}$	---	---
214	$>10^{8.1}$	$10^{7.04}$	---
215	$>10^{8.1}$	---	---
216	$10^{6.93}$	---	---
217	$10^{7.11}$	---	---
218	$10^{6.20}$	---	---
219	---	$<10^{4.76}$	---
227	---	$<10^{4.54}$	---
228	$10^{6.04}$	$<10^{3.95}$	---
229	$<10^{3.91}$	$<10^{3.91}$	---
230	$<10^{4.16}$	$<10^{4.16}$	---

Table C.4: Continued from previous page

Residue #	Protection Factor (continued)		
	mCherry	mRojoB	tdTomato
231	---	$<10^{2.85}$	---

[a]Protection factors were calculated for assigned backbone amides in tdTomato, mCherry, and mRojoB. The lower bound eschange rate constant 4.8×10^{-4} s^{-1} was used to calculate an upper bound for the protection factors of fast exchangers. The upper bound exchange rate constant 1.6×10^{-7} s^{-1} was used to calculate a lower bound for the protection factors of the slow exchangers. Protection factors for unassigned backbone amides or amides whose exchange rate constant error were >10% are not presented.

Appendix D

Global Unfolding of Red Fluorescent Protein Variants

D.1 Introduction

Protein function often requires the protein be properly folded. Protein stability may refer to thermostability or kinetic stability. Thermostability describes the difference in free energy between the fully folded (native) and unfolded (denatured) states, where kinetic stability depends on the activation energy barrier between the native state and transition state for unfolding. Life has evolved under a wide range of conditions including extreme temperatures, and naturally occurring proteins with T_ms of over 100°C have been discovered. For example, the hyperthermophilic archaea *Pyrococcus furiosus* lives at an optimal temperature of 100°C and expresses a protein with a melting temperature of close to 200°C [239]. Some organisms have evolved under extreme pH or saline conditions, as well. The melting temperature, T_m, is a parameter describing thermostability defined as the temperature at which a protein is 50% unfolded at equilibrium. Protein stability can also be measured using chemically induced unfolding to probe the free energy difference between the native and denatured states of the protein [240].

Protein stability may be compromised outside of the natural environment of the protein, and reduced protein stability in recombinantly expressed proteins or purified protein therapeutics is an important issue in biochemistry [92]. In addition, mutations that change physical properties can compromise stability and impair protein function [92, 241]. Therefore, designing proteins with improved stability is important for both basic and applied research efforts [242]. For example, an extremely stable green fluorescent protein was designed to withstand 80°C overnight without denaturing [92]. Another GFP with improved stability,

superfolder GFP [243], was used as a template when designing a supercharged fluorescent protein with reduced tendency to aggregate, by introducing charges of +30 and -30 [244].

One major concern when designing new fluorescent proteins is photophysical property-enhancing mutations may adversely affect protein folding and stability. This issue was of particular importance during the development of monomeric red fluorescent proteins, which were all derived from obligate oligomers [21, 21, 22, 245]. Initial disruption of the interfaces of wild-type DsRed caused a nearly complete loss of fluorescence [22], which may have been due to a decrease in stability of the resulting monomer. Additional mutations were introduced to restore fluorescence in monomeric RFPs; however, all monomeric RFPs derived from DsRed have significantly compromised quantum yields relative to the wild-type.

Fluorescent proteins have been shown to be both highly kinetically and thermally stable. For example, 3 naturally occurring variants of GFP were found to have T_ms of $> 80°C$ as detected by the loss of secondary structure via circular dichroism [246]. The loss of fluorescence has also been commonly used to monitor fluorescent protein unfolding [80,87,158–161]. GFP is resistant to unfolding at high concentrations of urea [247], guanidine hydrochloride (GuHCl) [87] and over a wide range of pH [248]. In addition, Stepaneko et al. found that DsRed maintained fluorescence when incubated in high concentrations of denaturant ($>$ 6 M GuHCl) for more than a week, indicating that it is highly kinetically stable, however, the dimeric and monomeric variants dimer2 and mRFP1 were were less kinetically stable under the same conditions [41]. These results are consistent with the destabilizing effects of point mutations and of the loss of protein-protein interfaces when developing monomeric RFPs. There are many examples in the literature of protein interfaces increasing stability, including several studies that demonstrated that quaternary structure stabilizes the tertiary structure of some proteins [170]. For example, a point mutation in the dimeric HIV-1 protease decreased K_d for dimerization more than 7-fold. The resulting mutant showed a decrease in global stability, suggesting the dimer interface was stabilizing [249]. In addition, the thermostability of quinoprotein glucose dehydrogenase was increased by increasing the hydrophobic interaction of the dimer interface [237]. Yet another example of oligomerization enhancing protein stability was demonstrated in a study of *E. coli* protein dihydrofolate reductase mutants. The mutations that destabilized the monomer were counterbalanced by oligomerization and increased stability of the resultant dimer [250]. Finally, a study probing the stability enhancement

effect of protein-protein interactions used over 1,600 proteins with known protein-protein interactions in the extensively characterized proteome of Baker's yeast. The study concluded that proteins were stabilized (defined in the study as enhanced thermodynamic stability and resistance to aggregation, oligomerization and degradation) by protein-protein interactions [251].

The work described here explores the role of protein-protein interfaces in and the effect of point mutations on the stabilities of monomeric RFP variants relative to the covalent dimer, tdTomato. Using circular dichroism and fluorescence to monitor protein folding, both temperature and chemical denaturant were used to disrupt tertiary structure and compare protein stabilities of RFP variants to assess the effect protein directed development had on protein stability.

The goals for the directed development of the red fluorescent proteins studied here included monomerization [22], improved quantum yield [23, 252], and increased wavelength of emission [25, 26]. The disruption of the AB interface of wild-type tetramer DsRed was required for the generation of tdTomato [22]. The residual interface in tdTomato was disrupted when generating the first monomeric RFP, mRFP1 [22]. mCherry was developed from mRFP1 to increase brightness and improve maturation efficiency among other properties [23]. Finally, the the wavelength of emission was increased in mRojoB [25] and mRaspberry [26]. Of the proteins studied, mRojoB has the longest wavelength of emission, with a λ_{em} of 631 nm. However, the quantum yield of mRojoB is significantly lower (Φ=0.06) than those of tdTomato (Φ=0.69), mCherry (Φ=0.22), and mRaspberry (Φ=0.15). Often during fluorescent protein directed development, optimization of one physical property comes at the expense of another useful property [33]. Clearly, monomerization and optimization of emission wavelength was accompanied by a decrease in quantum yield during directed development of monomeric RFPs. In addition, the absorption spectrum of mRojoB is not stable over time, indicating a change in chromophore structure or environment. Whether other physical properties, such as stability and chromophore susceptibility to modification, were affected during directed development is explored here. Temperature-dependent fluorescence, absorption and circular dichroism spectroscopy were used to monitor protein denaturation and covalent modification to the chromophores of tdTomato, mCherry, and mRojoB. The preliminary data presented in this chapter provide a starting point for understanding the relative stabilities of RFP variants.

D.1.1 Using Temperature-Dependent Fluorescence, Absorption, and Circular Dichroism to Monitor Fluorescent Protein Unfolding

Fluorescence and Absorption Fluorescence is often used to monitor fluorescent protein denaturation since FPs must be properly folded to fluoresce in solution [80,87,158–161]. The temperature dependence of fluorescence and absorption of tdTomato, mCherry and mRojoB was measured to better understand the relative protein stabilities. The effect of temperature on fluorescence and absorption of the chromophores are shown. In addition, factors other than protein denaturation that affect fluorescence and absorption of the mature chromophore are discussed including bond vibration and covalent modification of the chromophore.

Circular Dichroism The effect of directed development on protein stability was further explored using circular dichroism to monitor protein denaturation. Circular dichroism can be used to detect secondary structural features like α-helices or β-sheets [253–255]. These structural elements absorb left and right circularly polarized light differently which can be detected with a CD spectrometer [253]. As a protein unfolds, secondary structure is lost or modified, and the CD signal changes as a result.

Previous Denaturation Studies of FPs Changes in fluorescence [80, 87, 158–161] and absorption [94, 97, 162] spectra indicate changes in the local environment of the chromophore. The loss of fluorescence in FPs is often attributed to protein denaturation, increased flexibility of the chromophore, or exposure to fluorescence quenchers [80, 87, 158–161]. Protection of the chromophore by the surrounding amino acids is required for fluorescence in FPs as highlighted by the fact that the isolated chromophore is not fluorescent outside of the β-barrel above 77 K [163]. Therefore a loss of fluorescence could be attributed to protein denaturation, but may also be due to increased thermally induced bond vibrations, rotations or librations near the chromophore that may stimulate non-radiative relaxation even in the native state of the protein [92]. Inconsistencies in the protein denaturation curves of GFP when monitored by fluorescence or circular dichroism have been observed. One study showed that CD and fluorescence produced the same chemically induced denaturation curves [87], whereas another study found the curves differed depending on which signal was monitored [165]. Both thermally induced bond vibrations and protein denaturation may decrease fluorescence during thermal denaturation. However chemically induced denaturation will not

increase thermally induced vibrations in the native state. Therefore, one might expect a discrepancy between thermally induced denaturation curves measured using fluorescence and circular dichroism and should exercise caution when relating fluorescence loss to protein denaturation.

An additional challenge when measuring RFP stability was covalent modification to the chromophore. The acylimine bond in the mature chromophore of RFPs has been shown to cleave under denaturing conditions, although the precise mechanism is unknown (Figure 3.2) [29, 101]. The absorption profile of the cleaved chromophore is shifted to shorter wavelengths and thus more closely resembles the absorption of the off-target GFP-like form of the chromophore. The irreversibility of RFP denaturation due to covalent modification of the chromophore, and inability to perform the experiments under equilibrium conditions due to the high kinetic stability of the RFPs prevented a thorough analysis of RFP thermostability. Regardless, the ability of an FP to fluoresce under harsh conditions like elevated temperature [256] or high concentrations of denaturant is desirable, and comparing this property among FP variants could be useful in designing new variants or when selecting the appropriate FP to use for an experiment. For example, when studying a thermophilic organism using an FP, the FP must be stable at the elevated temperature in which the thermophile lives and functions. Therefore, the relative abilities of tdTomato, mCherry and mRojoB to maintain fluorescence under elevated temperatures or denaturing conditions were compared.

D.2 Methods

D.2.1 Temperature-Dependent Fluorescence and Absorption Spectroscopy Methods

Temperature Dependent Fluorescence and Absorption in the Absense of Denaturant

The temperature dependence of fluorescence and absorption from the chromophores of tdTomato, mCherry and mRojoB was measured using an Applied Photophysics Chirascan Plus CD Spectrometer equipped with a fluorometer. Several iterations of temperature-dependent fluorescence and absorption data were collected. Table D.1 lists the purpose of each experiment performed.

The protein samples used for these experiments were expressed and purified as described in section 2.2.1. Samples of ^{2}H, ^{15}N-labeled tdTomato, ^{1}H, ^{15}N-labeled mCherry, and ^{1}H, ^{13}C, ILV methyl-labeled

mRojoB were used. 2 mL 1 μM protein samples in 20 mM Tris pH 7, 50 mM NaCl, and 5 mM DTT were placed in a 1 cm quartz cuvette. The sample concentrations were optimized such that the maximum absorptions were less than 0.1. Fluorescence and absorption spectra were collected in 5°C increments with 5-minute equilibration times during temperature ramping from 20-90°C and back down to 20°C. The bandwidth for excitation was 5 nm, and the emission monochromator slit width was set to 4 mm (18 nm). The excitation wavelengths used were 540 nm, 575 nm and 590 nm for tdTomato, mCherry, and mRojoB, respectively. The emission spectra were recorded with a 5 nm step size from 560-700 nm, 595-650 nm, and 610-700 nm, for tdTomato, mCherry and mRojoB, respectively. To monitor absorption from the aromatic side chains as well as from the mature chromophore, absorption spectra were collected from 250 nm to 650 nm with a 5 nm step size and a 1 nm bandwidth using the same sample conditions.

Fluorescence and absorption spectra were baseline corrected by subtracting the fluorescence and absorption spectra of the buffers. The fluorescence and absorption at the wavelength of maximum emission and absorption, respectively, were plotted as a function of temperature for each protein. The temperature dependence of the fluorescence signal at the wavelength of maximum emission of the mature chromophore was monitored. The absorption and fluorescence were normalized by dividing the absorption or fluorescence at the relevant temperature by that at 20°C.

Temperature Dependent Fluorescence and Absorption in the Presence of Denaturant

The temperature-dependent fluorescence measured in the presence and absence of denaturant were collected using 2 mL samples of 1 μm protein in 2 mM phosphate buffer pH 8 in a 1 cm quartz cuvette. The protein samples were expressed in LB media as described in section 2.2.1, but were purified on a sizing column in 20 mM phosphate buffer pH 8. The experiments were performed in the presence and absence of 6 M GuHCl. For this set of experiments, the temperature was ramped from 25-90°C in 5° increments with 3-minute equilibration times. The emission spectra were recorded from 555-650 nm at 2 nm intervals using an excitation wavelength of 540 nm. A 10 nm bandwidth for excitation was used for mCherry and mRojoB to obtain sufficient signal, while only a 1 nm bandwidth was needed to obtain sufficient signal for tdTomato. The emission monochromator slit width was set to 2 mm (9 nm). The fluorescence intensities at the wavelength of maximum emission for each protein were plotted as a function of temperature. Absorption

Table D.1: Experiments performed to assess the effect of temperature and chemical denaturant on fluorescence and absorption.

Experiment	Purpose
1) Monitor Fluorescence During Heating and Cooling	Determine whether fluorescence is recoverable upon cooling
2) Effect of Denaturing Agent on Fluorescence	Determine whether denaturing agent induced unfolding contributes to fluorescence loss
3) Temperature Dependence of Absorption	Assess whether loss of absorption contributes to loss of fluorescence

spectra were collected at room temperature from 250 to 650 nm with a 10 nm step size for each protein before, after heating to 90°C and after heating to 90°C in the presence of 6 M GuHCl using a Bio-Tek Instruments PowerWave X microplate reader. Absorption spectra at each temperature during the ramping were not collected under these sample conditions.

D.2.2 Temperature-Dependent Circular Dichroism Methods

The secondary structure as a function of temperature was probed for tdTomato, mCherry, and mRojoB using an Applied Photophysics Chirascan Plus CD Spectrometer. Since ions like chloride and Tris absorb strongly in the UV, the proteins were purified in their absence in 20 mM sodium phosphate pH 8. Following purification, the protein samples were buffer swapped into 5 mM citrate buffer pH 3.3 for data collection. CD spectra were collected from 190-260 nm with a 1 nm step size and a 1 nm bandwidth on 200 μL 1 μM protein in a 1 mm quartz cuvette. Spectra were collected from 20-90°C at 5°C increments, with 3-minute equilibration times between measurements. The actual temperature of the sample was recorded using a TCU probe. The CD values were normalized for protein concentration. The fraction folded at each temperature was calculated using the difference in the CD_{200nm} values from the fully folded state at 20°C and the fully denatured state of mRojoB at 90°C. Neither mCherry nor tdTomato fully unfolded after temperature ramping to 90°C, and thus the % change in CD_{200nm} for mRojoB between the native and denatured states was used to calculate an estimated CD_{200nm} value for the fully unfolded states of mCherry and tdTomato. The fraction folded was plotted as a function of temperature and fit to a generalized logistic function [205], Equation D.1, using Mathematica [257].

$$CD_{210\ \mathrm{nm}} = A + \frac{B - A}{1 + e^{C(T - T_M)}} \tag{D.1}$$

where T is the temperature, T_m is the inflection point of the sigmoidal curve, A is the lower asymptote, B is the upper asymptote, and C affects the steepness of the curve. Two inflection points were present, and therefore the data were fit to two sigmoidal curves per protein.

D.3 Results

D.3.1 Temperature-Dependent Fluorescence and Absorption Spectroscopy Results

Fluorescence

Fluorescence is often used to measure FP unfolding [80, 87, 158–161]. Temperature dependent fluorescence experiments were performed on tdTomato, mCherry, and mRojoB to gain insight into relative susceptibilities to fluorescence loss and denaturation at elevated temperatures. The initial temperature ramping and cooling data were used to assess whether fluorescence loss was reversible. A comparison of the temperature-dependent fluorescence in the presence or absence of denaturant was used to determine whether chemically induced denaturation affected fluorescence. Temperature-dependent absorption data were collected to complement the temperature-dependent fluorescence data. The absorption spectra were used to determine what contribution to the loss of fluorescence was due to changes in absorption. Fluorescence decreased as a function of temperature for tdTomato, mCherry, and mRojoB. Data collected in 20 mM Tris pH 7, 50 mM NaCl and 5 mM DTT with 5-minute equilibration times showed that the only RFP that had significant fluorescence (10%) at 90°C was mCherry (Figure D.1). In addition, 80% of original mCherry mature chromophore fluorescence was recovered upon sample cooling to 20°C, whereas no fluorescence was recovered for mRojoB and only 4% for tdTomato after the sample was heated to 90°C (Figures D.1 and D.2).

The effect of adding denaturant was tested by comparing the loss of fluorescence in the presence and absence of 6 M GuHCl. In phosphate buffer pH 8 in the absence of denaturant, mRojoB showed the smallest change in fluorescence over most of the temperature range retaining more than 35% of original fluorescence at

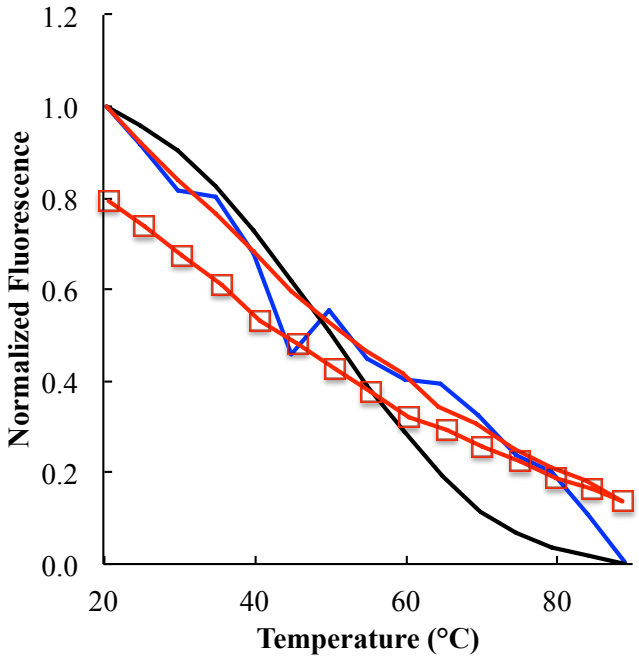

Figure D.1: Normalized fluorescence at the wavelengths of maximum emission of the mature chromophores of tdTomato (black), mCherry (red) and mRojoB (blue) as a function of temperature. Samples were heated from 20-90°C, at 5° increments, with 5-minute equilibration times between measurements. 80% and 4% fluorescence were recovered for mCherry and tdTomato, respectively, when the samples returned to 20°C following the temperature ramping (red line with squares and following figure).

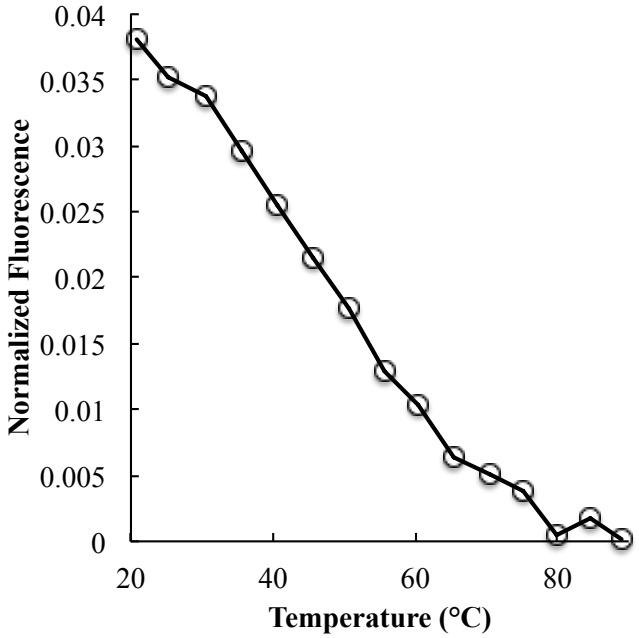

Figure D.2: Normalized fluorescence at the wavelength of maximum emission of the mature chromophore of tdTomato during cooling from 90 to 20°C. 4% fluorescence was recovered for tdTomato, when the sample was returned to 20°C following the temperature ramping from 20 to 90°C. (See Figure D.1 for the fluorescence during temperature ramping from 20 to 90°C).

75°C whereas mCherry and tdTomato retained 23% and 6%, respectively. Again mCherry was the only RFP that had significant fluorescence (≈10%) at 90°C (Figure D.3a). Upon addition of 6 M GuHCl, fluorescence was lost by 90°C for all three RFPs, but mCherry was the only RFP that had significant fluorescence (≈20%) at 74°C (Figure D.3b). Notably, the buffer used in these experiments eliminated the complicating possibility that the double bonds in the chromophore could be reduced by DTT, which would alter the wavelength of absorption and fluorescence.

Absorption

Absorption from the mature chromophores decreased with temperature using samples in 20 mM Tris pH 7, 50 mM NaCl and 5 mM DTT with 5-minute equilibration times. mCherry was the only RFP that had significant absorption from the mature chromophore (≈60%) at 90°C (Figure D.4). In addition, 80% of the initial absorption from the mature chromophore of mCherry was recovered upon sample cooling to 20°C, whereas no absorption from the mature chromophore of tdTomato or mRojoB was detected. Absorption from the immature form of the chromophore of mRojoB (the absorption peak appearing at 500 nm) also decreased with temperature. However, absorption at 500 nm was recovered in mRojoB following temperature ramping and cooling (Figure D.5).

The absorption spectra of tdTomato collected in phosphate buffer at room temperature showed little change after sample heating from 20-90°C (Figure D.6). After sample heating, the ratio of absorption from the mature to immature chromophores of mCherry and mRojoB decreased by 40 and 80%, respectively (Figure D.6). Upon addition of 6 M GuHCl, the absorption spectra post temperature ramping showed complete loss of the peak from the mature chromophore for all three proteins and the formation of a new peak near 400 nm (Figure D.7).

D.3.2 Temperature-Dependent Circular Dichroism Results

Circular dichroism spectroscopy is a useful technique for monitoring the secondary structure of proteins, and is often used to monitor protein denaturation [253]. It is complementary to temperature-dependent fluorescence or absorption spectroscopy as it monitors the secondary structure directly through the interaction of UV light and amide bonds [253] rather than indirectly using the assumption that FPs must be

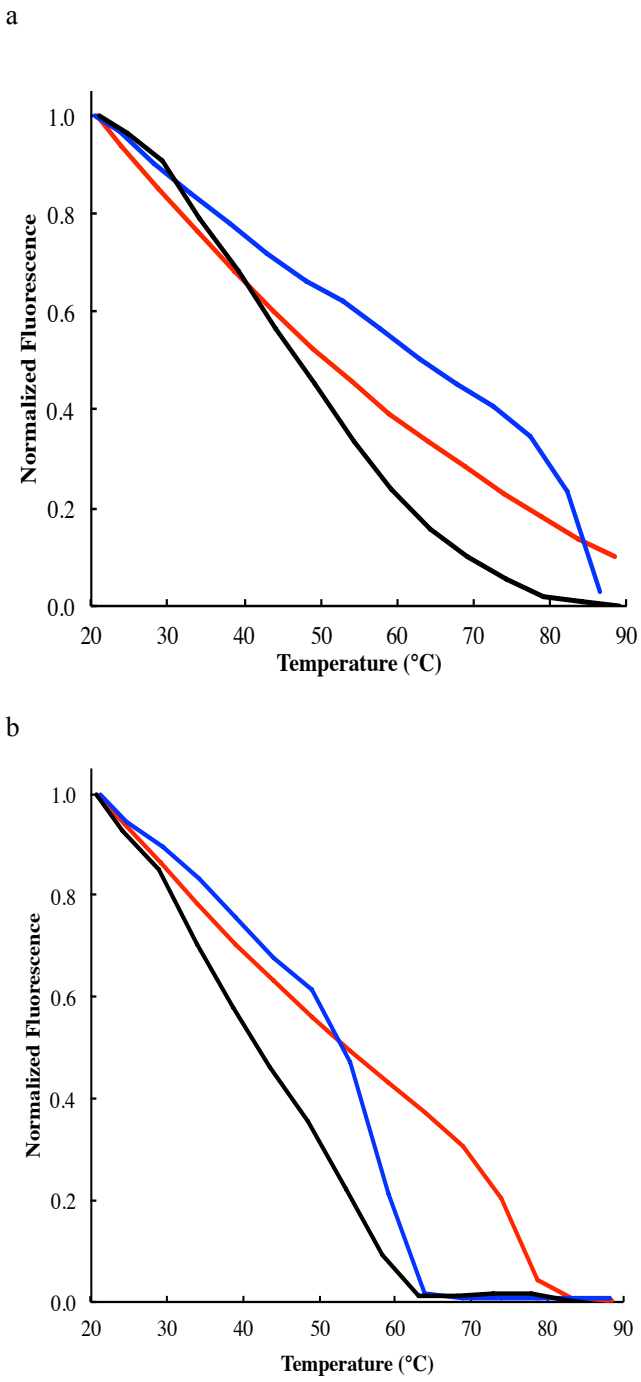

Figure D.3: The normalized fluorescence at the wavelengths of maximum emission of the mature chromophores of tdTomato (black), mCherry (red) and mRojoB (blue) as a function of temperature during ramping from 20-90°C, at 5°C increments, with 3-minute equilibration times between measurements in the absence (a) and presence (b) of 6 M GuHCl. These experiments were performed in phosphate buffer pH 8 with 3-minute equilibration times, (as opposed to 20 mM Tris pH 7, 50 mM NaCl, and 5 mM DTT and 5-minute equilibration times used in Figure D.1).

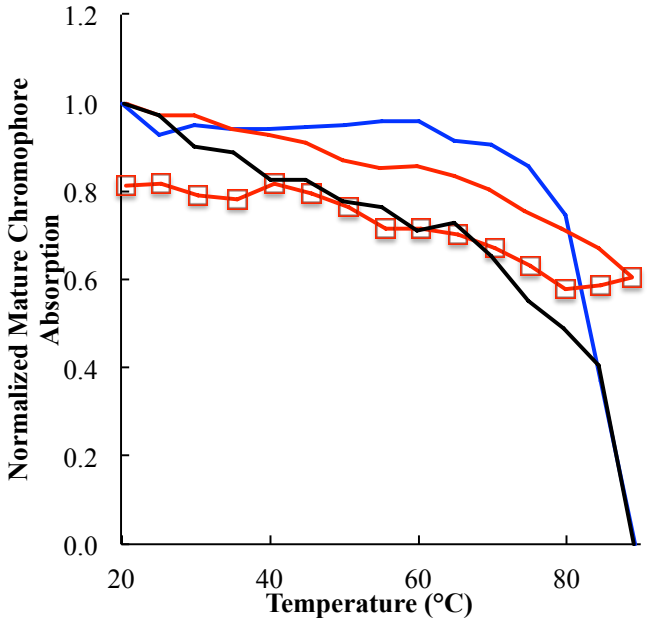

Figure D.4: The normalized absorption at the wavelengths of maximum absorption of the mature chromophores of tdTomato (black), mCherry (red) and mRojoB (blue) as a function of temperature during ramping from 20-90°C, at 5° increments. The samples were in 20 mM Tris pH 7, 50 mM NaCl, and 5 mM DTT, and the data were collected with 5-minute equilibration times between measurements. The absorption spectra were also collected from 90-20°C following the temperature ramping, but only the absorption peak from the chromophore of mCherry remained after heating to 90°C (red line with squares).

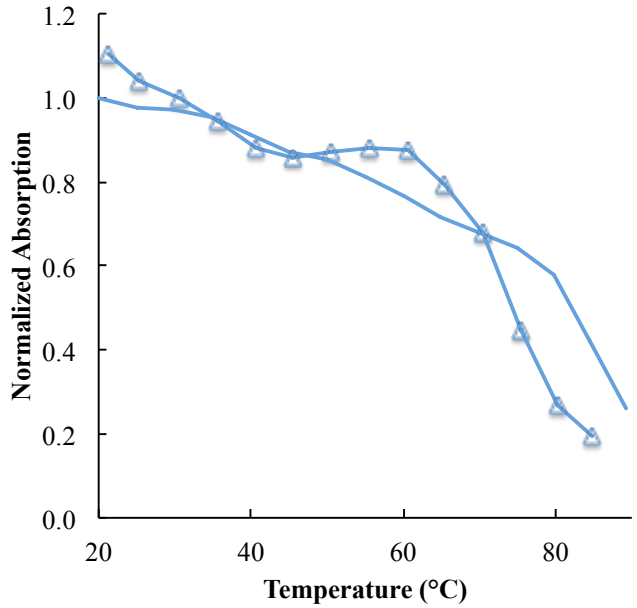

Figure D.5: The normalized absorption at 500 nm for mRojoB as a function of temperature during ramping from 20-90°C, at 5° increments (blue line). The sample was in 20 mM Tris pH 7, 50 mM NaCl, and 5 mM DTT, and the data were collected with 5-minute equilibration times between measurements. The loss of absorption is reversible as shown (with open triangles).

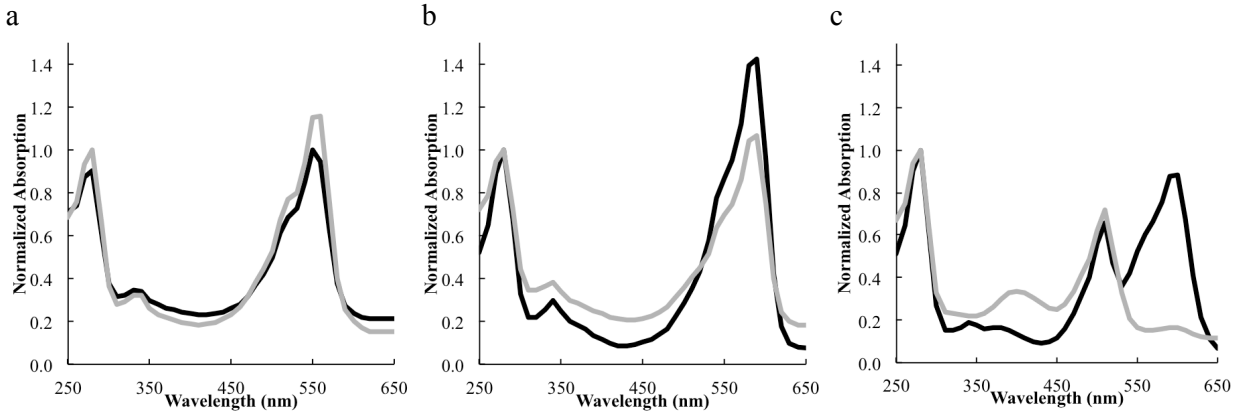

Figure D.6: Absorption spectra at 25°C of tdTomato (a), mCherry (b), and mRojoB (c) before (black) and after (grey) heating to ≈90°C in phosphate buffer pH 8 in the absence of 6 M GuHCl. The plots are normalized to an absorption of one at 280 nm for each spectrum. The absorption spectrum of mRojoB has an additional peak at 500 nm from the immature form of the chromophore, even before sample heating [25].

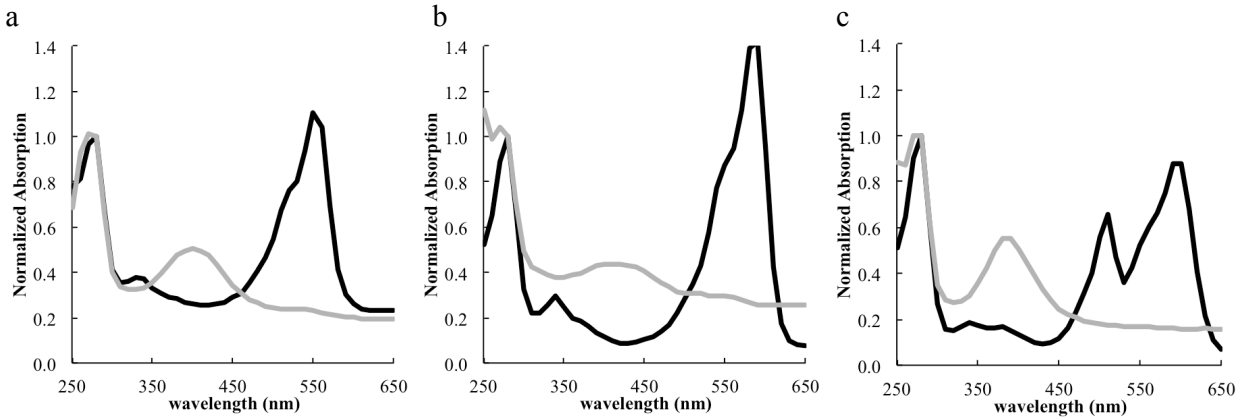

Figure D.7: Absorption spectra at 25°C of tdTomato (a), mCherry (b), and mRojoB (c) before (black) and after (grey) heating to ≈90°C in the presence of 6 M GuHCl. The plots are normalized to an absorption of one at 280 nm for each spectrum. The absorption spectrum of mRojoB has an additional peak at 500 nm from the immature form of the chromophore, even before sample heating [25].

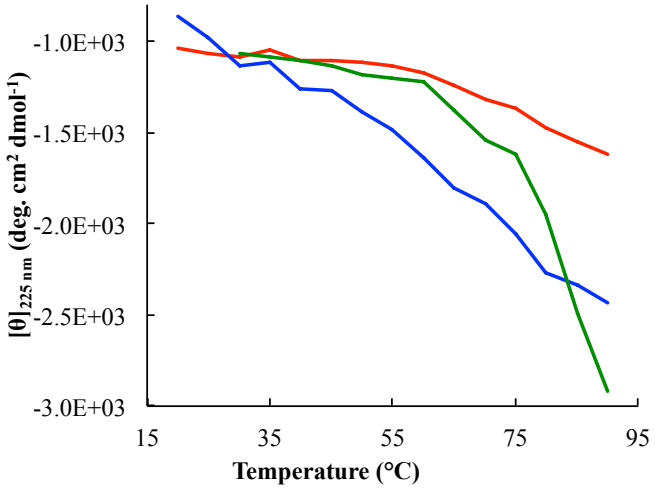

Figure D.8: The circular dichroism signal at 225 nm, a peak common to all three RFPs tested, was monitored as a function of temperature for 1 μM mCherry (red), mRaspberry (green) and mRojoB (blue) in 2 mM phosphate buffer pH 8 and 6 M GuHCl in the case of mRojoB. The incubation period between data points was 3 minutes for mCherry and mRojoB and 10 minutes for mRaspberry.

fully folded in order to fluoresce. Temperature dependent CD experiments were performed on a set of RFPs to evaluate their relative stabilities. The circular dichroism spectra of tdTomato, mCherry, mRojoB and mRaspberry show positive peaks at $\approx$ 200 nm similar to previously reported CD spectra of fluorescent proteins [102, 119, 158, 159, 246, 258, 259].

The temperature dependence of secondary structure was probed in acidic conditions after preliminary results from an experiment performed in phosphate buffer pH 8 showed that complete denaturation of the RFPs could not be achieved through temperature ramping to 90°C with 3-minute (mCherry) or 10-minute (mRaspberry) incubation periods, nor upon the addition of 6 M GuHCl (mRojoB) (Figure D.8). In addition, the secondary structure of mCherry was not fully denatured after more than two hours at 90°C in phosphate buffer pH 8 (Figure D.9). Therefore, a denaturing agent was added to destabilize the secondary structure. Minimal differences were observed between the CD spectra of mCherry at room temperature in phosphate pH 8 and citrate buffer pH 3.3 (Figure D.10). The fraction folded was calculated for the proteins in citrate buffer and monitored as a function of temperature (Figure D.12). Two inflection points appear in the data indicating that denaturation of these RFPs may be more than a two-state process. The temperatures of the inflection points are given in Table D.2.

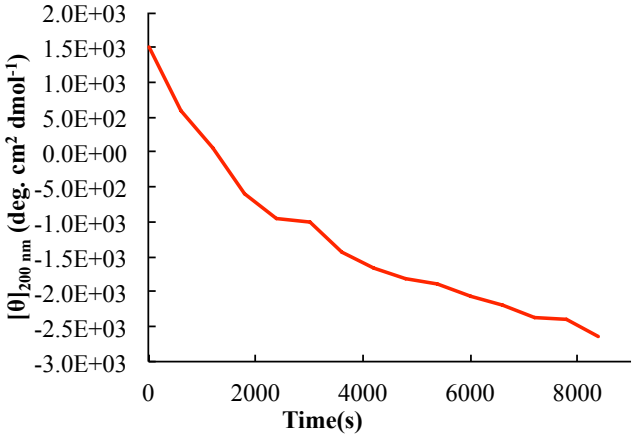

Figure D.9: The circular dichroism signal at 200 nm as a function of time for mCherry in phosphate buffer pH 8 and 90°C. Freshly expressed and purified protein was used. This freshly purified sample was purified in phosphate buffer in the absence of Tris or chloride ions, and so the CD spectrum was collected from 180 nm to 260 nm instead of from 210 nm to 260 nm, thereby allowing the monitoring of the CD peak at 200 nm attributed to β-sheet structure of mCherry.

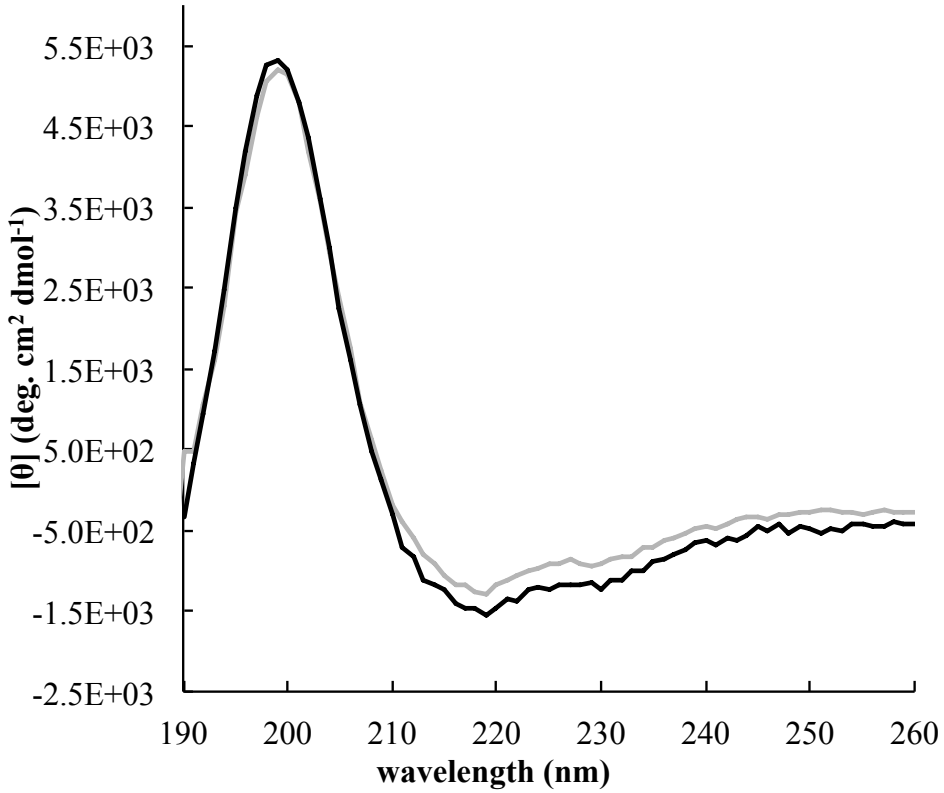

Figure D.10: The circular dichroism spectra of mCherry in phosphate buffer pH 8 (black) versus citrate buffer pH 3.3 (grey) at room temperature.

Figure D.11 shows the CD spectra of tdTomato, mCherry and mRojoB in citrate buffer at temperatures ranging from 25-90°C. A shift in the wavelength of maximum CD signal from 200 to 190 nm during the temperature ramping was observed in the sample of tdTomato (Figure D.11a). The positive peak at 190 nm is retained in the CD spectrum of tdTomato, even after sample cooling to 30°C (Figure D.14).

Table D.2: The inflection point temperatures in the fraction folded versus temperature plots for tdTomato, mCherry and mRojoB.[a]

Protein[b]	Temperature (°C)[c]
$mRojoB_1$	42.9±0.7
$mCherry_1$	54.8±1.4
$tdTomato_1$	56.6±0.3
$mRojoB_2$	70.7±0.7
$tdTomato_2$	74.5±3.0
$mCherry_2$	94.6±1.4

[a] The experiments were performed in citrate buffer pH 3.3.
[b] The subscripts denote the first or second inflection points in the curve.
[c] The errors are the standard errors calculated by Mathematica during fitting.

D.4 Discussion

Red fluorescent proteins are valuable tools for studying intracellular processes. Most commonly used RFPs are monomeric variants, developed from the wild-type tetramer, DsRed. During RFP directed development, monomeric, red-shifted variants were generated at the expense of quantum yield. Whether other physical properties, such as protein stability, were affected by the directed development process as well was explored using temperature-dependent fluorescence and circular dichroism spectroscopy.

D.4.1 Temperature-Dependent Fluorescence and Absorption Spectroscopy Indicate Multiple Processes Affect Fluorescence

Denaturation, chromophore modification, and thermally induced increases in vibration all contributed to the observed temperature-dependent loss of fluorescence. The shapes of the temperature-dependent loss of fluorescence curves provided clues as to which of these processes is causing the decrease in fluorescence, however it is important to note that these experiments were not performed under equilibrium conditions.

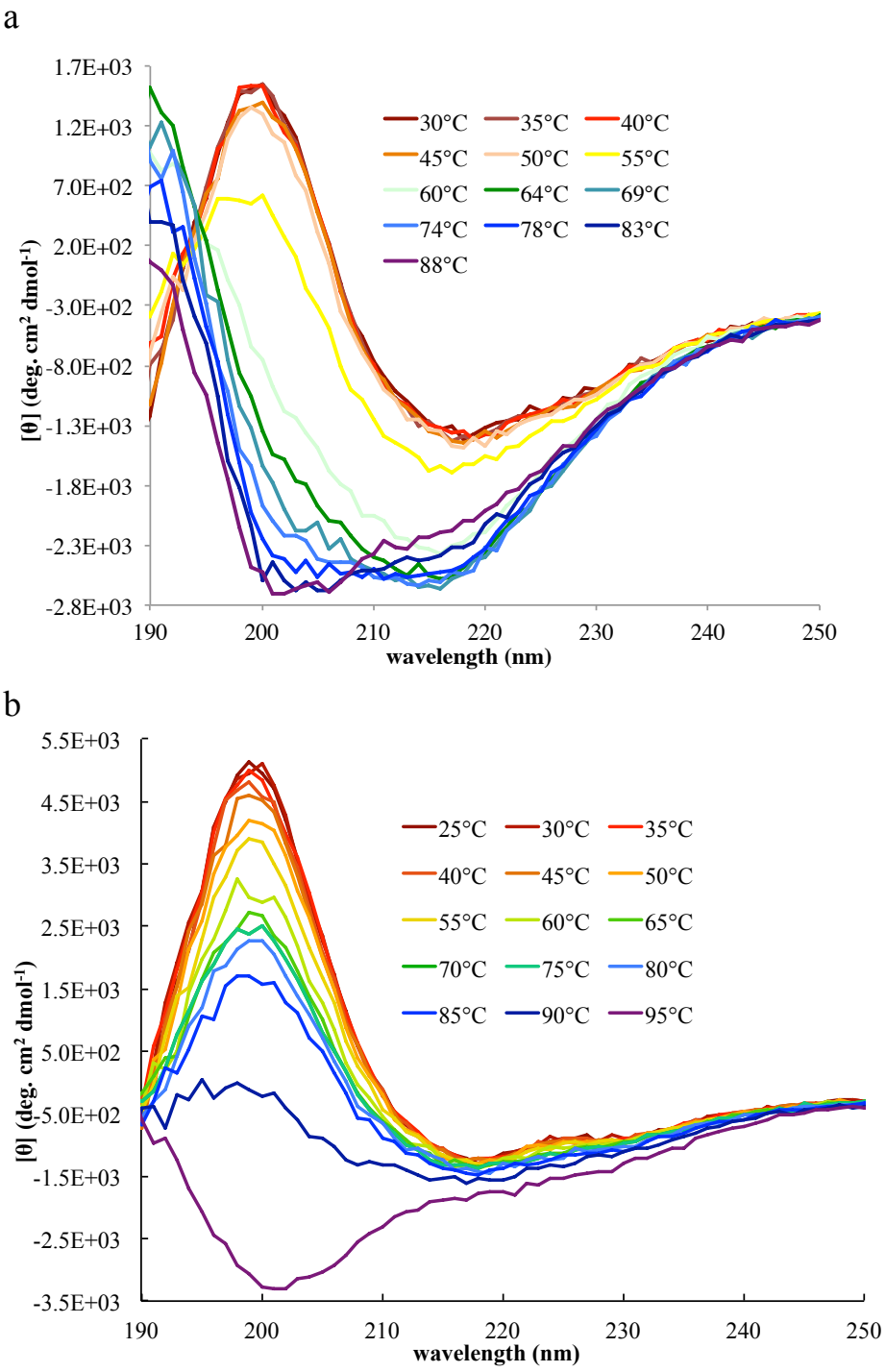

Figure D.11: Continued on following page

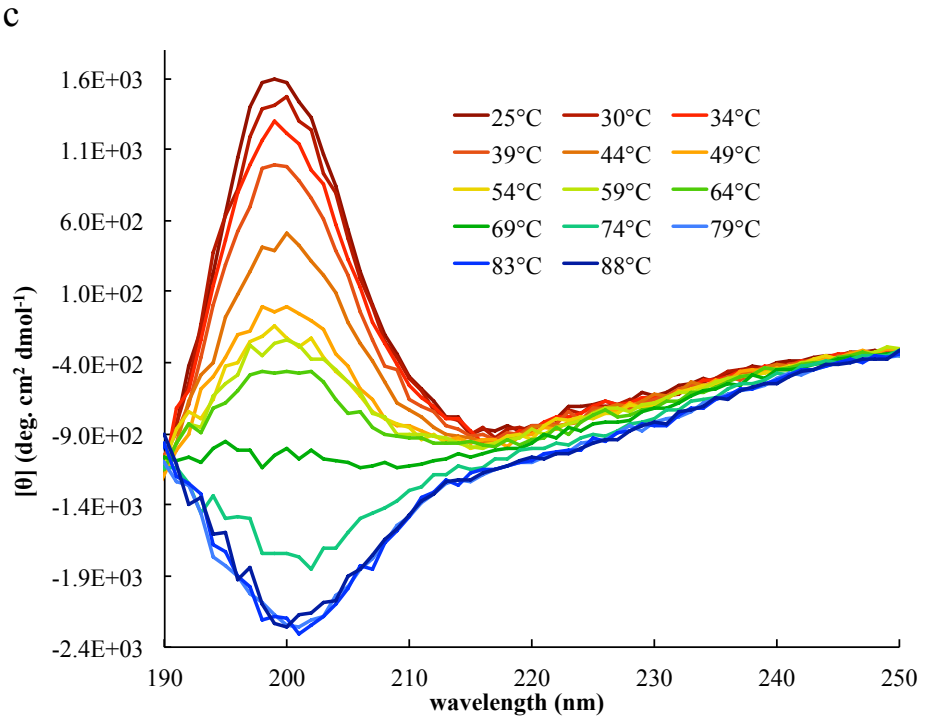

Figure D.11: The CD spectra of tdTomato (a), mCherry (b), and mRojoB (c) in 5 mM citrate buffer pH 3.3 during temperature ramping from 30-90°C, 25-95°C, and 20-90°C respectively.

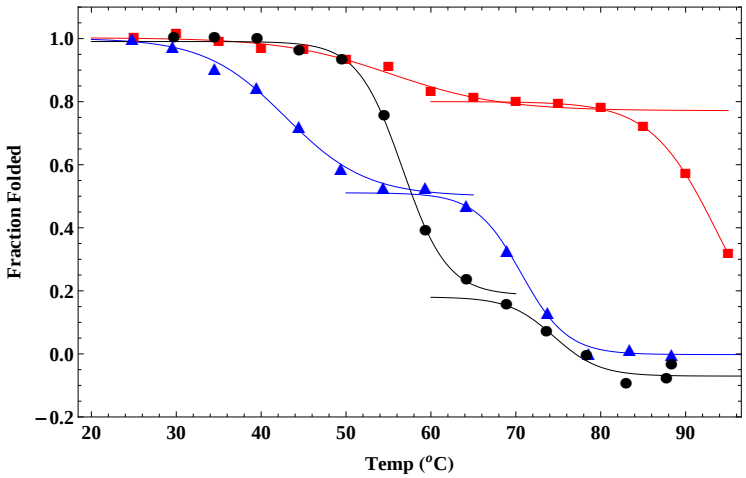

Figure D.12: The circular dichroism signal at 200 nm, a peak common to all three RFPs tested, was used to calculate the fraction folded at each temperature. The fraction folded was monitored as a function of temperature for 1 μM tdTomato (black), mCherry (red), and mRojoB (blue) in 5 mM citrate buffer pH 3.3. The data are fit to two sigmoidal curves for each protein.

(Previous studies have shown that some fluorescent proteins do not reach equilibrium for days at elevated temperatures [41, 165].) Where the fluorescence of the monomers generally decreases steadily with temperature in the absence of denaturant, the decrease in fluorescence for tdTomato follows a sigmoidal curve (Figures D.1 and D.3). Also of note is a sharp change in the slope of fluorescence versus temperature at 80°C for mRojoB in phosphate buffer, and similar slope changes for mCherry (70°C) and mRojoB (50°C) when denaturant is added (Figures D.1 and D.3). Fluorescence loss in the monomers is likely due to increased vibration at lower temperatures and to protein denaturation once the cooperative denaturation temperature has been reached [92]. This temperature is marked by the inflection point in the curve for mRojoB in phosphate buffer pH 8 at 80°C, and in the curves for both mCherry and mRojoB in the presences of denaturant at 70°C and 50°C respectively (Figures D.1 and D.3).

The sigmoidal shape of the temperature-dependent fluorescence curve of tdTomato in the absence of denaturant suggests a cooperative process causing the loss of fluorescence (Figures D.1 and D.3a). Sigmoidal temperature or chemical-induced denaturation curves indicate cooperativity in the process [260]. These are consistent with tdTomato unfolding, resulting in a loss of fluorescence. Another possible interpretation of the sigmoidal shape is that the fluorescence loss in tdTomato is occurring upon disruption of the dimer interface. The single inflection point indicates a two-state process. The two states may be tdTomato with and without the interface intact. When the dimer is incubated at high temperatures (or in the presence of denaturant) perhaps the interface is disrupted leaving two monomeric subunits that are incapable of fluorescing.

It is known that disruption of the dimer interface abolishes fluorescence [22]. During the development of a monomeric RFP, the interruption of the dimer interface in dimer2 (the same interface present in tdTomato) produced a monomeric protein with very low quantum yield (although the value was not reported) [22]. This indicates that the AC interface of tdTomato is important for fluorescence. If sample heating disrupts this interface, the fluorescence of tdTomato would be lost even if residual secondary structure were retained. Using circular dichroism to monitor the secondary structure may help elucidate whether fluorescence loss is occurring due to protein denaturation or disruption of the dimer interface, since the secondary need not change during de-dimerization.

Although the AC interface appears to be important in maintaining the high quantum yield of td-

Tomato, its precise role is unknown. Perhaps its role is the protection of the gap between β-strands 7 and 10 from entry by fluorescence quenchers. Upon disruption of the interface in tdTomato this gap would be more exposed to solvent. This exposed gap may contribute to the compromised quantum yields in mRojoB and mCherry relative to the dimer by allowing more fluorescence quenchers to reach the chromophore. Another possibility is that the AC interface provides stabilizing interactions between β-barrels that rigidify residues on the timescale of fluorescence. Some inward facing residues at the AC interface form contacts with the chromophore, and so disruption of the interface might perturb the environment of the chromophore (Figure D.13).

When denaturing agent was added to the solution, the fluorescence loss of tdTomato, mCherry, and mRojoB could be at least partially attributed to covalent modification of the chromophore as indicated by the abolition of the peak from the mature chromophore in the absorption spectra post sample heating (Figure D.7). In addition, denaturing agent induced the cooperative transition at lower temperatures for mCherry and mRojoB, causing complete fluorescence loss at lower temperatures than in the absence of denaturant (Figure D.3).

In the presence of 6 M GuHCl, the fluorescence of tdTomato was more sensitive to temperature than was the fluorescence of mCherry or mRojoB, and the temperature-dependent loss of fluorescence curve was no longer sigmoidal (Figure D.3). The dimer interface may have already been disrupted by the presence of 6 M GuHCl, and the steady decrease in fluorescence due to increased vibration, as seen at lower temperatures for mCherry and mRojoB. A previous study comparing fluorescence intensities for DsRed, dimer2, and mRFP1 over a range of denaturant concentrations also found that the fluorescence of dimer2 was the least tolerant to denaturant [41]. It is interesting that this heightened susceptibility to fluorescence loss is consistent between the tandem dimer, tdTomato, and dimer2, since it has been shown that covalent linkage of two monomers can increase the thermostability of the resulting tandem dimer [261]. The addition of denaturant may be disrupting the dimer interface, causing loss of secondary structure, or both. The use of another method to measure protein denaturation, such as circular dichroism which can be used to monitor the secondary structure of proteins, would be useful in furthering the understanding of relative stabilities of fluorescent proteins. Because several possible factors may be contributing to the loss of fluorescence aside from protein

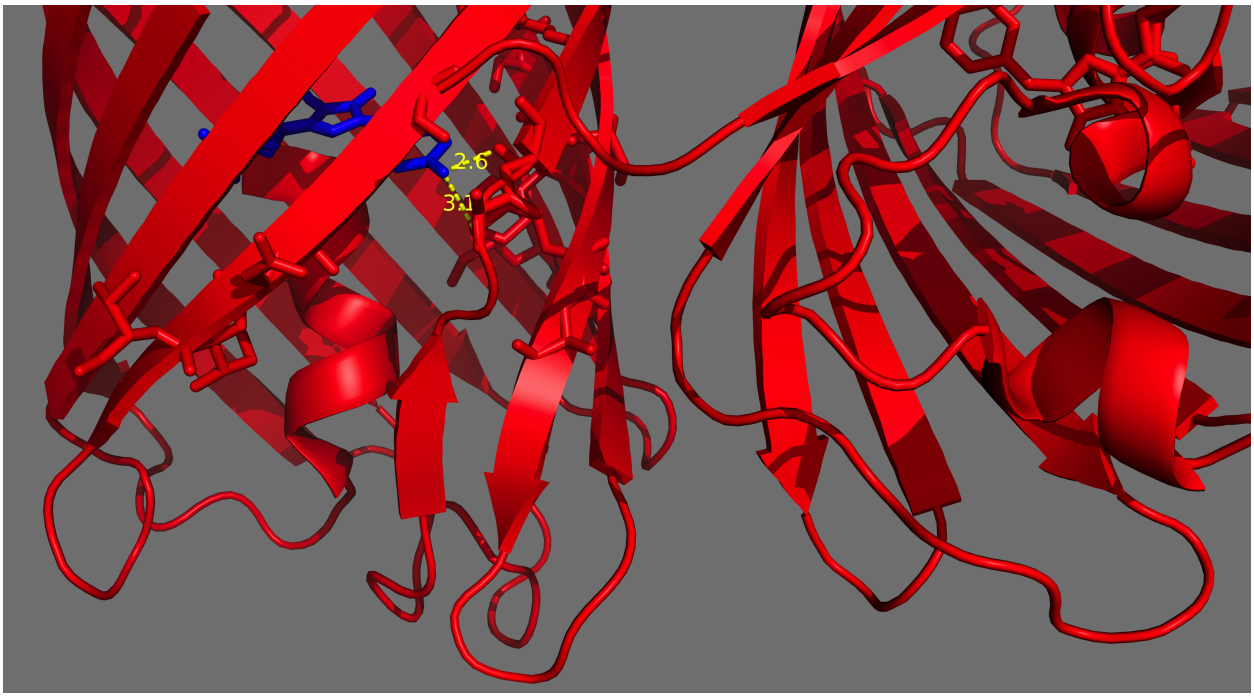

Figure D.13: The two subunits present in tdTomato are shown here, using the crystal structure of DsRed (PDB 1G7K). The chromophore is shown in blue in the left subunit. Some residues in strands 7-10 near the interface are shown as sticks to better depict atoms in this region that may interact with the chromophore. Two residues in DsRed, serine 146, and lysine 163 have side chain atoms that are positioned 3.1 and 2.6 angstroms from the chromophore tyrosine phenol oxygen, although lysine 163 has been mutated to a glutamine in tdTomato. These residues and others may form important contacts with the chromophore, and thus, if structurally perturbed during the disruption of the AC interface, may affect the quantum yield.

denaturation, it is difficult to use the temperature-dependent fluorescence data to confidently assess the relative stabilities of the RFPs.

The relative susceptibilities of the mature chromophore to modification were probed using absorption spectroscopy. The absorption spectra of the mature chromophores of tdTomato, mCherry, and mRojoB show peaks at 554, 587 and 600 nm, respectively. The undesirable development of a green chromophore sometimes occurs during the maturation process of RFPs [262]. For example, a population of GFP-like protein forms during mRojoB maturation that absorbs at 500 nm and is present prior to sample heating [25] (Figures D.6 and D.7). Changes in the absorption spectra occur following sample heating suggesting changes to the chromophore or its environment (Figures D.6 and D.7). In particular, the appearance of a peak at 400 nm after heating in the presence of denaturant can be attributed to the formation of the protonated GFP-like chromophore [46] (Figure D.7). This peak at 400 nm also appears after heating mRojoB to 90° even in the absence of denaturant (Figure D.6) suggesting that the chromophore of mRojoB is most susceptible to chromophore covalent modification. Samples of DsRed and TagRFP denatured in ≈1 M NaOH absorb at 450 nm-|approximately 100 nm green shifted from the wavelength of the mature chromophore [29, 263]. The absorption spectra of folded GFP and partially denatured GFP by GuHCl, acid or base exhibit smaller shifts in wavelength of absorption [91, 248]. Based on the results of these previous studies, the increase in intensity of a peak at 500 nm post sample heating in phosphate buffer pH 8 in the absorption spectrum of mCherry and mRojoB was attributed to chromophore covalent modification at the acylimine bond, rather than change in chromophore environment due to protein denaturation (Figure D.6).

The relative susceptibilities to covalent modification of the mature chromophores of tdTomato, mCherry and mRojoB upon sample heating depended on the sample conditions and incubation times at each temperature. Based on the lack of change in the absorption spectra, the chromophore of mCherry is the most resistant to covalent modification upon sample heating in 20 mM Tris pH 7, 50 mM NaCl and 5 mM DTT with 5-minute equilibration times between temperatures (Figure D.4). The absorption of the mature chromophores of mRojoB and tdTomato falls off rapidly at temperatures above 80°C (Figure D.4). In phosphate buffer pH 8 with 3-minute equilibration times the chromophore of tdTomato is the most resistant to covalent modification upon sample heating (Figure D.6). Although these temperature-dependent absorption

data seem to contradict one another, differences in experimental procedure may account for the different results, and more data should be collected to determine the source of this apparent discrepancy in the data. An important difference between these two temperature-dependent experiments was that in the former, the samples were kept at higher temperatures for a longer period of time due to the increased incubation periods, as well as the fact that the temperature was ramped back down to 20°C at 5° increments as opposed to simply returning the sample back to room temperature in about 5 minutes. In addition, differences in sample conditions (0% compared to > 99% D_2O) and protein concentrations (> 0.5 mM compared to 1 μM) may also be affecting the results, and more data should be collected to better understand the differences in covalent modification of the chromophores.

The absorption of the mature chromophore for all three proteins is eliminated upon sample heating in the presence of denaturant which is consistent with covalent modification of the chromophore (Figure D.7). No changes in the chromophore structure after denaturation of GFP in acid or guanidine hydrochloride have been reported [29, 158]. The chromophore in GFP does not contain the acylimine bond that is thought to be labile in the chromophore of red fluorescent proteins [29].

In 20 mM Tris pH 7, 50 mM NaCl and 5 mM DTT, 80% of the original absorption from the mature chromophore of mCherry is recovered post sample heating (Figure D.4). Therefore fluorescence loss can be at least partially attributed to factors other than covalent modification of the chromophore. The loss of absorption from the mature chromophore of mRojoB under the same conditions is irreversible, and only 4% of the original absorption is recovered in tdTomato (Figure D.2). Reversible loss of absorption may be due to increased flexibility in the chromophore, as extinction coefficients are also affected by chromophore planarity [16]. Similar to the mature chromophore of mCherry, the loss of absorption from the off-target GFP-like chromophore of mRojoB (as monitored by the absorption peak at 500 nm) is reversible (Figure D.5). One interpretation of this data is that the secondary structure of mRojoB is disrupted at higher temperatures allowing for increased flexibility in the immature chromophore. Upon cooling, the protein refolds, and the environment of the immature chromophore is re-rigidified, thus allowing for the recovery of absorption at 500 nm. Partial recovery of absorption from the mature chromophore of DsRed has been reported after denaturation in acid, but the percent recovery is dependent on the incubation time [161]. Up

to 90% fluorescence was recovered in GFP following complete denaturation in acid, base or guanidine [248]. These two previously reported results suggest FP denaturation is at least partially reversible under certain conditions. The experimental procedure could possibly be optimized for conditions in which RFP unfolding were reversible in order to better measure protein thermostability.

D.4.2 Temperature-Dependent Circular Dichroism Consistent with the Presence of Unfolding Intermediates

Protein secondary structural information can be obtained from circular dichroism spectroscopic measurements of [253]. A positive peak at 190 nm and two negative peaks at 208 and 222 nm is indicative of α helix structure, while a positive peak at 200 nm and a negative between 210 and 220 nm is generally indicative of β sheet structure [254]. Deconvolution of the CD spectrum of GFP, which is similar to the spectra measured for mCherry, mRaspberry and mRojoB, showed the majority of the secondary structure to be β sheet, which is in agreement with the crystal structures of FPs [258]. Although the CD signal arising from β-sheets is smaller than that for α helices, the signal-to-noise ratio of 1 μM samples of tdTomato, mCherry, and mRojoB were ample and indicative of β sheet structure at room temperature.

Temperature-dependent CD measurements were used to further assess the relative stabilities within a set of RFPs. Again, the experiments were not performed under equilibrium conditions. When thermally denaturing mCherry, mRojoB, and mRaspberry in phosphate buffer pH 8, the samples did not fully unfold after heating to 90°C indicating that the secondary structures of the proteins were extremely stable (Figure D.8). This finding is consistent with previous measurements of the thermo and kinetic stabilities of other FPs. For example, melting temperatures higher than 80°C have been measured for several green fluorescent protein variants, and high stabilities of FPs have been confirmed using other methods, such as hydrogen-deuterium exchange and chemically induced denaturation [163, 165, 246, 248].

Upon sample heating in citrate buffer pH 3.3, the positive peak at 200 nm decreased for each protein, representing a loss of β-sheet structure (Figure D.11). However, again, the samples for mCherry and tdTomato did not reach equilibrium even after heating to 90°C. In addition, the presence of two inflection points when monitoring the temperature dependence of CD suggests more than two-state denaturation (Fig-

ure D.12). While two-state chemically induced denaturation of other RFPs has been observed previously [41], these data indicate more than two states when thermally inducing denaturation of tdTomato, mCherry and mRojoB in citrate buffer pH 3.3.

For tdTomato, the residual structure after heating suggests that the denaturation may be even more complex. Under acidic conditions, tdTomato retains residual secondary structure after heating to 90°C, while mCherry and mRojoB do not (Figure D.11). The CD spectra for tdTomato at 30°C is characteristic of a β-sheet, while those at temperatures higher than 60°C are characteristic of an α-helix. The peak at 190 nm, indicative of α helix character, is still present in the spectrum of tdTomato collected at 30°C post temperature ramping (Figure D.14). The spectra for mCherry and mRojoB before heating are representative of β-sheet character, and a peak at 190 nm is not apparent in mCherry or mRojoB at higher temperatures (Figure D.11). These data indicate different denaturation pathways for the dimer compared with the two monomers. Literature accounts exist for trifluoroethanol induced β-sheet to α-helix transitions [264], however, thermally-induced α-helix to β-sheet transitions are more commonly studied since secondary structure transitions from α-helix to β-sheet are important for prion and amylogenic diseases [265].

As discussed previously, at least two separate processes are likely occurring during denaturation: denaturation of the secondary structure and cleavage of the acylimine bond in the chromophore. These two separate processes may account for the two inflection points observed in the CD versus temperature data for mCherry and mRojoB (Figure D.12). Interestingly, the chromophore of Kaede RFPs is only covalently bound to the C-terminus of the protein [266]. Thus, the protein is actually two polypeptide chains when fully mature and properly folded. The denaturation process of Kaede RFPs should be compared with mCherry and mRojoB to gain insight into the sources of the two inflection points in the data from temperature-dependent CD experiments. However, a partially denatured intermediate for GFP, which contains no labile acylimine bond, has been proposed, suggesting that more than two-state denaturation may occur independent of covalent modification of the chromophore [158, 165].

Although these experiments cannot be used to calculate precise melting temperatures due to the irreversibility of the denaturation process under these conditions, the data can be used to compare the relative stabilities under these conditions. The two inflection points for the temperature-dependent CD

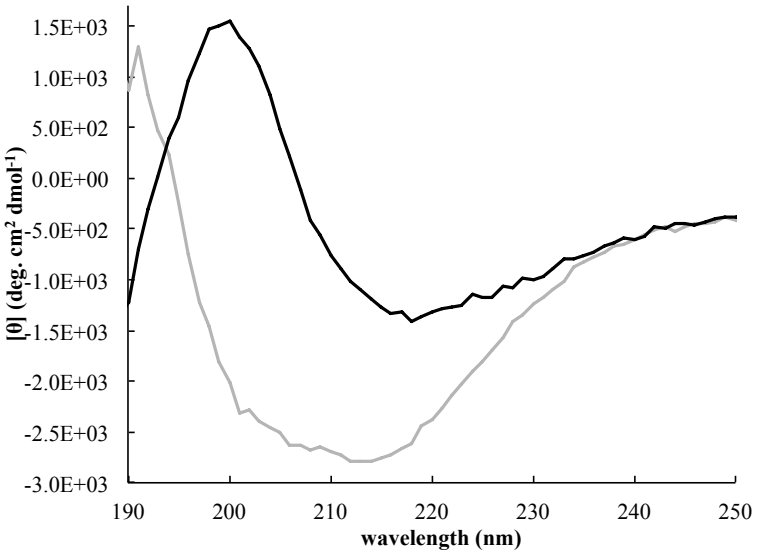

Figure D.14: The 30°C CD spectra of tdTomato in citrate buffer pH 3.3 before (black) and after (grey) heating from 30-90°C.

curves occur at different temperatures for the two monomers, despite high similarity in amino acid sequence (only five differences) and crystal structures [25] (Figures D.12 and 2.8, and Table D.2). As previously explained, the crystal structures of mCherry and mRojoA, only one residue different from mRojoB, overlay with an RMSD of less than 0.3Å (Figure 2.8). One possible interpretation of the lower temperatures of the two inflection points in mRojoB is that it is less stable, (although whether less thermostable or less kinetically stable has not been probed), than mCherry. mRojoB may be less stable than mCherry in part because it was developed with the goal of increasing the wavelength of fluorescence emission rather than preserving stability. The optimization of one physical property at the expense of another physical property is a common trend in fluorescent protein development [33]. By contrast, the goal for directed development of mRFP1, from which mCherry was developed, was regaining fluorescence after the disruption of the dimeric interface. Since the chromophore must be in a well folded protein to fluoresce [160, 267], perhaps the selection pressure used to develop mRFP1 had the effect of thermodynamically stabilizing the structure. However, no data were collected for mRFP0.1, the RFP from which mRFP1 was developed, or mRFP1, to test this idea that stabilization of mRFP1 relative to mRFP0.1 contributed to fluorescence recovery. From mRFP1, mCherry was developed with the goal of increased brightness. This developmental pressure may have preserved the putative protein stability regained in mRFP1. Thus, the apparent increased stability of mCherry relative to mRojoB may be attributable to different selective pressures during directed development.

Comparison of the stability of tdTomato relative to the two monomers is complicated by the shift in the CD spectrum from a positive peak at 200 to 190 nm, consistent with a shift in secondary structure after sample heating. However, the first inflection point observed in the temperature-dependent CD curve for tdTomato occurs at a higher temperature than in mCherry or mRojoB (Table D.2). These two results are consistent with tdTomato being more stable than the monomers, although the denaturation pathway for tdTomato appears to be more complicated. The residual interface in tdTomato as well as the smaller number of mutations relative to wild-type DsRed may be factors contributing to increased stability relative to the monomeric RFPs studied.

D.5 Summary: RFPs are Stable, and May Involve and Intermediate in the Denaturation Pathway

Fluorescent proteins have been found to be very stable at increased temperatures [268], low or high pH [30] and in the presence of denaturants [41]. The structures of tdTomato, mCherry, mRaspberry, and mRojoB appear quite stable as well, although denaturation experiments were not performed under equilibrium conditions. More than two-state sigmoidal melting curves were observed when using citrate buffer at pH 3.3 which may be reflective of an intermediate in the denaturation pathway. The first and second inflection points in the curves for mCherry occur at higher temperatures than those in mRojoB, suggesting decreased stability in mRojoB relative to mCherry. In addition, a peak at 190 nm suggests residual structure is present in tdTomato after heating. These melting studies confirm that these RFPs are highly stable despite the introduction of many potentially destabilizing mutations and support the idea that a partially denatured intermediate is present in the denaturation pathway. In addition, due to multiple mechanisms by which fluorescence and absorption may be lost, one must be cautious when drawing conclusions about the relative thermostabilities of RFPs using temperature-dependent fluorescence. Notable conclusions from the temperature-dependent fluorescence and absorption experiments include the ability of mCherry to maintain fluorescence at higher temperatures than tdTomato or mRojoB and to recover a larger percent of fluorescence after heating to 90°C in the absence of denaturant. These results may prove useful when selecting which RFP to use to study thermophilic organisms, for example.